ABSTRACT

Title of dissertation: LARGE EDDY SIMULATION
OF FIRE EXTINCTION PHENOMENA

Sébastien Vilfayeau, Doctor of Philosophy, 2015

Dissertation directed by: Professor Arnaud Trouvé
Department of Mechanical Engineering

The simulation of fire phenomena using classical Computational Fluid Dynamics (CFD) methods has made remarkable progress in the past 20 years. However, the occurrence of flame extinction is still a challenge for combustion modeling in general, and for fire modeling in particular. The study is performed using FireFOAM; FireFOAM is an advanced Large Eddy Simulation (LES) fire modeling software developed by FM Global and is based on a general-purpose open-source software called OpenFOAM. A new flame extinction model based on the concept of a critical value of the flame Damköhler number is incorporated into FireFOAM. The objective of the present study is to evaluate the ability of CFD-based fire models to simulate the effects of flame extinction in two different configurations (under-ventilated compartment fire and turbulent line fire in controlled co-flow, *i.e.* nitrogen or water-mist). Comparisons between experimental data and numerical results provide a suitable test bed to evaluate the ability of CFD-based fire models to describe the transition from extinction-free conditions to conditions in which the flame experiences partial or total quenching.

LARGE EDDY SIMULATION OF FIRE EXTINCTION PHENOMENA

by

Sébastien Vilfayeau

Dissertation submitted to the Faculty of the Graduate School of the
University of Maryland, College Park in partial fulfillment
of the requirements for the degree of
Doctor of Philosophy
2015

Advisory Committee:
Dr. Arnaud Trouvé, Chair/Advisor
Dr. Andre Marshall
Dr. Peter Sunderland
Dr. Johan Larsson
Dr. Yi Wang
Dr. Elaine Oran, Dean's Representative

Foreword

"*Imagination is more important than knowledge.*" - Albert Einstein

"*The important thing is not to stop questioning. Curiosity has its own reason for existing. One cannot help but be in awe when he contemplates the mysteries of eternity, of life, of the marvelous structure of reality. It is enough if one tries merely to comprehend a little of this mystery every day. Never lose a holy curiosity.* - Albert Einstein

Dedication

To my brother, Benoit. From where you are now, you will always be in my heart.

To my parents, Philippe and Isabelle. To my brother and sister, Jérôme and Juliette.

Acknowledgments

This research project is funded by FM Global under the Strategic Research Program for Fire Modeling. It was a real pleasure to have spent a summer at FM Global and to have been directly exposed to the state-of-the art of fire research. This project is also part of a university-industry partnership sponsored by the National Science Foundation (NSF-GOALI grant program; Award #1236788); the NSF-GOALI project is a joint collaboration between the Department of Fire Protection Engineering at UMD, FM Global, and United Technologies Research Center. Research and Teaching Assistantship support was provided by the Department of Fire Protection Engineering and the Keystone Engineering Program.

First and foremost I would like to thank my advisor, Professor Arnaud Trouvé, for giving me the invaluable opportunity to work on challenging and extremely interesting projects over the past four years. Thanks for indoctrinating me into the ways of science, combustion and computer simulations, for his steadfast support, limitless patience, and encouragement that he has given to me, and for his commitment to excellence in research.

I would also like to acknowledge the invaluable help of Dr. Vivien Lecoustre. I have a profound admiration and respect for his knowledge. I am very honored to have the opportunity to collaborate with him and to learn from him and its expertise on extinction phenomena.

I would also like to thank my committee members, Dr. Peter Sunderland, Dr. Andre Marshall, Dr. Johan Larsson, Dr. Yi Wang, and Dr. Elaine Oran for their

precious help, comments and advice.

I owe my gratitude to all the people who have made this thesis possible and who have made my life as a graduate student at University of Maryland in College Park one that I will cherish forever.

I would like to thank the whole Fire Protection Engineering Department Faculty and staff members for their generous support, help and cordial environment which contribute to the excellent work ambiance, propitious to high-level research and learning.

I would like to thank my fellow colleagues and graduate students James White and Eric Link who performed the measurements in Chapter 6, for their precious help and contributions on flame extinction. Special thanks to my colleagues Taylor Myers for his stimulating discussions on mutli-phase flow with droplets particles. I am not forgetting my fellow graduate students for the joy they brought me working with them and for the friendships we developed. I would like to thank Ning Ren, Ayodeji Ojofeitimi, Salman Verma , Blaise Delmotte, Luis Bravo, Ben Trettel, Simon Roblin, David Souvandy, Maria Theodori, Cong Zhang.

I would like to thank the interviewees Christine Pongratz, Dr. Dr. Fabian Bräanström and Dr. Virginie Drean for their time and great feedback about the usage of fire modeling software by the industry and by fire safety engineers.

My sincere thanks to Thierry Huttler who taught me that perseverance, determination, patience and a good sense of humor and anticipation leads to success.

Table of Contents

List of Figures

1 Introduction

1.1 Fire Dynamics

1.1.1 Definition

"*Fire Dynamics is the study of how chemistry, fire science, material science and the mechanical engineering disciplines of fluid mechanics and heat transfer interact to influence fire behavior. In other words, Fire Dynamics is the study of how fires start, spread and develop.*" - National Institute of Standards and Technology (NIST) [8].

1.1.2 Compartment Fire

Compartment fires (also called enclosure fires) feature specific complex phenomena associated with smoke accumulation, restricted air ventilation, and in a number of cases interactions with automatic fire suppression systems such as sprinkler [9–11]. In compartment fires, the fuel sources are typically flammable objects, *i.e.* solid. There are various materials within a solid with their own thermal properties such as heat of vaporization, conductivity, density, heat capacity, etc. Like liquid evaporation, solid pyrolysis is an endothermic process and the phase change

from solid to gas phase is controlled by the gas-to-solid heat transfer processes (also called the thermal heat feedback). The rate of formation of these vapors (also called the fuel mass loss rate) is an unknown quantity in fire configurations and corresponds to a variable that is an integral part of the combustion problem as discussed in chapter 5. Pyrolysis of natural and man-made items produces toxic chemicals. Toxic chemicals are a major health concern and have many health effects (skin, eye and sensory organ, respiratory, cardiovascular and blood, mutations, ecological (Colborn et al. 2010)). However, it remains a highly technical challenge and is left out of the present study. In fire, the flow is buoyancy-driven (*i.e.* dominated by the buoyant acceleration due to density difference and independent of the initial fuel stream characteristics). Turbulence features moderate velocities on the order of several meters per second corresponding to low-to-intermediate Reynolds numbers. Slow mixing and long residence times characteristic of fire tend to enhance soot formation and radiative losses. An important feature of compartment fires with multiple flammable objects is the upper layer: when it reaches a sufficiently high temperature (approximately 800 K–900 K), a dramatic increase in the fire size called flash-over may also be observed; flash-over corresponds to a rapid fire spread phase (*i.e.* a rapid series of spontaneous ignition events) involving all flammable objects and materials present in the fire room and driven by radiant emissions from the hot and sooty upper layer [9–11]. On the other hand, the presence of a smoke layer may also have an opposed effect on the heat release rate. In typical large fire situations, the smoke layer descends to the floor and occupies most of the compartment volume, so that large sections of the flame are supplied with vitiated air, *i.e.* a mixture of

pure air and re-circulating combustion products. Air vitiation has the double effect of changing the oxidizer stream composition (an oxygen dilution effect) as well as its temperature (a pre-heating effect). The dilution effect has a negative impact on the flame burning rate, whereas the preheating effect has a positive impact. Due to inherent heat losses in the compartment system, the dominant effect is oxygen dilution and the net effect of air vitiation is to decrease the burning rate [12]. Sufficient levels of air vitiation will result in sub-critical oxygen concentrations and consequent (partial or total) flame extinction (defined as a sudden transition from burning to non-burning conditions) [13, 14] (chapter 5). An example of a traditional fire development in a compartment fire as described previously (*i.e.* flash-over followed by the descend of the smoke layer to the floor) can be visualized on the NIST website (http://www.nist.gov/fire/upload/NS_multi.wmv).

1.1.3 Fire Suppression

Fire suppression is a key aspect of fire dynamics in order to predict the fire growth and/or the fire spread. The flame Heat Release Rate (HRR) is a function of two parameters: the combustion efficiency (χ_a) and the fuel mass loss rate ($\dot{m}_F$), and is defined as:

$$\dot{Q}_{fire} = \chi_a \times \dot{m}_F \times \Delta H_F \tag{1.1}$$

where ΔH_F is the heat of combustion.

There are two major processes to reduce the flame HRR and suppress the flame (Fig. 1.1). The first process is surface cooling and consists of fire weakening due

to a decrease in the fuel mass loss rate ($\dot{m}_F$), as a result of a reduced thermal heat feedback (smoke layer cooling; radiation blockage) or flame spread inhibition (pre-wetting of virgin fuel surfaces like in sprinkler applications). The second process is flame cooling and corresponds to fire weakening due to a decrease in the combustion efficiency (χ_a), as a result of an increase in heat losses by thermal radiation in large-scale pool fires (emission of products of incomplete combustion - soot, CO, etc), evaporative cooling (water-mist in fire suppression applications), or oxygen displacement (injection of inert gaseous agents like nitrogen; oxygen starvation in under-ventilated fires).

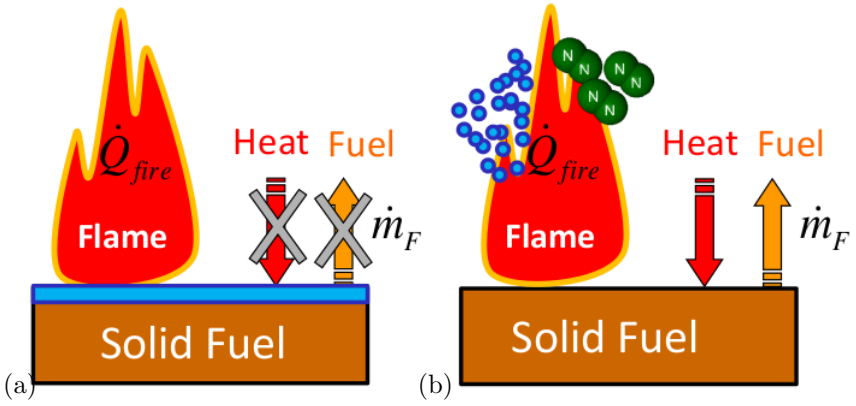

Figure 1.1: Schematic of the two suppression processes. a) Surface cooling due to radiation blockage and surface pre-wetting; b) Flame cooling due to water-mist and nitrogen injections.

Note that a primary goal of suppression systems is to control the fire size and the smoke layer height in order to provide a certain amount of time for individuals to leave the building safely. This exit time is calculated via human evacuation models (also named as Egress Models) [1].

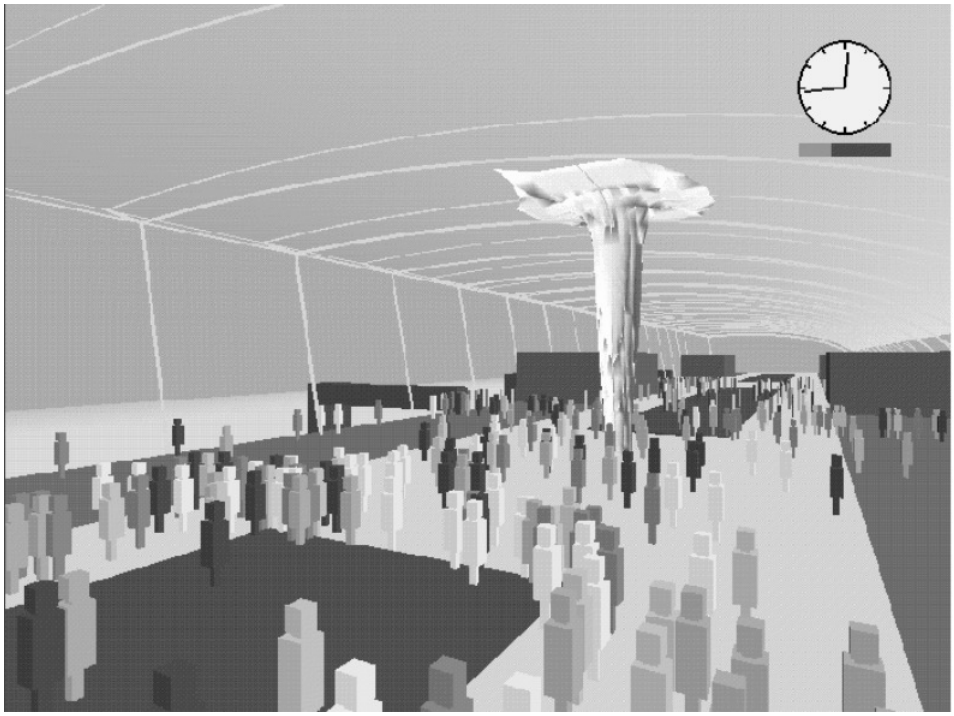

Figure 1.2: Simulation of smoke spread and human egress in the design for the Brussels airport passenger terminal [1].

1.2 Fire Modeling

We now turn to a discussion of the different fire modeling approaches (Zone modeling vs CFD).

1.2.1 Introduction

Recently, due to the fast development of Computational Fluid Dynamics (CFD) techniques and computer hardware, CFD fire modeling has become a promising approach to bring advanced fire science into fire protection practice. Significant progress has been made by CFD modeling [12, 15] in fire safety studies related to fire detection, smoke management, and egress design. The early adoption and

success of CFD fire models are due to the relatively simple requirements of these applications, where a design fire with a given heat release rate history is usually specified, and only smoke transport is modeled (see appendix A). The buoyancy induced turbulent flow is the most critical physical model in these applications, while details of gas phase combustion, heat transfer, solid fuel degradation, and water transport are unimportant or even irrelevant. Zone modeling has been widely used by fire protection engineers for this kind of applications (section 1.2.2).

On the other hand, applications related to industrial fire protection require understanding and modeling of a much wider range of physical phenomena related to the interaction of active fire protection systems with a growing fire. For example, in a warehouse rack storage fire scenario, given ignition, the incipient fire heats up solid combustibles through convective and radiative heat transfer, and spreads vertically and laterally along solid surfaces; the growing fire entrains air while rising up to the ceiling; the hot air and combustion products activate sprinklers when the thermal link reaches a critical temperature; water spray is injected downward with the designed flow pattern and flow rate; water droplets interact with fire in the gas phase flow through mass/momentum/energy transport; the penetrated droplets reach the solid fuel surface and cascade down through the fuel array pre-wetting the unburned fuel and interacting with the burning fuel to achieve fire suppression. All the physical and chemical processes involved need to be modeled and solved numerically on a discrete mesh, while proper model coupling and numerical behavior need to be maintained.To this end, CFD fire solver has been developed (section 1.2.3).

1.2.2 Zone Modeling

In many compartment fire configurations, the flow confinement and buoyancy forces lead to a natural stratification of the gaseous environment into two zones: a ceiling layer resulting from the accumulation of high temperature combustion products mixed with entrained air; a floor layer corresponding to fresh air at ambient temperature. This two layer description is the basis of an early and remarkable computer-based modeling strategy developed in the 1980s and known as zone modeling [16–19]. Zone modeling is the precursor of current fire modeling approaches based on computational fluid dynamics (CFD). Zone modeling uses a classical control volume analysis in which a two-layer decomposition is applied to every room present in an arbitrarily complex building system (Fig. 1.3). The time evolution of the depth of the ceiling layer as well as that of the bulk variables that characterize each layer are calculated using simplified conservation statements for mass and energy combined with the Bernoulli equation and engineering correlations to describe convective transport. The zone modeling strategy provides a simple and cost-effective approach to simulate compartment fire dynamics; the primary objective of zone models is to simulate smoke and heat transport inside a building for a given fire location and size [12].

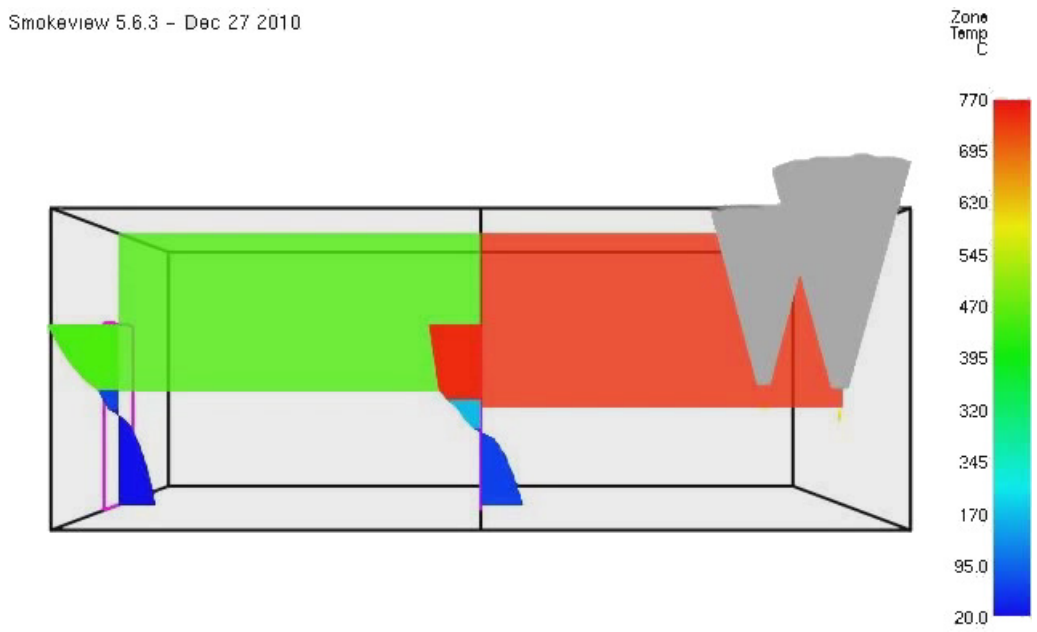

Figure 1.3: CFAST simulation [2]. Two sofas are located in the right compartment. The first sofa is burning and the second sofa ignites when it receives a heat flux of 20 kW m^{-2}.

The heat release rate associated with the combustion process is prescribed by the user with the implicit understanding that fire growth and fire spread (fire growth may be loosely defined as the intensification of the heat release rate associated with a given fuel source, whereas fire spread may be defined as the extension of the active fuel source area, including possibly the ignition of secondary fuel sources) would require more elaborate approaches with higher levels of spatial and temporal resolution, as provided by a CFD treatment.

1.2.3 Computational Fluid Dynamics (CFD)

Important progress has been made over the past decade in the area of CFD. CFD is divided into three categories. Reynolds-averaged Navier-Stockes equations

(RANS) are time-averaged equations of motion for fluid flow, *i.e.* conservation of mass, momentum and energy. In the momentum equation, the Reynolds stress is computed by a turbulence closure model. Large eddy simulation (LES) is a technique in which the smallest scales of the flow are removed through a filtering operation, and their effect modeled using sub-grid scale models. This allows the largest and most important scales of the turbulence to be resolved, while greatly reducing the computational cost incurred by the smallest scales. For high-fidelity LES calculations, the grid has to be sufficiently fine to resolve 80 % of the kinetic energy [20]. This method requires greater computational resources than RANS methods, but is far cheaper than DNS. Direct numerical simulation (DNS) resolves the entire range of turbulent length scales. No closure or sub-grid-scale models are needed, but it is extremely expensive. The computational cost is proportional to $Re^{9/4}$ where Re is a characteristic Reynolds number. DNS is intractable for flows with complex geometries or flow configurations. Due to the nature of fire, *i.e.* large scale flow (from a few centimeters up to several meters) and strongly unsteady transient phases, LES is the dominant CFD approach for fire simulations. Two solvers represent the state-of-the-art of fire modeling: FDS developed by the National Institute of Standards and Technology, USA (`http://firemodels.github.io/fds-smv/`), and FireFOAM developed by FM Global, USA (`http://code.google.com/p/firefoam-dev/`).

1.2.4 FireFOAM and its applications

Given the need to handle a wide range of interacting physical phenomena and complex geometry in industrial scenarios (Fig. 1.4) , the requirements for a CFD

code capable of modeling large-scale industrial fire growth and suppression far exceed the level of a typical in-house research code. The CFD package of choice should be capable of massive parallelization and handling unstructured computational meshes. Given the extent of new models and code implementation, an open-source platform allowing for collaborative model development is the preferred choice. OpenFOAM [21] has been chosen as the CFD platform for the model development. The object-oriented code structure of OpenFOAM [22] enables multiple alternative sub-models to co-exist. Unstructured mesh codes, like OpenFOAM, have complex addressing rules compared to the structured mesh codes and, therefore, cannot take advantage of an FFT-based direct linear solver. As a result, the code may be slower in a single processor mode than those designed for a cartesian grid, such as FDS [23]. However, the capability of massive parallelization and flexibility of local mesh refinement do effectively alleviate the speed issue. The open-source fire modeling code that has been developed on the OpenFOAM platform is called FireFOAM [24, 25]. The code is designed to model industrial fire growth and suppression. It integrates the main gas phase CFD solver with numerous sub-models in the form of object libraries, including diffusion-controlled combustion, turbulence [25], pyrolysis [26, 27], Lagrangian droplet transport [28, 29], surface water film [30, 31], radiation, soot [32], wall boundary layer [33], etc.

In addition to the development and validation of separate-effect models (see chapter 3 on verification test cases), many validation exercises for both fire growth and suppression have been performed to evaluate the integrated FireFOAM model. These studies include fire growth between vertical parallel panels [34], rack storage

fire growth [35], and rack storage suppression under uniform water flux [29]. Figure 1.4 is an example of the latest FireFOAM modeling of rack storage fire suppression with sprinklers [36]. The model results show good quantitative agreement of heat release rates in all three phases, from ignition to fire growth and steady burning. For the suppression cases, HRR can not be measured experimentally under a large movable ceiling, so only the modeled HRRs are included in Fig. 1.4. The model reproduces the suppression effectiveness of the two sprinkler protection schemes: K14 sprinklers suppress the fire rapidly with only one sprinkler activated at around 40s, while with K11.2 sprinklers, both in the tests and simulation, the fire spreads to the pallets at the end of the fuel array with multiple sprinkler activations. In this application, the main suppression mechanism is surface cooling. The thermal cooling of the fuel surface provided by the water flow is achieved through the blockage of radiative and convective heat transfer from the gas phase, as well as the convective cooling by the water flow. The reduced solid phase temperature due to surface cooling leads to a local reduced burning rate and to possible suppression of the burning region [36]. It is noted that gas phase extinction, another suppression mechanism that is more relevant to water mist system [37], is not considered in the current gas phase model, is the subject of this manuscript, and is discussed in the next section.

(a)

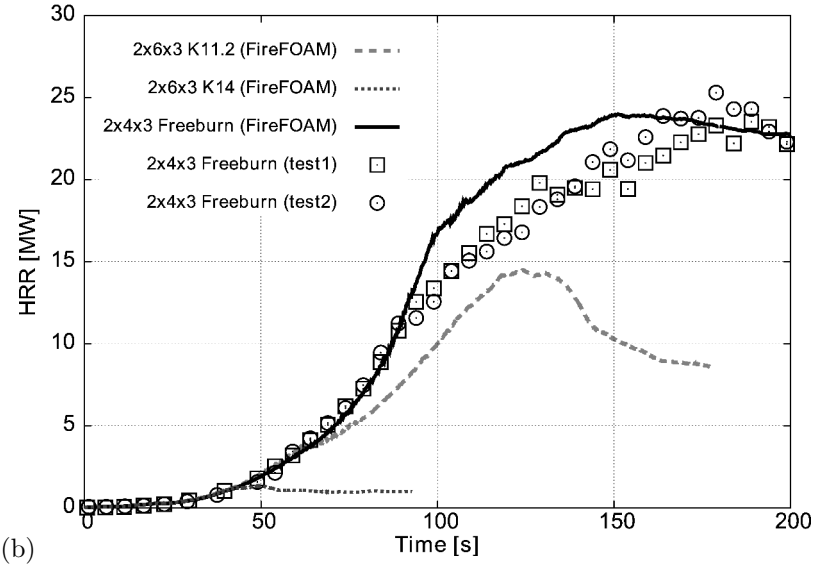

(b)

Figure 1.4: a) Snapshot of fire from FireFOAM modeling (left) and fire test (right) for the FM Global rack storage experiment; b) Heat release rate history comparison [36].

1.3 Extinction Modeling

First, the different extinction models described in this section use a single-step global combustion equation and should be differentiated from other numerical work on extinction using finite rate detailed chemistry which have access to more accurate description of chemical time scales.

1.3.1 Current extinction models

Extinction is a physical phenomenon depending on a variety of different factors evolving in time such as oxygen concentration, temperature, or flame residence time. Deriving a simple model to predict extinction becomes a difficult task. In addition, it should be noticed that modeling fire extinction using a Large Eddy Simulation (LES) approach, commonly used by the scientific fire community in research and engineering applications such as Fire Dynamics Simulator (FDS) or FireFOAM, becomes an even more complex challenge. Indeed, sub-grid scale quantities such as flame temperature and flame stretch are unresolved in LES simulation and require additional physical modeling.

For the past decades, researchers have tried to address the issue of flame extinction modeling in the context of LES [14, 38–40]. Previous extinction models have been developed and are presented next.

Hu *et al.* [14, 38] have adapted combustion modeling capabilities used in computational fluid dynamics solvers to the treatment of under-ventilated compartment fires. More specifically, they considered two models proposed to describe: diffusion flame extinction due to air vitiation; and the emission of carbon monoxide (CO) and unburnt hydrocarbon (HC) mass in a compartment fire. Their flame extinction model is based on a flammability diagram parametrized in terms of vitiated air properties (temperature and mass fraction). The CO/HC mass model is based on: a transport equation for fuel mass, a comparison of this fuel mass to a Burke-Schumann chemical-equilibrium expression, and an interpretation of the difference

as a measure of incomplete combustion. Both models were implemented into FDS. The models performance was tested via detailed comparisons with an experimental database corresponding to reduced-scale compartment fires with a prescribed fuel mass loss rate.

A similar model was implemented in FDS. Indeed, the previous extinction model in FDS v2 uses the concept of a limiting flame temperature [41], below which combustion is not supported. In brief, the model examines a grid cell and determines if combustion of the fuel in that cell as a stoichiometric mixture would raise the temperature of that mixture in excess of the limiting flame temperature. As initially developed in FDS v2, this model examines only the fuel and oxygen concentrations, and assumes the gas is air with a constant specific heat. The resulting criterion is a linear function that gives the limiting oxygen concentration as a function of the local temperature. This approach has two fundamental problems. First, specific heat from ambient temperature to flame temperature is not constant (for air it increases by more than 25 %). Second, diluent gases can have specific heat capacities that are significantly different than air. For example air at room temperature has a specific heat capacity of 1.0 kJ/(kg K) and water vapor is 1.9 kJ/(kg K).

In order to improve the previous extinction model in FDS, Vaari *et al.* [39] have proposed an improved flame extinction criterion and implemented it into FDS for gaseous suppressants under the lumped species model with transport-limited combustion (infinitely fast chemistry). The criterion considers the total enthalpy of

the gas mixture as a function of temperature and evaluates whether a limiting adiabatic flame temperature can be obtained due to combustion in a cell. The model has been validated against a number of experiments in the cup-burner apparatus, a standard means of obtaining the minimum flame-extinguishing concentrations (MEC) for a variety of fuel-suppressant combinations. The results indicate that the model can reproduce the MEC values for all common inert gas agents, as well as some of the fluorinated halocarbon agents. It should be noted that this extinction model has been tested in DNS mode with a very fine grid. The performance of this model in LES with unresolved flame-based quantities such as temperature is still unknown.

More recently, Snegirev *et al.* [40] have formulated a simplified approach to capture the major flame extinction mechanisms and calibrated their model against the measurement data for critical strain rates of laminar diffusion counter-flow flames with fuel and (or) oxidizer streams diluted by nitrogen. The model is based on the perfectly stirred reactor concept, thereby assuming rapid reactant mixing in the reaction zone, where reactants are delivered in stoichiometric proportions. Model simplicity is achieved by considering a single-step global reaction model. They demonstrate that this model is able to replicate critical strain rates at extinction of both counter- and co-flow flames in a range of experimental configurations including opposed gaseous streams and evaporating liquid pool with a normally impinging oxidizer stream, in the entire range of gaseous diluent concentration enabling flaming combustion. The model correctly predicts the minimum extinguishing concentrations of different inert diluents (argon, nitrogen, water vapor and carbon dioxide)

used in practical fire suppression systems. The application of this extinction model in an LES fire modeling software is an on-going effort.

Despite the relative success of these extinction models (when compared to their respective validation cases) in describing the transition from extinction-free conditions to partial or total quenching, these models (Hu *et al.*, Vaari *et al.*) are not expected to perform well for low or highly strained flames. Indeed, these previous models are based on the concept of a critical flame temperature and do not include the effect of flame residence time. Concerning the extinction model based on the perfectly stirred reactor approach (Snegirev *et al.*) including strain rate effects (residence time), it has not yet been validated in a LES framework. In addition, these extinction models have not been validated for a thermally-driven fuel mass loss rate. Therefore, a new unified extinction model able to capture all different kind of extinction mechanisms (*i.e.* aerodynamic, thermal and dilution quenching) is needed.

1.3.2 A new approach towards a universal extinction model

The simulation of fire phenomena using classical CFD methods has made remarkable progresses in the past 20 years. However, the modeling of flame extinction is still a challenge in numerical combustion in general, and for fire modeling in particular. As described in section 1.1.3, diffusion flames may be extinguished by a number of different mechanisms, *i.e.*, by aerodynamic, thermal, or dilution quenching [3, 42–48]:

- **Aerodynamic quenching:** flame weakening due to flow-induced perturba-

tions (*i.e.*, decrease in flame residence time).

- **Thermal quenching:** flame weakening due to heat losses (*e.g.*, heat losses by convection/conduction to walls, by thermal radiation, by water evaporative cooling in fire suppression applications).

- **Quenching by dilution:** flame weakening due to changes in fuel stream or oxidizer stream composition (*e.g.*, air vitiation in under-ventilated fires).

Laminar flame theory suggests that all these different mechanisms may be characterized by a single flame extinction criterion known as a Damköhler number criterion [42–44] the Damköhler number Da is defined as the ratio of a characteristic fuel-air mixing time divided by a characteristic chemical time, $Da = (\tau_{mixing}/\tau_{chemical})$, and extinction is predicted to occur for values of Da that are critically low. Theoretical analysis shows that the characteristic mixing time τ_{mixing} scales like the inverse of flame stretch, noted χ_{st}, with χ_{st} defined as the stoichiometric value of the scalar dissipation rate. Theoretical analysis also shows that the characteristic chemical time $\tau_{chemical}$ scales like $exp\,(T_a/T_{st})$, where T_{st} is the flame temperature and T_a an activation temperature. Assuming Arrhenius-like combustion chemistry, T_a gives a measure of the sensitivity of the combustion chemistry to changes in temperature. Thus, we find that the Damköhler number is a function of flame stretch and flame temperature, $Da \sim (1/\chi_{st})\,/exp\,(T_a/T_{st})$. Figure 1.5 presents a typical flammability map obtained for heptane-air non-premixed combustion; this map has been constructed using large activation energy asymptotic theory [3].

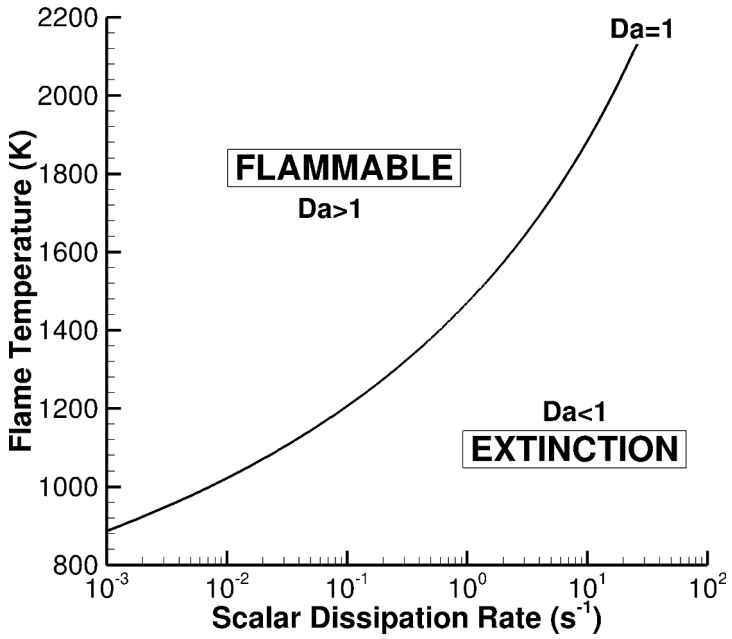

Figure 1.5: Flammability map for heptane-air laminar diffusion flames using flame stretch, χ_{st}, and flame temperature, T_{st}, as coordinates. The solid line corresponds to the extinction limit, $Da = 1$ [3].

The discussion on the flame Damköhler number serves to illustrate some of the current challenges found in combustion modeling since it shows that flame extinction is controlled by flame-based quantities like stretch and temperature that are unresolved in a LES simulation. The occurrence of flame extinction may also be followed by re-ignition, and the modeling of under-ventilated fires or fire suppression, requires both an extinction model and a re-ignition model.

1.4 Objective and Author's Contributions

1.4.1 Objectives

The research conducted as part of this thesis focuses on multi-physics aspects of fire extinction due to radiation heat losses, oxygen dilution and evaporative cooling. The purpose is to develop, implement and validate a new flame extinction/re-ignition model based on the Damköhler number concept into a LES framework. To this end, LES simulations are carried out in two configurations to evaluate the extinction/re-ignition model for different aspects of flame extinction.

In the first configuration (*i.e.* the under-ventilated compartment fire), the objective is to evaluate the ability of current CFD-based fire modeling capabilities to treat flame extinction and thermally-driven MLR [49]. The extinction model is first formulated using the concept of a mixture fraction and validated for different compartment fires scenario, *i.e.* steady over-ventilated fires, steady under-ventilated fires, unstable fires with partial flame quenching, transient fires leading to total flame quenching. While the present study is focused on evaluating simulations with thermally-driven MLR (see section 5.4.1), a series of preliminary tests was also performed using a prescribed MLR approach in which $\dot{m}_f''$ is directly estimated from measured variations of the heptane pool mass.

In the second configuration, a turbulent, methane-fueled, buoyancy-driven, diffusion flame is exposed to air-nitrogen or air-water-mist co-flow. While several experiments have been developed for stuides of fire suppression like the under-

ventilated compartment fire configuration [50, 51] discussed above; few suppression experiments have been conducted to explore and evaluate extinction mechanisms in well-controlled turbulent flames. Relevant data are needed to develop and validate models to simulate weakening and extinction of fires under the challenge of suppression. To this end, a broad collaborative project was established between University of Maryland, FM Global, and United Technologies Research Center exploring flame, momentum, and radiation interactions with fire suppressants. This study focuses on the response of a low-velocity turbulent flame to a diluted oxidizer stream in a canonical configuration having the essential features of suppressed accidental fires [52]. The aim is to test and validate the extinction model into this new configuration for extinction by gaseous agents like nitrogen (chapter 6) and then by water-mist (chapter 7). Th extinction model in this study is re-formulated to avoid using the concept of a mixture fraction.

The aim of this study is to first bring basic information on flames at ambient condition and near the extinction limit, such as flame structure, heat release rate, temperature and velocity, and secondly, to understand flame extinction in those different scenarios by testing the extinction/re-ignition model.

1.4.2 Author's Contributions

The current work is an extension of previous efforts by Dr. Praveen Narayanan [53], who has performed DNS simulations in three configurations to highlight different aspects of flame extinction (owing to stretch, radiation heat loss and evaporative cooling), where the validity of the Damköhler number based criterion is examined.

Dr. Narayanan also performed an asymptotic study of diffusion flame extinction. The current work builds upon this by developing sub-grid scale models to reconstruct the flame temperature and the scalar dissipation rate which are required to compute the cell-based Damköhler number. Two models have been proposed. The first one (model 1) uses mixture fraction and the second one (model 2) is independent of mixture fraction; model 1 is applied to under-ventilated compartment fire simulations; model 2 is applied to turbulent buoyant line burner simulations in which the flame is weakened due to co-flow dilution and the stoichiometric mixture fraction is changing with time.

The candidate has first conducted a series of benchmark tests to evaluate the numerical performance of FireFOAM. Those tests have established a reliable numerical framework to implement the new extinction model.

The candidate has primarily been involved (in terms of code development) in the implementation of the extinction/re-ignition model (chapter 4), and the thermally-driven fuel mass loss rate boundary condition (section 5.4.1).

The candidate's role has been to perform LES simulations in the two configurations and to highlight the different flame extinction mechanisms and the relative weight of re-ignition to the total heat release rate by introducing new diagnostics.

The candidate also performed a detailed grid convergence study by studying the flame temperature, and velocity fields, including mean quantities and rms fluctuations, and the ratio between resolved and the total turbulent kinetic energy. The study on turbulent line burner flames are well-resolved: more than 90% of the turbulent kinetic energy is resolved in the flame region. This well-resolved grid-converged

approach is the continuation of earlier work on wall-resolved vertical wall flames conducted by Dr. Ning Ren [33].

1.4.3 Outline of the Thesis

In Chapter 2, the numerical solver is presented in detail. The governing equations for diffusion flame are introduced, followed by a review of the sub-grid scale and physical models in FireFOAM for the gas, liquid and solid phases, as well as the radiation solver.

In Chapter 3, a series of benchmark tests is presented to evaluate the numerical performance of FireFOAM, *i.e.* the different numerical choices (PISO solver, temporal and spatial schemes, grid resolution, etc) in FireFOAM-2.2.x for the gas, solid and liquid phase solvers.

Chapter 4 discusses the theory of flame extinction. Then, it presents the new flame extinction/re-ignition (model 1 and model 2) based on the Damköhler number concept and implemented in FireFOAM, as well as a series of test cases to verify that the model has been implemented correctly.

In Chapter 5, the extinction model is validated for different compartment fire scenarios using a thermally- driven MLR , *i.e.* steady over-ventilated fires, steady under-ventilated fires, unstable fires with partial flame quenching, transient fires leading to total flame quenching.

In Chapter 6, the extinction model is validated for a turbulent, methane-fueled, buoyancy-driven, diffusion flame exposed to air-nitrogen co-flow (including cases with full flame extinction for sufficient levels of nitrogen dilution).

In Chapter 7, the extinction model is validated for a turbulent, methane-fueled, buoyancy-driven, diffusion flame exposed to air-water-mist co-flow (including cases with full flame extinction for sufficient levels of water loading).

In Chapter 8, conclusions and recommendations for future work are given.

2 FireFOAM

2.1 Introduction

FireFOAM [24, 25] is based on OpenFOAM, a free, open-source, general-purpose, CFD software [21]. OpenFOAM is an object-oriented, C++-based, second-order accurate, finite-volume solver with implicit time integration; the solver features advanced meshing capabilities (structured/unstructured polyhedral mesh) and a massively parallel computing capability using MPI protocols.

FireFOAM is a large eddy simulation (LES) fire dynamics solver that uses a Favre-filtered compressible flow formulation and provides a choice between several modeling options for the treatment of turbulence, combustion and thermal radiation.

2.2 Governing Equations

FireFOAM solves transport equation of mass, momentum, species and sensible enthalpy [54], written as follows.

Mass:

$$\frac{\partial \overline{\rho}}{\partial t} + \frac{\partial (\overline{\rho} \widetilde{u}_j)}{\partial x_j} = 0 \tag{2.1}$$

Momentum:

$$\frac{\partial(\overline{\rho}\widetilde{u}_i)}{\partial t} + \frac{\partial(\overline{\rho}\widetilde{u}_i\widetilde{u}_j)}{\partial x_j} = -\frac{\partial \overline{p}}{\partial x_i} + \frac{\partial}{\partial x_j}\left(\overline{\rho}(\nu + \nu_{sgs})\left(\frac{\partial \widetilde{u}_i}{\partial x_j} + \frac{\partial \widetilde{u}_j}{\partial x_i} - \frac{2}{3}\frac{\partial \widetilde{u}_k}{\partial x_k}\delta_{ij}\right)\right) + \overline{\rho}g_i \tag{2.2}$$

Sensible Enthalpy:

$$\frac{\partial\left(\overline{\rho}\widetilde{h}_s\right)}{\partial t} + \frac{\partial(\overline{\rho}\widetilde{u}_j\widetilde{h}_s)}{\partial x_j} = \frac{D\overline{p}}{Dt} + \frac{\partial}{\partial x_j}\left(\overline{\rho}\left(\alpha + \frac{\nu_t}{Pr_t}\right)\frac{\partial \widetilde{h}_s}{\partial x_j}\right) + \overline{\dot{\omega}'''_{h_s}} - \frac{\partial \dot{\overline{q}}}{\partial x_k} \tag{2.3}$$

Specie Mass Fraction:

$$\frac{\partial\left(\overline{\rho}\widetilde{Y}_k\right)}{\partial t} + \frac{\partial(\overline{\rho}\widetilde{u}_j\widetilde{Y}_k)}{\partial x_j} = \frac{\partial}{\partial x_j}\left(\overline{\rho}\left(D_{Y_k} + \frac{\nu_t}{Pr_t}\right)\frac{\partial \widetilde{Y}_k}{\partial x_j}\right) + \overline{\dot{\omega}'''_{Y_k}} \tag{2.4}$$

State Relation:

$$\overline{P} = \overline{\rho}R\widetilde{T} \tag{2.5}$$

where $\tilde{}$ is the Favre filter operator, ρ is the mass density, u is the velocity, ν is the molecular viscosity, ν_{sgs} is the sub-grid scale viscosity, p is the pressure, g is the gravity, Y_k is the species mass fraction, D_{Y_k} is the molecular diffusivity, h_s is the sensible enthalpy, α is the thermal diffusivity, the specific gas constant R is related to the universal gas constant $R_u(8315\,\mathrm{J\,kmol^{-1}\,K^{-1}})$ and the gas molecular weight MW by $R = R_u/MW$.

The filtered chemical source terms, $\overline{\dot{\omega}'''_{Y_k}}$, and the volumetric heat release rate (HRR), $\overline{\dot{\omega}'''_{h_s}}$, require closure modeling. In this study, an Eddy dissipation Concept (EDC) model (section 2.5) will be used to estimate the chemical source terms, $\overline{\dot{\omega}'''_{Y_k}}$, and the volumetric heat release rate (HRR), $\overline{\dot{\omega}'''_{h_s}}$. The radiation source term, $\frac{\partial \dot{\overline{q}}}{\partial x_k}$, will be described in the radiation section (2.6). The Lewis number is defined as:

$$Le_k = \frac{\alpha}{D_{Y_k}} = \frac{Thermal\ Diffusivity}{Mass\ Diffusivity\ of\ species\ k} \tag{2.6}$$

We assume $Le_k = 1$.

PISO and SIMPLE type of solution algorithms are used to couple the above equations. Additional information about the iteration procedure and discretization scheme can be found in section 2.3 and [55].

2.3 Pressure Based Segregated Compressible Solver

2.3.1 Definition

Pressure vs Density based

- **Density based solver**: the velocity (u) is reconstructed from the momentum (ρu) equation and the continuity equation used to obtain the density (ρ) field while the pressure field is determined from the equation of state.
- **Pressure based solver**: the velocity is obtained from the momentum equation and the pressure field is extracted by solving a pressure or pressure correction equation which is obtained by manipulating continuity and momentum equations.

N.B: The ideal gas law is not solved directly to get the pressure, but is only used to derive the pressure correction equation, obtained from the continuity and momentum equation, as described next.

Coupled vs Segregated

- **Coupled solver**: solves pressure (or density) and momentum equations simultaneously.
- **Segregated solver**: solves pressure (or density) and momentum equations sequentially.

Compressible vs Incompressible

- **Compressible solver**: accounts for the change of density due to pressure. Includes pressure wave formation that has to be handle by the numerics. CFL condition is based on the flow velocity (v) and the speed of sound (c) to handle acoustic waves:

$$\frac{\Delta t}{\Delta x} max\left(c + |v|\right) \leq 1 \tag{2.7}$$

- **Incompressible solver**: does not account for the change in density due to pressure ($Ma < 0.3$), even though the density can vary due to change in temperature. CFL condition is based on the flow velocity:

$$\frac{\Delta t}{\Delta x} max\left(|v|\right) \leq 1 \tag{2.8}$$

N.B: Note that even if FireFOAM is "compressible", the CFL criterion does not include the speed of sound to take into account acoustic waves. Indeed, fully implicit schemes are employed, so that acoustic motion does not limit the time step for the low Mach number scenarios found in most fires (1 10m/s). For example, if $M \sim 0.02$, we have $c \sim 50|v|$. The Δt is then limited primarily by sound wave

propagation in equation 2.7, reducing the allowable Δt by 1/50 compared to an incompressible formulation.

2.3.2 Introduction

It has been shown that there is a fundamental limitation of density-based solvers close to the incompressibility limit [56]. At the same time, based on the flow classification characterized by a Mach number (Ma), for $Ma < 0.3$ the compressibility effects are negligible. This covers a large fraction of flow regimes.

Idea: assemble a solution algorithm capable of handling the low Mach number limit and extend it to compressible flow. Formally, such a method should be able to simulate the flow at all speeds [57].

2.3.3 Segregated Solver

From a numerical point of view, a pressure-based matrix system does not look very attractive: large matrix, with a combination of variables and different nature equations with uncertain performance of linear equation solvers. A step forward could be achieved by deriving a "proper" equation governing pressure and assembling a coupling algorithm. In this way, momentum and pressure could be solve separately (1/4 of the storage requirement of the density-based solver) and handle by external coupling algorithms such as SIMPLE (Semi-Implicit Method for Pressure Linked Equations) or PISO (Pressure Implicit with Splitting of Operator) algorithm [58].

In this case, the first step would be to derive the pressure equation to obey mass

continuity, which will be examined below. To summarize, a segregated solver able to solve a complex and coupled set of equations by iterating over different steps and in specified order until convergence is reached (see section 2.3.6.1).

2.3.4 Derivation of the Momentum Equation in Compressible Flows

Handling Compressibility Effects in Pressure-Based Solvers

In this section, we will explain the derivation of the pressure-based solver for compressible flows as implemented into FireFOAM-2.2.x. The idea behind the derivation of the pressure-based algorithm and pressure-velocity coupling does not suffer from singularity in the incompressible limit and may behave well across the range of speeds. Memory usage for a segregated solver is also considerably lower than a couple one, which may be useful in large-scale simulations.

Spatial and Temporal Discretization

The spatial and temporal discretization of any set of differential equations results in algebraic equations that can be written as

$$\boldsymbol{a}_P \phi_P + \sum_N \boldsymbol{a}_N \phi_N = \mathbf{R}_P - \nabla P \tag{2.9}$$

where P denotes the cell-center of the control volume, where the differential equation is approximated, the index N denotes the grid node of all surrounding control volumes involved in the discretization and $\mathbf{R}_P$ comprises all the known and right hand side terms that emerged from discretization and ∇P is the pressure

gradient. Note that both $\boldsymbol{a}_P$ and $\boldsymbol{a}_N$ are vectors multiplying a scalar field ϕ produces a gradient (vector field). In the semi-discretization formulation, the notation is as follows:

- Scalars in lowercase: a
- Vectors in bold: $\boldsymbol{a} = a_i$
- Tensors in bold capitals: $\mathbf{A} = A_{ij}$

For simplicity, we shall introduce the $\mathbf{H}(\boldsymbol{\phi})$ operator, containing the off-diagonal part of the momentum matrix and any associated right hand side (r.h.s) contributions:

$$\mathbf{H}(\boldsymbol{\phi}) = \mathbf{R}_P - \sum_N a_N \boldsymbol{\phi}_N \tag{2.10}$$

Using a semi-discrete form of the discretized momentum equation, where $\phi_P = u_P$, the following emerges:

$$a_P^{\mathbf{u}} \mathbf{u}_P = \mathbf{H}(\mathbf{u}) - \nabla P \tag{2.11}$$

Compressible Momentum Equation

The compressible form of the continuity equation introduces density into the system

$$\frac{\partial \rho}{\partial t} + \nabla . (\rho \mathbf{u}) = 0 \tag{2.12}$$

In reacting flows, the ideal gas law is assumed to connect the pressure p to the density ρ:

$$\rho = \frac{P}{RT} = \psi P \tag{2.13}$$

where ψ is compressibility:

$$\psi = \frac{1}{RT} \tag{2.14}$$

The momentum equation includes a divergence of velocity term ($\nabla.u$), note the presence of (non-constant) density in all terms.

$$\frac{\partial(\rho\mathbf{u})}{\partial t} + \nabla.(\rho\mathbf{u}\mathbf{u}) - \nabla.\left[\mu\left(\nabla\mathbf{u} + (\nabla\mathbf{u})^T\right)\right] = \rho\mathbf{g} - \nabla\left(P + \frac{2}{3}\mu\nabla.\mathbf{u}\right) \tag{2.15}$$

The final step is to include the pressure decomposition [59]. The pressure is split into a reference or ambient pressure (p_0), hydrostatic pressure ($\rho g.x$) and a dynamic pressure (p_d), as follows:

$$p = p_0 + \rho\boldsymbol{g}.\boldsymbol{x} + p_d \tag{2.16}$$

where p_0 is a constant and $p_0 + \rho\boldsymbol{g}.\boldsymbol{x}$ is the pressure which would exist in the same body of fluid at rest. p_d is the remaining part of the pressure that arises only from the effect of the motion of the fluid.

This expression can be substituted into the pressure term in the momentum equation and the resulting differential equation emerges as implemented in `FireFOAM-2.2.x/solver/UEqn.H`:

$$\frac{\partial(\rho\mathbf{u})}{\partial t} + \nabla.(\rho\mathbf{u}\mathbf{u}) - \nabla.\left[\mu\left(\nabla\mathbf{u} + (\nabla\mathbf{u})^T - \frac{2}{3}\nabla.\mathbf{u}\right)\right] = -\boldsymbol{g}.\boldsymbol{x}\nabla\rho - \nabla p_d \quad (2.17)$$

2.3.5 Derivation of the Pressure equation in Compressible Flows

Compressible Pressure Equation

We start the discussion from the semi-discretized form of the momentum equation (see section 2.3.4)

$$a_P^{\mathbf{u}}\mathbf{u}_P = \mathbf{H}(\mathbf{u}) - \nabla P \quad (2.18)$$

and

$$\mathbf{u}_P = (a_P^{\mathbf{u}})^{-1}\left(\mathbf{H}(\mathbf{u}) - \nabla P\right) \quad (2.19)$$

The next step is to substitute this term into the continuity equation. However, the pressure will not be obtained directly, we need to handle the density-pressure relation. First, we consider the transformation of the rate-of-change term $(\partial\rho/\partial t)$. Using the chain rule on $\rho = \rho(P, T)$ it follows:

$$\frac{\partial\rho}{\partial t} = \left(\frac{\partial\rho}{\partial P}\right)_T \frac{\partial P}{\partial t} + \left(\frac{\partial\rho}{\partial T}\right)_P \frac{\partial T}{\partial t} \quad (2.20)$$

The temperature is, for one outer iteration of the PISO algorithm (see section

2.3.6.1), regarded as fixed (*i.e.* "frozen") [60], we can write

$$\frac{\partial \rho}{\partial t} \approx \left(\frac{\partial \rho}{\partial P}\right)_T \frac{\partial P}{\partial t} \tag{2.21}$$

From the ideal gas law, it follows

$$\left(\frac{\partial \rho}{\partial P}\right)_T = \psi \tag{2.22}$$

We can now focus on the divergence term in the continuity equation and substitute the expression for u and present ρ in terms of P as appropriate

$$\nabla.(\rho \mathbf{u}) = \nabla.\left[\rho (a_P^{\mathbf{u}})^{-1} \mathbf{H}(\mathbf{u})\right] - \nabla.\left[\rho (a_P^{\mathbf{u}})^{-1} \nabla P\right] \tag{2.23}$$

The first term of the RHS is under divergence and represent convection of pressure if we would substitute ρ by ψP.

N.B.: It is unclear why in FireFOAM, ρ is not replaced by ψP in the divergence term. It would be more accurate and avoid extra inner iterations in order to get the updated-converged ρ.

$$\nabla.\left[\rho (a_P^{u})^{-1} \mathbf{H}(\mathbf{u})\right] = \nabla.(F_P P) \tag{2.24}$$

where F_P is the flux representing in the convective effects in the pressure

$$F_P = \psi \left(a_P^{\mathbf{u}}\right)^{-1} \mathbf{H}(\mathbf{u}) \tag{2.25}$$

and is evaluated from the pressure solution (see section 2.3.6.1).

The second term produces a Laplace operator and needs to be preserved. The working variable is pressure and we will leave this term in the current form. Note

the additional ρ pre-factor, which will remain untouched; otherwise the term would be a non-linear function of P.

Combining the above terms, we reach the compressible form of the pressure equation:

$$\frac{\partial(\psi P)}{\partial t} + \nabla.\left[\rho(a_P^{\mathbf{u}})^{-1}\mathbf{H}(\mathbf{u})\right] - \nabla.\left[\rho(a_P^{\mathbf{u}})^{-1}\nabla P\right] = 0 \tag{2.26}$$

Note that the pressure equation is in standard form: it consists of a rate of change, a convection term and a diffusion term.

Applying the pressure decomposition, $p = p_0 + p_d + \boldsymbol{\rho} g.\boldsymbol{x}$ we can find the final form of the pressure equation as implemented in `FireFOAM-2.2.x/solver/p_rghEqn.H`.

$$\frac{\partial(\psi p_d)}{\partial t} + \boldsymbol{g}.\boldsymbol{x}\frac{\partial(\psi\rho)}{\partial t} + \nabla.\left[\rho(a_P^{\mathbf{u}})^{-1}\mathbf{H}(\mathbf{u})\right] - \nabla.\left[\rho(a_P^{\mathbf{u}})^{-1}\nabla p_d\right] - \nabla.\left[\rho(a_P^{\mathbf{u}})^{-1}\boldsymbol{g}.\boldsymbol{x}\nabla\rho\right] = 0 \tag{2.27}$$

2.3.6 PISO Algorithm

Now that the momentum and pressure equations have been derived, one need an algorithm to solve this system of equations. In FireFOAM, a PISO algorithm is used.

Pressure Correction Equation

The SIMPLE algorithm prescribes that the momentum predictor will be solved using the available pressure field. The role of the pressure in the momentum equation is to enforce that the velocity field will obey mass continuity.

After the first momentum solution, the velocity field does not obey mass conservation. Therefore, the pressure field after the first pressure corrector will contain two parts:

- Physical pressure, consistent with global flow field
- A "pressure correction" component, which enforces the continuity and counterbalances the error in the initial pressure guess.

Only the first component should be built into the physical pressure field. In SIMPLE, this is handled by severely under-relaxing the pressure.

Under-relaxation and PISO

Having 2 under-relaxation coefficients which balance each other is very difficult tuning. The idea of PISO is as follows:

- Pressure-velocity system contains 2 complex coupling terms
  - ⋆ Non-linear convection term, containing $u - u$ coupling
  - ⋆ Linear pressure-velocity coupling
- On low CFL number (small time-step), the pressure velocity coupling is much stronger than the non-linear coupling.
- It is therefore possible to repeat a number of pressure correctors without updating the discretization of the momentum equation (using the new fluxes).
- In such a step, the first pressure corrector will create a conservative velocity field, while the second and following will establish the pressure distribution.

Since multiple pressure correctors are used with a single momentum equation, it is no longer necessary to under-relax the pressure.

On the negative side, the derivation of PISO is based on the assumption that momentum and energy discretization may be safely frozen through pressure correctors, which is only true at small time-step.

2.3.6.1 PISO Algorithm

PISO is very useful in simulations where the time-step is controlled by external issues and temporal accuracy is important. In such cases, the assumption of slow variation over non-linearity holds and the cost of momentum assembly and solution can be safely avoided like in Large Eddy Simulation.

Sequence of operations as implemented in `FireFOAM-2.2.x/solver/fireFoam.C`:

1. Use the available pressure field p^* from previous corrector or time-step. Conservative fluxes corresponding to p^* are also available

2. Discretise the momentum equation with the available flux field

3. Solve the momentum equation using the guessed pressure (`FireFOAM-2.2.x/solver/UEqn.H`). This step is called momentum predictor

$$a_P^{\mathbf{u}}\mathbf{u}_P = \mathbf{H}(\mathbf{u}) - \nabla p^* \tag{2.28}$$

4. Calculate the new pressure based on the velocity field (`FireFOAM-2.2.x/solver/p_rghEqn.H`). This is called a pressure correction

step

$$\frac{\partial(\psi p_d)}{\partial t}+\boldsymbol{g}.\boldsymbol{x}\frac{\partial(\psi\rho)}{\partial t}+\nabla.\left[\rho(a_P^{\mathbf{u}})^{-1}\mathbf{H}(\mathbf{u})\right]-\nabla.\left[\rho(a_P^{\mathbf{u}})^{-1}\nabla p_d\right]-\nabla.\left[\rho(a_P^{\mathbf{u}})^{-1}\boldsymbol{g}.\boldsymbol{x}\nabla\rho\right]=0 \tag{2.29}$$

5. Based on the pressure solution, assemble conservative face flux F (`FireFOAM-2.2.x/solver/p_rghEqn.H`)

$$F=\left((a_P^{\mathbf{u}})^{-1}\,\mathbf{H}(\mathbf{u})\right)_f.\mathbf{s}_f-\left(\rho(a_P^{\mathbf{u}})^{-1}g.x\nabla\rho\right).\mathbf{s}_f \tag{2.30}$$

6. Reconstruct the pressure based on pressure decomposition $p=p_0+p_d+\rho\boldsymbol{g}.\boldsymbol{x}$ (`FireFOAM-2.2.x/solver/p_rghEqn.H`)

7. Solve the continuity equation (`FireFOAM-2.2.x/solver/rhoEqn.H`) and update the density ρ

$$\frac{\partial\rho}{\partial t}+\nabla.\left(\rho\mathbf{u}\right)=0 \tag{2.31}$$

8. Explicitly update cell-centered velocity field with the assembled momentum coefficients (`FireFOAM-2.2.x/solver/p_rghEqn.H`)

$$\mathbf{u}_p=(a_P^{\mathbf{u}})^{-1}\left(\mathbf{H}(\mathbf{u})-\nabla p\right) \tag{2.32}$$

9. Return to step 4 if convergence is not reached. In OpenFOAM, this loop is called inner loop and is set to 2 iterations. `FireFOAM-2.2.x/solver/fireFoam.C`

10. Proceed from step 1 for a new iteration. In OpenFOAM, this loop is called outer loop and is at least greater than 3 iterations to ensure mass conservation (see section 3.2.1. `FireFOAM-2.2.x/solver/fireFoam.C`

Please noticed energy and species mass equations (`FireFOAM-2.2.x/solver/YhsEqn.H`) are solved, in series, in the outer loop at step 3 after the momentum equation.

2.4 Turbulence model

In LES, not all the scales of the flow are resolved, the large scales are resolved by the grid and the sub-grid scales are reconstructed by the turbulence model. The sub-grid viscosity plays an important role providing the unresolved transport of mass, momentum and energy, as shown in Eq. 2.2 to 2.4. In addition, the turbulence model provides the mixing time scale used in the combustion model. Therefore, the choice of turbulence model is crucial. Each turbulence model has its own limitations and has been designed for certain kind of applications. Here, two turbulence models will be presented. They belong to the family of sub-grid scale (SGS) models of the eddy-viscosity type [61]. The first one is called the constant-coefficient one-equation eddy-viscosity model (onEqEddy model in FireFOAM) and the second one is its dynamic version, the dynamic coefficient one-equation eddy viscosity model (LDKGS model in FireFOAM).

2.4.1 Constant coefficient one-equation eddy viscosity model

This model, also called oneEqEddy model in OpenFOAM (verification test, see section 3.2.4), is based on solving a transport equation for the SGS turbulent kinetic energy k_{sgs} [22], which is:

$$\frac{\partial\left(\overline{\rho}k_{sgs}\right)}{\partial t}+\frac{\partial\left(\overline{\rho}k_{sgs}\widetilde{u}_i\right)}{\partial x_i}=\frac{\partial}{\partial x_i}\left(\overline{\rho}\left(\nu+\nu_{sgs}\right)\frac{\partial k_{sgs}}{\partial x_i}\right)+P-\varepsilon_{sgs} \tag{2.33}$$

The sub-grid eddy dissipation rate is $\varepsilon_{sgs} = C_e k_{sgs}^{3/2}/\Delta$, where the dissipation term model coefficient is $C_e = 1.048$ and Δ is the filter width, which is proportional to the grid size and for an anisotropic grid, is defined as $\Delta = (\Delta_x \Delta_y \Delta_z)^{1/3}$. The sub-grid eddy viscosity is calculated from the sub-grid kinetic energy:

$$\nu_{sgs} = C_k k_{sgs}^{1/2} \Delta \tag{2.34}$$

where $C_k = 0.094$. The production term, P, is expressed as:

$$-\frac{2}{3}\overline{\rho}\left(k_{sgs} + \nu_{sgs}\frac{\partial \tilde{u}_k}{\partial x_k}\right)\frac{\partial \tilde{u}_i}{\partial x_i} + 2\overline{\rho}\nu_{sgs}\tilde{S}_{ij}\tilde{S}_{ij} \tag{2.35}$$

where the first term corresponds to the variation of turbulent kinetic energy due to thermal expansion and the second due to strain rate. The strain rate tensor has been defined here in tensor notation as:

$$\tilde{S}_{ij} = \frac{1}{2}\left(\frac{\partial \tilde{u}_i}{\partial x_j} + \frac{\partial \tilde{u}_j}{\partial x_i}\right) \tag{2.36}$$

We now introduce the turbulent mixing time scale, τ_{sgs}, used in the combustion model:

$$\tau_{sgs} = \frac{k_{sgs}}{\varepsilon_{sgs}} = \frac{1}{C_e}\frac{\Delta}{k_{sgs}^{1/2}} \tag{2.37}$$

2.4.2 Dynamic-coefficient one-equation eddy-viscosity model

We now introduce the dynamic version of the k-equation model [62] (verification test, see section 3.2.4). Indeed, it would be challenging for the k-equation

model to simulate a flame with a transition from laminar to turbulent flow using constant coefficients SGS model, *i.e.* constant values of the C_e and C_k coefficient. In others words, in a laminar flow undergoing a transition to turbulence the sub-grid-scale kinetic energy must undergo a rapid transition from $k = 0$ to some finite value characteristic of the turbulent state. The idea behind the dynamic model is to sample information on the GS level to evaluate the SGS model coefficient. More information to calculate C_e and C_k can be found in [62, 63].

2.5 Combustion Model

In FireFOAM, combustion is described using a global single-step combustion equation combined with the Eddy Dissipation Concept (EDC) model [64]. EDC is used for modeling a turbulent diffusion flame assuming that the reaction is primarily controlled by turbulent mixing and the fuel mass reaction rate is expressed as:

$$\overline{\dot{\omega}'''_{Y_F}} = \frac{\overline{\rho}}{\tau_{EDC}} min\left(\widetilde{Y}_f, \frac{\widetilde{Y}_{O_2}}{r_s}\right) \tag{2.38}$$

where $\overline{\rho}$ is the (LES-filtered mass density), $\widetilde{Y}_f$ and $\widetilde{Y}_{O_2}$ the (LES-filtered) fuel and oxygen mass fractions, r_s the stoichiometric oxygen-to-fuel mass ratio. In the fully-developed turbulent flow region, the EDC mixing time scale is taken from the turbulence model(see Eq. 2.37): $\tau_{EDC} = \tau_{sgs}/C_{EDC}$ and $C_{EDC} = 4$ [65]. However, this description assumes turbulent mixing and does not apply to regions where the flow is quasi-laminar,*i.e.* the flame base region. In these regions, fuel-air mixing is controlled by molecular diffusion and we may write: $\tau_{EDC} = C_{diff}\,(\Delta^2/\alpha)$, where C_{diff} is a model coefficient ($C_{diff} = 0.4$ [65]) and α the thermal diffusivity. We

finally combine these two expressions and write:

$$\tau_{EDC} = min\left(\tau_{sgs}/C_{EDC}, C_{diff}\Delta^2/\alpha\right) \tag{2.39}$$

2.6 Radiation model

Thermal radiation is known to be an important heat transfer mechanism in large-scale fires. Because of the wavelength dependence, modeling radiation heat transfer in a flame is a difficult task. There are a number of radiation models with varying degrees of complexity in the literature [66]. These can be classified into two main groups: grey and non-grey models. Grey models assume that radiation does not vary with wavelength. In many combustion problems, an optically thin medium assumption is also made in applying grey gas models. The optically thin limit assumption neglects the self-absorption of the gas, and utilizes the Planck mean absorption coefficient, simplifying the radiation treatment. Non-grey narrow-band and wide-band models taking into account the variation of radiative properties with wavelength are more complex and more costly than the grey models, but are more accurate.

2.6.1 Constant Radiant Fraction Model

In the constant radiant fraction approach, the description of thermal radiation is simplified by assuming a grey non-scattering and non-absorbing/optically thin medium (*i.e.* the optical thickness $\tau = \kappa L$ of the radiating gas is below 0.1, where κ is the gas Planck mean absorption coefficient and L a characteristic length), hence

$\overline{\kappa I} = 0$. In the RTE equation (Eq. 2.42), we assume that the flame only emits radiation isotropically, *i.e.*, $\overline{\kappa I_b} \approx \frac{\dot{q}_r'''}{4\pi}$. The RTE simplifies to:

$$\frac{d\overline{I}}{ds} = \frac{\chi_{rad}\overline{\dot{\omega}_{h_s}'''}}{4\pi} \tag{2.40}$$

where I is the radiation intensity, s the distance along a particular ray, $\overline{\dot{\omega}_{h_s}'''}$ the local heat release rate per unit volume, and χ_{rad} is the radiant fraction. The radiative power density(*i.e.*, the radiation source term that appears in the enthalpy equation 4.16) is then obtained as the integral of the right-hand side of Eq. 2.40 over angular space:

$$\dot{q}_r''' = \int_{4\pi} \left(\frac{\chi_{rad}\overline{\dot{\omega}_{h_s}'''}}{4\pi} \right) d\Omega = \chi_{rad}\overline{\dot{\omega}_{h_s}'''} \tag{2.41}$$

2.6.2 Grey Gas Model

In the grey gas approach available in FireFOAM, the radiative transfer equation (RTE) is solved using the finite volume discrete ordinate (FVDOM) method [67] (verification test, see section 3.2.5). The change of radiative intensity I along a direction s in an emitting-absorbing non-scattering grey medium is written as:

$$\frac{d\overline{I}}{ds} = \overline{\kappa I_b} - \overline{\kappa I} \tag{2.42}$$

where I_b is the black-body intensity with $I_b = \sigma\tilde{T}^4/\pi$ and κ is the absorption coefficient of the grey gas. In most flame analyses using the grey gas radiation model, κ is taken to be the Planck mean absorption coefficient, κ_p. Since a flame is a multicomponent, non-homogeneous and non-isothermal medium, the evaluation

of κ_p is performed locally based on the partial-pressure-weighted sum of a_k for each participating species k at the local temperature.

$$\kappa_p = P\left(X_{CO_2} a_{CO_2} + X_{H_2O} a_{H_2O} + X_{CH_4} a_{CH_4}\right) \tag{2.43}$$

where P is pressure (atm), X_k the species k mole fraction, a_k the Planck mean absorption coefficient of species k $(m^{-1}.atm^{-1})$. a_k is described using temperature-dependent curve-fit expressions given in [68]. Radiation to Turbulence Interaction (RTI) is neglected, $\overline{\kappa I} \approx \overline{\kappa}\overline{I}$. Finally, emission is assumed to be equal to absorption, $\varepsilon = \kappa$.

The radiative intensity is given by the integration of radiative intensity over the solid angle.

$$\dot{q}_r''' = \int_{4\pi} \mu I(\Omega) d\Omega \tag{2.44}$$

where μ is the direction cosine and $d\Omega$ is the solid angle.

2.6.3 Wide-Band Model

In the Wide-Band model, the radiative transfer equation (eq. 2.42) is solved for each band (table 2.1). For each solid angle, the total radiative intensity is the sum of the radiative intensity for each bands calculated with the Planck mean absorption coefficient in appendix B.

Table 2.1: Limit of the spectral bands for methane (CH_4).

Bands	Major Species	Wavelength(λ) [µm]	Wavenumber(ω) [1/cm]
1	CO_2, H_2O, CH_4	1.00-2.63	10000-3800
2	CO_2, H_2O	2.63-2.94	3800-3400
3	CH_4	2.94-4.17	3400-2400
4	CO_2	4.17-4.70	2400-2174
5	CO_2, H_2O, CH_4	4.70-10.0	2174-1000
6	CO_2, H_2O	10.0-200	1000-50

2.7 Diagnostics

2.7.1 Thermocouples

In order to compare numerical results to thermocouple temperatures from the experiment, a thermocouple (TC) model has been incorporated into FireFOAM [65]. The thermocouple model is based on the thermal balance for the thermocouple bead given by:

$$\rho_{TC} C_{p,TC} V_{TC} \frac{dT_{TC}}{dt} = \varepsilon_{TC} \left(G - \sigma T_{TC}^4 \right) A_{TC} + h \left(T_g - T_{TC} \right) A_{TC} \tag{2.45}$$

where ρ_{TC} , $C_{P,TC}$, V_{TC}, A_{TC}, ε_{TC} designate the mass density, heat capacity, volume, surface, and emissivity of the thermocouple bead, T_{TC} is the thermocouple bead temperature, T_g the local gas temperature, h a convective heat transfer coefficient,

G the average irradiation received by the thermocouple bead, and σ the Stefan-Boltzmann constant. Material properties of the bead are those of nickel. The default value for the bead diameter is 0.001 m. The default emissivity is 0.9 assuming the bead is mostly covered of soot. The default values for the bead density and specific heat are 8908 kg/m^3 and 0.44 kJ/kg/K, respectively. The TC model in Eq. 2.45 provides a numerical description of the deviations of thermocouple temperature from gas temperature (verification test, see section 3.5.1).

3 Code Verification

3.1 Introduction

The purpose of this chapter is to evaluate the different numerical choices (PISO solver, temporal and spatial schemes, grid resolution, etc) in FireFOAM-2.2.x for the gas, solid and liquid phase solvers. First, for the gas phase solver, an helium plume case is used to determine the number of PISO loops required to enforce mass conservation. Then, two different test cases (Lamb-Oseen vortex with a co-flow and Taylor Green vortex) have been selected to evaluate the numerical dissipation of spatial and temporal schemes. Next, the Finite Volume Discrete Ordinary Method (FvDOM) is evaluated by considering radiative heat transfer in a duct with a participating medium for different path lengths. Lastly, a 2D laminar counterflow flame is used to check the reaction rate mechanism using the eddy dissipation concept assuming a fast chemistry. Second, for the solid phase solver, a semi-infinite wall aims to determine the grid resolution required to solve accurately the heat transfer equation through a wall. Finally, for the liquid phase solver, mass and energy conservation have been checked for different configurations (multiple droplets with no evaporation, droplets with evaporation in dry and humid air).

3.2 Gas Phase

3.2.1 Helium Plume

The aim of this test case is to evaluate the number of PISO loops (see section 2.3.6.1) required to enforce mass conservation. Helium is injected through a $5 \times 50\,\mathrm{cm}^2$ slot burner at $1\,\mathrm{g/s}$ surrounded by an $50 \times 75\,\mathrm{cm}^2$ air-co-flow at $42\,\mathrm{g/s}$. Mesh resolution is $4^3\,\mathrm{mm}^3$ corresponding to 12 cells across the burner.

Figure 3.1 shows helium mass fraction and the velocity magnitude along the burner, and the velocity magnitude across the burner (Fig. 3.1c) at t=20 s.

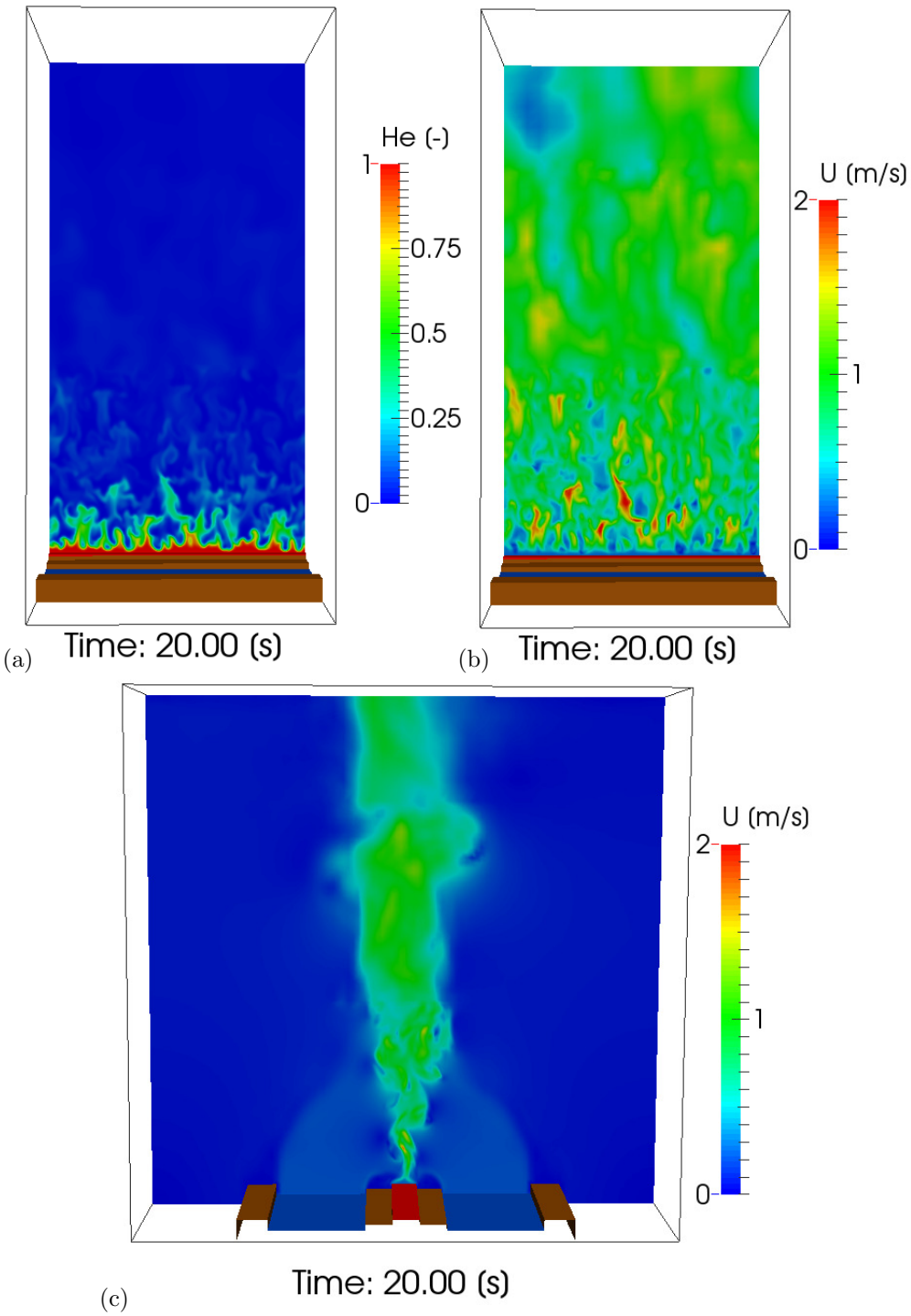

Figure 3.1: Helium plume profile at 20 s. a) Helium mass fraction along the burner; b) Velocity magnitude along the burner; c) Velocity magnitude across the burner.

The helium mass flow rate, $\dot{m}_{He}$, is computed at 6 different heights using equation 3.1 and averaged over the constant z plane and over a period of 20 s (Fig. 3.2).

$$\dot{m}_{He} = \overline{\rho}\widetilde{u}_z\widetilde{Y}_{He} - \overline{\rho}(D_{Y_k} + D_t)\frac{\partial \widetilde{Y}_{He}}{\partial n} \tag{3.1}$$

where ρ is the density, u_z the vertical velocity, Y_{He} the helium mass fraction, D_{Y_k} the molecular mass diffusivity, D_t the turbulent mass diffusivity and n the normal to the surface.

The average mass flow rate and the computational time are reported in Table 3.1 for 1, 2 and 3 PISO loops. 3 PISO loops are required to enforce mass conservation with a relative error less than 0.5 %. For 2 and 3 PISO loops, the computational time increases by a factor 1.9 and 2.6.

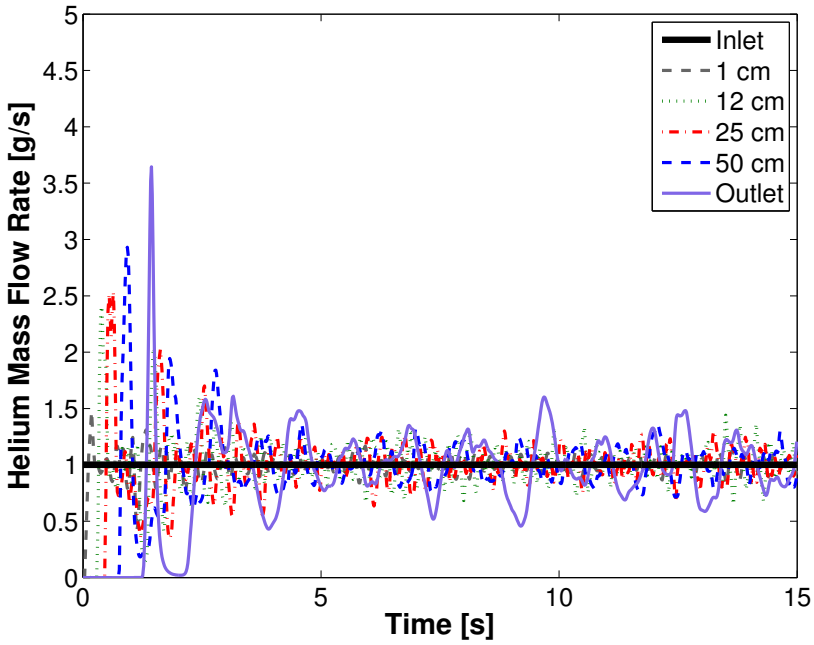

Figure 3.2: Helium mass flow rate as function of time at different heights (0 cm(inlet), 1 cm, 12 cm, 25 cm, 50 cm, 1 m(outlet)).

Table 3.1: Helium mass flow rate at 6 different heights and the total computational time for 40 CPUs for 20 s of simulation.

Height	**PISO** **1 Loop**	**PISO** **2 Loops**	**PISO** **3 Loops**
Inlet	1 g/s	1 g/s	1 g/s
1 cm	1 g/s	1 g/s	1.0032 g/s
12 cm	1.2 g/s	1.1 g/s	1.0026 g/s
25 cm	1.3 g/s	1.1 g/s	1.0011 g/s
50 cm	1.3 g/s	1.1 g/s	1.0022 g/s
Outlet	1.3 g/s	1.1 g/s	1.0019 g/s
Time	1.53 h	2.5 h	3.37 h

Source code: see appendix C.1.1

3.2.2 Lamb-Oseen vortex with co-flow

In this section, the aim is to evaluate the numerical error/dissipation (spatial and temporal) when solving the Navier-Stokes equation. An analytical solution is known by using the Lamb-Oseen vortex model [69], a line vortex that decays due to viscosity. A co-flow is superposed to the vortex in order to add convective effects. Therefore, this study is relevant for our general purpose, *i.e.* turbulent reacting flow modeling in which the turbulent flow might be inaccurately simulated due to numerical dissipation.

Initialization

The domain is 0.1 m long and the co-flow velocity is 0.1 m/s. The vortex velocity is initialized using equation 3.2 and parameters in table 3.2.

$$\begin{aligned} u_x(x,y) &= u_{max}\left(\frac{y-y_c}{r_c}\right) exp\left(\frac{1}{2} - \frac{(x-x_c)^2+(y-y_c)^2}{2r_c^2}\right) + u_{coflow} \\ u_y(x,y) &= -u_{max}\left(\frac{x-x_c}{r_c}\right) exp\left(\frac{1}{2} - \frac{(x-x_c)^2+(y-y_c)^2}{2r_c^2}\right) \end{aligned} \tag{3.2}$$

Table 3.2: Vortex parameter.

Parameter	**Value**	**Units**	**Comments**
r_c	0.005	m	core radius of vortex
u_{max}	0.5	m/s	Maximum Velocity
u_{coflow}	0.1	m/s	Co-flow Velocity
(x_c, y_c)	(0, 0)	(m,m)	center location
ν	1.0×10^{-5}	m^2/s	kinematic viscosity

Figure 3.3 shows the initialization of the velocity components in the x and y directions using equation 3.2. In OpenFOAM, the velocity vector has been initialized using the utility *funkySetFields*. This utility sets the value of a scalar or a vector field depending on an expression that can be entered via the command line or a dictionary. It can also be used to set the value of fields on selected patches. *funkySetFields* is available by downloading swak4Foam (https://openfoamwiki.net/index.php/Contrib/swak4Foam).

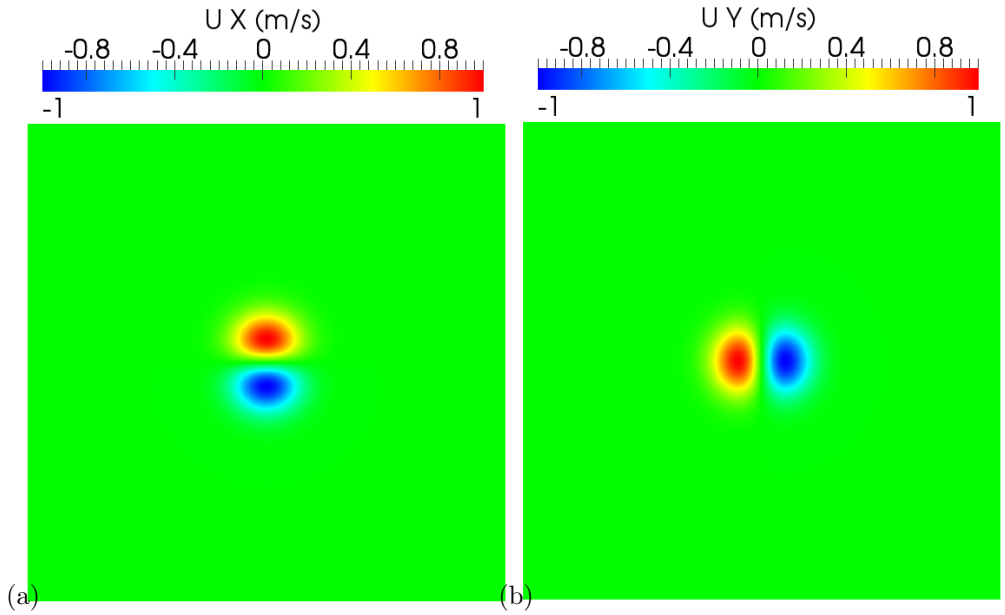

Figure 3.3: Initialisation of velocity field for a a single vortex. a) u_x; b) u_y.

Analytical Solution

Equation 3.3-3.4 are analytical expressions valid for the Lamb-Oseen vortex for the core radius r_c and the maximum velocity u_{max}.

$$r_c(t)^2 - r_c^2(t=0) = 2\nu t \tag{3.3}$$

$$u_{max}(t) = u_{max}(t=0)\left(\frac{2\nu t}{r_c^2(t=0)} + 1\right)^{-3/2} \tag{3.4}$$

The analytical radial velocity is defined as:

$$u_\theta(r) = u_{max}\left(\frac{r}{r_c}\right) exp\left(\frac{r_c^2 - r^2}{2r_c^2}\right) \tag{3.5}$$

The vorticity vector $\overrightarrow{\omega} = \nabla \times \overrightarrow{u}$ is defined in cylindrical coordinates by:

$$\overrightarrow{\omega} = \begin{pmatrix} \frac{1}{r}\frac{\partial u_z}{\partial \theta} - \frac{\partial u_\theta}{\partial z} \\ \frac{\partial u_r}{\partial z} - \frac{\partial u_z}{\partial r} \\ \frac{1}{r}\left(\frac{\partial r u_\theta}{\partial r} - \frac{\partial u_r}{\partial \theta}\right) \end{pmatrix} \tag{3.6}$$

The analytical expression of the vorticity is:

$$\omega_z = \frac{u_{max}}{r_c} exp\left(\frac{1}{2} - \frac{r^2}{2r_c^2}\right)\left(2 - \frac{r^2}{r_c^2}\right) \tag{3.7}$$

Results

Figure 3.4 shows the vorticity magnitude at different times. The vortex maximum vorticity is decreasing as a function of time due to viscosity. the simulation is performed over a period of 2 s corresponding to 2 loops over the domain.

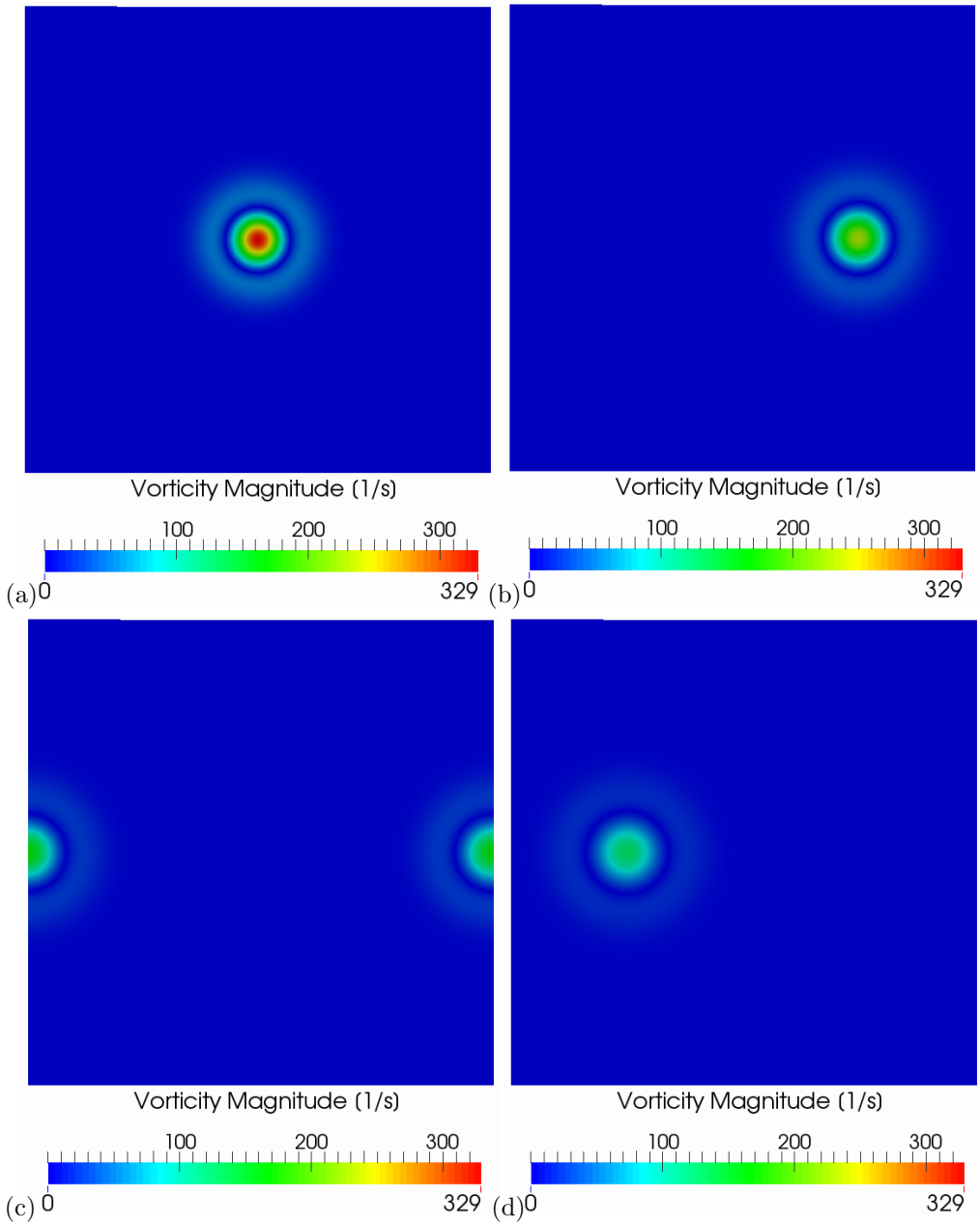

Figure 3.4: Vorticity magnitude for a a single vortex with coflow at different time using 40 cells across the radius. a) t=0 s; b) t=0.25 s; c) t=0.5 s; d) t=0.75 s.

CFL=0.5

We start our discussion with a time step controlled by the CFL criterion with $CFL = 0.5$ which corresponds to an initial time step of 125 µs for a grid resolution $r_c/\Delta x = 40$. Simulations have been performed using a second order spatial scheme and first (euler) or second (backward) order temporal scheme.

Figure 3.5 shows that qualitatively the first order (euler) scheme for time integration is more dissipative than the second order scheme (backward).

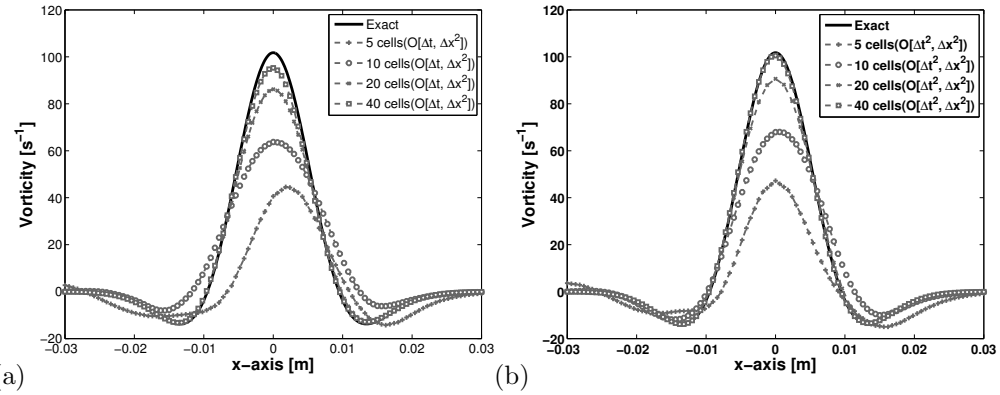

Figure 3.5: Vorticity of a single vortex for different grid size. The solid black line represents the analytical solution. (a) Grey symbols represents euler numerical scheme (first order time integration) (b) grey symbols represents backward numerical scheme (second order time integration).

Figure 3.6 shows the corresponding rms error based on the vorticity as function of the grid resolution (5, 10, 20 and 40 cells across the core radius). The euler scheme is a first order temporal scheme and the truncation error is $O(\Delta t)$. The backward scheme is a second order temporal scheme and the truncation error is $O(\Delta t^2)$. For both schemes, the error decreases as the mesh is refined. The gradient of euler

scheme is parallel to the dashed gray line, indicating first order accuracy of the numerical scheme. However, the gradient of the backward scheme is not parallel to the solid gray line from 10 to 40 cells. This suggests that temporal errors are important in this case. Therefore, in the next test, the time step will be constant and small in order to reduce temporal error and only focused on the spatial error.

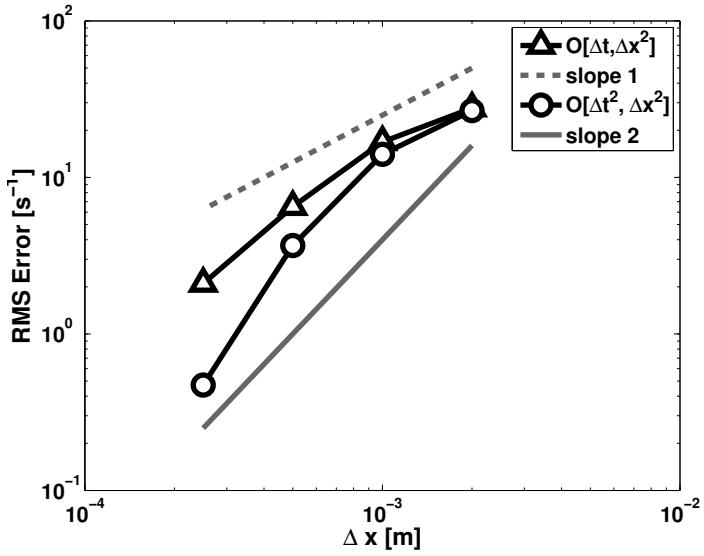

Figure 3.6: Rms error (CFL=0.5). Triangle symbols correspond to the euler numerical scheme (first order time integration) and circle symbols to the backward numerical scheme (second order time integration).

Figure 3.7 presents the vorticity magnitude for a single vortex with coflow at 2 s for 10 and 20 cells and for the euler and backward schemes. For 10 cells across the core radius, the vorticity magnitude is lower and the shape of the vortex is not conserved leading the vortex to an "eye" shape. This indicates that in addition to dissipation errors (amplitude errors), at lower resolution, dispersion errors (phase errors) are also important.

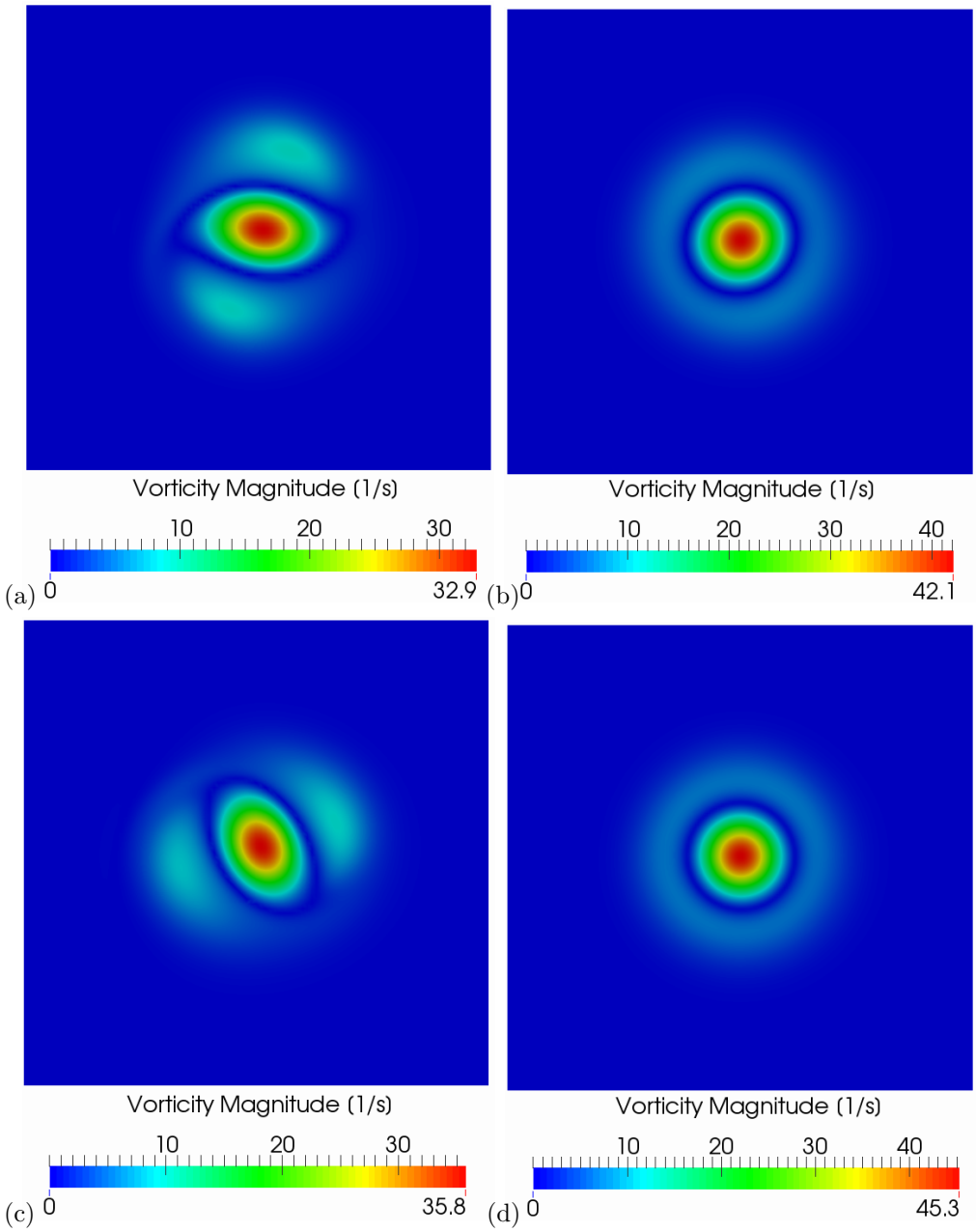

Figure 3.7: Vorticity magnitude for a a single vortex with coflow at t=2 (s). a) 10 cells (euler); b) 20 cells (euler); c) 10 cells (backward); d) 20 cells(backward).

Δt =2.5 µs

We now turn our discussion to a configuration in which the time step has been fixed and set to 2.5 µs in order to reduce the temporal errors. Figure 3.8 shows the rms error based on the vorticity as function of the grid resolution (5, 10, 20 and 40 cells across the core radius). Both the euler and backward scheme are parallel to the solid gray line, indicating second order accuracy of the numerical scheme. In this case, the temporal error has been dramatically reduced in order to only reveal the error due to spatial discretization.

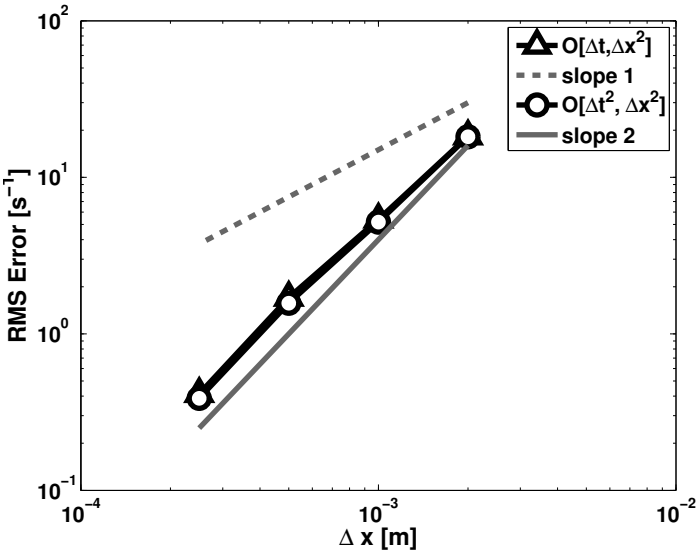

Figure 3.8: Rms error (Δt =2.5 µs) . Triangle symbols correspond to the euler numerical scheme (first order) and circle symbols to the backward numerical scheme (second order).

Conclusion

The numerical dissipation is controlled by the order of the spatial scheme (upwind or central, *i.e.* first or second order) and then by the grid resolution. For a constant error level, lower order methods require more points than high order methods. 40 cells across the core radius is required to get good solution. However, a grid resolution of 20 cells across the core radius is deemed acceptable, the relative error is 7% ($< 10\%$). For a very coarse mesh, dispersion errors (phase errors) start to be as important as dissipation errors (amplitude errors).

Source code: see appendix C.1.2

3.2.3 Taylor-Green vortex

In this section, the Taylor-Green vortex test case is used to measure the preservation of kinetic energy and the enstrophy growth for different temporal schemes (euler, crank-Nicholson and backward). From a well-resolved initial condition, the inviscid Taylor-Green vortex [70, 71] begins stretching and producing even smaller scales. The domain $x_i \in [0, 2\pi)$ is periodic and the grid spacing is $\Delta x_i = 2\pi/64$.

The initial conditions are

$$\rho = 1, \tag{3.8a}$$

$$u = sin(x)cos(y)sin(z), \tag{3.8b}$$

$$v = -cos(x)sin(y)cos(z), \tag{3.8c}$$

$$w = 0, \tag{3.8d}$$

$$p = 100 + \frac{[cos\,(2z) + 2]\,[cos\,(2x) + cos\,(2y)] - 2}{16} \tag{3.8e}$$

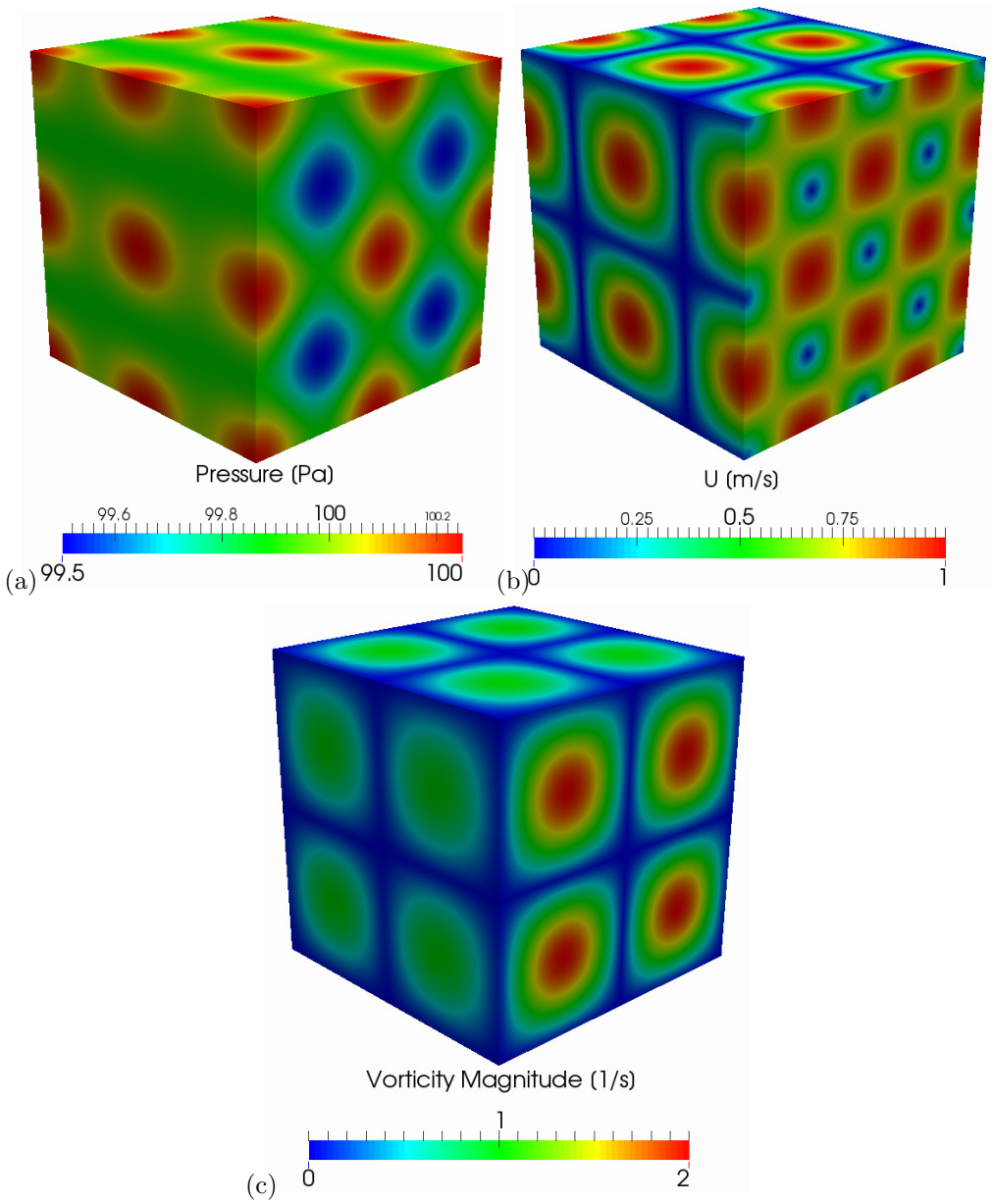

Figure 3.9: Initial conditions for the Taylor-Green vortex. a) pressure; b) velocity magnitude; c) vorticity magnitude.

The numerical results are compared to the semi-analytical solution for the enstrophy growth by Brachet et al. [72] for $t \leq 4\,\mathrm{s}$, where $t \leq 3.5\,\mathrm{s}$ was considered well-converged. In the inviscid problem the kinetic energy should remain constant

while the enstrophy grows rapidly. For an incompressible flow, the vorticity equation is obtained by taking the curl of both sides of the equation of motion [59].

$$\frac{\partial \vec{\omega}}{\partial t} = -\vec{u} \cdot \nabla \vec{\omega} + \vec{\omega} \cdot \nabla \vec{u} + \nu \nabla^2 \vec{\omega} \tag{3.9}$$

Equation 3.9 can also be written as

$$\frac{D \vec{\omega}}{Dt} = \vec{\omega} \cdot \nabla \vec{u} + \nu \nabla^2 \omega \tag{3.10}$$

The Taylor-Green vortex being inviscid ($\nu = 0$), enstrophy grows, i.e. vorticity production, will be only due to stretching (∇u)

$$\frac{D \vec{\omega}}{Dt} = \vec{\omega} \cdot \nabla \vec{\omega} \tag{3.11}$$

Figure 3.10 shows the temporal evolution of the mean kinetic energy, $\langle \rho u_i u_i \rangle / 2$, and enstrophy $\langle \omega_i \omega_i \rangle / 2$, normalized by their initial values. The brackets denote averaging over the computational domain.

$$\langle q \rangle = \frac{1}{V} \int_0^V q(x, y, z)\, dv \tag{3.12}$$

It is seen in Fig. 3.10 that the Euler and Backward temporal schemes are dissipative. After 4s, numerical dissipation leads to under-predictions in the kinetic energy and enstrophy. For the current grid, both temporal schemes agree with the semi-analytical results for the enstrophy growth.

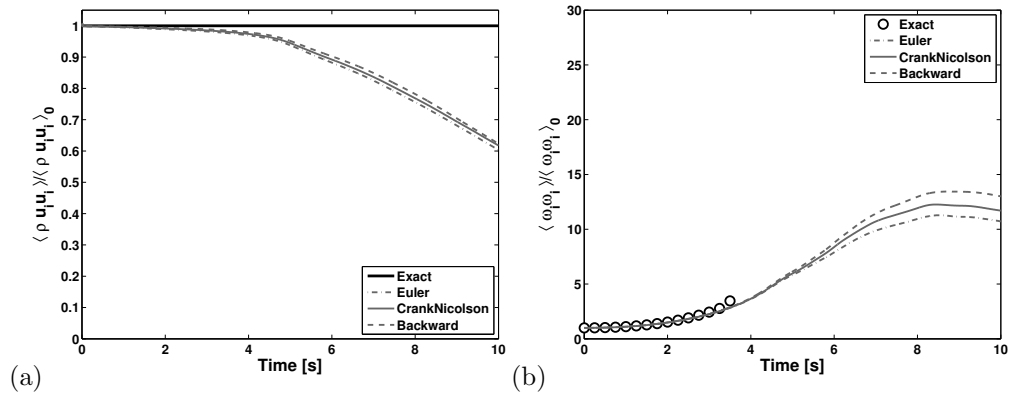

(a) (b)

Figure 3.10: Mean quantities for the Taylor-Green vortex on a 64^3 grid. The zero subscripts denotes the initial value. (a) Kinetic energy; (b) Enstrophy. The semi-analytical solution of Brachet *et al.* (1983) are the black symbols.

In order to provide a quantitative comparison of the two numerical schemes, the mean kinetic energy normalized by its initial value is reported in table 3.3 at $t = 5\,\mathrm{s}$; at this time, vortices smaller than the grid size have been produced and the dissipation effect has become evident. The mean enstrophy normalized by its initial value is also tabulated at $t = 3.5\,\mathrm{s}$; this is the last time for which the semi-analytical solution is known.

Table 3.3: Accuracy metrics for the Taylor-Green vortex, with the semi-analytical result of Brachet et al. [72]

	Euler	**CrankNicolson**	**Backward**	**Brachet et al. [72]**
	$O(\Delta t, \Delta x^2)$	$O(\Delta t^2, \Delta x^2)$	$O(\Delta t^2, \Delta x^2)$	
Energy t=5 s	0.936	0.945	0.952	1.00
Enstrophy t=3.5 s	2.83	2.85	2.89	3.46

Table 3.4 reports quantitative metrics for the Taylor-Green vortex for high-order accurate solvers [71].

Table 3.4: Accuracy metrics for the Taylor-Green vortex for others high-order solvers [71], with the semi-analytical result of Brachet et al. [72]

	Hybrid	**Stan**	**WENO**	**Brachet et al. [72]**
	$O(\Delta t^4, \Delta x^6)$	$O(\Delta t^4, \Delta x^6)$	$O(\Delta t^4, \Delta x^5)$	
Energy t=5 s	1.00	0.976	0.916	1.00
Enstrophy t=3.5 s	3.33	3.23	3.13	3.46

Figure 3.11 shows the Taylor-Green vortex solution at different times. The Q-criterion is used to visualize the vortex, with $Q = 0.1$. The Taylor-Green vortex is observed to stretch and to produce gradually smaller scales. The 3D structure are colored by vorticity magnitude to illustrate the enstrophy growth, *i.e.* the

production of vorticity.

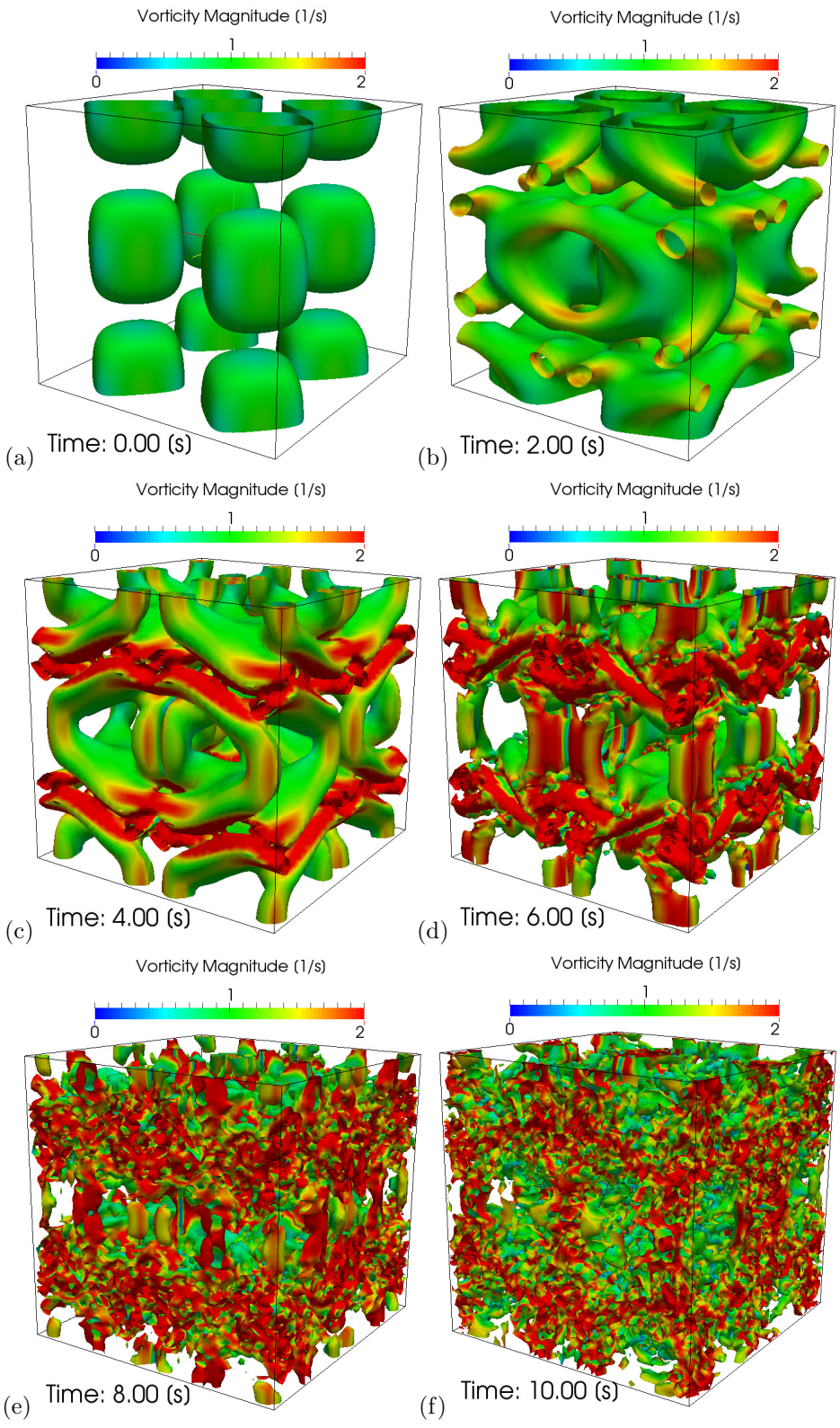

Figure 3.11: Taylor-Green vortex at different times using the Q-criterion with Q=0.1 colored by vorticity magnitude.

Grid Convergence

By definition, the second order spatial and temporal schemes used in FireFOAM are more dissipative than higher order schemes, as reported in table 3.4. Therefore, in order to reach the same level of accuracy, the grid has to be refined. Table 3.5 shows the normalized kinetic energy and enstrophy for 64^3 and 128^3 cells. A mesh twice finer is required to have an accuracy comparable to the Stan solver.

Table 3.5: Accuracy metrics for the Taylor-Green vortex for different mesh resolution, with the semi-analytical result of Brachet et al. [72]

	64^3 **Cells**	128^3 **Cells**	**Brachet et al. [72]**
	$O(\Delta t^2, \Delta x^2)$	$O(\Delta t^2, \Delta x^2)$	
Energy t=5 s	0.952	0.965	1.00
Enstrophy t=3.5 s	2.89	3.23	3.46

Source code: see appendix C.1.2

3.2.4 Decaying Isotropic Turbulence

In this section, we present a canonical flow for LES which tests whether the sub-grid stress model has been coded properly. This test is more a validation test than a verification, but is a complementary test to others verification tests performed in the previous sections. In this section, we test FireFOAM turbulence models against the low Reynolds number data of Comte-Bellot and Corrsin (CBC) [73].We use a periodic box of side $L = 9 \times 2\pi$ cm (≈ 0.566 m) and $\nu = 1.5 \times 10^{-5}$ m^2/s for the

kinematic viscosity. The non-dimensional times for these data are: $x/M = 42$ (initial condition), 98, and 171, where M is the characteristic mesh spacing of the CBC wind tunnel and x is the downstream location of this data station. Considering the mean velocity in the CBC wind tunnel experiment, these correspond to dimensional times of $t = 0.00\,\mathrm{s}$, $0.28\,\mathrm{s}$, and $0.66\,\mathrm{s}$ in our simulations. The initial condition for the simulation is generated by superimposing Fourier modes with random phases such that the spectrum matches that of the initial CBC data. Figure 3.12 shows the initial and final states of the velocity field in the 3D periodic domain. The flow is unforced and the total energy decays with time due to viscous dissipation.

We will now define the different turbulent length scales of this flow and calculate the corresponding wave-numbers (κ).

- **Maximum length scale (L)**: largest eddies in the flow, constrained by the physical boundaries of the flow. $L = 0.566\,\mathrm{m}$.

$$k_L = \frac{2\pi}{L} = 11\ [1/\mathrm{m}] \tag{3.13}$$

- **Kolmogrov length scale (η_k)**: smallest eddies in the flow, $\eta_k = 2.9 \times 10^{-4}\,\mathrm{m}$

$$k_\eta = \frac{2\pi}{\eta} = 21,666\ [1/\mathrm{m}] \tag{3.14}$$

- **Nyquist limit**: smallest eddies resolved by the grid. The characteristic wavenumber, k_c, corresponds to one period and is defined as:

$$k_c = \frac{2\pi}{2\Delta} = 355\ [1/\mathrm{m}] \tag{3.15}$$

where Δ is the filter width and is defined as $\Delta = (\Delta_x \Delta_y \Delta_z)^{1/3}$.

In LES, the filter and grid have to be sufficiently fine to resolve 80% of the energy everywhere [20]. For a 64^3 grid resolution, $k_{(0,\kappa_c)} = 0.82k$ and $\varepsilon_{(0,\kappa_c)} = 0.17\varepsilon$, which means that 82% of the total energy is resolved by our grid and 83% of the dissipation rate is contained in the sub-grid scale range computed by the turbulence model. The total kinetic energy (k) and dissipation rate (ε) have been defined as follows:

The contribution to the kinetic energy k from motions in wavenumber range (κ_a, κ_b) is

$$k_{(\kappa_a,\kappa_b)} = \int_{\kappa_a}^{\kappa_b} E(\kappa) d\kappa \tag{3.16}$$

and the contribution to the dissipation rate ε from motions in the range (κ_a, κ_b) is

$$\varepsilon_{(\kappa_a,\kappa_b)} = \int_{\kappa_a}^{\kappa_b} 2\nu\kappa^2 E(\kappa) d\kappa \tag{3.17}$$

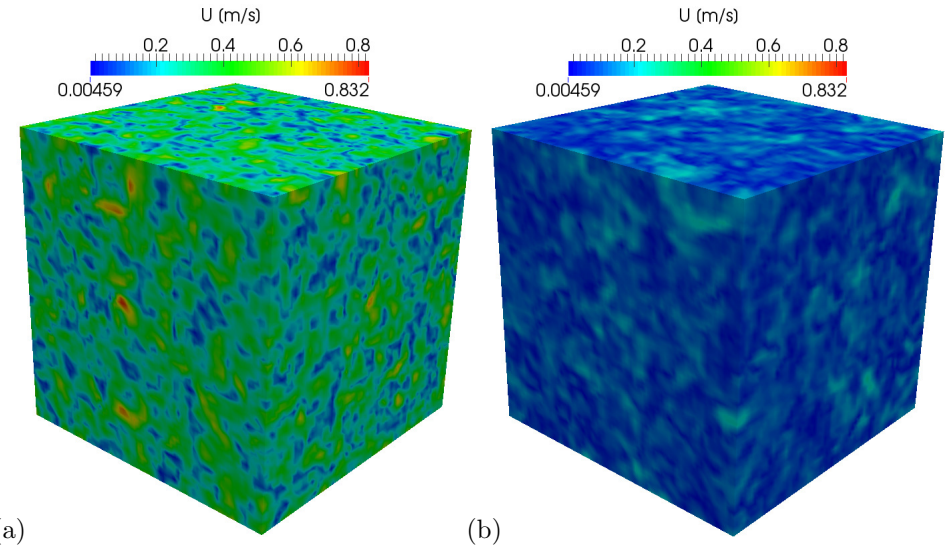

(a) (b)

Figure 3.12: Velocity magnitude for the isotropic turbulence field. a)t=0 [s]; b) t=1 [s].

Smagorinsky

The sub-grid stress is modeled using a gradient diffusion hypothesis and the turbulent viscosity is modeled with the constant coefficient Smagorinsky, C_s, equal to 0.2.

Figure 3.13.a shows the kinetic energy decay curve for a 64^3 grid resolution. The discrepancy between FireFOAM and CBC is less than 10%. The agreement between experiment and computational data is good.

Figure 3.13.b presents the corresponding spectral data comparison using the method in [74]. The three black solid lines are the CBC spectral data for the points in time corresponding to dimensional times of $t = 0.0\,\mathrm{s}$, $0.28\,\mathrm{s}$, $0.66\,\mathrm{s}$. The initial FireFOAM velocity field is specified to match the CBC kinetic energy up to the grid

Nyquist limit. Kinetic energy is slightly under-predicted for low wavenumber containing most of the energy and well-predicted for intermediate wavenumber (before the Nyquist limit).

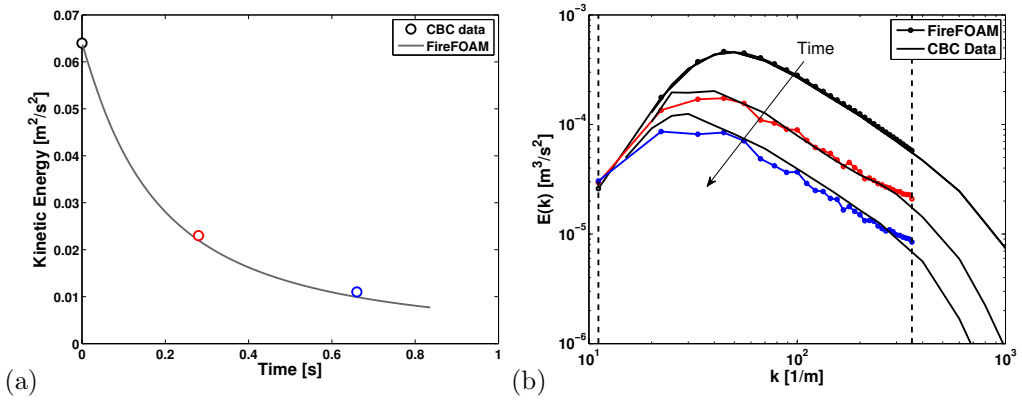

Figure 3.13: Kinetic Energy comparison between CBC data and FireFOAM using Smagorinsky turbulence model for a 64^3 grid resolution. a) Kinetic Energy decay over time; b) Energy spectra versus wavenumber. The first vertical dashed line represents the wavenumber for the maximum length scale (κ_L) and the second vertical dashed line represents the wavenumber for the Nyquist limit (κ_c).

Figure 3.14 shows the dissipation rate spectra for a 64^3 grid resolution. We observe that most of dissipation occurs in scales smaller than the grid size, *i.e.* for $\kappa_c < \kappa < \kappa_\eta$.

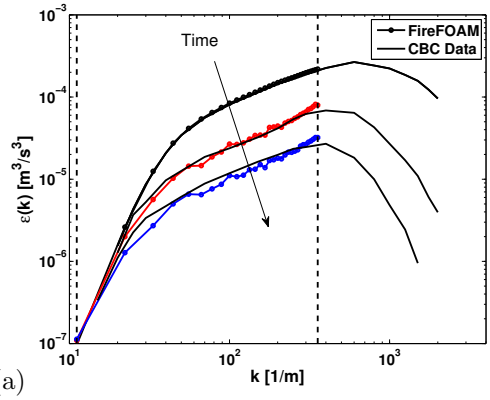

(a)

Figure 3.14: Dissipation rate, $\varepsilon(\kappa) = 2\nu\kappa^2 E(\kappa)$, comparison between CBC data and FireFOAM using the Smagorinsky turbulence model for a 64^3 grid resolution. Dissipation spectra versus wavenumber. The first vertical dashed line represents the wavenumber for the integral length scale (κ_L) and the second vertical dashed line represents the wavenumber for the Nyquist limit (κ_c).

Constant-coefficient one-equation eddy-viscosity model

This model, also called oneEqEddy model in OpenFOAM, is based on solving a transport equation for the sub-grid scale turbulent kinetic energy (k_{sgs}). The sub-grid scale eddy viscosity is calculated from the sub-grid kinetic energy, $\nu_{sgs} = C_k k_{sgs}^{1/2} \Delta$, with $C_k = 0.094$.

Figure 3.15.a shows the kinetic energy decay curve for a 64^3 grid resolution. The discrepancy between FireFOAM and CBC is less than 20%. Agreement between experiment and computational data is acceptable.

Figure 3.15.b presents the corresponding spectral data comparison. Kinetic energy is under-predicted for low wavenumber containing most of the energy, and well-predicted for intermediate wavenumber (before the Nyquist limit).

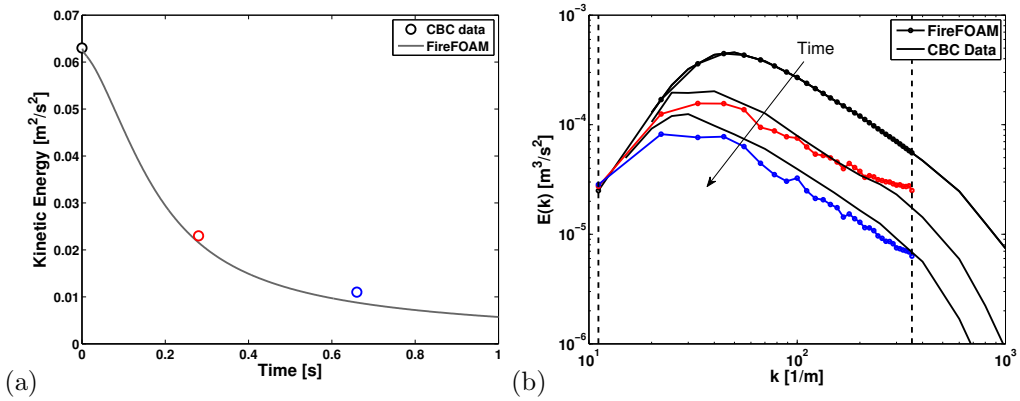

Figure 3.15: Constant-coefficient one-equation eddy-viscosity model, see caption of Fig. 3.13.

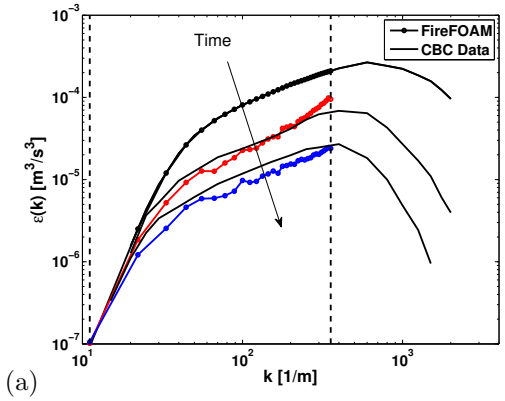

Figure 3.16: Constant-coefficient one-equation eddy-viscosity model, see caption of Fig. 3.14.

Dynamic-coefficient one-equation eddy-viscosity model

This model, also called LDKSGS in FireFOAM is based on solving a transport equation for the sub-grid scale turbulent kinetic energy (k_{sgs}). The sub-grid scale eddy viscosity is calculated from the sub-grid kinetic energy, $\nu_{sgs} = C_k k_{sgs}^{1/2} \Delta$. Now, C_k is computed locally and dynamically by sampling information on the GS level

to evaluate the SGS model coefficient (see section 2.4.2). Figure 3.17-a shows the value of C_k at 0.25 $[s]$, ranging from 0.0 to 2.48 within the domain with an average value of 0.05. Figure 3.17-b depicts the mean value of C_k as function of time for the constant and dynamic one-equation eddy viscosity model.

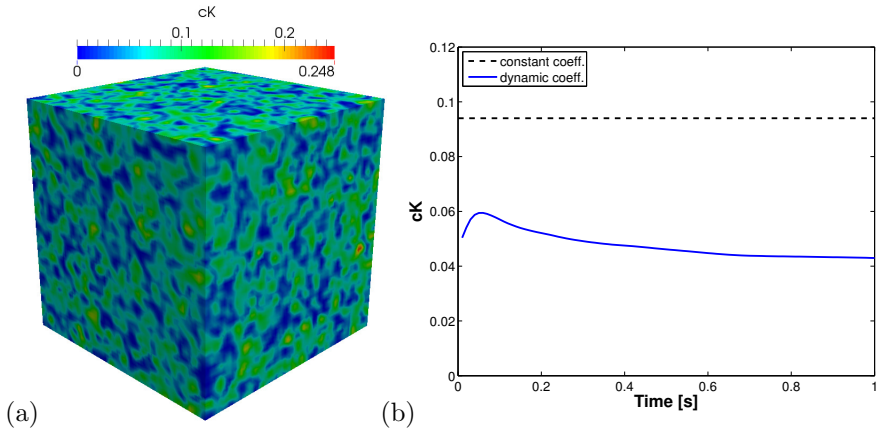

(a) (b)

Figure 3.17: Dynamic-coefficient for a 64^3 grid resolution of the CBC experiment.

Figure 3.18.a shows the kinetic energy decay curve for a 64^3 grid resolution. The discrepancy between FireFOAM and CBC is less than 14%. Agreement between experiment and computational data is acceptable.

Figure 3.18.b presents the corresponding spectral data comparison. Kinetic energy is under-predicted for low wavenumber containing most of the energy and over-predicted for intermediate wavenumber (before the Nyquist limit).

Comparisons with simulations show that the standard and dynamic one-equation eddy viscosity model lead to a small 'pile-up' of energy near the cutoff wavenumber, an issue that have been noticed in some previous work [75]. For this issue, it has been noticed that the filter type (box, gaussian, sharp spectral, etc) plays an

important role.

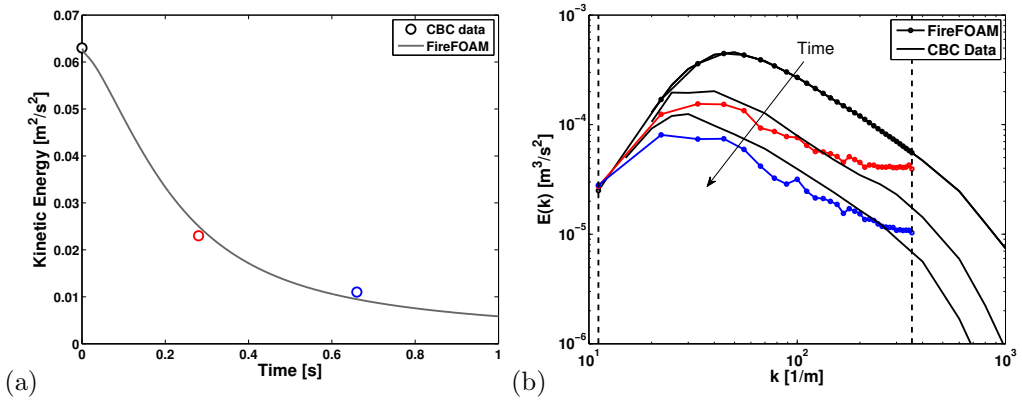

Figure 3.18: Dynamic coefficient one-equation eddy viscosity model, see caption of Fig. 3.13.

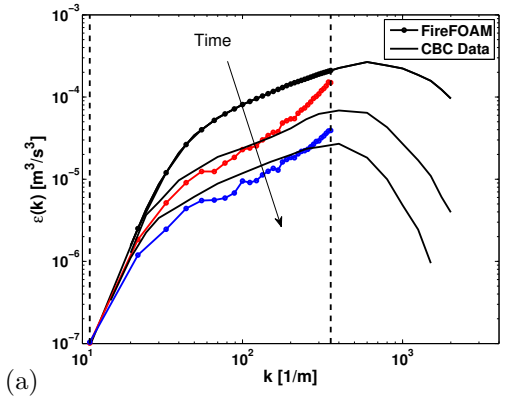

Figure 3.19: Dynamic coefficient one-equation eddy viscosity model, see caption of Fig. 3.14.

Source code: see appendix C.1.3

3.2.5 Radiative Heat Transfer in a duct with a participating medium

In this section, the aim is to evaluate the Finite Volume Discrete Ordinary Method (FvDOM) in OpenFOAM, see section 2.6.2. We consider heat transfer in an infinitely long duct with a square section [76]. All fours walls are cold ($T_w = 0\,\mathrm{K}$) and black ($\varepsilon = 1.0$), containing a medium of constant emissive power and constant absorption coefficient. We want to determine the radiative heat transfer flux received at the wall boundaries. We use a two-dimensional mesh of 10×10. The angular discretization is $N_\phi = 4$ and $N_\theta = 4$, corresponding to 64 solid angles. Figure 3.20 shows the non-dimensional surface heat flux for the three different optical thicknesses. Results agree with the analytical solution of this problem [76]. Small discrepancies can be explained by the limitation of the FvDOM method as reported in [77]. In this configuration, the Discrete Transfer Method (DTM) is more accurate than the Finite Volume (FVM) and the Discrete Ordinary Method (DOM).

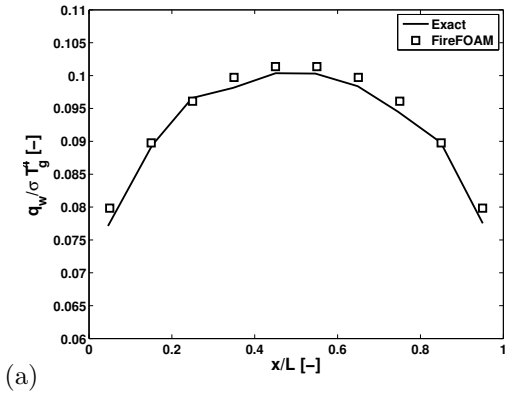

(a)

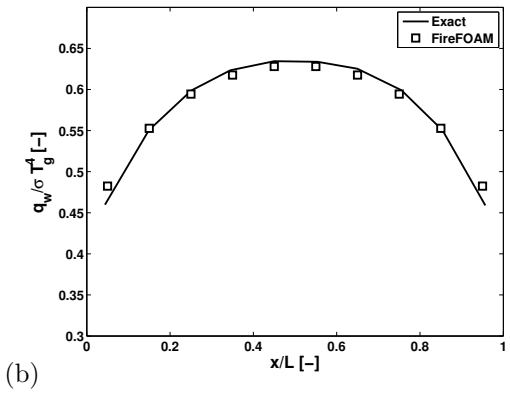

(b)

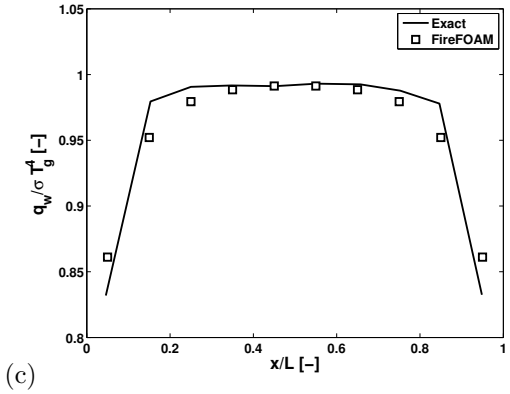

(c)

Figure 3.20: Non-dimensional wall radiative heat flux over non-dimensional length for three different optical thicknesses cases. a) $\kappa L = 0.1$; b) $\kappa L = 1.0$; c) $\kappa L = 10$.

Source code: see appendix C.1.4

3.2.6 2D laminar CounterFlow Flame

This section describes a 2D laminar counterflow flame to check the combustion model using the eddy dissipation concept assuming fast chemistry. In order to achieve fast chemistry, the time scale used in the EDC model is set to a small value (190 µs). Species mass fraction, heat release rate (HRR), temperature and enthalpy (total, sensible and chemical) are plotted in mixture fraction space in order to verify that energy and species mass fraction equations (4.16 and 2.4) are correctly implemented into FireFOAM-2.2.x. The domain is square and is 0.02 m long using 50 cells in the direction normal to the flame front. Fuel and air are injected on each side at 0.1 m/s and at 293 K. Gravity and radiation are turned off. Methane and air react as:

$$CH_4 + 2O_2 + 7.52N_2 \rightarrow CO_2 + 2H_2O + 7.52N_2 \tag{3.18}$$

The corresponding stoichiometric mixture fraction is 0.055 and the adiabatic flame temperature is 2226 K [4].

The Burke-Schumann solution [54] relates flame variables (Y_{CH_4}, Y_{O_2}, h_s, T) to mixture fraction (z) as follows:

- On the oxidizer side ($z < z_{st}$)

$$\begin{aligned} Y_{CH_4}(z) &= 0 \\ Y_{O_2}(Z) &= Y_{O_2,A}\left(1 - \frac{z}{z_{st}}\right) \\ h_s(z) &= zh_{s,F} + (1-z)h_{s,A} + Y_{CH_4,F}\Delta H_F z \\ T(z) &= zT_F + (1-z)T_A + Y_{CH_4,F}\frac{\Delta H_F}{C_P}z \end{aligned} \tag{3.19}$$

- On the fuel side ($z > z_{st}$)

$$\begin{aligned} Y_{CH_4}(z) &= zY_{CH_4,F} + (z-1)\frac{Y_{O_2,A}}{s} = Y_{CH_4,F}\frac{z - z_{st}}{1 - z_{st}} \\ Y_{O_2}(Z) &= 0 \\ h_s(z) &= zh_{s,F} + (1-z)h_{s,A} + Y_{CH_4,F}\Delta H_F z_{st}\frac{1-z}{1-z_{st}} \\ T(z) &= zT_F + (1-z)T_A^{\infty} + Y_{CH_4,F}\frac{\Delta H_F}{c_P}z_{st}\frac{1-z}{1-z_{st}} \end{aligned} \tag{3.20}$$

NB: Please notice that Burke-Schumann assumes infinitely fast chemistry for mass fraction (Y_{CH_4}, Y_{O_2}), sensible enthalpy (h_s) and temperature (T), and also constant specific heat (c_P) for temperature.

Figure 3.21 shows species mass fraction as a function of mixture fraction. Oxygen and methane are closed to a burke-schumann type of solution (Eq. 4.36 and Eq. 4.37), meaning this reaction is almost infinitely fast and the corresponding Damköhler number is very large. As expected, the inert specie, N_2, is a linear function of mixture fraction.

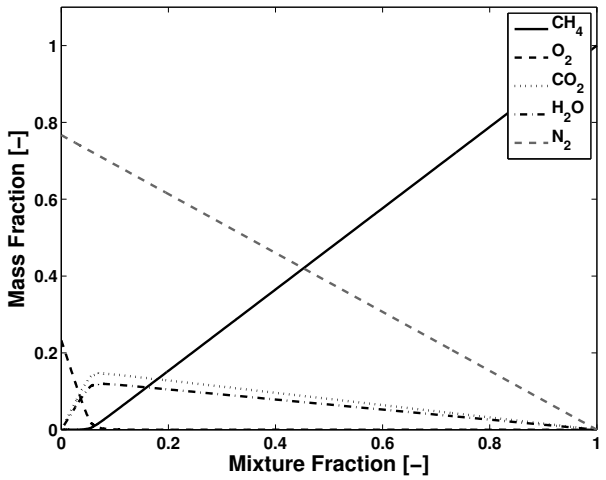

Figure 3.21: Species mass fraction as a function of mixture fraction.

Figure 3.22 shows the heat release rate (HRR) as function of mixture fraction. The maximum HRR is located at the stoichiometric mixture fraction and only takes positive value as expected.

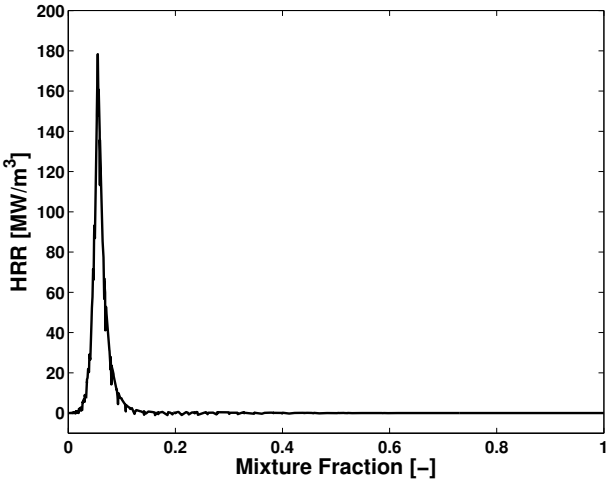

Figure 3.22: Heat Release Rate (HRR) as a function a mixture fraction.

Figure 3.23 shows the total, sensible and chemical enthalpy as a function of mixture. The sensible enthalpy is computed as the scalar transported in the energy equation using the combustion source term (Fig. 3.22). The sensible enthalpy is also compared against the Burke-Schumann solution using Eq. 4.36 and Eq. 4.37. The difference around the stoichiometric mixture fraction is due to the finite rate EDC model that does not match the infinitely fast reaction assumption in Burke-Schumann. FireFOAM assumes unity Lewis numbers, which means thermal and mass diffusivity are equal. Hence, the total enthalpy is a linear function of mixture fraction in an adiabatic configuration.

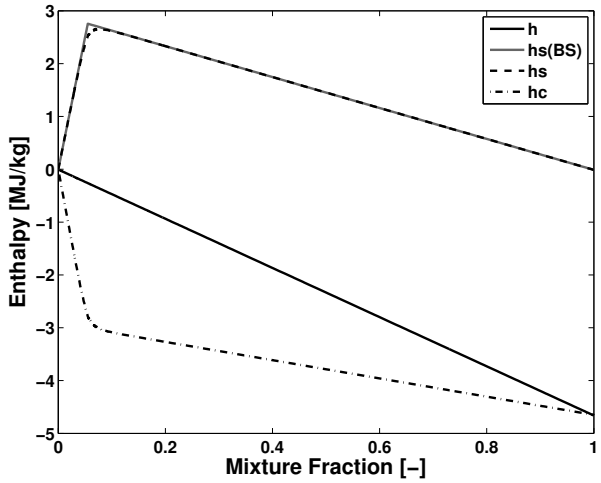

Figure 3.23: Enthalpy as function of mixture fraction. h, hs and hc respectively denotes the total, sensible and chemical enthalpy. The solid gray line denotes the Burke-Schumann solution assuming infinitely fast chemistry (Eq. 4.36 and Eq. 4.37).

Figure 3.24 shows temperature as a function of mixture fraction. The Burke-Schumann solution (Eq. 4.36 and Eq. 4.37) is also plotted assuming an infinite Damköhler number and constant heat capacity. The adiabatic flame temperature is

2226 K. FireFOAM calculates heat capacity as a function of mixture composition and temperature from a set of coefficients taken from JANAF tables of thermodynamics. The deviation from the Burke-Schumann solution is due to the difference between the variable heat capacity in FireFOAM-2.2.x and a constant heat capacity assumption.

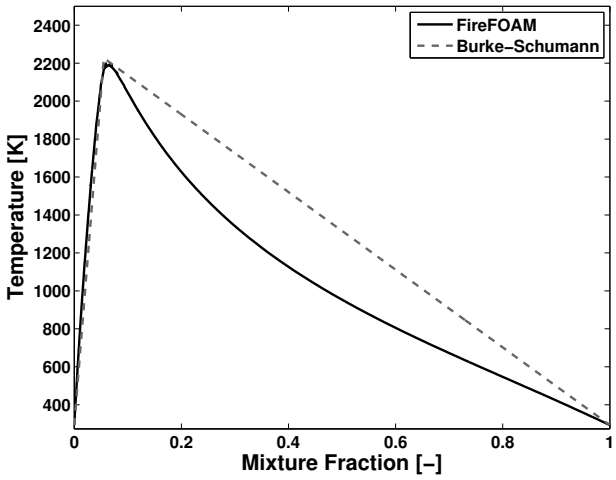

Figure 3.24: Temperature as a function a mixture fraction. The gray dashed line represents the Burke-Schumann temperature assuming a constant heat capacity.

Source code: see appendix C.1.5

3.3 Solid Phase

3.3.1 Semi-infinite wall

This section presents a verification test for the wall heat transfer solver in order to determine the wall resolution required to accurately predict the wall temperature. A 1D, 2.54 cm thick, wall is subject to a constant net heat flux, $q_s'' = 20\,\mathrm{kW/m^2}$

at $x = 0\,\mathrm{m}$ and a constant temperature, $T_\infty = 298.15\,\mathrm{K}$ at $x = 2.54\,\mathrm{cm}$. Material properties of the wall correspond to M-Kaowool. The mass density, thermal conductivity and specific heat are: $\rho = 272\,\mathrm{kg/m^3}$, $k = 0.04\,\mathrm{W/m/K}$ and $C_p = 900\,\mathrm{J/kg/K}$, respectively.

FireFOAM solves a 1D transient heat transfer equation:

$$\frac{\partial T}{\partial t} = \frac{k}{\rho C_p}\frac{\partial^2 T}{\partial x^2} \tag{3.21}$$

The analytical solution is calculated assuming a semi-infinite solid [78] and a constant surface net heat flux: $q_s'' = q_0''$.

$$T(x,t) - T_i = \frac{2q_0''(\alpha t/\pi)^{1/2}}{k} exp\left(\frac{-x^2}{4\alpha t}\right) - \frac{q_0'' x}{k} erfc\left(\frac{x}{2\sqrt{\alpha t}}\right) \tag{3.22}$$

where α is the thermal diffusivity with $\alpha = k/(\rho C_p)$.

Figure 3.25 displays the transient wall temperature at different times (t=4, 12, and 20 s) compared to the analytical solution. The grid design to accurately predict the wall temperature is 20 cells across the wall with an expansion ratio of 1.2, *i.e.* $\Delta x \sim 250\,\mu\mathrm{m}$. The grid is refined close to $x = 0\,\mathrm{m}$ in order to correctly resolve the region of the highest temperature gradient.

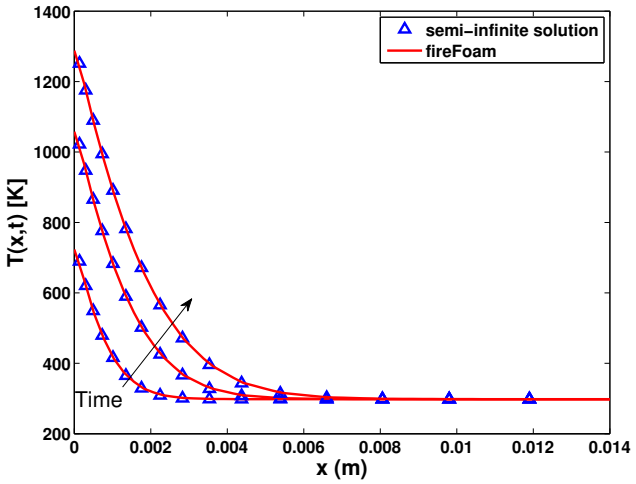

Figure 3.25: Transient wall temperature at 4, 12 and 20 s.

Source code: see appendix C.2.1

3.4 Liquid Phase (Lagrangian solver)

This section represents verification test for the LES spray solver in order to test satisfaction of global conservation laws. Tests on the conservation of mass for non-evaporating and evaporating droplets are conducted, mass for both phases (liquid and gas) are monitored, conservation of energy is verified for a dry and saturated environment, and calculation of the evaporation rate is checked.

Table 3.6: Test Cases matrix.

Test Case	**Droplet**	**Humidity**	**Evap.**	**Verification**	**Validation**
Cons. of Mass	Spray	Dry	off	X	
Cons. of Mass and Energy	Spray	Dry	on	X	
Cons. of Mass and Energy	Spray	Saturated	on	X	
Evaporation Rate	Single	Dry	on		X
Evaporation Rate	Single	31 %	on		X

The water mass in the gas phase, $m^g_{H_2O}$, is obtained by integrating the gaseous water mass-density over the domain.

$$m^g_{H_2O} = \int \rho Y_{H_2O} dV \tag{3.23}$$

where Y_{H_2O} is the mass fraction of water in the gas-phase.

The water mass flow rate leaving the domain, $\dot{m}_{H_2O}$, is obtained by integrating the mass flux of water, $\dot{m}''_{H_2O}$, over the boundary area.

$$\dot{m}_{H_2O} = \int \dot{m}''_{H_2O} dA \tag{3.24}$$

with

$$\dot{m}_{H_2O} = \overline{\rho}\widetilde{u}_z\widetilde{Y}_{H_2O} - \overline{\rho}(D_{Y_k} + D_t)\frac{\partial \widetilde{Y}_{H_2O}}{\partial n} \tag{3.25}$$

where ρ is the mass density, u_z the vertical velocity, D_{Y_k} the molecular diffusivity and D_t the turbulent diffusivity.

Relative humidity

This section explains how the simulation is initialized to take into account the relative humidity in air. Given the relative humidity and the temperature of an ideal gas mixture of air and water, we can determine the composition (Y_{H_2O}, Y_{O_2}, Y_{N_2}). Begin with the definition of relative humidity:

$$h_r = \frac{P_{H_2O}}{P^*_{H_2O}} \tag{3.26}$$

where P_{H_2O} is the partial pressure of water and $P^*_{H_2O}$ is the saturated pressure at a given temperature. Finally, the water mole fraction is the ratio between the partial pressure of water and the pressure.

N.B.: Note that in the experiment, the relative humidity is calculated from a dry bulb and wet bulb temperature. The droplet temperature is supposed to reach in few second the wet bulb air temperature.

$$X_{H_2O} = \frac{P_{H_2O}}{P} \tag{3.27}$$

3.4.1 Test: Conservation of Mass (no-evaporation)

In a $6 \times 6 \times 8\,\mathrm{m}^3$ open domain, 7.41 mm water droplets are injected with a cone nozzle type-injector at a volume flow rate of $63.92 \times 10^{-3}\,\mathrm{m}^3/\mathrm{s}$ for 10 s. The evaporation model is turned off. Assuming water mass density of $1000\,\mathrm{kg}/\mathrm{m}^3$, the total mass injected is 63.92 kg and the total mass of water leaving the domain computed is 63.92 kg (see Fig. 3.26). The total mass of water is conserved.

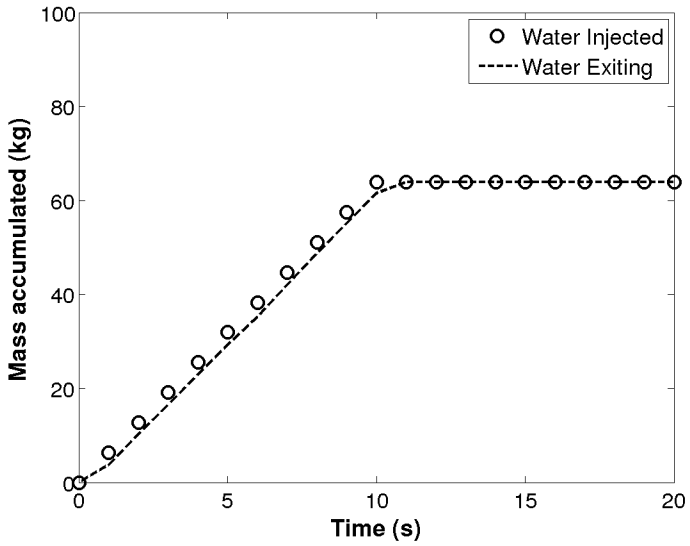

Figure 3.26: Mass accumulated into the domain. Symbols represents water injected and dashed line water leaving the domain.

Source code: see appendix C.3.1

3.4.2 Test: Conservation of Mass and Energy (V=constant)

The dimensions of the box are 1 m on a side and the initial air temperature is 200 °C. The box is well-insulated (*i.e.* adiabatic wall) and rigid (constant volume). The droplets diameter is 200 µm, the droplets temperature is 20 °C, and the total mass of water droplets is 0.01 kg. The mesh resolution is $\Delta x = 10$ cm. All the droplets are injected at initial time and uniformly distributed over the 1000 cells of the domain (see figure 3.27). The initial mass fraction of water vapor is 0. All the droplets are evaporated within 10 s.

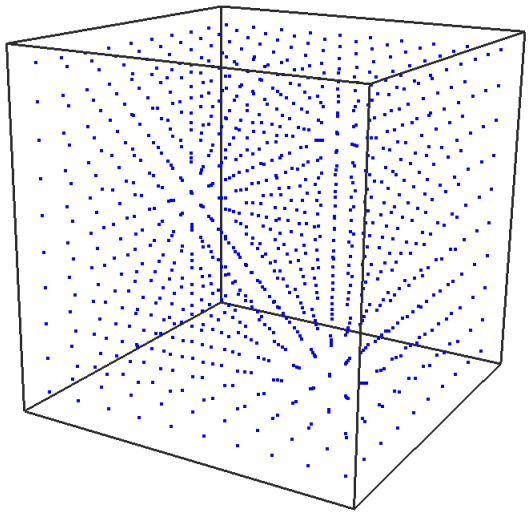

Figure 3.27: Initial water droplet distribution at initial time.

Analytical solution

The change in the enthalpy of the droplets should be equal to the change in the enthalpy of the gas minus the work performed due to pressure. In a constant volume case, it is the internal energy of the system that is conserved. The internal energy can be expressed in terms of the enthalpy, pressure and density:

$$e = h - \frac{p}{\rho} \tag{3.28}$$

In differential form:

$$de = dh - \frac{1}{\rho}dp - pd\left(\frac{1}{\rho}\right) = dh - \nu dp - pd\nu \tag{3.29}$$

Multiplying by mass and noting that the volume, V, is constant yields:

$$dE = dH - Vdp \tag{3.30}$$

The enthalpy decrease of the liquid water droplets is equal to the enthalpy gain of the gas (both expressed in units J) minus the pressure increase times the volume in units of Pa and m^3, respectively.

$$\Delta H_{air} - V\Delta p = \Delta H_{H_2O} \tag{3.31}$$

The change phase of water from liquid to vapor (ΔH_{H_2O}) occurs in three steps. First, the water droplet is raised to the boiling temperature ($T_{eb} = 100\,^{\circ}\mathrm{C}$). The change in enthalpy of this process corresponds to $m_{H_2O}C_{pH_2O,f}(T_{eb} - T_{1,H_2O})$. Then, the water droplet evaporates and the change in enthalpy of this process is $m_{H_2O}H_v$, where H_v is the latent heat of vaporization. Finally, the water vapor is raised to the final gas temperature and the change in enthalpy corresponds to $m_{H_2O}C_{pH_2O,g}(T_{2,air} - T_{eb})$.

$$\begin{aligned} m_{air}C_{p,air}(T_{1,air} - T_{2,air}) - V\rho_{air}R(T_{1,air} - T_{2,air}) = \\ m_{H_2O}C_{pH_2O,f}(T_{eb} - T_{1,H_2O}) + m_{H_2O}H_v + m_{H_2O}C_{pH_2O,g}(T_{2,air} - T_{eb}) \end{aligned} \tag{3.32}$$

Figure 3.28 displays the mass of water vapor and temperature within the box as a function of time. The symbols denotes the steady-state analytical solution obtained from equation 3.32 using parameters in table 3.7. Conservation of energy is checked by comparing the FireFOAM final temperature in the system to the analytical solution. In this test, the thermodynamic model of FireFOAM is de-activated and replaced by constant heat capacities.

Table 3.7: Parameters.

Parameter	Value	Units	Comments
m_{air}	0.7431	kg	mass of air
m_{H_2O}	0.01	kg	mass of water
$C_{p,air}$	1026	J/kg/K	heat capacity of air @ 200 °C
$C_{pH_2O,g}$	2036	J/kg/K	heat capacity of water vapor @ 200 °C
$C_{pH_2O,f}$	4187	J/kg/K	heat capacity of water @ 20 °C
H_v	2257	kJ/kg	latent heat of vaporization

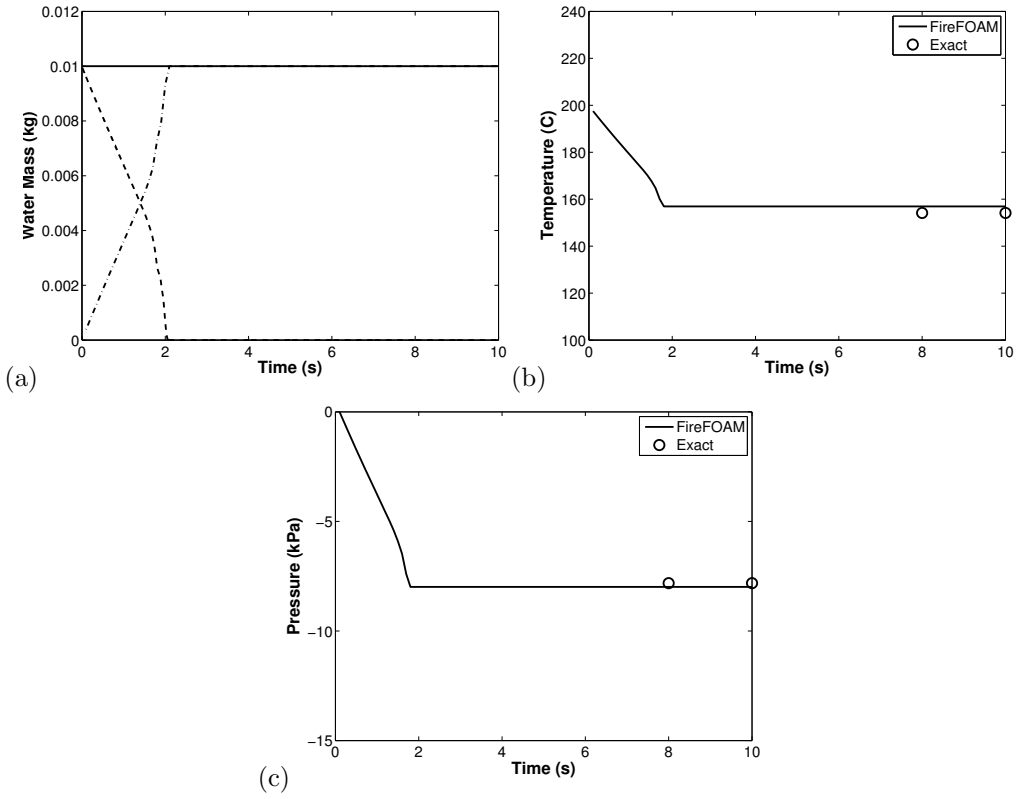

Figure 3.28: (a) Conservation of water mass in the system. The solid black curve is the total mass in the system, expressed as the sum of liquid water mass (dashed line) and the gas phase water mass (dashed-dotted); (b) Conservation of energy in the system based on temperature. The exact solution is calculated from equation 3.32. (c) Final drop in pressure.

Source code: see appendix C.3.2

3.4.3 Test: Conservation of Mass and Energy in a saturated environment (V=constant)

The dimensions of the box are 1 m on a side and the initial air temperature is 500 °C. The box is well-insulated (*i.e.* adiabatic wall) and rigid (constant volume). Droplets diameter is 200 µm, droplets temperature is 20 °C, and the total mass of water droplets is 0.01 kg. The mesh resolution is $\Delta x = 10\,\text{cm}$. All droplets are injected at initial time and uniformly distributed over the 1000 cells of the domain (see figure 3.27). The initial mass fraction of water vapor is 0. It is expected to reach the saturation state,*i.e.* $h_r = 100\%$. The analytical solution for the stationary state derives from the first principle of thermodynamics and the Clausius-Clapeyron equation.

The change phase of water from liquid to vapor is similar to the previous case, except that now the Clausius-Clapeyron equation is used to calculate the final mass of water vapor $m_{2,H_2O,g}$.

$$\begin{aligned} &m_{air}C_{p,air}(T_{1,air} - T_{2,air}) - V\rho_{air}R(T_{1,air} - T_{2,air}) = \\ &(m_{1,H_2O,l} - m_{2,H_2O,l})\left[C_{pH_2O,l}(T_{eb} - T_{1,H_2O}) + H_v + C_{pH_2O,g}(T_{eb} - T_{2,air})\right] \\ &\qquad + m_{2,H_2O,l}C_{pH_2O,l}(T_{2,air} - T_{1,H_2O}) \end{aligned} \tag{3.33}$$

$$\frac{P_{sat}}{P(=1atm)} = exp\left[\frac{-h_{fg}}{(Ru/MW_{H2O})}\left(\frac{1}{T_{2,air}} - \frac{1}{T_{boil}}\right)\right] \tag{3.34}$$

Based on the definition of partial pressure for water vapor,we find:

$$X_{H_2O,g} = \frac{P_{sat}}{P(=1atm)} \tag{3.35}$$

We can now derive the water vapor mass fraction,

$$Y_{H_2O,g} = X_{H_2O,g}\frac{MW_{H_2O}}{MW_{mix}} \tag{3.36}$$

and the final mass of water vapor at stationary sate:

$$m_{2,H_2O,g} = \frac{Y_{H_2O,g}m_{air}}{(1 - Y_{H_2O})} \tag{3.37}$$

Table 3.8: Parameters.

Parameter	**Value**	**Units**	**Comments**
m_{air}	0.4564	[kg]	mass of air
m_{H_2O}	0.1	[kg]	mass of water
$C_{p,air}$	1029	[J/kg/K]	heat capacity of air @ 45 °C
$C_{pH_2O,f}$	4187	[J/kg/K]	heat capacity of water vapor @ 45 °C
$C_{pH_2O,g}$	1802	[J/kg/K]	heat capacity of water @ 20 °C
H_v	2257	[kJ/kg]	latent heat of vaporization

Figure 3.29 displays the mass of water vapor, temperature, mass fraction of water vapor and relative humidity within the box as a function of time. The symbols denotes the steady-state analytical solution obtained from equation 3.33-3.34-3.36-3.37 using parameters in table 3.8. Conservation of energy is checked by comparing the FireFOAM final temperature in the system to the analytical solution.

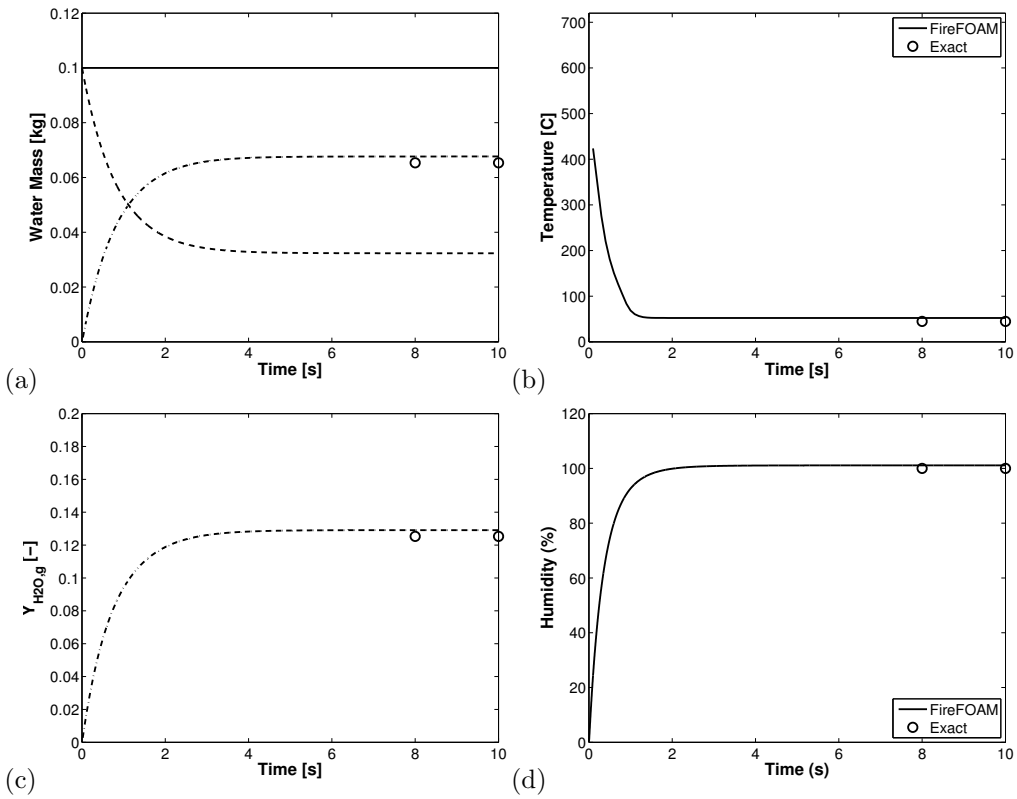

Figure 3.29: (a) Conservation of water mass in the system. The solid black curve is the total mass in the system, expressed as the sum of liquid water mass (dashed line), the gas phase water mass (dashed-dotted) and the exact solution (symbol) is calculated from equation 3.34 3.37; (b) Conservation of energy in the system based on temperature. The exact solution (symbol) is calculated from equation 3.33; (c) The mass fraction fraction of water vapor compared to analytical solution from equation 3.36; (d) The relative humidity compared to analytical solution from equation 3.34.

3.4.4 Test: Evaporation Rate (Ranz and Marshall)

In the test conducted by Rand and Marshall [79], one single water droplet is suspended in dry air at 24.9 °C. At the initial time, droplet diameter is 1050 µm and its temperature is 9.11 °C. The atmospheric pressure is equal to 98792 Pa.

Figure 3.30 shows the system water mass to demonstrate conservation of water

mass between the Lagrangian and Eulerian fields. The masses of the droplet and gas phases and their sum are monitored over the course of the droplet's lifetime (710 s). The total mass of the system remains constant, demonstrating that mass conservation is satisfied.

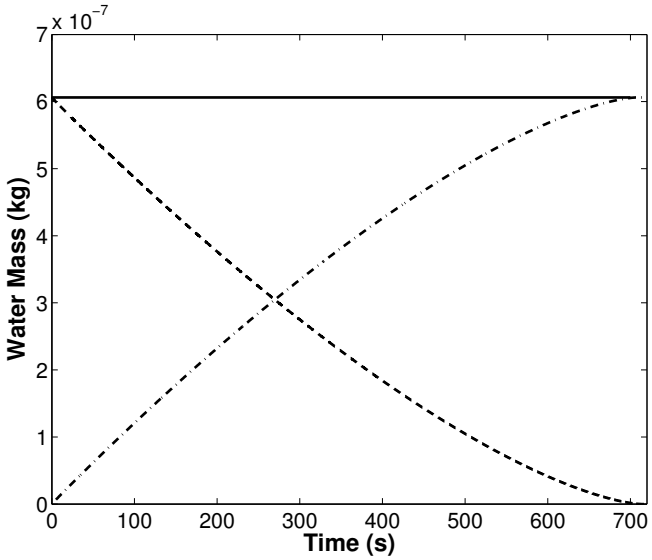

Figure 3.30: Conservation of water mass in the system (droplet diameter 1050 µm). The solid black curve is the total mass in the system, expressed as the sum of liquid water mass (dashed line) and the gas phase water mass (dashed-dotted).

The temporal evolution of the droplet size which is measured and calculated by the two models is plotted on figure 3.31. First of all, we note the linear evolution of the square diameter versus time which is consistent with the D^2 law for droplet evaporation. The evaporation constant K based on the evaporation model proposed by Turns [4] is lower than the simulation and experiment. In the Turns model, all the parameters (density, droplet, air temperature, binary diffusion, etc) are constant during the evaporation process. On the other hand, in the simulation, the cell

temperature, for example, will decreases as a function of time as the droplet is getting evaporated.

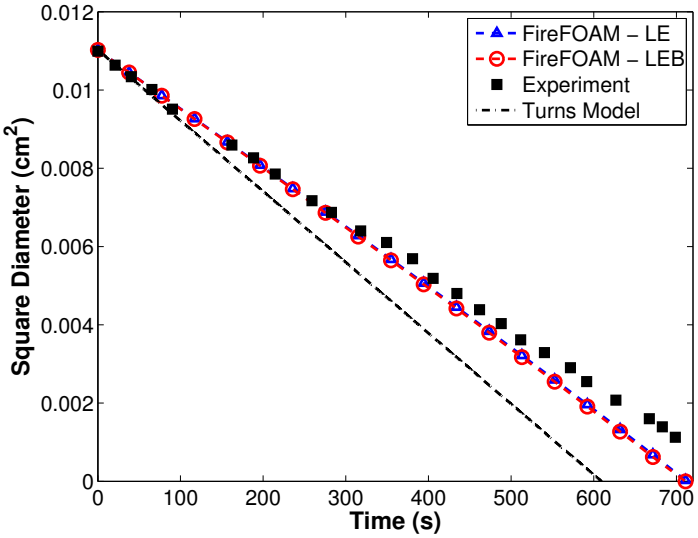

Figure 3.31: Droplet size versus time in the test conducted by Ranz and Marshall (LE refers to the liquid evaporation model and LEB to the liquid evaporation boiling model in OpenFOAM-2.2.x). The dashed line denotes the evaporation model from Turns [4].

3.4.5 Test: Evaporation Rate (Kincaid and Longley)

In the test campaign conducted by Kincaid and Longley [5, 6], the evaporation rate of individuals droplet from 300 to 1600 µm are measured when subjected to different temperature, humidity and gas velocity conditions over a certain time period (between 10 and 120 s). Gas temperature, relative humidity and air velocity are constant in each test, their range tested in the series of experiment are from 10 to 31 °C, from 22 to 81 % and from 0 to 3 m/s.

We first choose to simulate a configuration relevant to water-mist application,*i.e.* a

zero relative velocity between air and the droplet. The dry bulb and wet bulb air temperature are 22 and 12 °C, corresponding to a relative humidity of 31 %. The droplet temperature is assumed to reach in a few seconds the wet bulb temperature. 22 test are run with an initial droplet diameter from 0.44 to 1.49 mm and a time period between 30 and 60 s.

Figure 3.32 shows the measured and computed evaporation rates for different droplet diameters. FireFOAM is reasonably accurate in the different configurations. The maximum relative error is below 20 %. This loss rate has the same definitions as in [5, 6]. It is computed as the ratio of the droplet mass variation $(m_p(t_0) - m_p(t_0 + \Delta t))$ divided by the time period Δt and made non-dimensional by the initial mass $m_p(t_0)$ and the period Δt:

$$Loss\ rate = \frac{m_p(t_0) - m_p(t_0 + \Delta t)}{\Delta t} \tag{3.38}$$

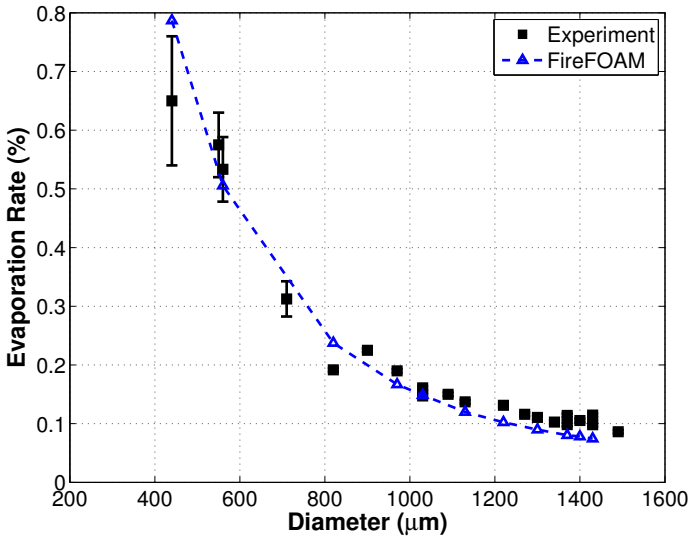

Figure 3.32: Rate of evaporation versus droplet diameter at initial time in tests conducted by Kincaid and Longley [5, 6].

3.5 Output Devices

3.5.1 Transient Thermocouple Response

A thermocouple is placed in the center of a 1 m cube with walls set to 600 °C and gas temperature set to 20 °C. The heat transfer coefficient is set to zero to eliminate convective heating. The gas temperature remains at 20 °C because there is no convective heat transfer from the walls. The thermocouple heats up according to the equation:

$$\rho_{TC} C_{p,TC} V_{TC} \frac{dT_{TC}}{dt} = \varepsilon_{TC} \left(G - \sigma T_{TC}^4 \right) A_{TC} \tag{3.39}$$

whose analytic solution is calculated using *ode45* function from Matlab.

Figure 3.33 displays the thermocouple response compared to the analytical solution.

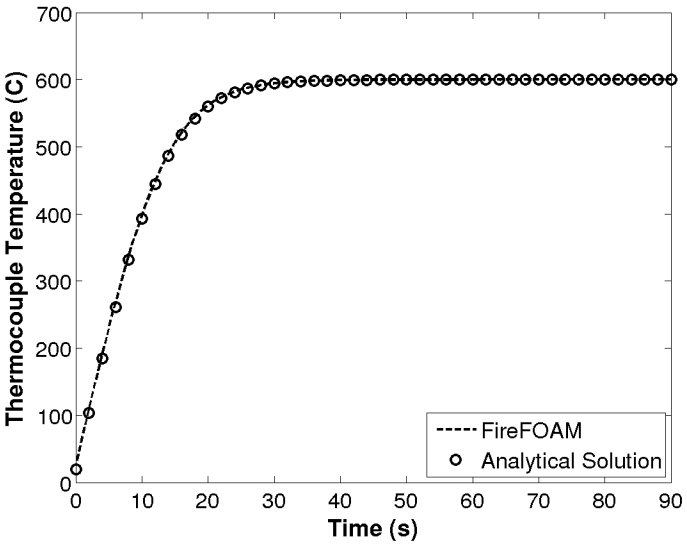

Figure 3.33: Time history of thermocouple temperature by walls at 600 °C.

4 Flame Extinction/Re-Ignition Model

4.1 Introduction

The occurrence of flame extinction is a challenge for combustion modeling in general, and for fire modeling in particular. Diffusion flames may be extinguished by a number of different mechanisms [3, 42–48]. For instance, diffusion flames may be extinguished by aerodynamic quenching, a mechanism in which the flame is weakened by fast flow-induced perturbations and a critical decrease in the flame residence time. Diffusion flames may also be extinguished by thermal quenching, a mechanism in which the flame is weakened by heat losses (*e.g.*, convective cooling to cold wall surfaces, radiative cooling, water evaporative cooling in fire suppression applications, etc) or by dilution quenching, a mechanism in which the flame is weakened due to changes in the fuel or oxidizer stream composition (*e.g.*, air vitiation in under-ventilated fires); in both thermal and dilution quenching, extinction occurs because of a critical increase in the flame chemical time. Laminar flame theory suggests that all these different phenomena may be explained by a single flame extinction criterion known as a Damköhler number criterion [42–44]: the Damköhler number Da is defined as the ratio of a characteristic fuel-air mixing time divided by

a characteristic chemical time, $Da = \left(\tau_{mixing}/\tau_{chemical)}\right)$, and extinction is predicted to occur for values of Da that are critically low. Theoretical analysis shows that the characteristic mixing time τ_{mixing} scales like the inverse of flame stretch, with flame stretch defined as the stoichiometric value of the scalar dissipation rate, noted χ_{st}; theoretical analysis also shows that the characteristic chemical time $\tau_{chemical}$ scales like $exp(T_a/T_{st})$, where T_{st} is the flame temperature and T_a an activation temperature (assuming Arrhenius-like combustion chemistry, T_a gives a measure of the sensitivity of the combustion chemistry to changes in temperature). Thus, we find that the Damköhler number is a function of flame stretch and flame temperature, $Da \sim (1/\chi_{st})/exp(T_a/T_{st})$.

The discussion on the flame Damköhler number serves to illustrate some of the current challenges found in combustion modeling since it shows that flame extinction is controlled by flame-based quantities like stretch and temperature that are unresolved in a large eddy simulation (LES). The occurrence of flame extinction may also be followed by re-ignition and the modeling of under-ventilated combustion, for instance, requires both an extinction model and a re-ignition model. We present in this section the new flame extinction/re-ignition implemented in FireFOAM and a series of test cases to verify that the model has been implemented correctly.

4.2 Chemistry Model

The combustion model in FireFOAM uses a classical global combustion equation:

$$C_nH_mO_p + \left(n + \frac{m}{4} - \frac{p}{2}\right) O_2 \rightarrow nCO_2 + \frac{m}{2} H_2O \ (GR1) \tag{4.1}$$

Global Reaction (GR1) corresponds to a normal combustion step in which fuel is oxidized into carbon dioxide and water vapor. When considering extinction, reaction (GR1) is enhanced by two additional steps:

$$C_nH_mO_p \rightarrow (C_nH_mO_p)^* \ (GR2) \tag{4.2}$$

$$(C_nH_mO_p)^* + \left(n + \frac{m}{4} - \frac{p}{2}\right) O_2 \rightarrow nCO_2 + \frac{m}{2} H_2O \ (GR3) \tag{4.3}$$

where global reaction (GR2) describes the flame extinction phenomenon, treated as a transformation of fresh fuel $C_nH_mO_p$ into non-burning fuel $(C_nH_mO_p)^*$, and global reaction (GR3) describes the re-ignition phenomenon, treated as a normal combustion step for $(C_nH_mO_p)^*$.

In this formulation, we have 6 chemical species: $C_nH_mO_p$, $(C_nH_mO_p)^*$, O_2, CO_2, H_2O, and N_2. Each species are transported separately and solved by a specie transport equation using chemical source terms in Eq. 4.7.

The closure expressions for the chemical reaction rates are based on the EDC model:

$$\begin{aligned}
\overline{\dot{\omega}'''_{EDC}} &= \frac{\overline{\rho}}{\tau_{EDC}} min\left(\widetilde{Y}_{C_nH_mO_p}, \frac{\widetilde{Y}_{O_2}}{r_s}\right) \\
\overline{\dot{\omega}'''_{R1}} &= (1 - FEF)\,\overline{\dot{\omega}'''_{EDC}} \\
\overline{\dot{\omega}'''_{R2}} &= FEF\overline{\dot{\omega}'''_{EDC}}
\end{aligned} \tag{4.4}$$

and

$$\begin{aligned}
\overline{\left(\dot{\omega}'''_{EDC}\right)^*} &= \frac{\overline{\rho}}{\tau_{EDC}} min\left(\widetilde{Y}_{(C_nH_mO_p)^*}, \frac{\widetilde{Y}_{O_2}}{r_s}\right) \\
\overline{\dot{\omega}'''_{R3}} &= FIF\overline{\left(\dot{\omega}'''_{EDC}\right)^*}
\end{aligned} \tag{4.5}$$

where $\overline{\dot{\omega}_{EDC}}$ and $\overline{(\dot{\omega}_{EDC})^*}$ are EDC-based fuel and non-burning fuel consumption rates for the fuel and non-burning fuel transport equation.

In Eqs. 4.4-4.5, FEF and FIF respectively designate a flame extinction factor and a flame re-ignition factor; these factors take values between 0 and 1 and give a measure of the local probabilities of extinction and re-ignition phenomena: $FEF = 0$ ($FIF = 0$) for cases without flame extinction (re-ignition); $FEF = 1$ ($FIF = 1$) for cases with complete extinction (re-ignition). The corresponding expression for the heat release rate per unit volume is:

$$\overline{\dot{\omega}'''_{h_s}} = \left(\overline{\dot{\omega}'''_{R1}} + \overline{\dot{\omega}'''_{R3}}\right) \Delta H_c \tag{4.6}$$

where ΔH_c is the heat of combustion (per unit mass of fuel).

Note:

The system of reactions (R1)-(R3) leads to the expressions for the species mass reaction rates:

$$
\begin{aligned}
\overline{\dot{\omega}'''_{C_nH_mO_p}} &= -\overline{\dot{\omega}'''_{R1}} - \overline{\dot{\omega}'''_{R2}} = -\left(1-FEF\right)\overline{\dot{\omega}'''_{EDC}} - FEF\overline{\dot{\omega}'''_{EDC}} = -\overline{\dot{\omega}'''_{EDC}} \\
\overline{\dot{\omega}'''_{(C_nH_mO_p)^*}} &= \overline{\dot{\omega}'''_{R2}} - \overline{\dot{\omega}'''_{R3}} = FEF\overline{\dot{\omega}'''_{EDC}} - FIF\overline{\left(\dot{\omega}'''_{EDC}\right)^*} \\
\overline{\dot{\omega}'''_{O_2}} &= -\frac{\left(n+m/4-p/2\right)W_{O_2}}{W_{C_nH_mO_p}}\left(\overline{\dot{\omega}'''_{R1}} + \overline{\dot{\omega}'''_{R3}}\right) \\
&= -\frac{\left(n+m/4-p/2\right)W_{O_2}}{W_{C_nH_mO_p}}\left[\left(1-FEF\right)\overline{\dot{\omega}'''_{EDC}} + FIF\overline{\left(\dot{\omega}'''_{EDC}\right)^*}\right] \\
\overline{\dot{\omega}'''_{CO_2}} &= \frac{nW_{CO_2}}{W_{C_nH_mO_p}}\left(\overline{\dot{\omega}'''_{R1}} + \overline{\dot{\omega}'''_{R3}}\right) \\
&= \frac{nW_{CO_2}}{W_{C_nH_mO_p}}\left[\left(1-FEF\right)\overline{\dot{\omega}'''_{EDC}} + FIF\overline{\left(\dot{\omega}'''_{EDC}\right)^*}\right] \\
\overline{\dot{\omega}'''_{H_2O}} &= -\frac{(m/2)W_{H_2O}}{W_{C_nH_mO_p}}\left(\overline{\dot{\omega}'''_{R1}} + \overline{\dot{\omega}'''_{R3}}\right) \\
&= \frac{(m/2)W_{H_2O}}{W_{C_nH_mO_p}}\left[\left(1-FEF\right)\overline{\dot{\omega}'''_{EDC}} + FIF\overline{\left(\dot{\omega}'''_{EDC}\right)^*}\right]
\end{aligned}
\tag{4.7}
$$

4.3 Flame Extinction Model

4.3.1 Extinction Model Equations

Flame extinction is treated via a critical Damköhler number criterion:

$$
FEF = 0.5 - 0.5\tanh\left(\frac{Da - Da_c}{0.02}\right) \tag{4.8}
$$

where Da is the Damköhler number and Da_c its critical (lower) value at extinction. Following results from previous theoretical studies, we assume $Da_c = 1$ [3, 48] and also write:

$$Da = C \times \frac{exp\left(T_a/T_{st}\right)}{\chi_{st}} \tag{4.9}$$

where C is a model coefficient, T_a an activation temperature, T_{st} the flame temperature, and χ_{st} the stoichiometric value of the scalar dissipation rate (χ_{st} gives a measure of the rate of fuel-oxidizer mixing at the flame location). C and T_a are fuel-dependent properties that are calibrated (see section 4.3.2). The flame-based quantities T_{st} and χ_{st} used in Eq. 4.9 are obtained via sub-grid-scale models and are discussed next.

4.3.1.1 First Flame Temperature Model Based on Mixture Fraction

We propose to estimate the flame temperature T_{st} as a linear combination between the mixing temperature T_{st}^m(*i.e.*, the temperature that would be obtained with pure fuel-air mixing and without combustion, $T_{st}^m = ZT_F + (1-Z)\,T_A$, with T_F and T_A the temperatures in the fuel and air supply streams) and the adiabatic flame temperature T_{st}^{ad} (*i.e.*, the temperature that would be obtained with combustion and in the absence of thermal losses):

$$T_{st} = (1 + H_{st})\,T_{st}^{ad} - H_{st}T_{st}^m \tag{4.10}$$

where H_{st} is an excess enthalpy variable introduced to provide a measure of the magnitude of non-adiabatic effects at the flame location (here, $H_{st} \leq 0$ so that one should interpret H_{st} as an enthalpy deficit variable; also $H_{st} = 0$ under adiabatic burning conditions while Hst = -1 under non-burning conditions). We write:

$$H_{st} = \frac{\Delta h_{st}}{Y_{C_nH_mO_P,F} Z_{st} \Delta H_c} \tag{4.11}$$

where Δh_{st} is the excess enthalpy at the flame location, $Y_{C_nH_mO_P,F}$ the fuel mass fraction in the fuel stream, Z_{st} the stoichiometric value of mixture fraction and ΔH_c is the heat of combustion (per unit mass of fuel). We also write:

$$\Delta h_{st} = \begin{cases} \Delta h \left(\frac{Z_{st}}{\widetilde{Z}} \right) & if\ \widetilde{Z} \leq Z_{st} \\ \Delta h \left(\frac{1-Z_{st}}{1-\widetilde{Z}} \right) & if\ \widetilde{Z} > Z_{st} \end{cases} \tag{4.12}$$

with

$$\Delta h = \widetilde{h} - h^{ad}(\widetilde{Z}) = \widetilde{h} - (h_F \widetilde{Z} + h_A(1 - \widetilde{Z})) \tag{4.13}$$

where $\widetilde{h}$ is the LES-filtered total enthalpy, $\widetilde{Z}$ the LES-filtered mixture fraction, and h_F and h_A the values of total enthalpy in the fuel and oxidizer supply streams.

4.3.1.2 Second Flame Temperature Model

In order to simulate flames with different streams and mixture fractions, we introduce an enhanced flame temperature model. The new formulation is independent of mixture fraction and requires to solve two additional energy equations for adiabatic sensible enthalpy $\widetilde{h}_s^{ad}$ and mixing sensible enthalpy $\widetilde{h}_s^m$. We estimate the flame temperature T_{st} as a linear combination between the mixing temperature T_{st}^m(*i.e.*, the temperature that would be obtained with pure fuel-air mixing and without combustion, $T_{st}^m \approx (0.07T_F + 0.93T_A)$, with T_F and T_A the temperatures in the fuel and air supply streams) and the adiabatic flame temperature T_{st}^{ad} (*i.e.*, the temperature

that would be obtained with combustion and in the absence of thermal losses):

$$T_{st} = (1 + H_{st})\, T_{st}^{ad} - H_{st} T_{st}^{m} \tag{4.14}$$

where H_{st} is an excess enthalpy variable introduced to provide a measure of the magnitude of non-adiabatic effects at the flame location (here, $H_{st} \leq 0$ so that one should interpret H_{st} as an enthalpy deficit variable; also $H_{st} = 0$ under adiabatic burning conditions while $H_{st} = -1$ under non-burning conditions). We write:

$$H_{st} = -\frac{\widetilde{h}_s^{ad} - \widetilde{h}_s}{\widetilde{h}_s^{ad} - \widetilde{h}_s^{m}} = \frac{\widetilde{h}_s - \widetilde{h}_s^{ad}}{\widetilde{h}_s^{ad} - \widetilde{h}_s^{m}} \tag{4.15}$$

where $\widetilde{h}_s$ is the LES-filtered sensible enthalpy, $\widetilde{h}_s^{ad}$ the LES-filtered adiabatic sensible enthalpy and $\widetilde{h}_s^{m}$ the LES-filtered mixing sensible enthalpy. We write:

Sensible Enthalpy:

$$\frac{\partial\left(\overline{\rho}\widetilde{h}_s\right)}{\partial t} + \frac{\partial(\overline{\rho}\widetilde{u}_j\widetilde{h}_s)}{\partial x_j} = \frac{D\overline{p}}{Dt} + \frac{\partial}{\partial x_j}\left(\overline{\rho}\left(\alpha + \frac{\nu_t}{Pr_t}\right)\frac{\partial\widetilde{h}_s}{\partial x_j}\right) + \overline{\dot{\omega}_{h_s}^{'''}} - \frac{\partial\overline{\dot{q}}}{\partial x_k} \tag{4.16}$$

The Eddy dissipation Concept (EDC) model is used to estimate the volumetric heat release rate (HRR), $\overline{\dot{\omega}_{h_s}^{'''}}$ (eq. 4.6). The radiation source term, $\frac{\partial\overline{\dot{q}}}{\partial x_k}$ is computed from the radiation model. The turbulent kinematic viscosity, ν_t is computed from the turbulence model.

Adiabatic Sensible Enthalpy:

$$\frac{\partial\left(\overline{\rho}\widetilde{h}_s^{ad}\right)}{\partial t} + \frac{\partial(\overline{\rho}\widetilde{u}_j\widetilde{h}_s^{ad})}{\partial x_j} = \frac{D\overline{p}}{Dt} + \frac{\partial}{\partial x_j}\left(\overline{\rho}\left(\alpha + \frac{\nu_t}{Pr_t}\right)\frac{\partial\widetilde{h}_s^{ad}}{\partial x_j}\right) + \overline{\dot{\omega}_{h_s}^{'''}} \tag{4.17}$$

where $\widetilde{h}_s^{ad}$ is the LES-filtered adiabatic sensible enthalpy, *i.e.* the sensible enthalpy in absence of heat losses due to radiation or cold walls, for example.

Mixing Sensible Enthalpy:

$$\frac{\partial\left(\overline{\rho}\widetilde{h}_s^m\right)}{\partial t}+\frac{\partial(\overline{\rho}\widetilde{u}_j\widetilde{h}_s^m)}{\partial x_j}=\frac{D\overline{p}}{Dt}+\frac{\partial}{\partial x_j}\left(\overline{\rho}\left(\alpha+\frac{\nu_t}{Pr_t}\right)\frac{\partial\widetilde{h}_s^m}{\partial x_j}\right) \tag{4.18}$$

where $\widetilde{h}_s^m$ is the LES-filtered mixing sensible enthalpy, *i.e.* the sensible enthalpy in absence of combustion and radiation.

Boundary Conditions

Each partial differential equations solving h_s, h_s^{ad} and h_s^m have specific boundary conditions defined as:

Sensible Enthalpy: The boundary conditions for sensible enthalpy are the one defined by the user during initialization, *i.e.* adiabatic, isothermal or net heat flux.

Adiabatic and Mixing Sensible Enthalpy:

- **solid walls:** A Von Neumann type of boundary condition is used and the solid walls are set adiabatic, *i.e.* no heat losses.

$$\frac{\partial\widetilde{h}_s^{ad}}{\partial n}=0 \tag{4.19}$$

- **inlet/entrainment:** We specify the net sensible heat flux with the convective and diffusive terms as:

$$\dot{m}_\infty^{''}h_{s,\infty}=\overline{\rho}\widetilde{u}_n\widetilde{h}_s^{ad}-\overline{\rho}\left(\alpha+\frac{\nu_t}{Pr_t}\right)\frac{\partial\widetilde{h}_s^{ad}}{\partial n} \tag{4.20}$$

where $h_{s,\infty}$ is the sensible enthalpy at reference temperature (T_F) in the far field based on species composition. $h_{s,\infty}=\sum_{i=1}^{n}Y_{i,\infty}h_i(T_F)$. For example, at ambient air conditions and compositions, $h_{s,\infty}=Y_{N_2,\infty}h_{N_2}(T_f)+Y_{O_2,\infty}h_{O_2}(T_f)$

Adiabatic flame temperature (T_{st}^{ad})

The adiabatic flame temperature is function of the fuel and oxidizer supply streams conditions, *i.e.* the far field fuel and oxygen mass fraction ($Y_{F,1}$ and $Y_{O_2,2}$) and the far field fuel and oxidizer temperature ($T_{F,1}$ and $T_{O_2,2}$), and can be computed using Burke-Schumann solution.

From Burke-Schumann: at the flame front, $z = z_{st}$, the adiabatic flame temperature is defined as:

$$T_{st}^{ad} = \frac{Y_{O_2,2}}{r_s Y_{F,1} + Y_{O_2,2}} T_{F,1} + \frac{Y_{F,1}}{r_s Y_{F,1} + Y_{O_2,2}} T_{O_2,2} + \frac{Y_{O_2,2} Y_{F,1}}{r_s Y_{F,1} + Y_{O_2,2}} \left(\frac{\Delta H_c}{c_p} \right) \quad (4.21)$$

where r_s is the stoichiometric oxygen-to-fuel mass ratio.

4.3.1.3 First Flame Stretch Model Based on Mixture Fraction)

In flamelet-based models, the scalar dissipation rate, χ, characterizes the effect of the external flow on the mixing and is defined as

$$\chi = 2D \left| \nabla Z \right|^2 \quad (4.22)$$

where D is the molecular diffusivity. The scalar dissipation rate is proportional to the square of the scalar gradient and it depends strongly on the small scales. It is not resolved by LES and, hence, needs to be modeled. We propose to use an algebraic closure models for the filtered scalar dissipation rate based on turbulent diffusivity. The filtered scalar dissipation rate is defined as

$$\widetilde{\chi} = 2D \widetilde{\left| \nabla Z \right|^2} = 2\widetilde{D} \left| \nabla \widetilde{Z} \right|^2 + \chi_{sgs} \quad (4.23)$$

The LES-filtered sub-grid scale scalar dissipation rate is evaluated based on the turbulent diffusivity model, given by

$$\chi_{sgs} = 2D_T \left| \nabla \widetilde{Z} \right|^2 \tag{4.24}$$

with $D_T = \frac{\nu_t}{Pr_t}$

where D_T the turbulent thermal diffusivity, ν_t the turbulent viscosity and Pr_t a turbulent Prandtl number ($Pr_t = 1$ in the OneEqEddy turbulence model).

We estimate flame stretch, χ_{st}, based on a classical laminar flamelet expression:

$$\chi_{st} = \frac{\widetilde{\chi}}{F(\widetilde{Z})} \tag{4.25}$$

where $\widetilde{\chi}$ is the LES-filtered scalar dissipation rate and $F(\widetilde{Z})$ an analytical function define as:

$$F(\widetilde{Z}) = \frac{exp\left(-2\sqrt{erf^{-1}(1-2\widetilde{Z})}\right)}{exp\left(-2\sqrt{erf^{-1}(1-2Z_{st})}\right)} \tag{4.26}$$

where $\widetilde{Z}$ is the LES-filtered mixture fraction and Z_{st} the stoichiometric mixture fraction.

4.3.1.4 Second Flame Stretch Model

The mixture fraction is defined as:

$$Z = \frac{Y_F r_s - Y_{O_2} + Y_{O_2,2}}{Y_{F,1} r_s + Y_{O_2,2}} \tag{4.27}$$

where $Y_{F,1}$ is the fuel mass fraction in the fuel stream, $Y_{O_2,2}$ the oxygen mass fraction in the oxidizer stream, r_s the stoichiometric oxygen-to-fuel mass ratio, and are constant values. The square of the mixture fraction gradient simplifies to:

$$\left|\nabla\widetilde{Z}\right|^2 = \frac{1}{\left(Y_{F,1}r_s + Y_{O_2,2}\right)^2}\left|r_s\nabla\widetilde{Y_F} - \nabla\widetilde{Y_{O_2}}\right|^2 \tag{4.28}$$

By assuming $F(\widetilde{Z}) \sim 1$ near stoichiometry , we can now estimate the LES-filtered sub-grid-scale rate of mixing independent of mixture fraction as:

$$\chi_{st} \approx \widetilde{\chi} = \frac{2D_{mix}}{\left(Y_{F,1}r_s + Y_{O_2,2}\right)^2}\left|r_s\nabla\widetilde{Y_F} - \nabla\widetilde{Y_{O_2}}\right|^2 \tag{4.29}$$

with $D_{mix} = \alpha_{th} + D_{turbulent} = \alpha_{th} + \frac{\nu_t}{Pr_t}$

where $\widetilde{\chi}$ is the LES-filtered scalar dissipation rate, α_{th} the laminar thermal diffusivity, $D_{turbulent}$ the turbulent thermal diffusivity, ν_t the turbulent viscosity and Pr_t a turbulent Prandtl number ($Pr_t = 1$ in the OneEqEddy turbulence model).

4.3.2 Extinction Model Calibration

The Damköhler-number-based flame extinction criterion includes two constants (C and T_a). C is a weak function of several flame parameters and is treated here as a constant. Since Da is dimensionless, C has the dimension of inverse time. The large activation energy asymptotic (AEA) analysis of Ref. [48] considers laminar flame extinction due to stretch, cooling and reactant dilution, and shows that all extinction events correspond to low values of Da and that occurs for a critical value of $Da \simeq 1$. Parameters C and T_a can therefore be obtained from the knowledge of flame stretch and flame temperature under reference extinctions conditions

identified by the subscript q, ref:

$$C = \chi_{q,ref} exp\left(\frac{T_a}{T_{q,ref}}\right) \tag{4.30}$$

4.3.2.1 Methane

Chan et al. [80] have studied the structure and extinction of methane-air flamelet with radiation and detailed chemical kinetic mechanism. The numerical results show that flame radiation can induce another extinction limit at a low scalar dissipation rate($0.029\ s^{-1}$), which is in addition to the well-known upper extinction limit caused by overstretching at a high value of scalar dissipation rate ($0.029\ s^{-1}$). Table 4.1 gives the scalar dissipation and temperature at extinction for the lower and upper extinction limits for methane. Based on those two extinction limits and equation 4.30, parameters C and T_a are calculated by solving a system of two equations with two unknowns (C and T_a). One finds $C = 1.9616 \times 10^{10}\,\mathrm{s}^{-1}$ and $T_a = 36856\,\mathrm{K}$.

Table 4.1: Extinction limits of methane of Ref. [80].

	$\chi_{q,ref}$	$T_{q,ref}$
Lower extinction limit	0.029 [s^{-1}]	1353 [K]
Upper extinction limit	18.4 [s^{-1}]	1773 [K]

N.B.: Lower (upper) extinction limit refers to the radiative (kinetic) extinction limit [81–83].

4.3.2.2 Ethylene

Narayanan et al. [48] have studied a Damköhler-number-based flame extinction criterion using large activation energy asymptotic (AEA) analysis and explored the extinction limits of laminar counter-flow diffusion flames as a function of flame stretch and radiant losses due to soot and gas-phase species. A parametrization of this Damköhler number criterion was performed in subsequent work for diffusion flame conditions with various levels of stretch, radiation losses, and air or fuel vitiation [3]. Table 4.2 gives the scalar dissipation and temperature at extinction for the lower and upper extinction limits for ethylene. Based on those two extinction limits and equation 4.30, parameters C and Ta are calculated by solving a system of two equations with two unknowns (C and Ta). One finds $C = 1.0671 \times 10^8\,\mathrm{s}^{-1}$ and $Ta = 24725\,\mathrm{K}$.

Table 4.2: Extinction limits of ethylene of Ref. [3] .

	$\chi_{q,ref}$	$T_{q,ref}$
Lower extinction limit	0.025 [s^{-1}]	1115 [K]
Upper extinction limit	61 [s^{-1}]	1720 [K]

4.3.2.3 Heptane

Following results from previous theoretical studies, we assume $Da_c = 1$ [3, 48] and the Damköhler number is written as:

$$Da_c = C \times \frac{exp\,(T_a/T_{st})}{\chi_{st}} \tag{4.31}$$

C and T_a are fuel-dependent properties that are calibrated by comparison with experimental data on extinction limits of heptane-air laminar diffusion flames [84]; we find $C = 36140\,\mathrm{s}^{-1}$ and $T_a = 15430\,\mathrm{K}$. The following paragraph explains how those two constants have been calculated.

Seiser *et al.* measure the strain rates at extinction for different oxidizer and fuel stream conditions in a counterflow flame configuration.

First, the strain rate, a_s, is related to the scalar dissipation rate, χ_{st}, as follows.

$$a_s = \frac{\chi_{st}\pi}{exp\left(-2\left[erfc^{-1}\left(2Z_{st}\right)\right]^2\right)} \tag{4.32}$$

where χ_{st} is the scalar dissipation rate at $Z = Z_{st}$, a_s is the characteristic strain rate, Z_{st} is the stoichiometric mixture fraction, $erfc^{-1}$ is the inverse complementary error function.

Second, the flame temperature is calculated using the Burke-Schumann approach assuming a constant heat capacity, c_p. For the upper extinction limit (*i.e.* high strain rate), heat losses is negligible and the flame is considered adiabatic. Hence, the adiabatic flame temperature may be expressed as:

$$T_{st}^{ad} = \frac{Y_{O_2,2}}{r_s Y_{F,1} + Y_{O_2,2}} T_1 + \frac{r_s Y_{F,1}}{r_s Y_{F,1} + Y_{O_2,2}} T_2 + \frac{Y_{O_2,2} Y_{F,1}}{r_s Y_{F,1} + Y_{O_2,2}} \left(\frac{\Delta H_c}{c_P}\right) \tag{4.33}$$

Using our extinction model (Eq. 4.31), the expression for strain rate, a_s (Eq. 4.32), the adiabatic flame temperature, T_{st}^{ad} (Eq. 4.33) and a matlab script, we can

calibrate our model to find C and T_a in order to match the strain rates at extinction for different oxidizer stream conditions (see Fig. 4.1).

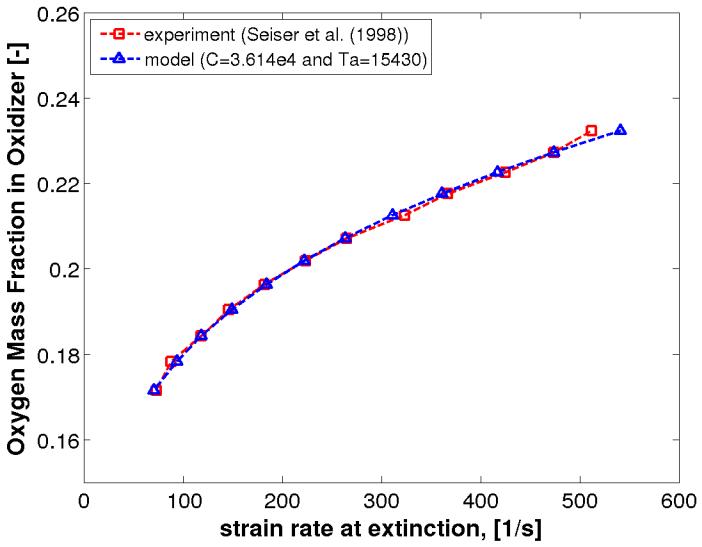

Figure 4.1: Mass fraction of oxygen in the oxidizer stream, $Y_{O_2,2}$, as a function of the strain rate a_s at extinction of non-premixed flames stabilized between counter-flowing streams: one stream is a mixture of n-heptane vapor and nitrogen, and the other is a mixture of air and nitrogen. The stoichiometric mixture fraction $Z_{st} = 0.1$.

Then, calibrating values of C and T_a (*i.e.* $C = 36140\,\mathrm{s}^{-1}$ and $T_a = 15430\,\mathrm{K}$) are used to calculate the strain rates at extinction for different fuel stream conditions (see Fig. 4.2).The discrepancies between experiment and extinction model are larger than those observed in Fig. 4.1 but are less than 25%. At this point, the Burke-Schumann approach using a constant c_p might be questionable or it might be due to the variation of mixture fraction.

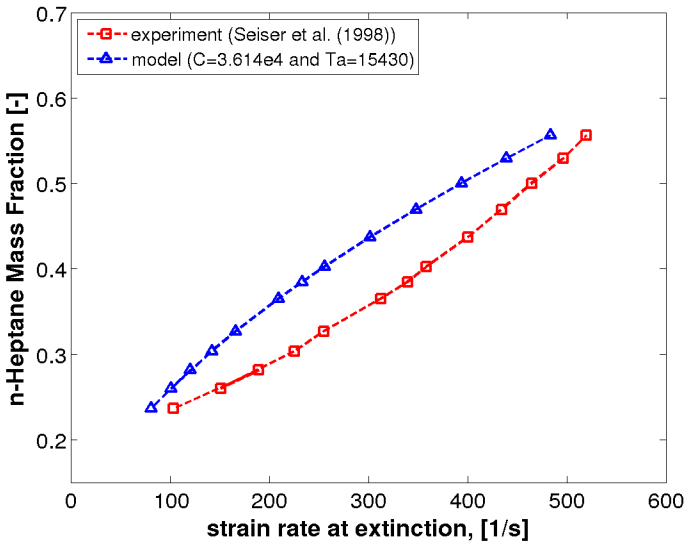

Figure 4.2: Mass fraction of fuel in the fuel stream as a function of the strain rate a_s at extinction of non-premixed flames stabilized between counterflowing streams. One stream is a mixture of n-heptane vapor and nitrogen, and the other stream is undiluted air.

4.3.2.4 Summary

For those 3 different fuels (methane, ethylene, heptane), the coefficients C and Ta are:

Table 4.3: Extinction model coefficients C and Ta.

Fuel	**C** [s^{-1}]	**Ta** [K]
methane	1.9616×10^{10}	36856
ethylene	1.0671×10^{8}	24725
heptane	3.6140×10^{4}	15430

Once coefficients C and Ta for the extinction model are known, the flamma-

bility map (Flame Temperature, T_{st}, as function of Scalar Dissipation Rate, χ_{st}) can be obtained.

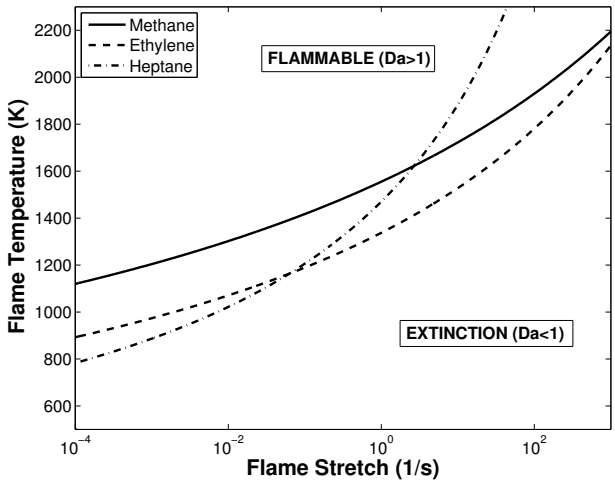

Figure 4.3: Flammability map for 3 different fuel using flame stretch, χ_{st}, and flame temperature, T_{st}, as coordinates. The lines correspond to the extinction limie, $Da = 1$, for methane, ethylene and heptane.

4.4 Flame Re-Ignition Model

From previous studies of DNS turbulent diffusion flames [7, 85–88], different flame re-ignition mechanisms have been identified and characterized:

- **Premixed ignition:** a spontaneous auto-ignition event in which fuel and oxidizer are thoroughly mixed prior to ignition.

- **Non-premixed ignition:** a spontaneous auto-ignition event in which fuel and oxidizer remain segregated at ignition time.

- **Edge flame propagation:** a piloted ignition event controlled by partially-premixed flame propagation (along the stoichiometric surface).

- **Flame-flame interaction:** a piloted ignition event controlled by interactions of burning and extinguished flame elements (normal to the stoichiometric surface).

Based on Hewson *et al.* [7], first and second (auto-ignition) re-ignition mechanisms are controlled by the temperature and related to the temperature at which the S curve becomes nearly level (Fig. 4.4), just below 1000 K, and is referred to as the crossover temperature and is the temperature below which chain termination reacts faster than chain branching. Below the threshold temperature, radical levels are reduced, which slows down the chain branching reaction. This is the chemical justification for the selection of this particular temperature range.

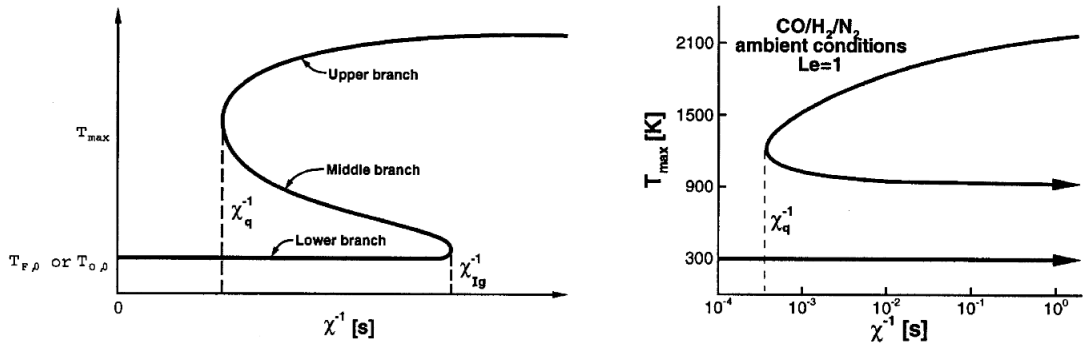

Figure 4.4: Typical S-curve showing the turning points corresponding to extinction (χ_q^{-1}) and ignition (χ_{ig}^{-1}). Left figure: typical theoretical behavior of the S-curve. Right figure: corresponding curve for the current ambient boundary conditions where spontaneous ignition is effectively not observed (picture adopted from [7]).

Hewson *et al.* mentioned that for the third and fourth types of re-ignition (edge-flame propagation and flame-flame interaction), re-ignition originate for the

heat transfer exchange from adjacent burning flames to a non-burning region, providing an ignition source. Mixing with burning flames is required, and reaction can occur, in some cases, below 1000 K. This kind of re-ignition is controlled by the mixing rate, high strain rate reduces the gap between burning and non-burning regions in the direction normal to the stoichiometric surface, and thereby promotes transport process that lead to re-ignition. It has not yet been found which mode of re-ignition is dominant in fire application. Therefore, developing a re-ignition model for LES solver is extremely challenging.

In FireFOAM, we decide to use a flame re-ignition model based on a critical temperature criterion; FIF is expressed as:

$$FIF = 0.5 + 0.5 \tanh\left(\frac{\widetilde{T} - T_{ign}}{0.1 T_{ign}}\right) \tag{4.34}$$

where $\widetilde{T}$ is the LES-filtered temperature and T_{ign} its critical (lower) value for re-ignition. As a preliminary step, we propose to use: $T_{ign} \approx 1000\,\mathrm{K}$ [7].

4.5 Verification Cases

4.5.1 2D laminar CounterFlow Flame

This section describes a 2D laminar counterflow flame to check that the flame temperature computed by the extinction model has been correctly implemented. In order to achieve fast reaction, the time scale used in the EDC model is set to 190 µs. Enthalpy (sensible, adiabatic and mixing), normalized excess enthalpy and temperature are plotted in the mixture fraction space. The square domain is 0.02 m

long using 50 cells in the normal direction to the flame front. Fuel and air are injected on each side at 0.1 m/s and at 293 K. Gravity is turned off. Methane and air reacts as:

$$CH_4 + 2O_2 + 7.52N_2 \rightarrow CO_2 + 2H_2O + 7.52N_2 \tag{4.35}$$

The corresponding stoichiometric mixture fraction is 0.055 and the adiabatic flame temperature is 2226 K [4].

Four simulations are performed (Table 4.5). First, the radiant fraction is set to zero in order to verify that $H_{st} = 0.0$ in an adiabatic configuration. Then, the radiant fraction is set to a uniform value of 0.30 in order to verify that the flame temperature model can take into account heat losses due to radiation. Finally, the oxygen mass fraction varies from 0.233 to 0.16 to show that the model can simulate extinction due to dilution effects.

Table 4.4: Radiant fraction and oxygen mass fraction parameters for case 1a-d.

Case	χ_{rad}	$Y_{O_2,\infty}$
1.a	0%	0.233
1.b	30%	0.233
1.c	0%	0.19
1.d	0%	0.16

4.5.1.1 Case 1.a ($\chi_{rad} = 0\%$; $Y_{O_2,\infty} = 0.23$)

We first start our discussion with a zero radiant fraction. In this configuration, exact solutions are $\widetilde{h}_s = \widetilde{h}_s^{ad}$, $H_{st} = 0.0$ and $\widetilde{T}(z_{st}) \approx T_{st} = 2226\,\mathrm{K}$.

Figure 4.5 shows the sensible, adiabatic sensible and mixing sensible enthalpy as function of mixture (Eq. 4.16, 4.17 and 4.18). The radiant fraction is set to zero. Hence, the sensible and adiabatic sensible enthalpy are identical.

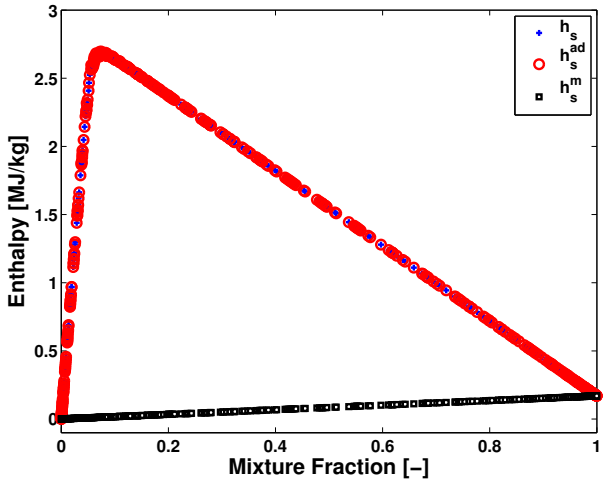

Figure 4.5: Enthalpy as function of mixture fraction. $\widetilde{h}_s$, $\widetilde{h}_s^{ad}$ and $\widetilde{h}_s^{m}$ denote the sensible, adiabatic and mixing enthalpy respectively(Eq. 4.16, 4.17 and 4.18).

Figure 4.6 depicts the normalized excess enthalpy variable (H_{st}) as function of mixture fraction. In an adiabatic configuration, $\widetilde{h}_s = \widetilde{h}_s^{ad}$ and $H_{st} = 0$.

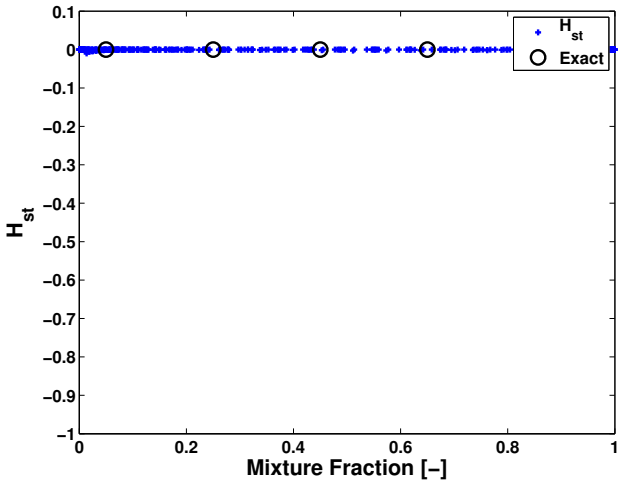

Figure 4.6: Excess enthalpy variable as function of mixture fraction (Eq. 4.15).

Figure 4.7 shows the LES-filtered temperature ($\widetilde{T}$) and the flame temperature T_{st} as function of mixture fraction. In an adiabatic configuration, $\widetilde{T}(z_{st}) \approx T_{st} = 2226\,\mathrm{K}$.

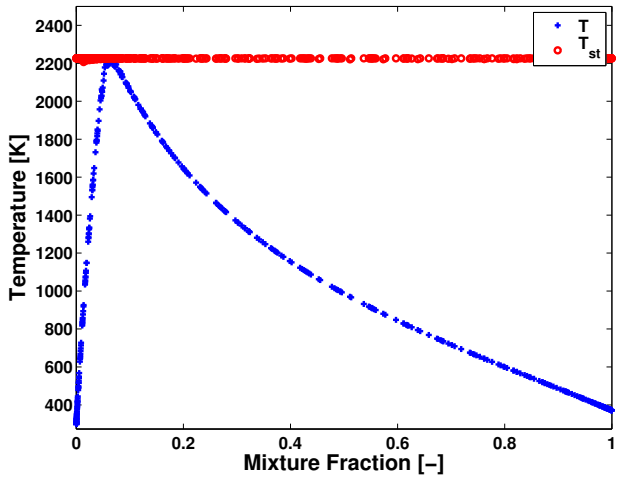

Figure 4.7: Temperature as function of mixture fraction. $\widetilde{T}$ and T_{st} denote the LES-filtered temperature and flame temperature respectively(Eq. 4.33).

It might be surprising that the flame temperature (T_{st}) is a constant as function of the LES-filtered mixture fraction ($\widetilde{z}$). Figure 4.8 depicts a sketch representing cell based quantities ($\widetilde{T}$, $\widetilde{h}_s$, $\widetilde{z}$) and the red dashed line the flame front (z_{st}). The concept is that in LES, if a cell contain fuel and oxygen ($0 < \widetilde{z} < 1$), a flame front is present and not resolved inside this cell. In addition, this flame front has an associated flame temperature (T_{st}).

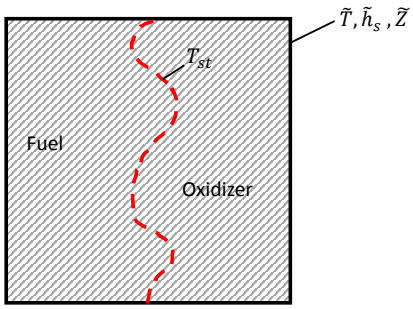

Figure 4.8: Sketch of a LES cell, the red dashed line represents the flame front inside a cell which is not resolved.

This first test demonstrates that the LES-filtered adiabatic and mixing sensible enthalpy ($\widetilde{h}_s^{ad}$ and $\widetilde{h}_s^{m}$) have been correctly implemented into FireFOAM and the flame temperature model predicts an adiabatic flame temperature in an adiabatic configuration ($\chi_{rad} = 0\%$) as expected.

Burke-Schumann

In this section, we use Burke-Schumann to compute the adiabatic and sensible enthalpy (h_s^{ad} and h_s^{m}) used to reconstruct the normalized excess enthalpy (H_{st}) and the flame temperature (T_{st}).

The Burke-Schumann solution [54] relates flame variables (h_s^{ad} and h_s^m) to mixture fraction (z) as follows:

- On the oxidizer side ($z < z_{st}$)

$$\begin{aligned} h_s^m(z) &= z h_{s,F} + (1-z) h_{s,A} \\ h_s^{ad}(z) &= z h_{s,F} + (1-z) h_{s,A} + Y_{CH_4,F} \Delta H_F z \end{aligned} \tag{4.36}$$

- On the fuel side ($z > z_{st}$)

$$\begin{aligned} h_s^m(z) &= z h_{s,F} + (1-z) h_{s,A} \\ h_s^{ad}(z) &= z h_{s,F} + (1-z) h_{s,A} + Y_{CH_4,F} \Delta H_F z_{st} \frac{1-z}{1-z_{st}} \end{aligned} \tag{4.37}$$

NB: Note that Burke-Schumann solution assumes infinitely fast combustion which is not assumed in the CFD solution.

Figure 4.9 shows sensible enthalpy as function of mixture fraction. The LES-filtered sensible enthalpy is compared against the Burke-Schumann solution using Eq. 4.36 and Eq. 4.37. The difference around the stoichiometric mixture fraction value is due to the infinitely fast combustion assumption in the Burke-Schumann solution.

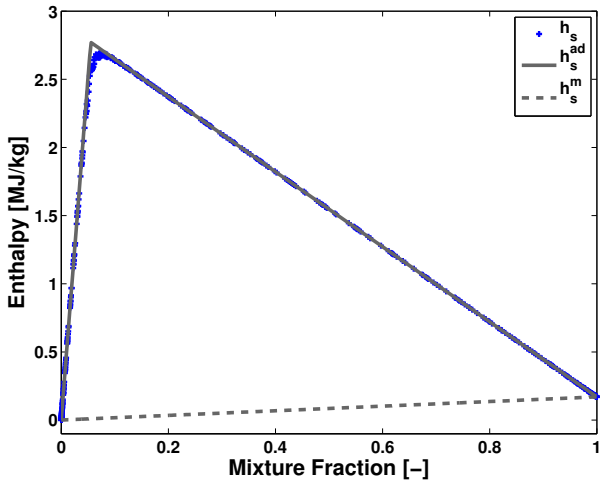

Figure 4.9: Enthalpy as function of mixture fraction. h_s, h_s^{ad} and h_s^m denote the sensible, adiabatic and mixing enthalpy respectively(Eq. 4.16, 4.36 and 4.37).

Figure 4.10 depicts the normalized excess enthalpy variable (H_{st}) as a function of mixture fraction. The deviation from the exact solution ($H_{st} = 0$) is due to the infinitely fast reaction assumption in the Burke-Schumann solution.

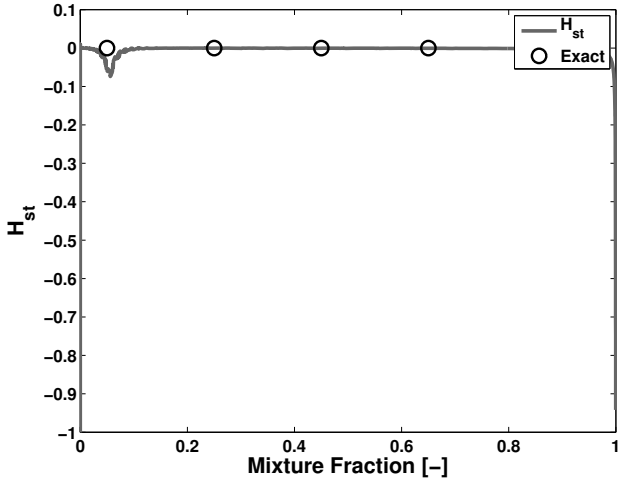

Figure 4.10: Excess enthalpy variable as function of mixture fraction.

Figure 4.11 shows the LES-filtered temperature ($\widetilde{T}$) and the flame temperature T_{st} as function of mixture fraction. The deviation from the exact solution ($T_{st} = 2226\,\mathrm{K}$.) is due to the infinitely fast reaction assumption in the Burke-Schumann solution.

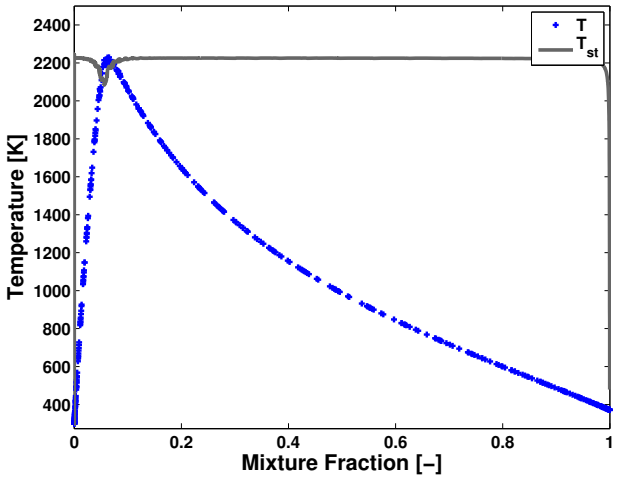

Figure 4.11: Temperature as function of mixture fraction. $\widetilde{T}$ and T_{st} denote the LES-filtered temperature and flame temperature respectively.

This comparison illustrates the advantage of solving two additional partial differential equations to compute h_s^{ad} and h_s^m, instead of using Burke-Schumann solution which assume infinitely fast reaction and is not valid for our kind of LES simulation. In addition, during an extinction event the reactant leakage effect becomes significant and the flame front is moving into the fuel or oxidizer side, *i.e.* the stoichiometric mixture fraction (z_{st}) needed in the Burke-Schumann model becomes unknown. Those assumptions seem acceptable for a counterflow flame in absence of extinction and in which the reaction time scale can be specified, but fail for more

realistic configuration like an under-ventilated compartment fire.

Flame Stretch

This section is aimed to verify that the flame stretch model has been implemented correctly. Figure 4.12 depicts the analytical function $F(\widetilde{Z})$ (eq. 4.26), the LES-filtered scalar dissipation rate $\widetilde{\chi}$ (eq. 4.23) and the flame stretch χ_{st} (eq. 4.25) in the mixture fraction space.

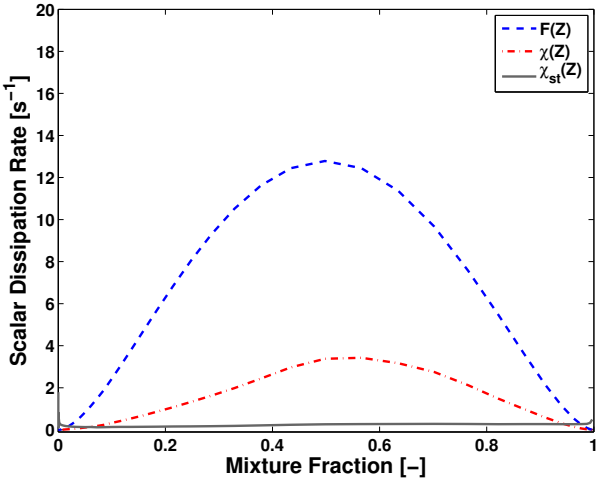

Figure 4.12: Flame stretch as function of mixture fraction. $F(\widetilde{Z})$, $\widetilde{\chi}$ and χ_{st} denote an analytical function (eq. 4.26), the LES-filtered scalar dissipation rate (eq. 4.23) and flame stretch (eq. 4.25) respectively.

In a counterflow flame, the flow time scale, τ_{fl}, is defined as:

$$\tau_{fl} = \frac{L}{V_f + V_o} \tag{4.38}$$

where L is the separation distance between the fuel and oxidizer side, V_f the inlet fuel velocity and V_o the inlet oxidizer velocity. In our configuration, $L = 0.02\,\mathrm{m}$,

$V_f = V_o = 0.1\,\mathrm{m/s}$ which means that the flow time scale is equal to 0.1 s.

Figure 4.13 shows the flame stretch as function of mixture fraction in a log-space to illustrate that in the reaction zone near stoichiometry $F\left(\widetilde{Z}\right) \sim 1$ and $\chi_{st} \approx \widetilde{\chi}$. As expected the scalar dissipation is approximately equaled to the flow time scale (0.1 s).

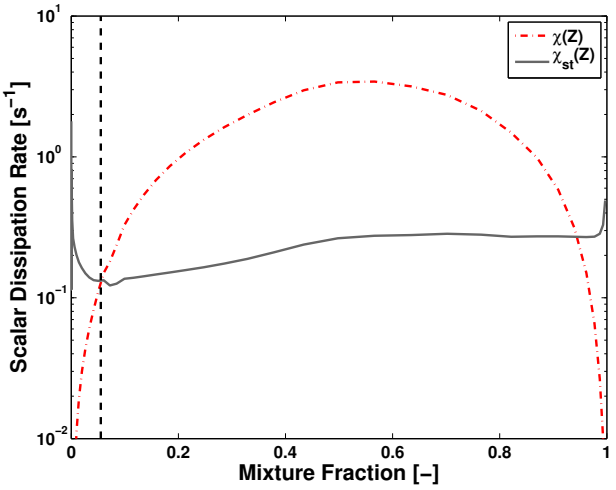

Figure 4.13: Flame stretch as function of mixture fraction. $\widetilde{\chi}$ and χ_{st} denote the LES-filtered scalar dissipation rate (eq. 4.23) and flame stretch (eq. 4.25) respectively. The vertical dashed line represents the stoichiometric line ($Z = Z_{st}$).

4.5.1.2 Case 1.b ($\chi_{rad} = 30\%$; $Y_{O_2,\infty} = 0.23$)

We now turn our discussion to a 30% radiant fraction. In this configuration, the exact solution is $H_{st} = -0.3$.

Figure 4.14 shows the sensible, adiabatic sensible and mixing sensible enthalpy as function of mixture. The radiant fraction is set to 30% and $\widetilde{h}_s < \widetilde{h}_s^{ad}$.

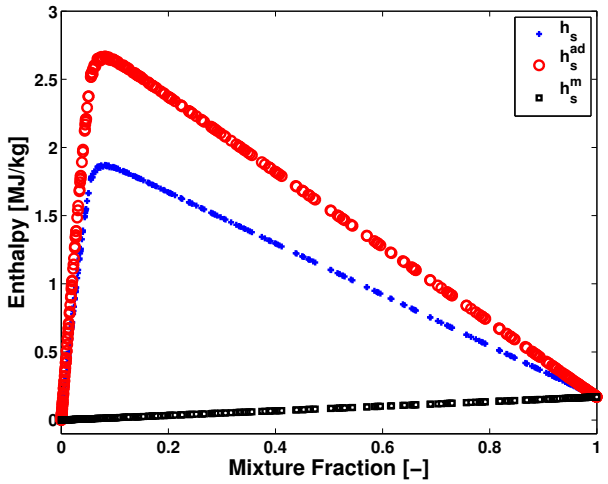

Figure 4.14: Case 1.b ($\chi_{rad} = 30\%$; $Y_{O_2,\infty} = 0.23$), see caption of Fig. 4.5.

Figure 4.15 depicts the normalized excess enthalpy variable (H_{st}) as function of mixture fraction. The radiant fraction is set to 0.30, *i.e.* $H_{st} = -0.30$.

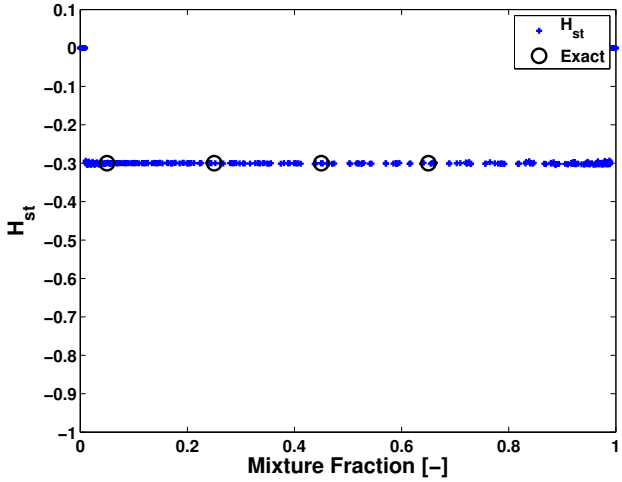

Figure 4.15: Case 1.b ($\chi_{rad} = 30\%$; $Y_{O_2,\infty} = 0.23$), see caption of Fig. 4.6.

Figure 4.16 shows the LES-filtered temperature ($\widetilde{T}$) and the flame temperature

T_{st} as function of mixture fraction. In this configuration, $\widetilde{T}(z_{st}) \approx T_{st} = 1660\,\mathrm{K}$.

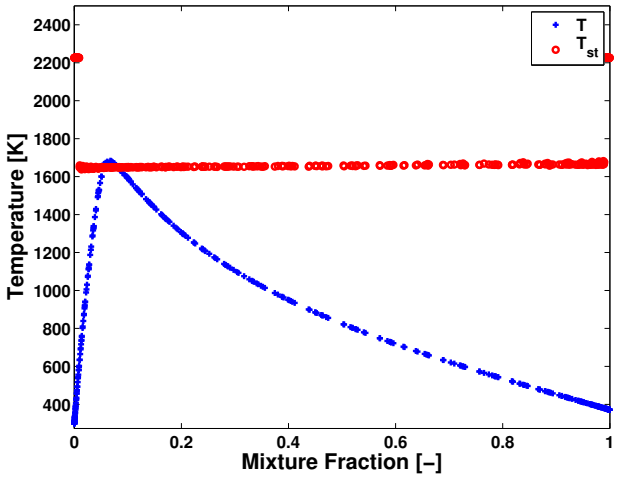

Figure 4.16: Case 1.b ($\chi_{rad} = 30\%$; $Y_{O_2,\infty} = 0.23$), see caption of Fig. 4.7.

This test shows that the flame temperature model can take into account heat losses due to radiation.

4.5.1.3 Case 1.c and 1.d ($\chi_{rad} = 0\%$; $Y_{O_2,\infty} = 0.16$ and 0.19)

Finally, the oxygen mass fraction varies from 0.233 to 0.16. In this configuration, exact solutions are $\widetilde{h}_s = \widetilde{h}_s^{ad}$, $H_{st} = 0.0$ and $\widetilde{T}(z_{st}) \approx T_{st}$ (Table 4.5).

Table 4.5: flame quantities ($\widetilde{h}_s$ and T_{ad}) for different oxygen mass fraction.

Case	$Y_{O_2,\infty}$	$max(\widetilde{h}_s)$ $[MJ/kg]$	T_{ad} $[K]$	z_{st} $[-]$
1.a	0.233	2.7	2,226	0.0544
1.c	0.19	2.22	2,000	0.0453
1.d	0.16	1.88	1,800	0.0385

Figure 4.17 shows the sensible, adiabatic sensible and mixing sensible enthalpy as function of mixture fraction. The radiant fraction is set to 0% and $h_s = h_s^{ad}$. However the maximum sensible enthalpy is decreasing as function of oxygen dilution (Table 4.5).

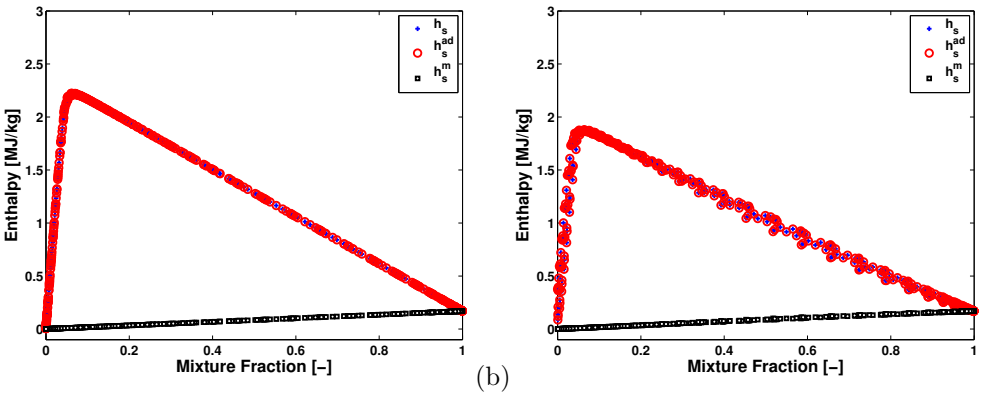

Figure 4.17: a) Case 1.c ($\chi_{rad} = 0\%$; $Y_{O_2,\infty} = 0.19$); b) Case 1.d ($\chi_{rad} = 0\%$; $Y_{O_2,\infty} = 0.16$). See caption of Fig. 4.5.

Figure 4.18 depicts the normalized excess enthalpy variable (H_{st}) as a function of mixture fraction. The radiant fraction is set to 0.00, *i.e.* $H_{st} = -0.0$.

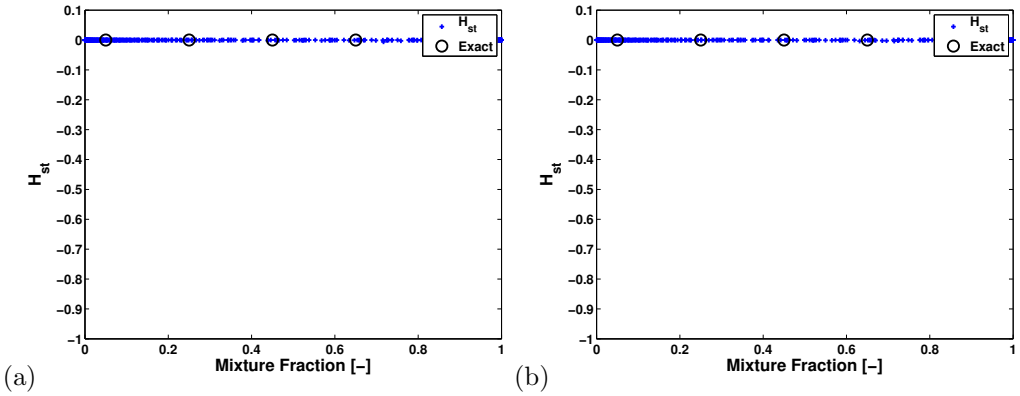

Figure 4.18: a) Case 1.c ($\chi_{rad} = 0\%$; $Y_{O_2,\infty} = 0.19$); b) Case 1.d ($\chi_{rad} = 0\%$; $Y_{O_2,\infty} = 0.16$). See caption of Fig. 4.6.

Figure 4.19 shows the LES-filtered temperature ($\widetilde{T}$) and the flame temperature T_{st} as functions of mixture fraction. In this configuration, the radiation fraction is set to zero and the decrease in the flame temperature is only due to dilution effect in the oxidizer stream ($Y_{O_2,\infty}$). $\widetilde{T}(z_{st}) \approx T_{st}$ and is function of oxygen mass fraction (see Table 4.5).

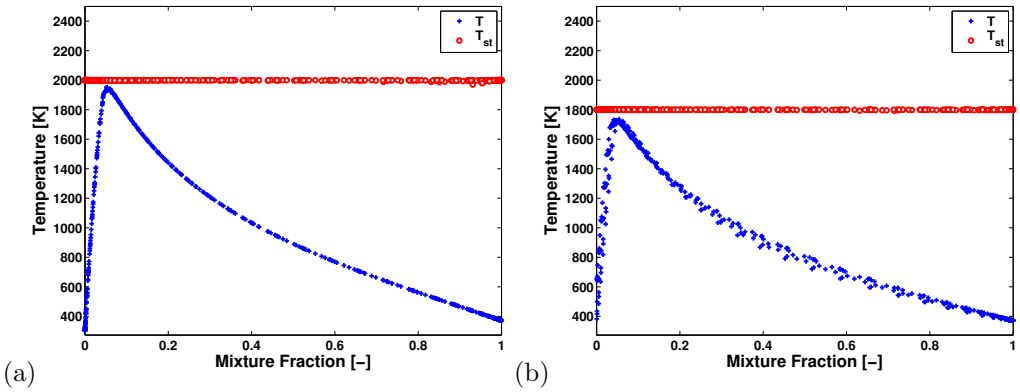

Figure 4.19: a) Case 1.c ($\chi_{rad} = 0\%$; $Y_{O_2,\infty} = 0.19$); b) Case 1.d ($\chi_{rad} = 0\%$; $Y_{O_2,\infty} = 0.16$). See caption of Fig. 4.7.

This case demonstrates the ability of the flame temperature model to take into account dilution effects through the adiabatic flame temperature (T_{st}^{ad}).

4.5.2 3D Turbulent Vertical Wall Fire

This section describes a 3D Turbulent Vertical Wall Fire [**?**, 33] in order to verify the ability of the flame temperature model to capture thermal losses for non-adiabatic walls (Fig. 4.20.b). The domain is 38 cm wide, 80 cm long and 151 cm high (Fig. 4.20.a). The left side of the domain is the vertical wall consists of three parts. The bottom part is a 6 cm high inert wall. Above the inert wall are a 1 m long burner and a 45 cm long buffer region. The propylene mass flow rate is set to 17.05 $g/m^2/s$. The radiant fraction is set to zero in order to only show heat losses due to cold walls. Two simulations are performed (Table 4.6). First, the buffer wall is set adiabatic in order to verify that $H_{st} = 0$. Then, the buffer wall is set isothermal in order to show the heat exchange with the cold wall, *i.e.* $H_{st} < 0$.

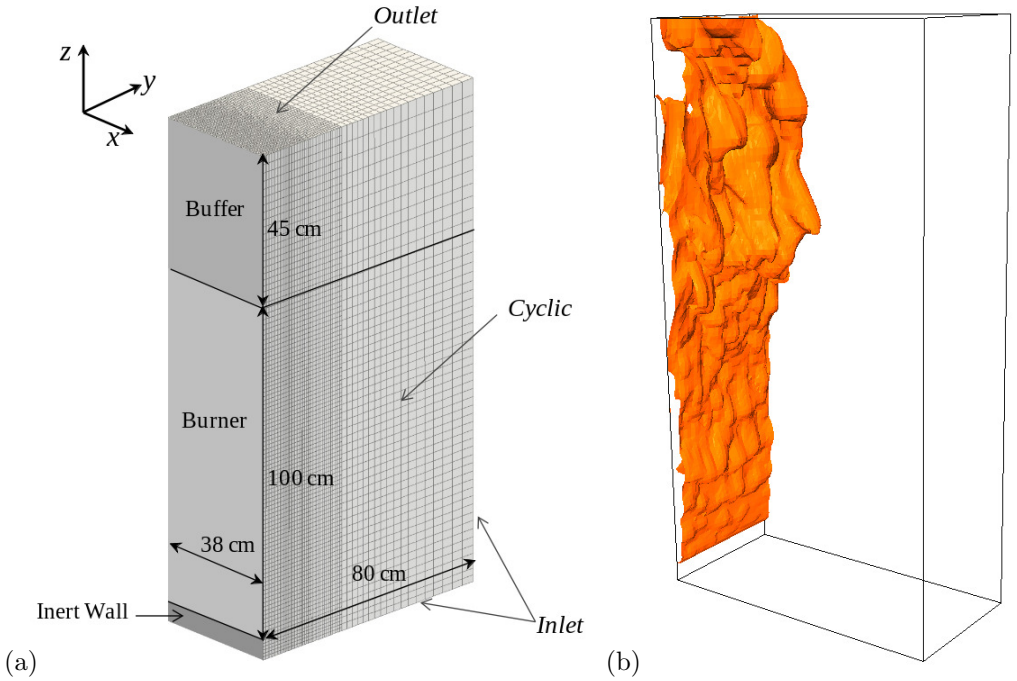

Figure 4.20: (a) Computational domain and grid setup (5mm). (b) Instantaneous view of the flame surface (the flame is identified as an iso-contour of the heat release rate per unit volume; we use 200 kW/m^3).

Table 4.6: Radiant fraction and wall boundary conditions parameters for case 2.a-b.

Case	χ_{rad}	**Wall B.C.**
2.a	0%	Adiabatic
2.b	0%	Isothermal

4.5.2.1 Case 2.a ($\chi_{rad} = 0\%$; Adiabatic Walls)

We first start our discussion with a zero radiant fraction and adiabatic walls. In this configuration, exact solutions are $\widetilde{h}_s = \widetilde{h}_s^{ad}$, $H_{st} = 0.0$ and $\widetilde{T}(z_{st}) \approx T_{st} =$

$2,334\ [K]$.

Figure 4.21 shows the sensible, adiabatic sensible and mixing sensible enthalpy as functions of mixture fraction. As expected, the sensible and adiabatic sensible enthalpy are equal. The scatter of points in fig. 4.21 is due to the scatter of combustion time scale. Indeed, EDC is used for modeling turbulent diffusion flame assuming that the reaction is primarily controlled by turbulent mixing. As the mixing time scale is spatially non-uniform, the reaction rate will also be non-uniform.

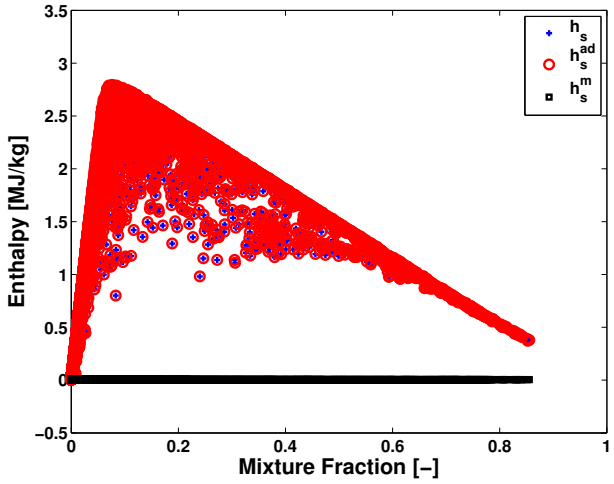

Figure 4.21: Case 2.a ($\chi_{rad} = 0\%$; Adiabatic Walls), see caption of Fig. 4.5.

Figure 4.22 depicts the normalized excess enthalpy variable (H_{st}) as a function of mixture fraction. The radiant fraction is set to 0.0 and the buffer wall is adiabatic, *i.e.* $H_{st} = 0.0$.

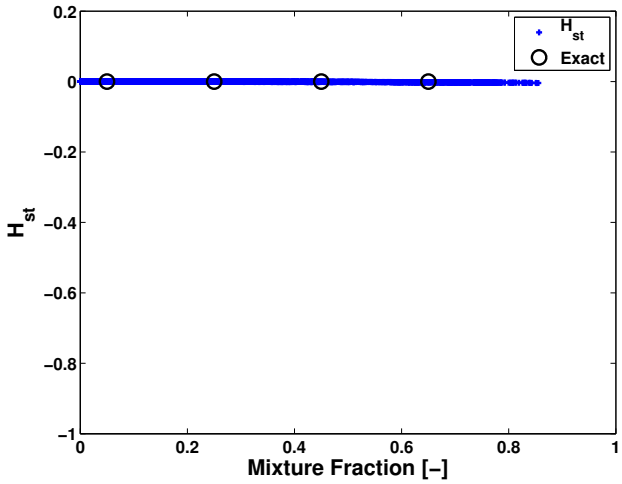

Figure 4.22: Case 2.a ($\chi_{rad} = 0\%$; Adiabatic Walls), see caption of Fig. 4.6.

Figure 4.23 shows the LES-filtered temperature ($\widetilde{T}$) and the flame temperature T_{st} as functions of mixture fraction. In an adiabatic configuration, $\widetilde{T}(z_{st}) \approx T_{st} = 2334\,\mathrm{K}$.

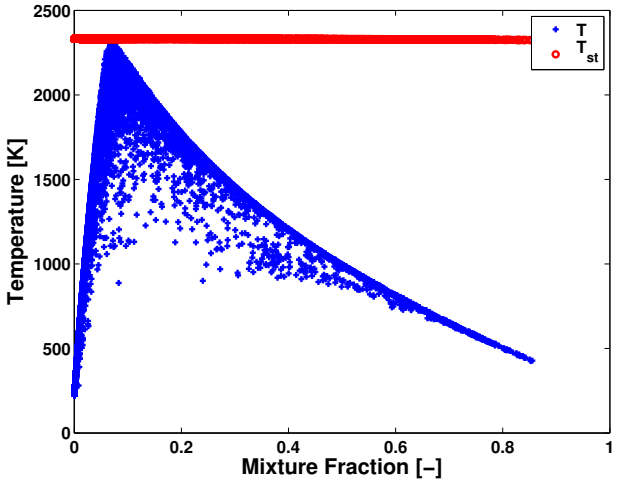

Figure 4.23: Case 2.a ($\chi_{rad} = 0\%$; Adiabatic Walls), see caption of Fig. 4.7.

4.5.2.2 Case 2.b ($\chi_{rad} = 0\%$; Isothermal Walls)

We now turn our discussion to the case with zero radiant fraction and isothermal walls. In this configuration, thermal losses are only due to heat exchange between the hot flame and the cold wall. In this configuration, the exact solution is unknown but $H_{st} \leq 0.0$.

Figure 4.14 shows the sensible, adiabatic sensible and mixing sensible enthalpy as functions of mixture.

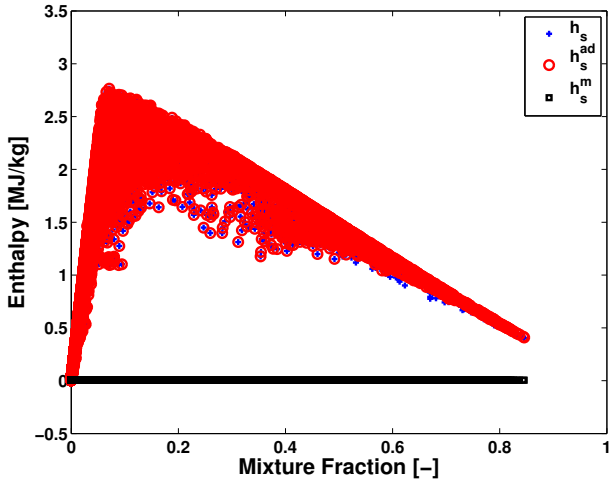

Figure 4.24: Case 2.b ($\chi_{rad} = 0\%$; Isothermal Walls), see caption of Fig. 4.5.

Figure 4.25 depicts the normalized excess enthalpy variable (H_{st}) as function of mixture fraction. The radiant fraction is set to 0.0 and the buffer wall is isothermal, *i.e.*$H_{st} \leq 0.0$.

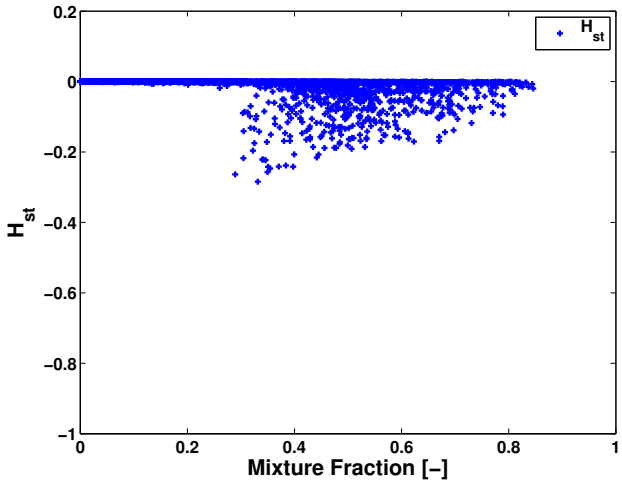

Figure 4.25: Case 2.b ($\chi_{rad} = 0\%$; Isothermal Walls), see caption of Fig. 4.6.

Figure 4.26 shows the LES-filtered temperature ($\widetilde{T}$) and the flame temperature T_{st} as function of mixture fraction.

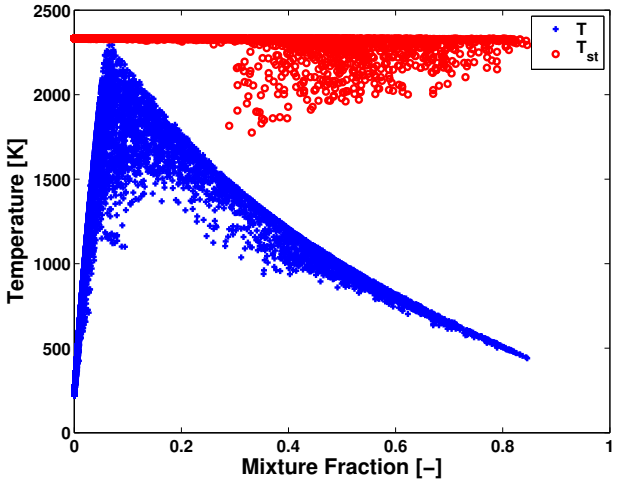

Figure 4.26: Case 2.b ($\chi_{rad} = 0\%$; Isothermal Walls), see caption of Fig. 4.7.

This test shows that the flame temperature model can take into account ther-

mal losses due to cold wall.

5 Results: Under-Ventilated Compartment Fire

5.1 Introduction

Two of the main challenges found in a CFD treatment of compartment fires are the possible transition to under-ventilated combustion and the sensitivity of the production rate of flammable vapors (*i.e.*, the fuel) to the fire room thermal environment [12]. The transition to under-ventilated combustion is typically observed as a consequence of a rapid increase in fire size called flash-over. After flash-over has occurred, the conditions inside the fire compartment switch from a fuel-limited to an oxygen-limited combustion regime. This combustion regime is characterized by an increased probability of flame extinction and increased emissions of products of incomplete combustion. It is also associated with a dramatic change in flame structure in which the flame is observed to migrate from the fuel sources towards the compartment vents, *i.e.*, towards the oxygen supply streams.

5.2 Experimental Configuration

The experimental configuration is a reduced-scale compartment previously studied at the University of Maryland [13, 14, 50, 51] . The compartment is cubic-shaped and has a $40^3\,\mathrm{cm}^3$ size. The walls are made of type-M Kaowool board. The compartment is vented by two identical slots located near the top and bottom of one of the vertical walls. Combustion inside the compartment is fueled by a round-shaped heptane pool centrally-located on the compartment floor. The global equivalence ratio inside the compartment is modified using different vent dimensions (*i.e.*, different values of the width W_v and height H_v of the vents) and different fuel pan sizes (*i.e.*, different diameters D). Details about the instrumentation may be found in Refs. [13, 14, 50, 51].

A wide variety of flame behaviors is observed in the experimental database [13, 14, 50, 51]. These flame behaviors belong to one of the following four categories: (R1) steady well-ventilated fires in which the flame is stabilized above the burner; (R2) steady under-ventilated fires in which the flame is stabilized near the vents; (R3) unsteady under-ventilated fires featuring large periodic oscillations and intermittent flame quenching; (R4) unsteady under-ventilated fires leading to complete flame extinction. The main parameter that controls transition from one flame regime to another has previously been identified as the fire room global equivalence ratio (GER). In short, regime R1 corresponds to small values of GER, regime R4 to large values, regime R3 to values close to 1 and regime R2 to values moderately above 1. Table 5.1 presents the parameters of the 4 cases considered in the present study (we

call these cases by the name of the regimes they are selected to represent).The fire room GER is evaluated as $GER = (r_s/Y_{O_2,a}) \times (\dot{m}_f/\dot{m}_a)$, where r_s is the stoichiometric oxygen-to-heptane mass ratio, $r_s \approx 3.52$; $Y_{O_2,a}$ the oxygen mass fraction in ambient air, $Y_{O_2,a} \approx 0.233$; $\dot{m}_f$ the total fuel MLR, and $\dot{m}_a$ the air mass flow rate though the lower compartment fire. In case R1, $\dot{m}_f \approx 0.14\,\mathrm{g/s}$ and $\dot{m}_a \approx 10\,\mathrm{g/s}$, we find $GER \approx 0.2$, which quantifies the amount of excess air still present.

Table 5.1: Ventilation and fuel source parameters in cases R1-R4. The global equivalence ratio in column 4 is estimated using average values of the measured fuel evaporation rate and vent flow rate of incoming fresh air.

Case	**Vent height x Width(cm)**	**Fuel Pan Diameter(cm)**	**GER**
R1	3 x 40	9.5	0.2
R2	1 x 40	19	2.6
R3	3 x 10	9.5	1.0
R4	1 x 2	9.5	12.0

5.3 Numerical Solver

FireFOAM solves the Favre filtered fully compressible NavierStokes equations (see section 2.2) and provides a choice between several modeling options for the treatment of turbulence, combustion and thermal radiation. The turbulent sub-grid scale stress is modeled by the eddy viscosity concept. The present study uses the constant coefficient one-equation eddy viscosity model, which solves a sub-grid scale (SGS) kinetic energy equation (see section 2.4.1). The turbulent combustion

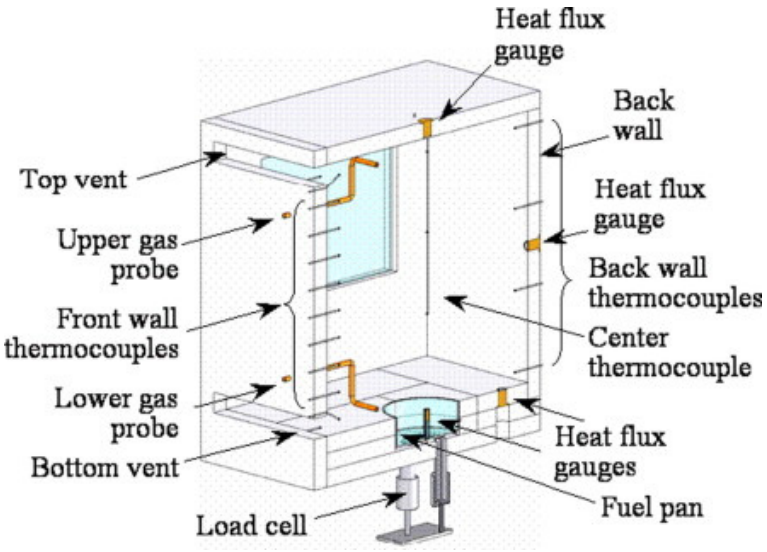

Figure 5.1: Schematic half-view of the experimental configuration.

model adopts the Eddy Dissipation Concept (see section 2.5). Extinction modeling is treated via the Damköhler approach newly implemented in FireFOAM for the purpose of this study using a mixture fraction approach to model the flame temperature and flame stretch (see section 4). In FireFOAM, the radiative transfer equation (RTE) is solved using the discrete ordinate method (see section 2.6). In the present study, the description of thermal radiation is simplified by assuming a gray and non-absorbing, optically-thin medium. The flame emission is described using the concept of a radiant fraction χ_{rad} (see section 2.6.1); we use $\chi_{rad} = 35\%$ [89]. The assumption of a non-absorbing medium is deemed acceptable in the present small-scale configuration. This assumption should be viewed as an intermediate step that conveniently avoids the difficulties associated with modeling soot formation.

5.4 Numerical Configuration

The computational domain includes the fire compartment and an adjacent air block (Fig. 5.2). The role of the air block is to avoid treating the vents as numerical boundary conditions and to bring more accuracy to the simulated vent flows. The fire compartment (adjacent air block) is $40 \times 40 \times 40\,\mathrm{cm}^3$ ($40 \times 40 \times 60\,\mathrm{cm}^3$). The computational mesh inside the fire compartment is unstructured and uses $145,680$ triangular prisms; the mesh resolution Δ_m is approximately 1 cm. The computational mesh in the air block is structured and uses a stretched rectangular grid with $55,000$ cells, a stretch ratio of $5\,\%$ and a maximum aspect ratio of 4. The air block mesh is constrained to match the grid lines of the fire compartment mesh at the location of the vents.

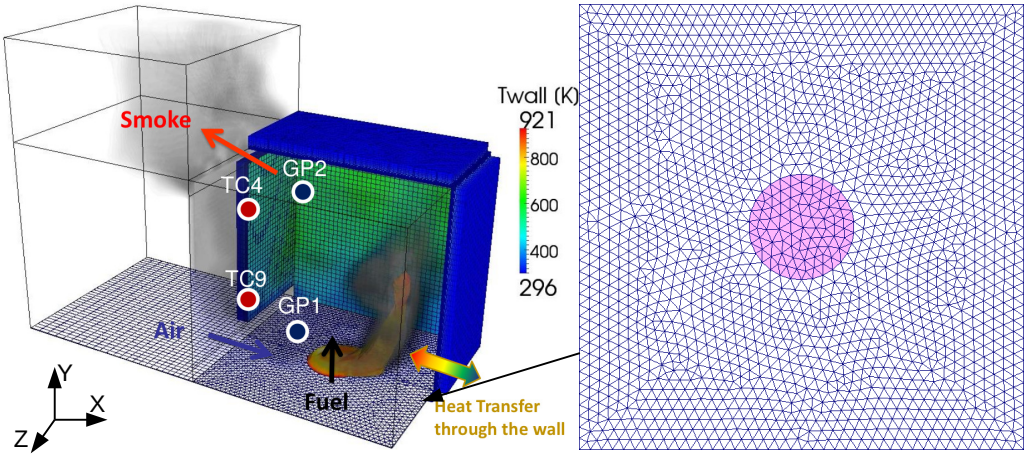

Figure 5.2: Numerical configuration showing the fire compartment and the adjacent air block. The compartment features a floor-level circular fuel pan and two vents located at the top and bottom of the west wall. The figure shows the footprint of the computational mesh (on the plane $z = 0$): the mesh is unstructured in the fire compartment and structured in the air block. The figure also shows the location of the thermocouples (TC4/TC9) and gas probes (GP1/GP2) used in subsequent figures.

Typical outflow and entrainment boundary conditions are used for the open boundaries at the top and sides in the air block. At the inlet, we use a thermal-feedback-driven fuel mass flow rate as discussed in the next section 5.4.1. At the wall, the temperature is calculated using a standard conjugate heat transfer approach (and use a one-dimensional solver to treat heat conduction through the solid walls (verification test, see section 3.3.1)).

5.4.1 Semi-Empirical Evaporation Model

5.4.1.1 Evaporation Rate

We now turn to a discussion of the new model implemented in FireFOAM for liquid fuel evaporation used in the under-ventilated compartment fire case. The heptane pool surface boundary conditions correspond to a constant position (the liquid regression is neglected), a prescribed temperature (98 °C corresponding the boiling temperature of heptane) and a mass evaporation rate, noted $\dot{m}_f''$ (in units of kg/s/m^2), that is treated as proportional to the net total gas-to-liquid heat flux, noted $\dot{q}_s''$, which is the sum of the net radiative heat flux, noted $\dot{q}_r''$ (see section 5.4.1.3), and the convective heat flux, noted $\dot{q}_c''$ (see section 5.4.1.2). We write: $\dot{m}_f'' = \left(\dot{q}_s''/H_v\right)$ where H_v is an effective heat of vaporization. Note that for the compartment fire case, while the thermodynamic value of H_v for heptane is equal to 0.45 MJ/kg, the apparent values of H_v in Refs. [50, 51] (calculated as the ratio of $\dot{q}_s''$ divided by $\dot{m}_f''$ with $\dot{q}_s''$ measured with a heat flux gauge and $\dot{m}_f''$ measured with a load cell) are much larger: $H_v = 2$ MJ/kg for cases R1, R3 and R4, and for case R2, $H_v = 1$ MJ/kg (featuring a larger fuel pan). Cases R1, R2,R3 and R4 are described in table 5.1. These high values may be interpreted as effective heats of vaporization that account for unresolved physics, *e.g.*, heat losses to the fuel container walls, *etc.* These results suggest that an accurate representation of evaporation processes may require using an advanced heptane pool model with a detailed representation of the in-liquid heat transfer. In the present study, we choose instead to use the

experimentally-determined effective heats of vaporization. In order to avoid possible uncontrolled oscillations and to represent thermal inertia effects in the heptane pool, the gas-to-liquid heat flux is both spatially-averaged (across the pool surface) and time-averaged (over a period of 4 s); we write $\dot{m}_f'' = \left(\int \overline{\dot{q}_s''} dA_f / H_v \right) / A_f$, where A_f is the pool surface area, and where $\overline{\dot{q}_s''(t)} = \int_{t-4s}^{t} \dot{q}_s''(t')dt'$. Finally, burn-out is described using an *ad hoc* model that increases H_v when the residual fuel mass is close to 0.

5.4.1.2 Convective Heat Flux

At the liquid fuel boundary, the convective heat flux is calculated as:

$$\dot{q}_c'' = -k\frac{\partial T}{\partial n} = -\left(\alpha + \alpha_{sgs}\right)\rho C_p \frac{T_w - T_g}{\delta n/2} \tag{5.1}$$

where k is the thermal conductivity of the gas, n is the spatial coordinate pointing into the solid, δn is the normal grid spacing, T_g is the gas temperature in the center of the first gas phase cell, T_w is the surface temperature, α is the molecular (or laminar) thermal diffusivity and α_{sgs} is the sub-grid scale (or turbulent) thermal diffusivity. At the liquid fuel surface, we assume that the convective heat flux is mainly laminar and use $\alpha_{SGS} = 0$.

5.4.1.3 Radiative Heat Flux

The net radiative heat flux, $\dot{q}_r''$, at the liquid-fuel surface is obtained by calculating the difference between the incident radiative flux and the emitted and re-radiated heat flux components. The surface emissivity is set to 0.9 for the heptane

pool.

FireFOAM was run using 16 processors on a large-scale Linux cluster; typical runs took on the order of 1,000 hours of CPU time.

5.5 Results and Discussion

5.5.1 Prescribed Mass Loss Rate

While the present study is focused on evaluating simulations with thermally-driven MLR (see section 5.4.1), a series of preliminary tests was also performed using a prescribed MLR approach in which $\dot{m}''_f$ is directly estimated from measured variations of the heptane pool mass [50, 51].

Grid Requirement

We first start an analysis of the different length scales and the grid requirement to resolve them. The purpose is to make sure that the boundaries inside the compartment controlling the system evolution are computed accurately, *i.e.* the vent mass flow rates, the wall and burner heat fluxes.

The grid resolution choices correspond to a trade-off between expected accuracy and computational cost and do not follow all recommended guidelines for grid design. The configuration shown in Fig. 5.1 features three types of relevant length scales:

- **Flame scales:** $L_f,\ D \sim O(10\,\text{cm})$ (height and width of the flame which are related to the fuel pan diameter)

- **Vent flow scales:** $W_v,\ H_v \sim O(1\,\text{cm})$ (the width and height of the vents)
- **Wall Boundary Layer:** $\delta_{BL} \sim O(1\,\text{cm})$

Recommended guidelines in fire modeling suggest using a mesh with characteristic ratios (D/Δ_m), (H_v/Δ_m) and (W_v/Δ_m) greater than 10. With our choices, the resolution of the flame region is marginal, $(D/\Delta_m) \approx 9.5$ in cases R1, R3 and R4, while that of the vent flows is generally poor, $(H_v/\Delta_m) = 1$ in cases R2 and R4 (Table 5.1).

Vent Flow Scales

This section serves to illustrate good agreement between the experimental and simulated vent mass flow rates, even though the computational grid is too coarse to resolve accurately the vent flow structure.

Based on the conservation of mass, species and energy, Dr. Quintiere derives a semi-empirical correlation to calculate the mass flow rate through vents for over-ventilated compartment fire [50].

$$\dot{m}_i = 0.5 C_d A_0 \sqrt{H} \rho_\infty \sqrt{g} \sqrt{2} \left(\frac{1 - \frac{T_\infty}{T}}{1 + \frac{T}{T_\infty}} \right)^{1/2} \tag{5.2}$$

$$\dot{m}_o = 0.5 C_d A_0 \sqrt{H} \rho_\infty \sqrt{g} \sqrt{2} \left(\frac{1 - \frac{T_\infty}{T}}{1 + \frac{T}{T_\infty}} \right)^{1/2} \tag{5.3}$$

where C_d is a flow coefficient with $C_d = 0.65$, A_0 the total vent area, H the compartment fire height, ρ_∞ the far-field (outside) density, T_∞ the far-field (outside)

temperature and T the average room temperature.

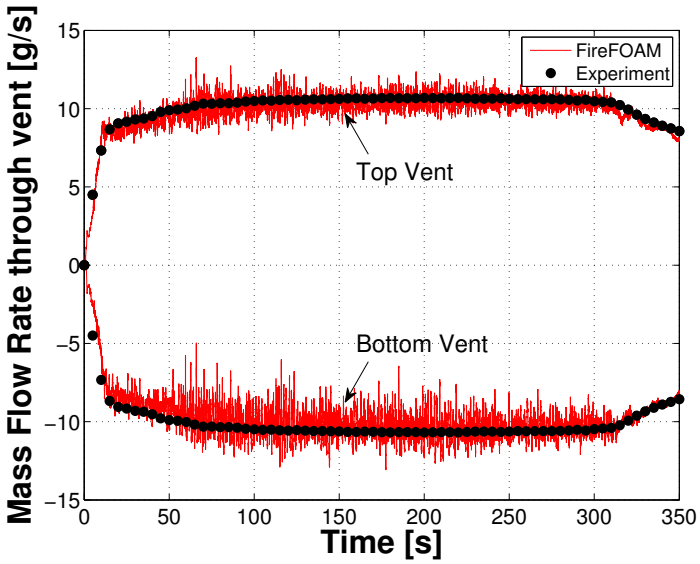

Figure 5.3: Mass flow rate through bottom and top vents. Comparison between numerical simulation (solid lines) and Quintiere's correlation (symbols), see Eq. 5.2 and 5.3.

Note that, while the vent flows are clearly under-resolved, this test shows that the simulated vent mass flow rates are in good agreement with measurements from Refs. [50, 51]. One possible explanation is that the magnitude of the vent flow rates is primarily determined by pressure differences between the compartment and the outside and that correct predictions of pressure differences may not require resolving the details of the vent flow. Based on this evidence, the current grid choices are deemed acceptable.

Wall Boundary Layer

While the vent mass flow rate controls the level of oxygen inside the room and the fresh air amount to the fire, the wall heat transfer mainly controls the room temperature and plays an important role in the compartment fire scenario. The convective heat transfer model is based on a classical gradient diffusion modeling approach with a turbulent diffusivity (see section 5.4.1.2); no law of the wall is used; the wall temperatures are calculated using a standard conjugate heat transfer approach. The wall are assumed to be mainly covered of soot and the wall emissivity is set to 1.

Figure 5.4 presents the simulated time variations of the net and convective heat flux measured at the three different wall location, as obtained in cases R3 and using a prescribed MLR approach; these variations are compared to measurements from a heat flux gauge. The experimental gauge heat flux is decomposed into a radiative and convective heat flux as followed:

$$\dot{q}''_{gauge} = \dot{q}''_r + \dot{q}''_c = \varepsilon_g G - \varepsilon_g \sigma T_g^4 + \dot{q}''_c \tag{5.4}$$

where T_g is the gauge temperature, G the irradiation received by the gauge, σ the Stefan-Boltzmann constant, $\dot{q}''_{gauge}$ the net gauge heat flux, $\dot{q}''_r$ the radiative heat flux and $\dot{q}''_c$ the convective heat flux. The gauge is water cooled such that $T_g = 300\,\mathrm{K}$. Figure 5.4 suggests that the wall heat transfer is dominated by radiative heat transfer ($\sim 75\%$) and that convective heat transfer has limited impact ($\sim 25\%$); in the present small-scale (optically-thin) compartment, radiative heat transfer is

controlled by the flame emissive power and by the wall temperatures.

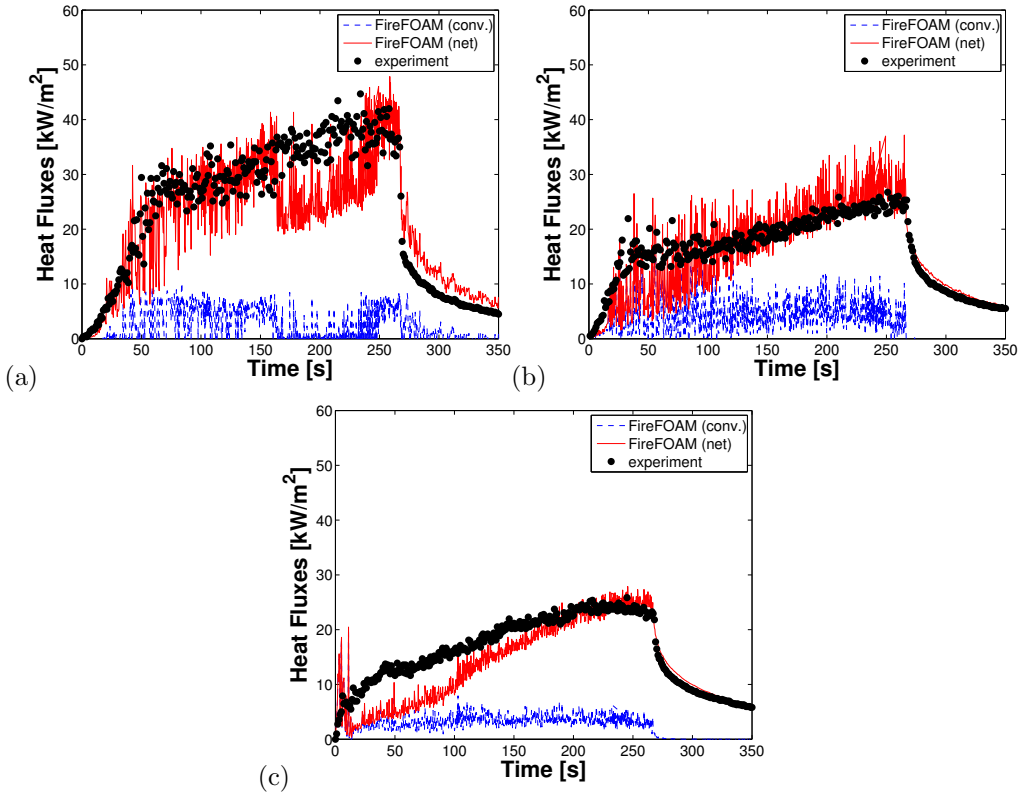

Figure 5.4: Wall heat flux at three different location inside the compartment fire. a) HF2 (x=0.15, y=0, z=0 m); HF3 (x=0.2, y=0.2, z=0 m); c) HF4 (x=0.0, y=0.4, z=0 m).

Figure 5.5 presents the simulated time variations of the net total heat flux $\dot{q}_s''$ evaluated at the center of the fuel pan, as obtained in cases R1-R4 and using a prescribed MLR approach; these variations are compared to measurements from a heat flux gauge. Figure 5.5 suggests that the gas-to-liquid thermal load is dominated by radiative heat transfer ($\sim$ 80%) and that convective heat transfer has limited impact ($\sim$ 20%); in the present small-scale (optically-thin) compartment, radiative heat transfer is controlled by the flame emissive power and by the wall temperatures.

At the liquid fuel surface, we assume that, for the under-ventilated compartment fire case, the convective heat flux is mainly laminar and then $\alpha_{SGS} = 0$. Good agreement between numerical and experimental net burner heat flux suggests that this assumption is deemed acceptable for the current study.

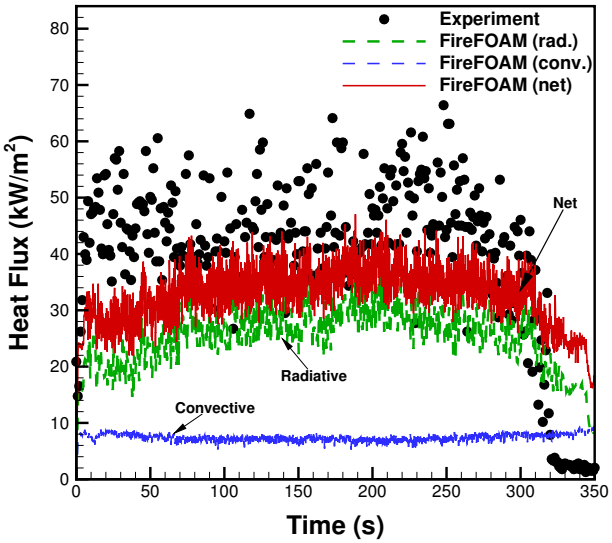

Figure 5.5: Heat flux at the center of the fuel pan. Comparison between experimental data (symbols; net heat flux) and numerical results (solid lines; convective, radiative and net heat fluxes) for case R1.

Case R1

We continue our discussion with case R1 (Fig. 5.6) and compare the experimental data to FireFOAM results obtained using a prescribed mass loss rate approach (Fig. 5.6a). This case corresponds to a well-ventilated combustion regime and features a classical pool-like flame structure. Agreement between experiment and computational data is good, in terms of temperature (Fig. 5.6c) and oxygen

concentrations (Fig. 5.6d). Note that in Fig. 5.6c, the experimental data for temperature correspond to uncorrected thermocouple measurements; these raw data are compared to simulation results using a virtual thermocouple model (see section 2.7.1).

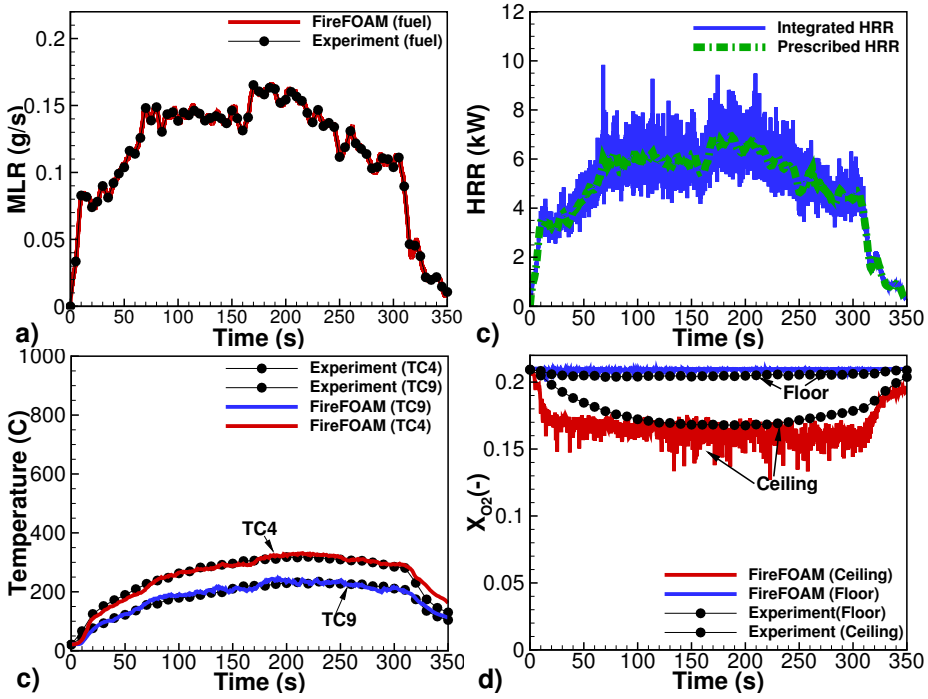

Figure 5.6: Comparison between experimental data (symbols) and FireFOAM results (solid lines) for case R1. (a) Mass loss rate (prescribed); (b) Heat release rate (compared to mass loss rate times heat of combustion); (c) Temperatures (near the vents); (d) Oxygen mole fraction.

Case R4

We now turn to case R4 (Fig. 5.7). This case corresponds to a severely underventilated combustion regime and features total flame extinction approximately 41 s after ignition. Fig. 5.7b compares the heat release rate to its theoretical well-

ventilated value (defined as the product of the fuel mass loss rate times the heat of combustion): the difference between the two curves provides evidence of flame extinction and suggests that the modified EDC model correctly responds to the effect oxygen starvation. However, the simulated flame does not fully extinguish and a residual flame remains present close to the fuel surface.

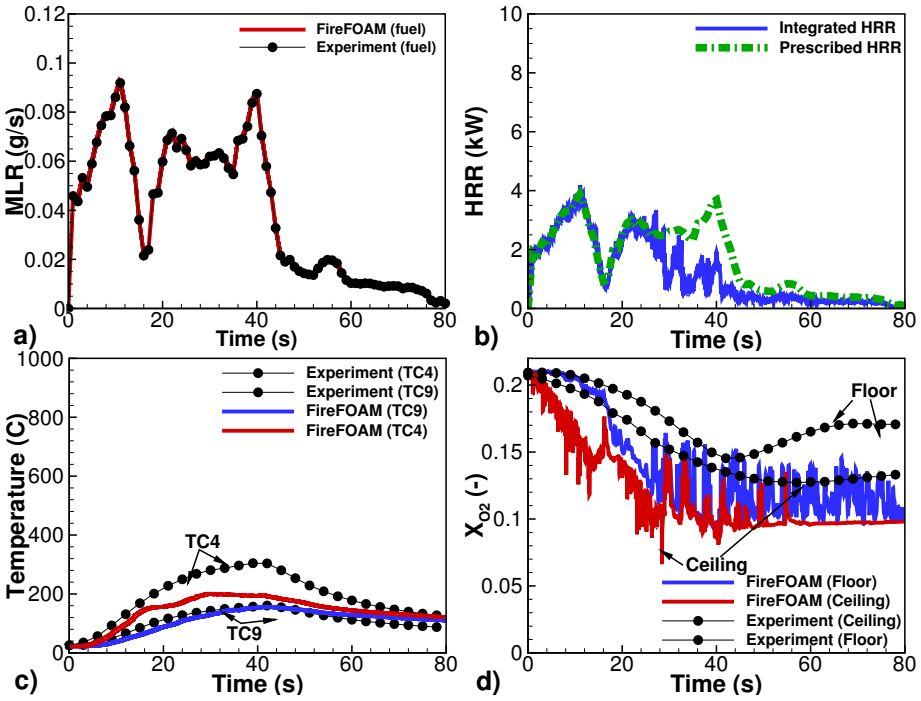

Figure 5.7: See caption of Fig. 5.6. Case R4.

Fuel pan heat flux

Figure 5.8 shows that heat flux variations feature a fast initial transient followed by a fully-developed phase and by a decay phase. The agreement between experimental data and numerical results is good during the fully-developed phase: the order of magnitude of the heat flux is correctly predicted (typical values of $\dot{q}''_s$

range from 15 to 50 $\mathrm{kW/m^2}$); discrepancies may be substantial for a particular case (for instance, in case R1, the simulated heat flux is under-estimated by approximately 30% on average) but the overall qualitative trends are correctly captured: cases R1 and R3 have the highest thermal loads; case R4 (featuring complete flame extinction at time $t \approx 40\ s$) has the lowest; and case R3 (featuring intermittent flame quenching) has large fluctuations. Note, however, that the comparison between experimental data and numerical results is poor during the decay phase: in the (prescribed-MLR) simulations, residual flames are sustained until complete fuel depletion and $\dot{q}_s^{''}$ remains large, whereas in the experiments, flames are extinguished once evaporation becomes sufficiently weak and $\dot{q}_s^{''}$ becomes low.

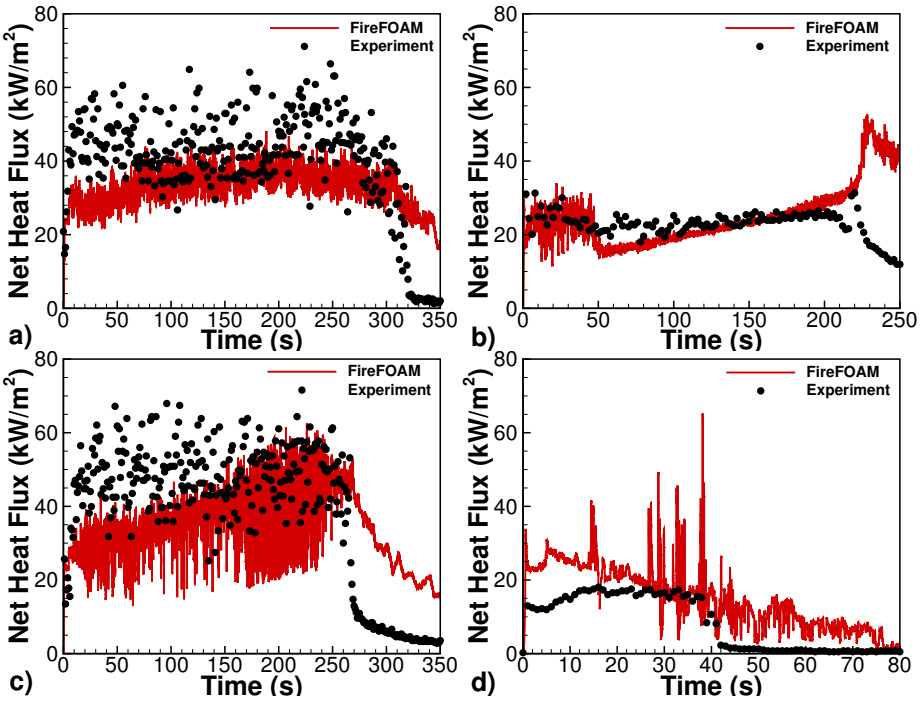

Figure 5.8: Net heat flux at the center of the fuel pan. Comparison between experimental data (symbols) and numerical results (solid lines; prescribed MLR tests). Cases: (a) R1; (b) R2; (c) R3; (d) R4.

Overall, these preliminary tests are encouraging and demonstrate that FireFOAM is capable of simulating the intensity of the thermal feedback (at least during the fully-developed phase), which is a pre-requisite to using a thermally-driven mass loss rate approach. In addition, the vent mass flow rate is computed accurately for the 4 cases, a necessary requirement to simulate the different GER scenario (GER is a function of the vent and fuel mass flow rate). Extra-results for cases R1, R2, R3 and R4 for a prescribed mass loss rate can be found in appendix D.

5.5.2 Thermally-Driven Mass Loss Rate

We now turn to a discussion of simulations with thermally-driven MLR. Note that to provide a numerical start of evaporation, a prescribed-MLR model is applied during the first 5 seconds of the simulations. We first consider case R1 (Fig. 5.9). Case R1 is representative of over-ventilated fire conditions for which combustion is fuel-limited and the flame is stabilized above the fuel source. Figure 5.9(a) shows that fuel evaporation is well predicted: during the fully developed stage, the discrepancies between measured and simulated MLR are less than 30% (the discrepancies are larger during the decay phase). Figure 5.9(a) also shows that case R1 is extinction-free and that the spatially-averaged rate of production of non-burning fuel $(C_7H_{16})^*$ is 0, $\dot{\Omega}_{(C_7H_{16})^*} = \iiint_V \left(\overline{\dot{\omega}'''_{GR2}} - \overline{\dot{\omega}'''_{GR3}}\right) dV = 0$, where V is the volume of the fire compartment.

Figure 5.9(b) presents the corresponding variations of the simulated heat release rate, noted HRR, $HRR = \iiint_V \overline{\dot{\omega}'''_{h_s}} dV$; these variations are compared to the fuel-limited estimate of HRR, noted HRR_{FL} and defined as the product of MLR times the heat of combustion, $HRR_{FL} = MLR \times \Delta H_F = \left(\dot{m}''_f \times A_f\right) \Delta H_F$. Figure 5.9(b) shows that in a time average sense $HRR \approx HRR_{FL}$, which suggests that the combustion efficiency, noted χ_a and defined as the ratio of the time-integrated HRR divided by the time-integrated HRR_{FL}, is close to 1, $\chi_a = \left(\int_0^\infty HRR(t')dt' / \int_0^\infty HRR_{FL}(t')dt'\right) \approx 1$.

Figures 5.9(c)-(d) present the variations of temperature and oxygen mole fraction

at selected representative locations. TC4 and TC9 are located near the vented wall, at 10 and 30 cm elevation respectively; GP1 and GP2 are located near the floor and ceiling at mid-point between the burner and the vented wall. Note that in Fig. 5.9(c), the experimental data correspond to raw thermocouple measurements and are not corrected for radiation losses; these raw data are compared to simulation results using a virtual thermocouple model (see section 2.7.1). Figures 5.9(c)-(d) show that in case R1, because the fire is well-ventilated, the ceiling layer temperature (oxygen mole fraction) remains moderate (high) and is approximately equal to 300 °C (0.17). The agreement between experimental data and numerical results is very good.

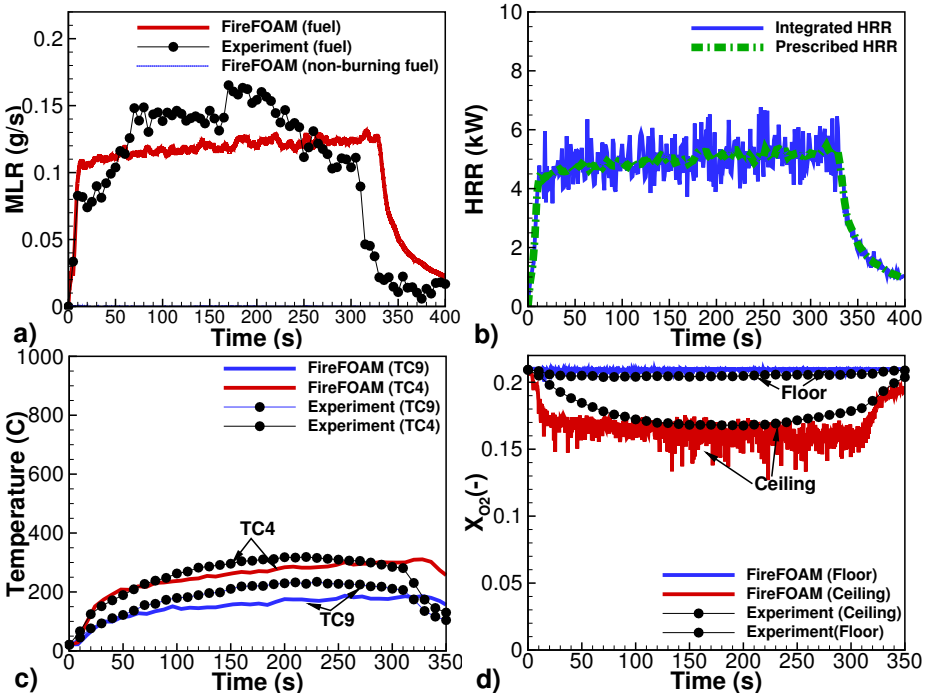

Figure 5.9: Comparison between experimental data (symbols) and numerical results (solid lines) for case R1. (a) Measured and simulated MLR, also compared to the simulated rate of formation of non-burning fuel $\dot{\Omega}_{(C_7H_16)^*}$ (0 in case R1); (b) Simulated HRR (gray solid line) compared to its fuel-limited estimate HRR_{FL} (black dashed line) (no experimental data in this plot); (c) Temperature (at TC4/TC9); (d) Oxygen mole fraction (at GP1/GP2).

Next we consider case R2 (Fig. 5.10). Case R2 is representative of under-ventilated fire conditions for which combustion becomes oxygen-limited and partial extinction is observed until the flame re-locates at the vents and continues burning extinction-free. Figure 5.10(a) shows that during the fully developed stage, fuel evaporation is again well predicted: discrepancies between measured and simulated MLR are less than 30%. Figure 5.10(a) also shows that case R2 features production of non-burning fuel (*i.e.*, flame extinction) during a short transient period at times

$t \approx 10\,\text{s}$–$20\,\text{s}$; this transient period corresponds to the displacement of the flame from the heptane pool to the bottom and top vents. Figure 5.11 compares the flame structures observed in cases R1 and R2 (at $t = 150\,\text{s}$) and suggests that in case R2, significant burning takes place outside of the fire compartment.

Because HRR is defined as the heat release rate inside the fire compartment, and because except for a short transient period case R2 is extinction-free, the difference between HRR and HRR_{FL} (Fig. 5.10(b)) gives a measure of the relative weights of burning inside and outside of the fuel compartment; we find that 37% of the burning takes place inside. Note that, once the flame is successfully stabilized at the vents (Fig. 5.11), it is supplied with fresh air and the combustion efficiency is close to 1; we find $\chi_a \approx 0.98$.

Figures 5.10(c)-(d) present the variations of temperature and oxygen mole fraction at TC4/TC9 and GP1/GP2 locations. In case R2, the compartment temperatures are high (approximately 700 °C) and the oxygen mole fractions are low (0 at GP2). The agreement between experimental data and numerical results is good for temperatures and fair for oxygen levels (GP1 lies in the flame zone and predictions will be affected by inaccuracies in predictions of the exact flame location).

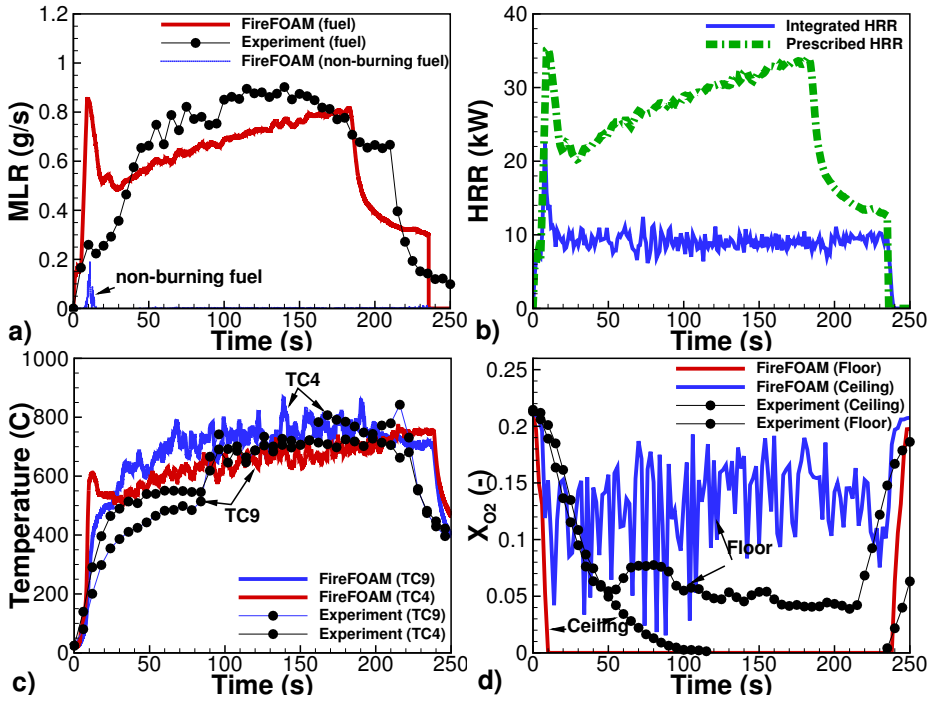

Figure 5.10: Case R2, see caption of Fig. 5.9.

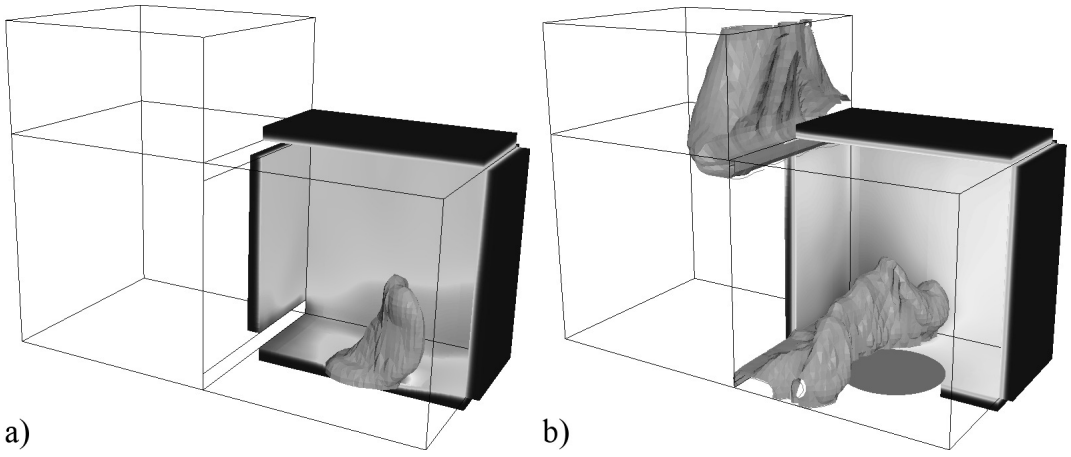

Figure 5.11: Instantaneous ($t = 150\,\mathrm{s}$) view of the flame surface (the flame is identified as an iso-contour of the heat release rate per unit volume; we use $200\,\mathrm{kW/m^3}$). Cases: (a) R1; (b) R2.

Next we consider case R3 (Fig. 5.12). Case R3 is representative of quasi-stoichiometric fire conditions that are unstable and feature periodic flame extinction and re-ignition (the instability frequency in case R3 is close to 1 Hz [50, 51]). Figure 5.12(a) presents the time variations of MLR and shows that fuel evaporation is still relatively well predicted but that discrepancies between measured and simulated MLR are increased (up to 40%). Figure 5.12(a) also shows that case R3 features significant production of non-burning fuel (*i.e.*, flame extinction); however, the numerical results suggest that a part of unburnt fuel produced by extinction events is later consumed through re-ignition and that the overall combustion efficiency remains close to 1. Figure 5.12(b) supports these results and shows that $HRR \approx HRR_{FL}$; we find $\chi_a = 0.98$. Figures 5.12(c) and 5.12(d) present the time variations of temperature and oxygen mole fraction at TC4/TC9 and GP1/GP2 locations. In case R3, the experimental data show little difference between the floor and ceiling locations, which suggest that a transition to a well-mixed single-layer structure of the compartment gas has occurred. The agreement between experimental data and numerical results is good, except for the oxygen level at GP1 (this may be due to poor resolution of the air inflow stream and/or to difficulties in simulating accurately the large oscillations that were experimentally observed).

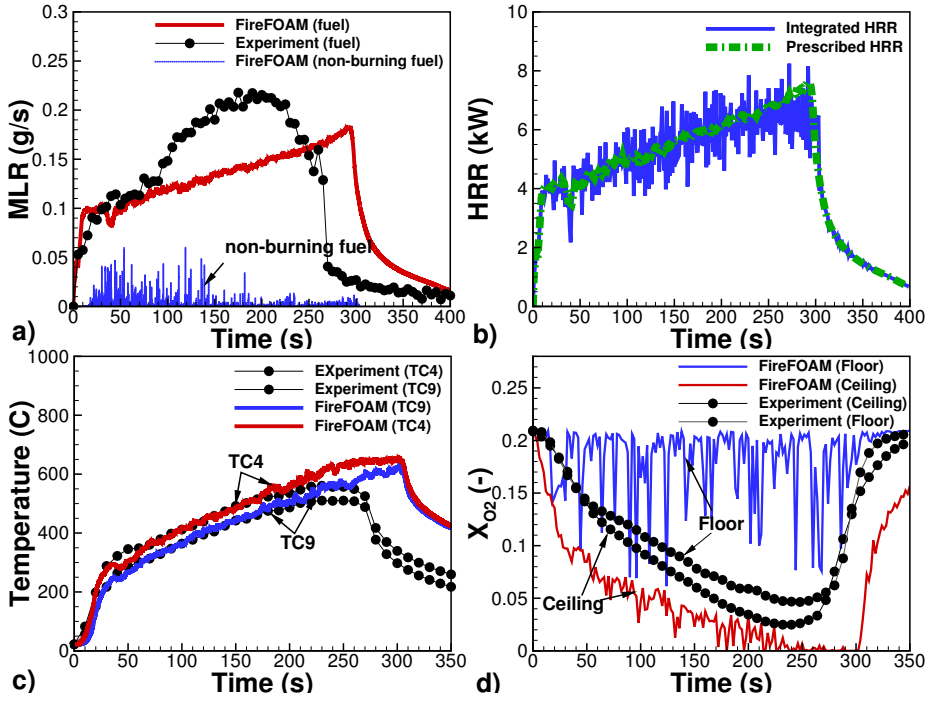

Figure 5.12: Case R3, see caption of Fig. 5.9.

We now turn to case R4 (Fig. 5.13). Case R4 is representative of ultra-rich fire conditions for which the combustion is driven to a complete extinction due to oxygen starvation. Figure 5.13(a) shows that, while some details of the measured fluctuations in the fuel evaporation rate may not be simulated accurately, the simulation successfully captures the gradual reduction in MLR followed by a complete extinction (at $t \approx 30\ s$ in FireFOAM vs at $t \approx 42\ s$ in the experiment). Figure 5.13(a) also shows that case R4 features production of non-burning fuel (*i.e.*, flame extinction) during a transient period at times $t \approx 20\,\text{s}$–$40\,\text{s}$; this transient period corresponds to a transition to complete flame extinction. Figure 5.13(b) supports these results and shows that HRR is 0 after $t = 40\ s$. The discrepancy between

HRR and HRR_{FL} in Fig. 5.13(b) gives a measure of the weight of flame extinction; we find $\chi_a \approx 0.87$.

Figures 5.13(c)-(d) present the corresponding variations of temperature and oxygen mole fraction at TC4/TC9 and GP1/GP2 locations. The agreement between experimental data and numerical results is fair for temperatures but poor for oxygen levels. Extinction is observed to occur when floor-level oxygen mole fractions fall below 0.15.

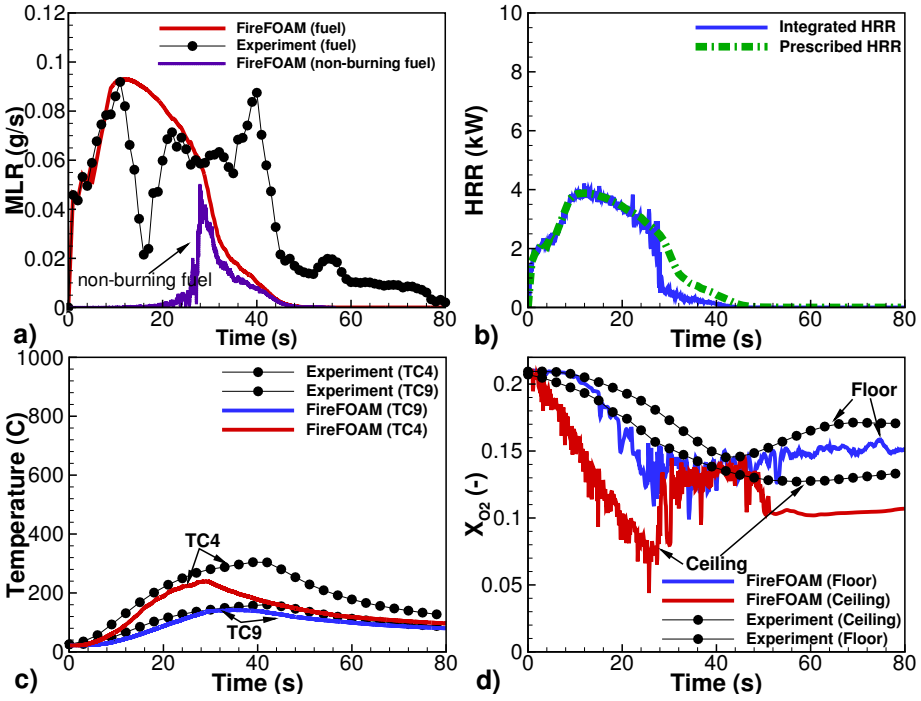

Figure 5.13: Case R4, see caption of Fig. 5.9.

Extinction model deactivated

We now consider the simulated case R4 in which the extinction model is being deactivated. The mass loss rate and heat release rate are computed and compared

to figure 5.13.

Figure 5.14(a) and (c) depicts the mass loss rate for the activated and deactivated case and show that more fuel has been released for the deactivated simulation. All the fuel released has been consumed, *i.e.* $\chi_a \approx 1$ (compared to $\chi_a \approx 0.87$ with the extinction model on). This illustrates the need and the effect of the extinction model on the heat release rate reduction due to oxygen starvation.

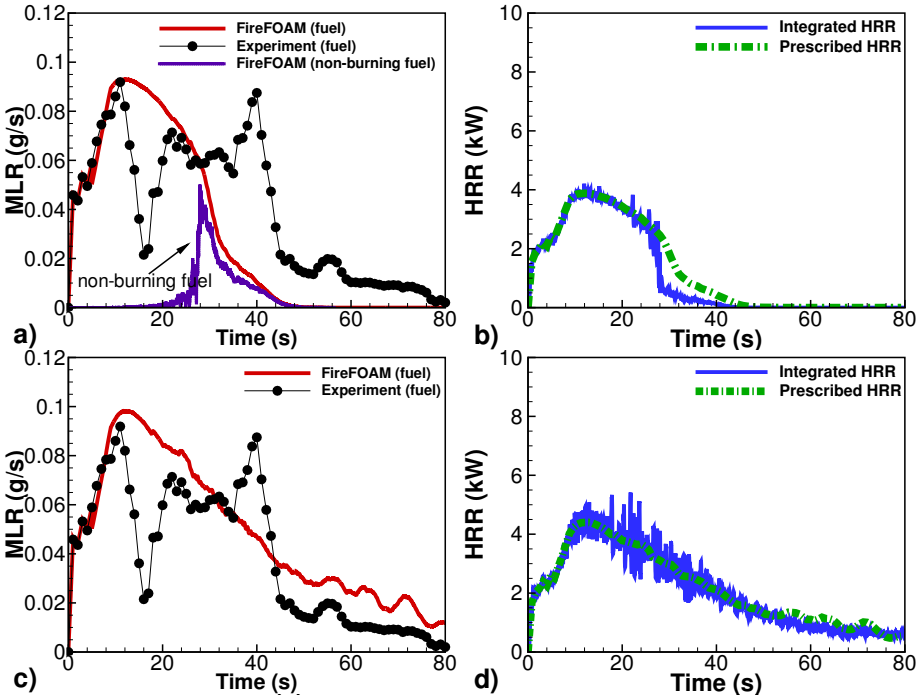

Figure 5.14: Case R4 with extinction model activated for a) and b), and deactivated for c) and d), see caption of Fig. 5.9.

Figure 5.15(a)-(b) compares the flame structure observed for the activated and deactivated extinction model at 60 s. While most of the flame burns above the burner, part of the fuel reached the top and bottom vent where it has access to fresh

oxygen in order to burn.

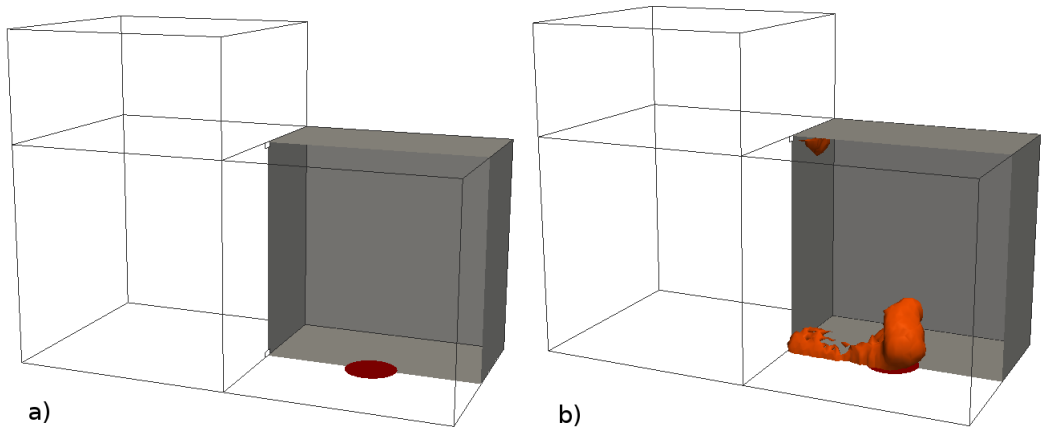

Figure 5.15: Instantaneous ($t = 60\,\mathrm{s}$) view of the flame surface (the flame is identified as an iso-contour of the heat release rate per unit volume; we use $200\,\mathrm{kW/m^3}$). Cases: (a) R4 with activated extinction model; (b) R4 with deactivated extinction model.

Grid Refinement Study

This section describes a grid refinement study and an evaluation of numerical quality on the extinction model. Grid size is always an issue in CFD, not only because it determines the computational cost, but also because it determines numerical accuracy (not only the spacial accuracy, but also the temporal accuracy because the grid size determines the time step). FireFOAM uses second order schemes. Reducing Δx leads to increased numerical accuracy as well as increased physical modeling fidelity since more length scales and flow dynamics are directly captured by the grid. It is mentioned in the previous section that vent flow fluctuations and wall heat flux dynamics are apparently correctly described by the current grid ($\Delta x \sim 1\,\mathrm{cm}$). In this section, we will only evaluate the grid refinement effect on the extinction model

by focusing on the mass loss rate and heat release rate. We refine the grid by a factor 2, *i.e.* $\Delta x \sim 5\,\text{mm}$. Case R4 is selected as it features total extinction and figure 5.13 is used as a reference.

Figure 5.16(a) shows that the simulation successfully captures the gradual reduction in MLR (at $t \approx 30\,\text{s}$ in FireFOAM vs at $t \approx 42\,\text{s}$ in the experiment). However, with 5 mm grid size the simulated flame does not fully extinguish and a residual flame remains present close to the fuel surface like in the prescribed MLR case. Figure 5.16(a) also shows that case R4 features production of non-burning fuel (*i.e.*, flame extinction) from $t \approx 20\,s$. Figure 5.16(b) supports these results and shows that HRR is close to 0 after $t = 40\,\text{s}$. The discrepancy between HRR and HRR_{FL} in Fig. 5.16(b) gives a measure of the weight of flame extinction; we find $\chi_a \approx 0.66$. Even if the flame is not fully extinguished compared to the 1 cm grid size, the 5 mm grid size correctly predicts the weight of extinction due to oxygen depletion, *i.e.* $\chi_a \approx 0.66$. Figures 5.16(c)-(d) present the corresponding variations of temperature and oxygen mole fraction at TC4/TC9 and GP1/GP2 locations and show no difference with the coarser mesh (Fig. 5.16(c)-(d)).

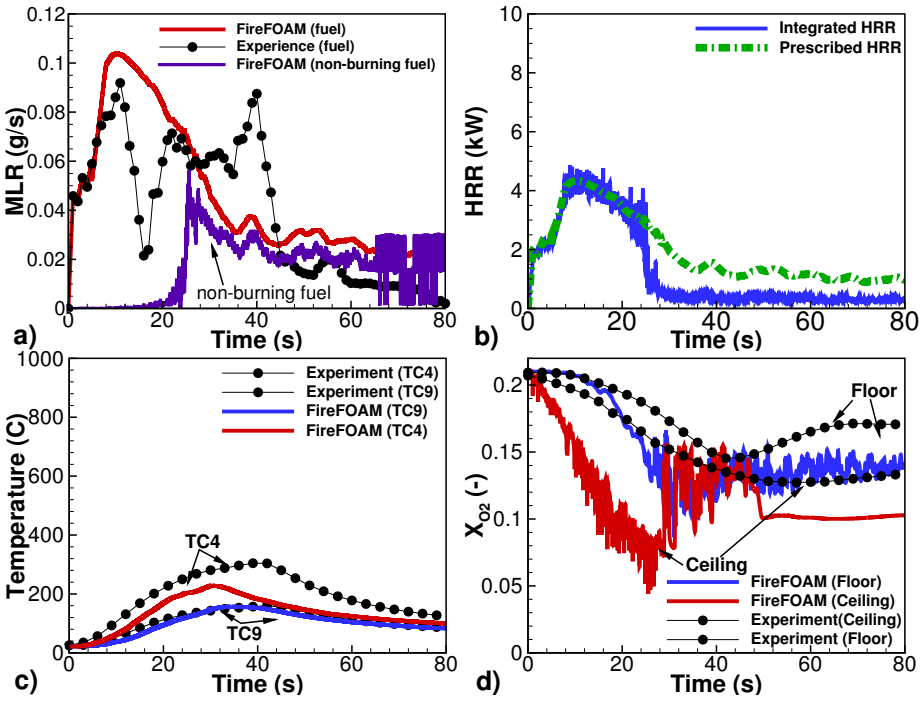

Figure 5.16: Case R4 ($\Delta x \sim 5\ mm$), see caption of Fig. 5.9.

Figure 5.17(a)-(b) compares the flame structure observed for a 1 cm and 5 mm grid size at 60 s. While the flame has been totally quenched for the 1 cm grid size, a residual flame remains present close to the fuel surface for 5 mm grid size.

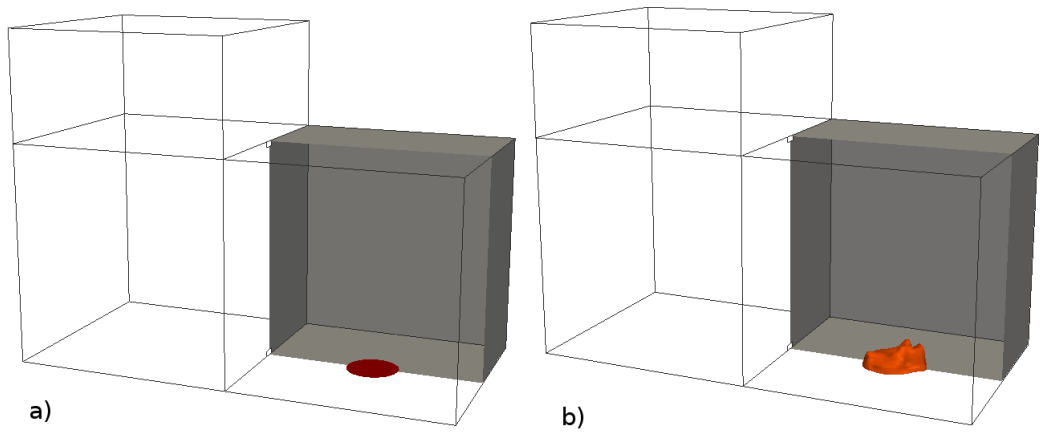

Figure 5.17: Instantaneous ($t = 60\,\mathrm{s}$) view of the flame surface (the flame is identified as an iso-contour of the heat release rate per unit volume; we use $200\,\mathrm{kW/m^3}$). Cases: (a) R4 ($\Delta x \sim 1\,\mathrm{cm}$) ; (b) R4 ($\Delta x \sim 5\,\mathrm{mm}$).

5.6 Conclusion

The present study is aimed at evaluating the ability of current CFD-based fire models to simulate compartment fires under poorly ventilated conditions. The study considers four cases that are taken from a previously developed experimental database and are representative of four different flame behaviors, *i.e.*, steady over-ventilated fires, steady under-ventilated fires, unstable fires with partial flame quenching, transient fires leading to total flame quenching. The numerical simulations are performed with a CFD solver called FireFOAM and using a new flame extinction model as well as a thermally-driven fuel evaporation model. The flame extinction model is based on the concept of a critical value of the flame Damköhler number. Overall, the agreement between experimental and computational results is good and shows that current CFD-based fire models are capable of describing

(at least qualitatively and to a certain extent, as documented in this thesis, quantitatively) the transition from over- to under-ventilated fire conditions, as well as the transition from extinction-free conditions to conditions in which the flame experiences quenching. The numerical results also allow a discussion of combustion efficiency, a parameter that is of significant practical importance (for instance for problems related to smoke explosion or toxic emissions) but for which data are generally unavailable. One open question that remains a concern is the level of grid resolution required for accurate simulations of gas-to-fuel-source heat fluxes (the thermal feedback). The present study is performed with a 1 cm grid resolution; this cell size is sufficient to capture flame scales but is not suitable to resolve vent flows or boundary layer flows. The relative success of the simulations may be due to a number of helpful factors. One factor is that the flames are characterized by small sizes (less than 10 kW) and are therefore unsteady laminar rather than fully turbulent; these flames do not feature a large range of length scales and do not represent a difficult computational challenge. Another factor is that radiation heat transfer apparently dominates the thermal feedback; in the present problem, radiation heat transfer is controlled by the flame and by the walls; and these features are suitably resolved by the computational grid.

6 Results: Turbulent Line Fire in Controlled Co-flow (Extinction by Nitrogen gaseous agent)

The general objective of this project is to support the development and validation of CFD models used to simulate the response of fires to the activation of a suppression system. The emphasis in the present study is on the problem of flame weakening and extinction when the fire is exposed to gaseous agents. The experimental component of the study is aimed at developing a new experimental database corresponding to a canonical slot burner configuration [52]. The configuration provides two-dimensional, plane, buoyancy-driven, methane-fueled, turbulent diffusion flames with controlled co-flow conditions. The co-flow currently allows for the supply of a mixture of air and nitrogen, including conditions for which the reduction in oxygen strength leads to full flame extinction; future work will also allow for a co-flow of air mixed with a water mist as discussed in chapter 7. The computational component of the study is aimed at evaluating flame extinction/re-ignition models using FireFOAM-2.2.x. Comparisons between experimental measurements and numerical results provide a suitable test bed to evaluate the ability of the LES fire

model to accurately describe flame response to a range of dilution conditions (section 6) or water mist loading (section 7), as well as the transition from extinction-free conditions to partial or total quenching.

6.1 Experimental Configuration

This work features the suppression of a buoyant, turbulent, methane diffusion flame via nitrogen dilution quenching. Flames are stabilized above a $5 \times 50\,\mathrm{cm}^2$ Wolfhard-Parker burner surrounded by a $50 \times 75\,\mathrm{cm}^2$ air co-flow (Fig. 6.1). A methane flow rate of 1.0 g/s is utilized. Assuming complete combustion, the total heat-release rate is roughly 50 kW in the unsuppressed flames. Nitrogen gas is introduced to the air co-flow to provide flame suppression. During experiments, the nitrogen flow rate varies between 0–50 g/s, mixing with the fixed air flow of 68.5 g/s to yield variations in X_{O_2} between 0.210 and 0.125. An additional small co-flow of pure oxygen is supplied along the length of the burner to provide a strengthened and stabilized flame base that resists liftoff extinction. The constant oxygen flow rate of (0.0800 ± 0.0008) g/s (1.2 cm/s from the tube surface) provides 2.0 % of the oxygen required for stoichiometric combustion of the flame. Flame suppression is monitored through simultaneous integral combustion efficiency measurement via calorimetry with O_2 and CO_2 consumption, oxidizer stream oxygen gas sampling, radiative loss fraction measurement via radiometer, flame luminosity measurement via photo-diode, and flame imaging. Flame imaging provides a robust flame height measurement technique. Flame extinguishment is the result of increasingly prevalent localized quenching, with global extinction occurring at $X_{O_2} = 0.127 \pm 0.001$. Flame

height first increases, then decreases when reducing X_{O_2}. The radiative loss fraction decreases linearly when reducing X_{O_2}. A sharp transition is noted at $X_{O_2} = 0.145$ (Fig. 6.3). Flame luminosity decreases monotonically when reducing X_{O_2}, where sharp bends in the trend demarcate transition between flame sooting regimes that are also visually identifiable via change in flame color from yellow to yellow-blue to blue (Fig. 6.3).

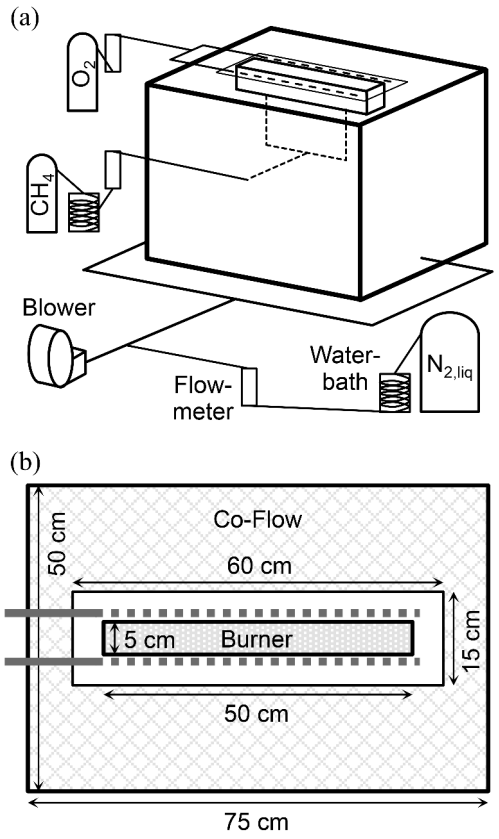

Figure 6.1: (a) Diagram of experimental facility. (b) Top-view of burner/co-flow outlet. Dashed line represents the oxygen anchor porous stainless-steel tubes.

Figure 6.2 presents front- and end-view photographs (fixed exposure settings).

It depicts the progressive suppression of a turbulent methane flame for varying X_{O_2}. Yellow and blue regions in the flame respectively mark soot incandescence and CH luminescence. As X_{O_2} is reduced, soot radiation diminishes, followed by flame extinguishement.

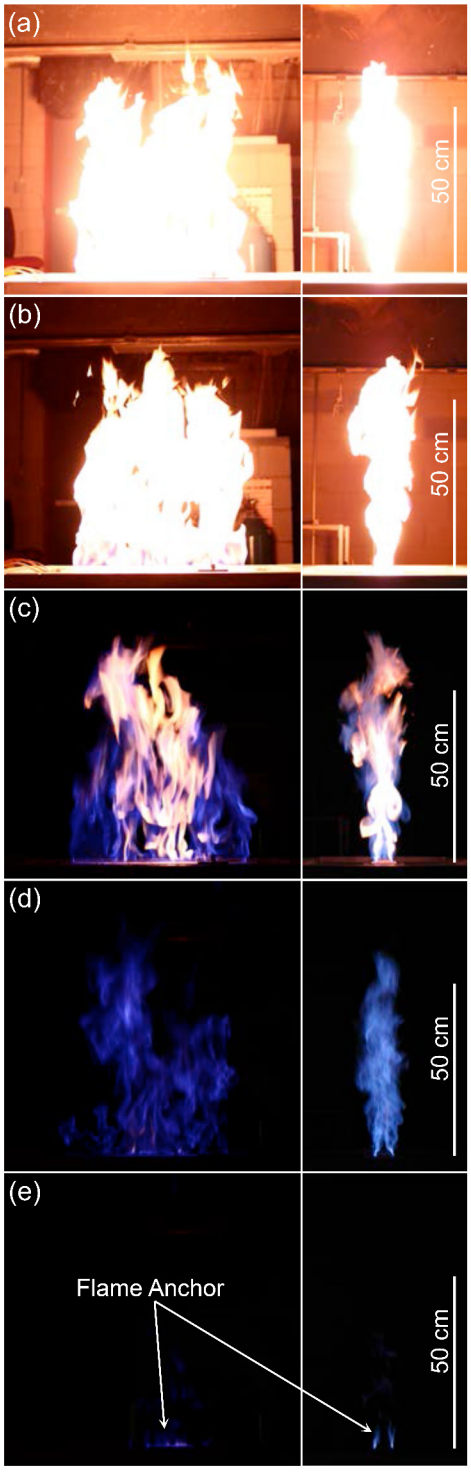

Figure 6.2: Simultaneous front- and end-view annchored methane flame image at selected X_{O_2}: a) 0.211; b) 0.175; c) 0.156; d) 0.141, e) 0.127. Exposure: 1/30s, f/2.0, ISO 1250. Color images.

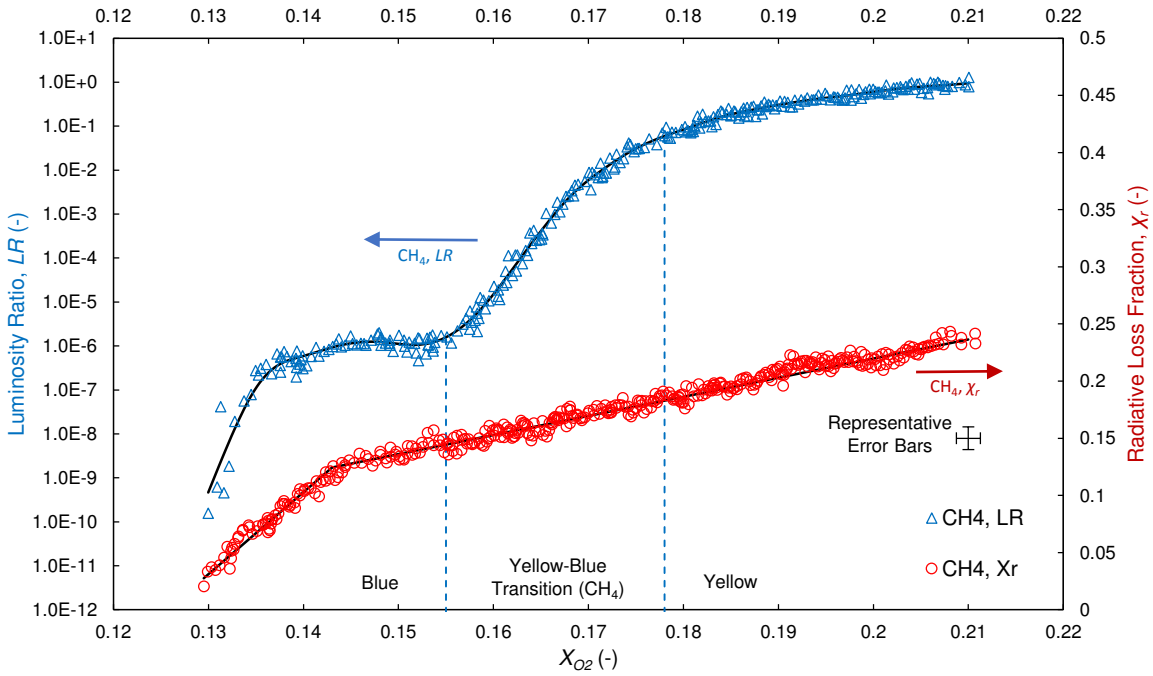

Figure 6.3: Flame luminosity and radiative loss fraction plotted as functions of X_{O_2} for the anchored condition.

6.2 Numerical Solver and Configurations

6.2.1 Numerical Solver

FireFOAM solves the Favre filtered fully compressible Navier-Stokes equations (section 2.2) and provides a choice between several modeling options for the treatment of turbulence, combustion and thermal radiation. The turbulent sub-grid scale stress is modeled by the eddy viscosity concept. The present study uses the dynamic coefficient one-equation eddy viscosity model in order to model accurately the transition from laminar to turbulent flow, which solves a sub-grid scale (SGS) kinetic energy equation and uses dynamic coefficients for C_e and C_k (section 2.4.2). The

turbulent combustion model adopts the Eddy Dissipation Concept (section 2.5). Extinction modeling is treated via the damköhler approach newly implemented in FireFOAM for the purpose of this study independent of mixture fraction (section 4.3.1.2 and 4.3.1.4). In FireFOAM, the radiative transfer equation (RTE) is solved using the discrete ordinate method. In the present study, the description of thermal radiation is simplified by assuming a prescribed radiant fraction approach (section 2.6.1) based on experimental results (Fig. 6.3). This assumption should be viewed as an intermediate step that conveniently avoids the difficulties associated with solving the full RTE equation with the contribution of gaseous species (CO_2, H_2O, CH_4 and soot).

6.2.2 Numerical Configuration

Computational Mesh

The computational domain is set to be a $2 \times 0.85 \times 2\,\mathrm{m}^3$ cubic box, which is large enough to avoid plume/boundary interactions and excessive boundary condition effects on the simulations. We use an automatic meshing tool provided in OpenFOAM, called SnappyHexMesh, for the mesh generation. A mesh with three refinement regions is generated (Fig. 6.4). The smallest cells are $4.2 \times 4.2 \times 4.2\,\mathrm{mm}^3$, uniformly placed inside a $0.3 \times 0.6 \times 0.6\,\mathrm{m}^3$ box above the burner surface, which we call level-one refinement zone. (Note that z denotes the vertical direction here.) This zone covers the continuous flame region where the combustion takes place and high gradients are present. The level-two refinement zone has a cell size of $8.4^3\,\mathrm{mm}^3$, and is located outside the first zone and within a 0.6 x 0.8 x 0.8m box. This second

refinement box provides a sufficiently large volume for the plume region. Cells are proportionally increased in the level-three. The largest cells near the outlet and sides are $16.7^3\,\mathrm{cm}^3$. The total number of cells is 1,757,629. The present resolution is considered marginal in the near-field region (12 cells across the width of the burner), but acceptable in the intermediate- and far-field regions (24 cells across the width of the flame at mid-flame height, *i.e.* at 25 cm elevation) in order to capture the majority of the turbulent kinetic energy (Fig. 6.16). However, the resolution of the flame base region may be questionable in order to capture accurately the transition from laminar to turbulent flow. Hence, a preliminary study includes a grid convergence analysis (table 6.1 and section 6.3.2) including detailed comparisons with forthcoming experimental measurements of centerline mean/fluctuating temperatures.

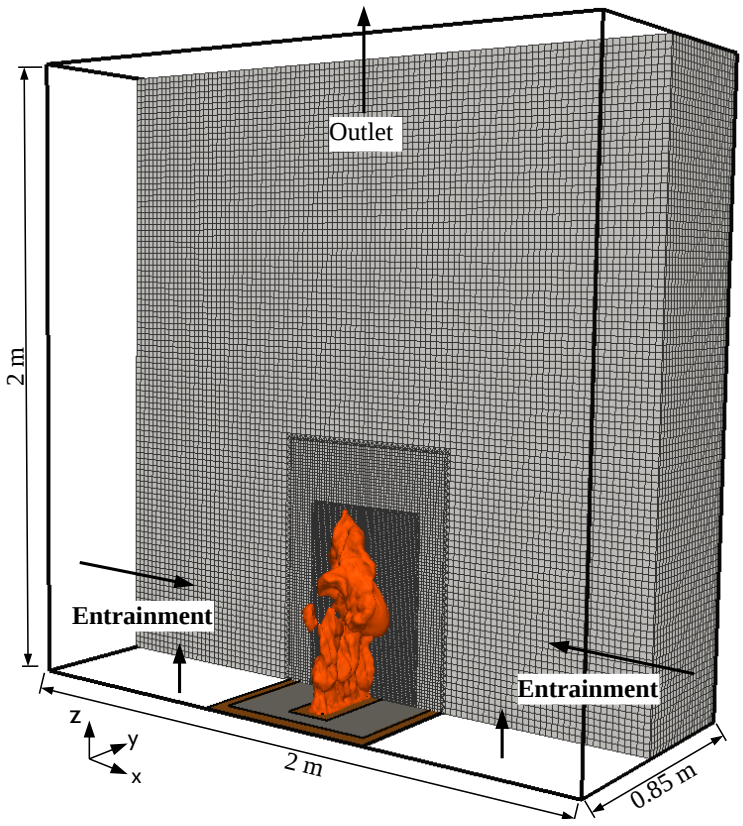

Figure 6.4: Computational domain and multi-level mesh refinement.

Table 6.1: Grid resolution summary.

$W_b/\Delta x$ [-]	$\langle \Delta t \rangle_T$ [ms]	Proc. [-]	CPU Time [h]	Cells [-]
4	1.68	16	57.6	175,326
8	0.76	32	473.6	530,906
12	0.5	64	2,688	1,757,629
16	0.35	256	12,800	4,288,916
20	0.30	256	31,080	8,211,603
24	0.25	256	58,000	11,846,537

N.B.: The performance of a solver is based on the CPU-hrs/time-steps/grid-cells number, which is around 1.1×10^{-5} µs in FireFOAM based on our study.

Boundary Conditions

Typical outflow and entrainment boundary conditions are used for open boundaries at the top and sides, respectively. At the inlet, we maintain a fixed value of fuel mass flow rate and enthalpy flow rate according to the specified heat release rate. Both convective and diffusive mass and energy fluxes are accounted for at the inlet. Note that the diffusive flux is important in a purely buoyant fire as convective velocities are small. Failure to account for the diffusive mass flux will lead to more fuel entering the computational domain and, therefore, yield a larger heat release rate than specified. Detailed boundary conditions are given in Table 6.2 and 6.3,

and divided in four categories:

- **Turbulent Equation:** any variable related to the turbulence solver, *i.e.* turbulent diffusivity (α_{sgs}), turbulent kinetic energy (k_{sgs}), and turbulent viscosity (μ_{sgs}).

- **Species Mass Fraction Equations:** All species directly injected are specified by their names, *i.e.* CH_4, N_2, and O_2. The rest of the species are specified in the file $Y_{Default}$.

- **Energy Equation:** any variable related to the energy equation, *i.e.* the temperature (T) used to calculate the initial sensible enthalpy and the radiative intensity I used to compute the radiation source term.

- **Pressure-Velocity Equations:** any variable related to the pressure-velocity set of equations, *i.e.* the net pressure (p), the ambient plus dynamic pressure (p_{rgh}), and the velocity (U).

Table 6.2: Prescribed flow boundaries (inlets).

	Co-Flow	**Anchor**	**Fuel**
$\boldsymbol{\alpha_{sgs}}$	fixed(0)	fixed(0)	fixed(0)
$\boldsymbol{k_{sgs}}$	fixed($1e^{-4}$)	fixed($1e^{-4}$)	fixed($1e^{-4}$)
$\boldsymbol{\mu_{sgs}}$	fixed(0)	fixed(0)	fixed(0)
$\boldsymbol{CH_4}$	fixed(0)	totalFlowRate-AdvectiveDiffusive(0)	totalFlowRate-AdvectiveDiffusive(1)
$\boldsymbol{N_2}$	fixed(Y_{N_2})	totalFlowRate-AdvectiveDiffusive(0)	totalFlowRate-AdvectiveDiffusive(0)
$\boldsymbol{O_2}$	fixed(Y_{O_2})	totalFlowRate-AdvectiveDiffusive(1)	totalFlowRate-AdvectiveDiffusive(0)
$\boldsymbol{Y_{Default}}$	fixed(0)	totalFlowRate-AdvectiveDiffusive(0)	totalFlowRate-AdvectiveDiffusive(0)
$\boldsymbol{I_{Default}}$	greyDiffusiveRadiation	greyDiffusiveRadiation	greyDiffusiveRadiation
$\boldsymbol{T}$	fixed(295)	fixed(295)	fixedEnthalpyFlux-Temperature(295)
$\boldsymbol{p}$	calculated	calculated	calculated
$\boldsymbol{p_{rgh}}$	buoyantPressure	buoyantPressure	buoyantPressure
$\boldsymbol{U}$	flowRateInletVelocity	flowRateInletVelocity	flowRateInletVelocity

Table 6.3: Free flow boudnaries.

	Entrainment	**Outlet**	**Blockage**
$\boldsymbol{\alpha_{sgs}}$	zeroGradient	zeroGradient	fixed(0)
$\boldsymbol{k_{sgs}}$	inletOutlet($1e^{-4}$)	inletOutlet($1e^{-4}$)	zeroGradient
$\boldsymbol{\mu_{sgs}}$	zeroGradient	zeroGradient	fixed(0)
$\boldsymbol{CH_4}$	inletOutlet	inletOutlet	zeroGradient
$\boldsymbol{N_2}$	inletOutlet	inletOutlet	zeroGradient
$\boldsymbol{O_2}$	inletOutlet	inletOutlet	zeroGradient
$\boldsymbol{Y_{Default}}$	inletOutlet	inletOutlet	zeroGradient
$\boldsymbol{I_{Default}}$	greyDiffusiveRadiation	greyDiffusiveRadiation	greyDiffusiveRadiation
$\boldsymbol{T}$	inletOutlet	inletOutlet	fixed(295)
$\boldsymbol{p}$	calculated	calculated	calculated
$\boldsymbol{p_{rgh}}$	totalPressure	buoyantPressure	buoyantPressure
$\boldsymbol{U}$	pressureInletOutletVelocity	inletOutlet	fixed(0)

Simulation Time

All simulations are carried out for 20 s. Turbulent statistics are collected for 12 s when the flow becomes statistically stationary, long enough for the first and second order turbulent statistics to be convergent (Fig. 6.5). FireFOAM is run on two large-scale Linux cluster:

- **Stampede** (University of Texas): a Dell PowerEdge cluster equipped with Intel Xeon Phi coprocessors with a peak performance of 2 PetaFlops (1 petaflop (PF) = 1 quadrillion math operations per second). Stampede is funded by the National Science Foundation. Linear scalabilty of FireFOAM on Stampede is reported in appendix E.

- **Deepthought2** (University of Maryland): a Dell PowerEdge cluster equipped with Intel Xeon Ivy Bridges processors with a peak performance of 200 TeraFlops.

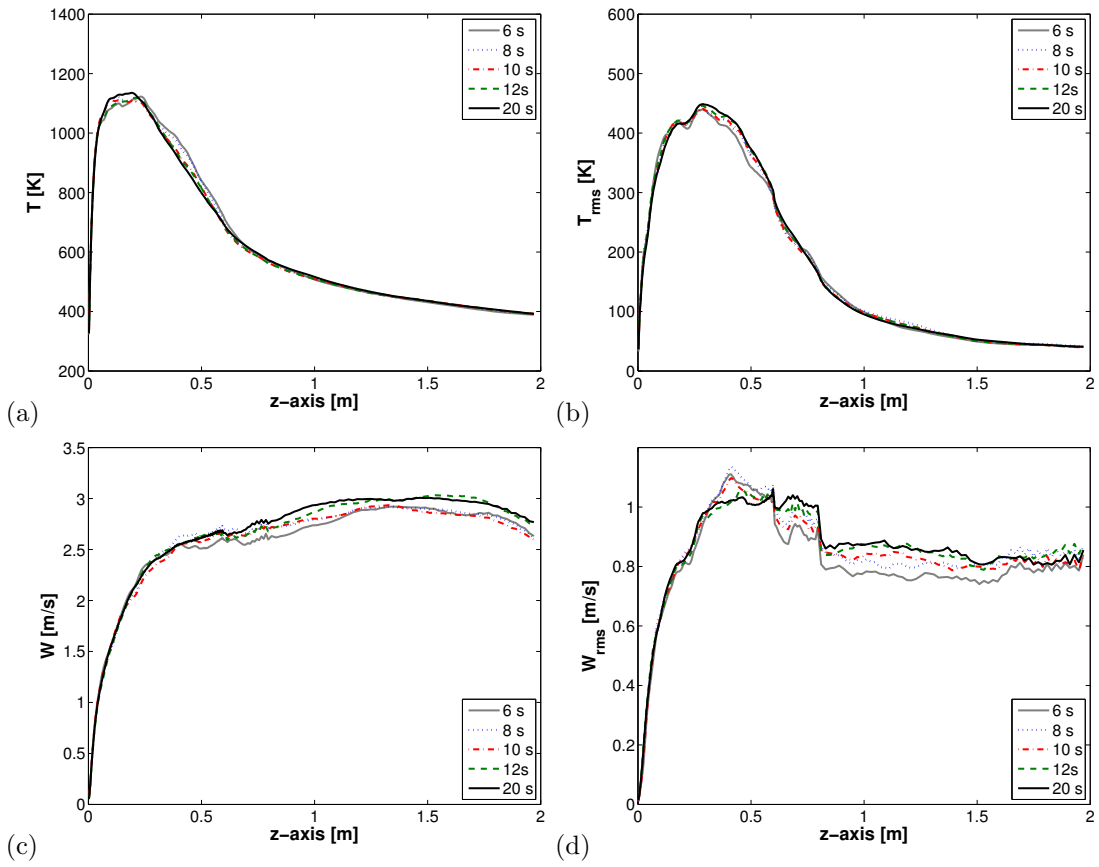

Figure 6.5: Centerline averaged profile for different averaging times. a) Temperature; b) Root mean squared temperature; c) Velocity; d) Root mean squared velocity.

6.3 Results and Discussion

6.3.1 Flame Topology

The flame topologies are illustrated using the finest resolution results ($\Delta x = 2\ mm$) for an undiluted case, $X_{O_2} = 0.21$. Figure 6.6 shows the flame surface identified as an iso-contour of the heat release rate per unit volume ($HRR = 200\,\mathrm{kW/m^3}$). Heat release rate is preferred to the classical stoichiometric mixture fraction visual-

ization. Indeed, for diluted cases, the stoichiometric mixture fraction is decreasing and unknown. Qualitatively, the comparison between the simulation and the experiment is good. The different structures formed near the burner are captured and the transition between laminar-to-turbulent flow is well described. This is due to two helpful factors. First, the blockage around the burner has severely reduced the laminar-to-turbulence transition length. Second, most of the turbulence kinetic energy ($> 80\%$) is resolved by the mesh (Fig. 6.16).

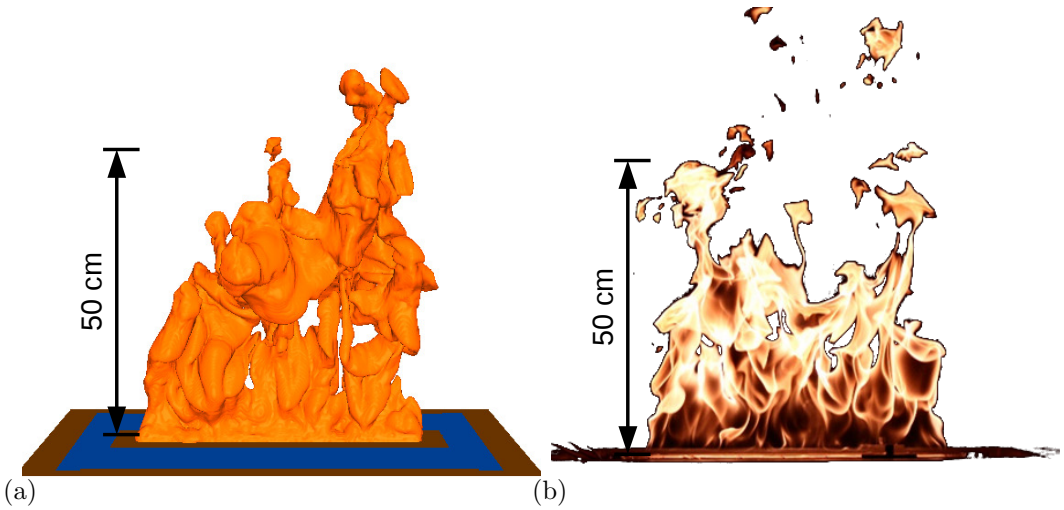

Figure 6.6: Instantaneous view of the flame surface for an undiluted case, $X_{O_2} = 21\%$. (a) In FireFOAM, the flame is identified as an iso-contour of the heat release rate per unit volume; we use $200\,\mathrm{kW/m^3}$; (b) In the experiment, the flame is described through visible flame emission.

Measured and simulated flame heights (L_f) are plotted as function of X_{O_2} in Fig. 6.7. As shown, L_f increases with reductions of X_{O_2}, in agreement with experimental data. This trend is due to the fact that, as X_{O_2} decreases, a greater

volume oxidizer must be entrained to support complete combustion. In addition, buoyancy-driven entrainment should decrease due to suppression; therefore the flame must lengthen to entrain the additional required oxidizer, where entrainment rate increases with rising elevation along the flame. As shown in Fig. 6.7, excellent agreement ($< 5\%$) is obtained between measured and simulated L_f. This small discrepancy is due to the definition of flame height. In the experiment, the flame height is defined by a 50% flame intermittency presence and relies on visible flame emissions. In FireFOAM, the flame height is calculated based on the maximum HRR elevation.

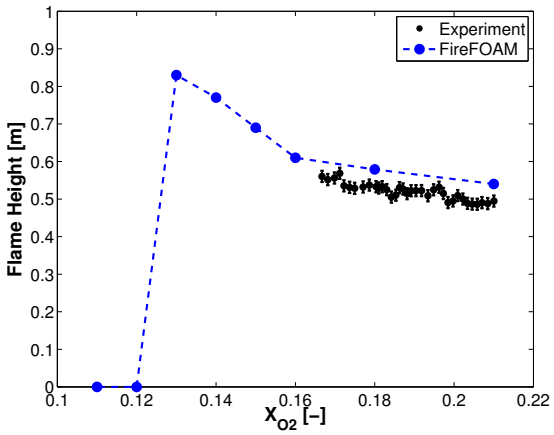

Figure 6.7: Measured and simulated L_f at varying X_{O_2}.

Figure 6.8 represents the flow vortical structures using the Q-criteria to visualize the turbulent field defined as:

$$Q = \frac{1}{2}\left(\Omega_{ij}\Omega_{ij} - S_{ij}S_{ij}\right) \tag{6.1}$$

When Q is positive, it represents locations in the flow where the rotation Ω_{ij}

dominates the strain and shear S_{ij}, it describes the vortex structure.

Different values of Q are used in order to highlight the difference of resolution between the three level refinement. Near the burner, the flow accelerate due to buoyancy forces, the turbulent kinetic energy increases (Fig. 6.14) and small eddies are formed (Fig. 6.8-c). From 60 to 80 cm, the effect of second level mesh refinement is observed, some medium eddies are still captured by the grid as illustrated by Fig. 6.8-b. Above 80 cm, small eddies are not anymore captured by the grid (Fig. 6.8-b). However, the grid can still capture the large eddies (Fig. 6.8-a).

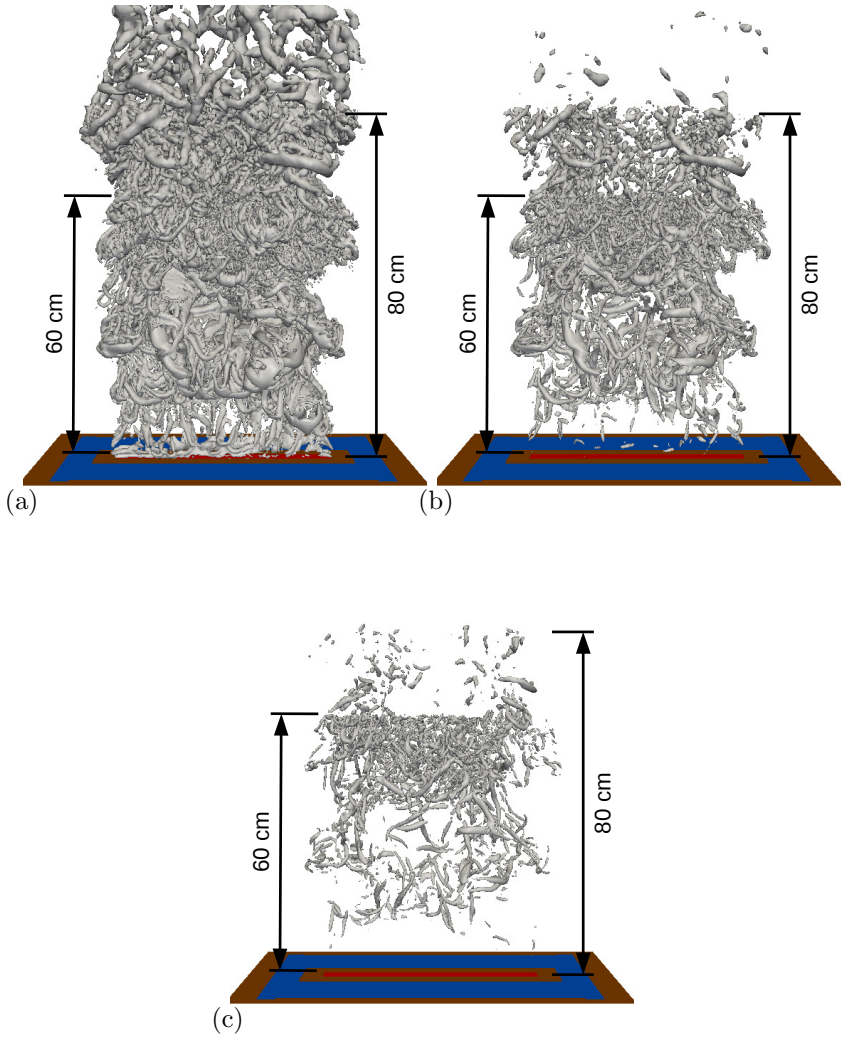

Figure 6.8: Instantaneous ($t = 20\,\mathrm{s}$) view of flow vortical structures (iso-contour of Q). a) $Q = 1000\,\mathrm{s}^{-2}$; b) $Q = 5000\,\mathrm{s}^{-2}$; c) $Q = 15{,}000\,\mathrm{s}^{-2}$.

Figure 6.9 shows simultaneous front- and end-view of the instantaneous (bottom) and mean (top) flame temperature. The instantaneous flame temperature on the flame surface is about 1800 K, which is a reasonable value considering that the adiabatic flame temperature is approximately 2200 K and that there is a 23% radiative loss. The mean temperature is about 1200 K and is lower than the instan-

taneous flame temperature (1800 K). The flame thickness increases with elevation. At mid-flame height, the flame thickness is about 10 cm.

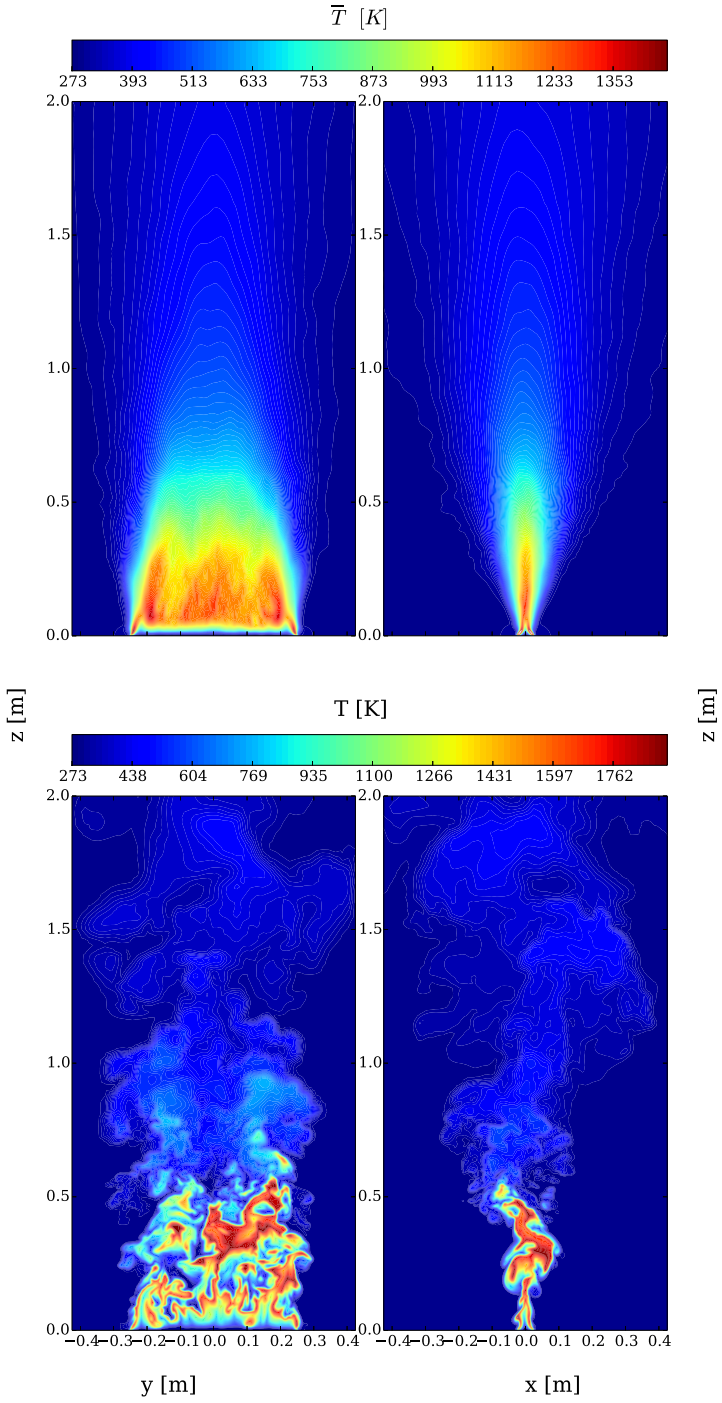

Figure 6.9: Temperature contour map; (top) average; (bottom) $t = 20\,\mathrm{s}$.

Figure 6.10, 6.11 and 6.12 shows simultaneous front- and end-view of the instantaneous (bottom) and mean (top) of the streamwise (vertical), spanwise, and cross-stream velocity. The fluctuation in the spanwise and cross-stream starts near the burner, indicating that the laminar-to-turbulence transition is very short (Fig. 6.11-6.12). The magnitude in the streamwise (vertical) direction is larger than in the other two directions, around 5 m/s compared to 0.1 m/s, characteristic of a buoyant plume. Similar to the mean temperature profile, the width of the mean velocity profile increases with elevation, and the peak velocity also increases with elevation due to buoyancy (Fig. 6.10). The vertical velocity contour maps are supplemented by an isoline corresponding to 15 cm/s which reveals the co-flow pattern (Fig. 6.10). Note that the velocity co-flow is more than 10 times smaller than the plume velocity.

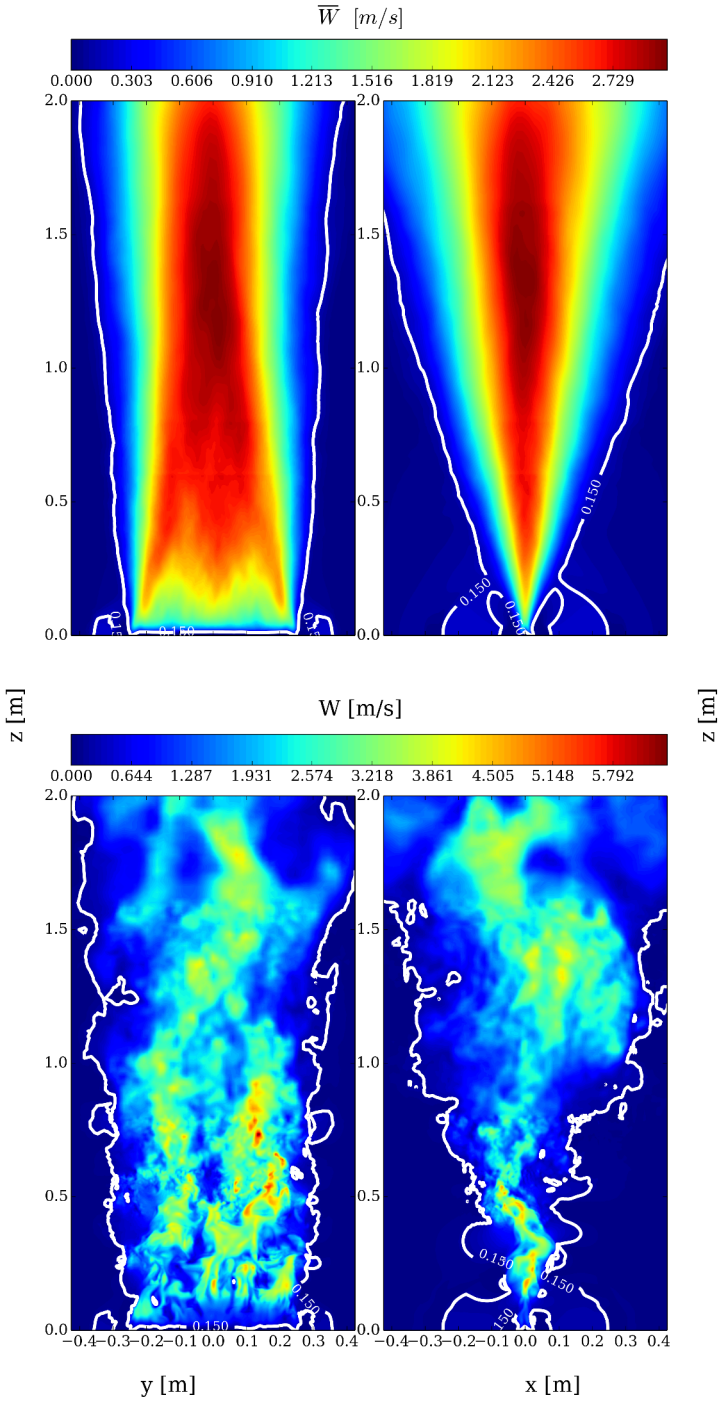

Figure 6.10: Vertical velocity contour map; (top) average; (bottom) $t = 20\,\mathrm{s}$.

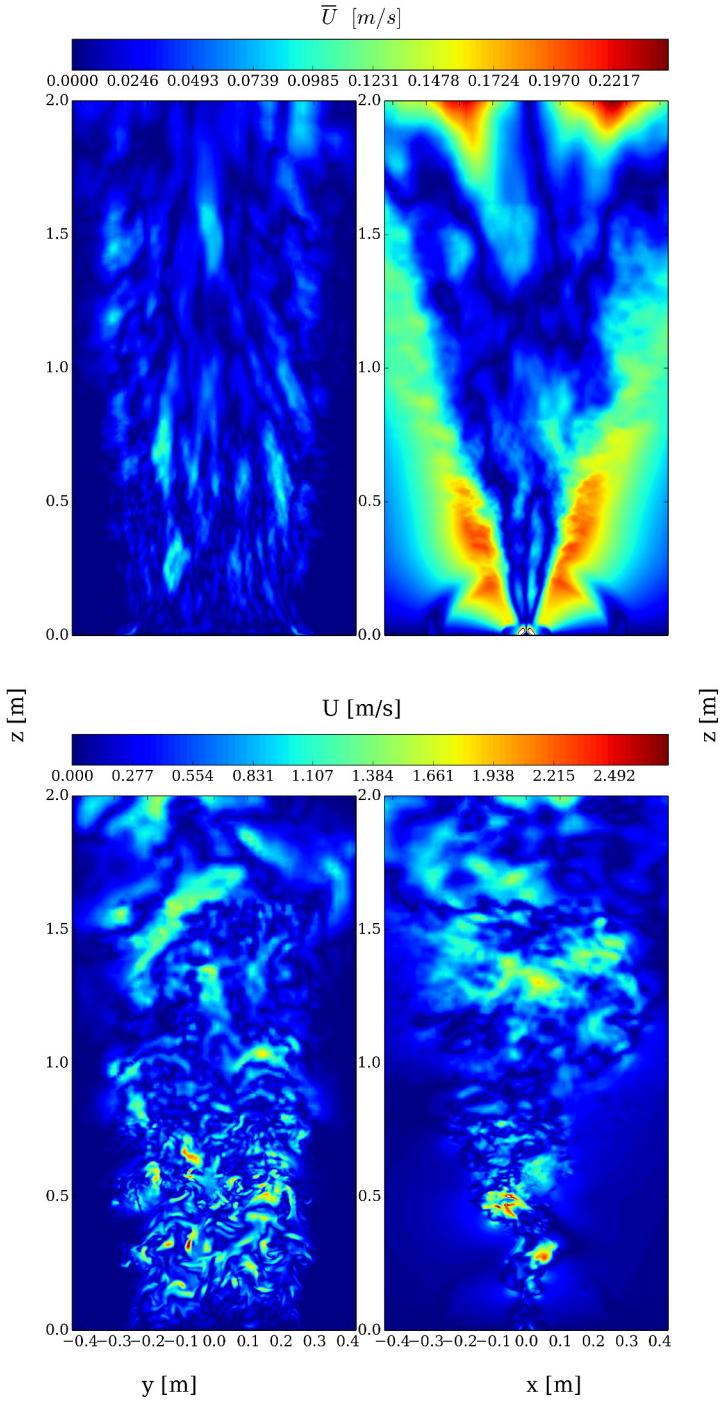

Figure 6.11: Spanwise velocity contour map; (top) average; (bottom) $t = 20\,\mathrm{s}$.

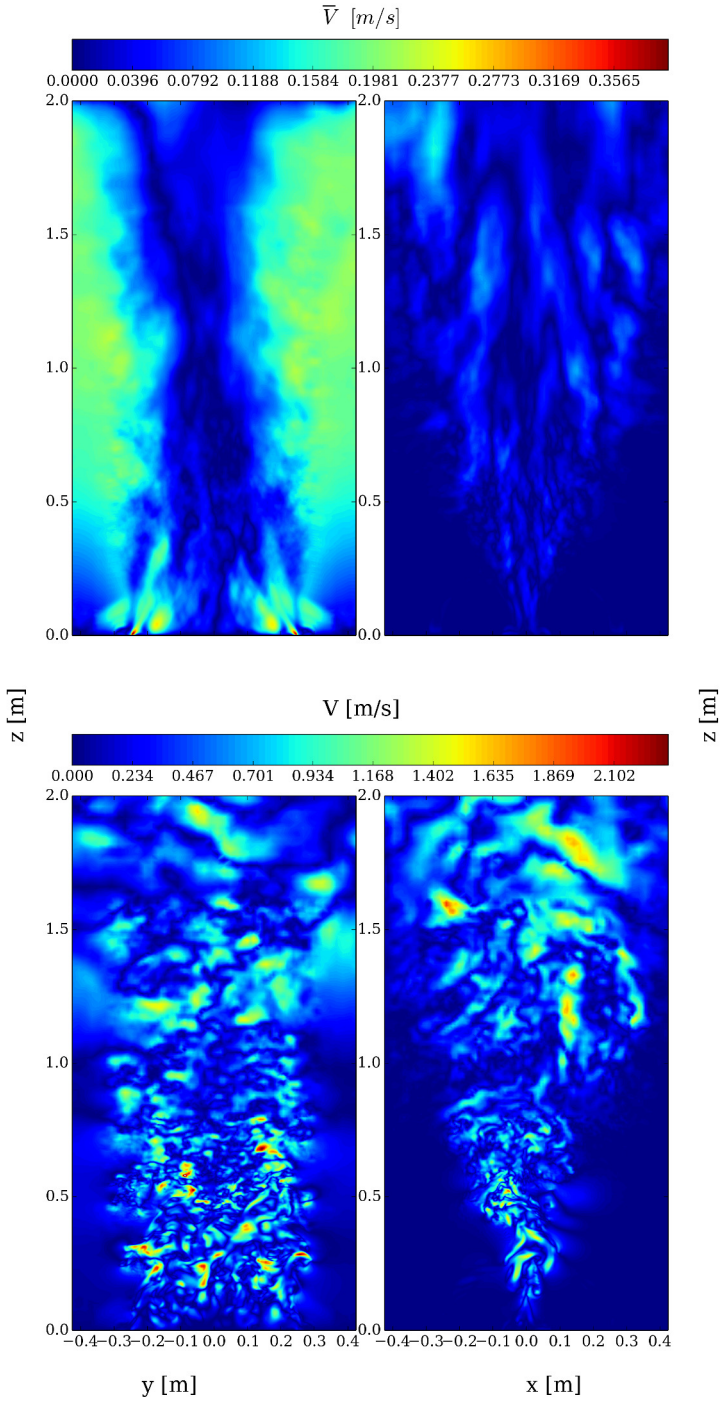

Figure 6.12: Cross-stream velocity contour map; (top) average; (bottom) $t = 20\,\mathrm{s}$.

6.3.2 Grid Convergence

Some simulations have been performed to determine the adequate grid resolution and serve to highlight the current numerical challenges which will have to be met before testing the extinction model.

Gas Phase Solver

We first start an analysis of the different length scales of the gas phase and the grid requirement to resolve them.

- **Flame:** $L_f \sim 50\,\text{cm}$, $W_b = 5\,\text{cm}$ (height and width of the flame which is related to the fuel burner width).
- **Diluted co-flow:** $W_{DCF} = 17.5\,\text{cm}$ (width of the diluted co-flow)

It is clear that the critical length scale is the burner width (W_b). With our baseline grid resolution ($\Delta x \approx 4\,\text{mm}$), we have 12 cells across this critical length scale, *i.e.* the burner width (W_b). Hence, we report the different grid resolution in table 6.1 as the ratio between the burner width (W_b) and the cell size (Δx).

Figure 6.13-a-c presents centerline variations of the mean gas temperature and mean vertical flow velocity. The simulations are performed at different computational grid resolution, *i.e.* ranging from 12 to 2 mm. The LES results are approximately grid-converged for $\Delta x \leq 4\,\text{mm}$, although some slight variations in peak values persist even at the highest levels of resolution. Peak mean vertical ve-

locities are close to 3 m/s; peak mean temperatures are relatively low and close to 1200 K.

Figure 6.13-b-d presents the corresponding centerline variations of the grid-resolved fluctuation intensities. The fluctuation intensities are measured in terms of root mean square (rms) values. The LES results are approximately grid-converged for $\Delta x \leq 4\ mm$, although some variations in peak values still persist. Peak fluctuation intensities for temperature are close to 40%; peak fluctuation intensities for vertical flow velocity are close to 30%.

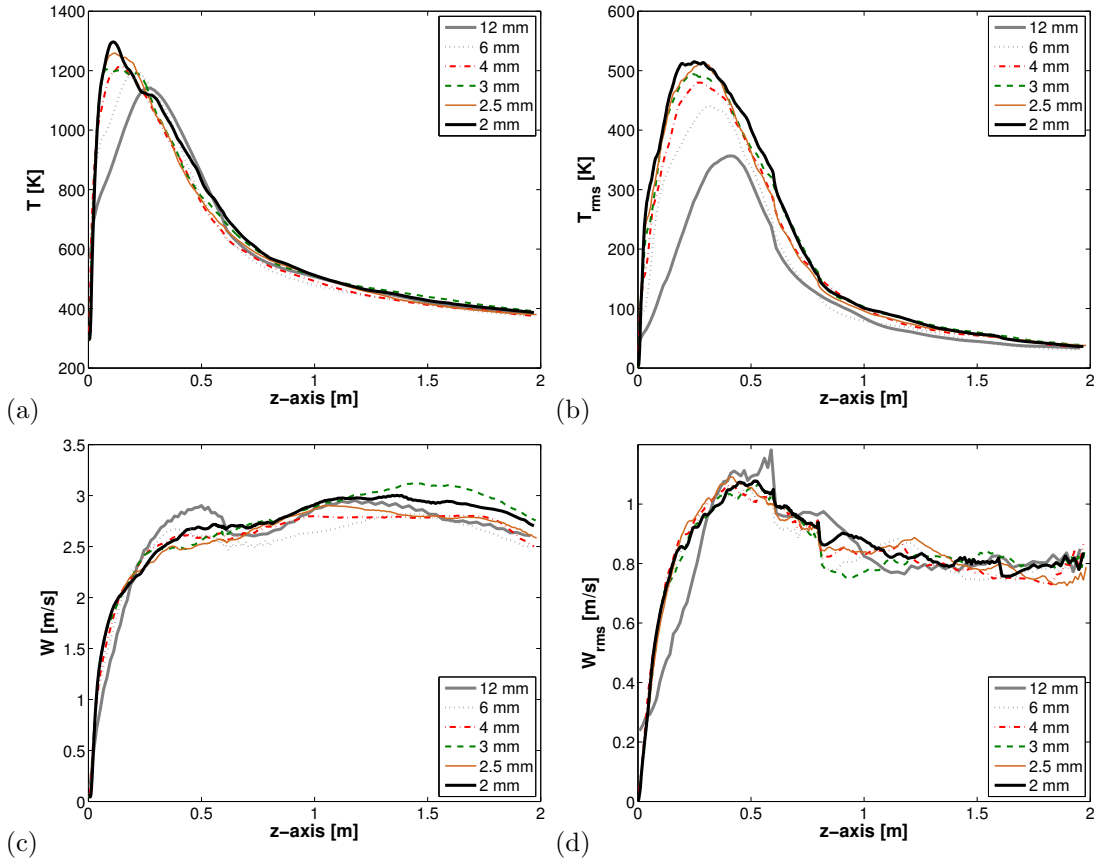

Figure 6.13: Centerline averaged profile for different grid resolution. a) Temperature; b) Root mean squared temperature; c) Velocity; d) Root mean squared velocity.

Previous studies have attempted to converge on quality assessment criteria for LES [20, 90]. First, for good quality LES calculation, the grid has to be sufficiently fine to resolve 80% of the kinetic energy [20]. Second, the SGS turbulent to molecular viscosity ratio has to be below 1 [90]. The following ratio is constructed based on the temporally averaged LES results,

$$M_E = \frac{\overline{k_{res}}}{\overline{k_{res}} + \overline{k_{sgs}}} \tag{6.2}$$

where $\overline{k_{res}} = \frac{1}{2}\langle(\widetilde{u}_i - \langle\widetilde{u}_i\rangle_T)\,(\widetilde{u}_i - \langle\widetilde{u}_i\rangle_T)\rangle_T$ is the mean resolved kinetic energy with $\langle\rangle_T$ denoting a temporal average, $\overline{k_{sgs}}$ stands for the mean sub-grid turbulent kinetic energy.

Figure 6.14 presents the spatial distribution of resolved turbulent kinetic energy and M_E. The M_E criteria is reached for the entire domain, *i.e.* $M_E > 0.8$.

Figure 6.15 presents the spatial distribution of instantaneous and mean turbulent to molecular viscosity ratio, supplement by an isoline corresponding to 1.0. The viscosity ratio criteria is reached everywhere below 80 cm which covers the entire flame region.

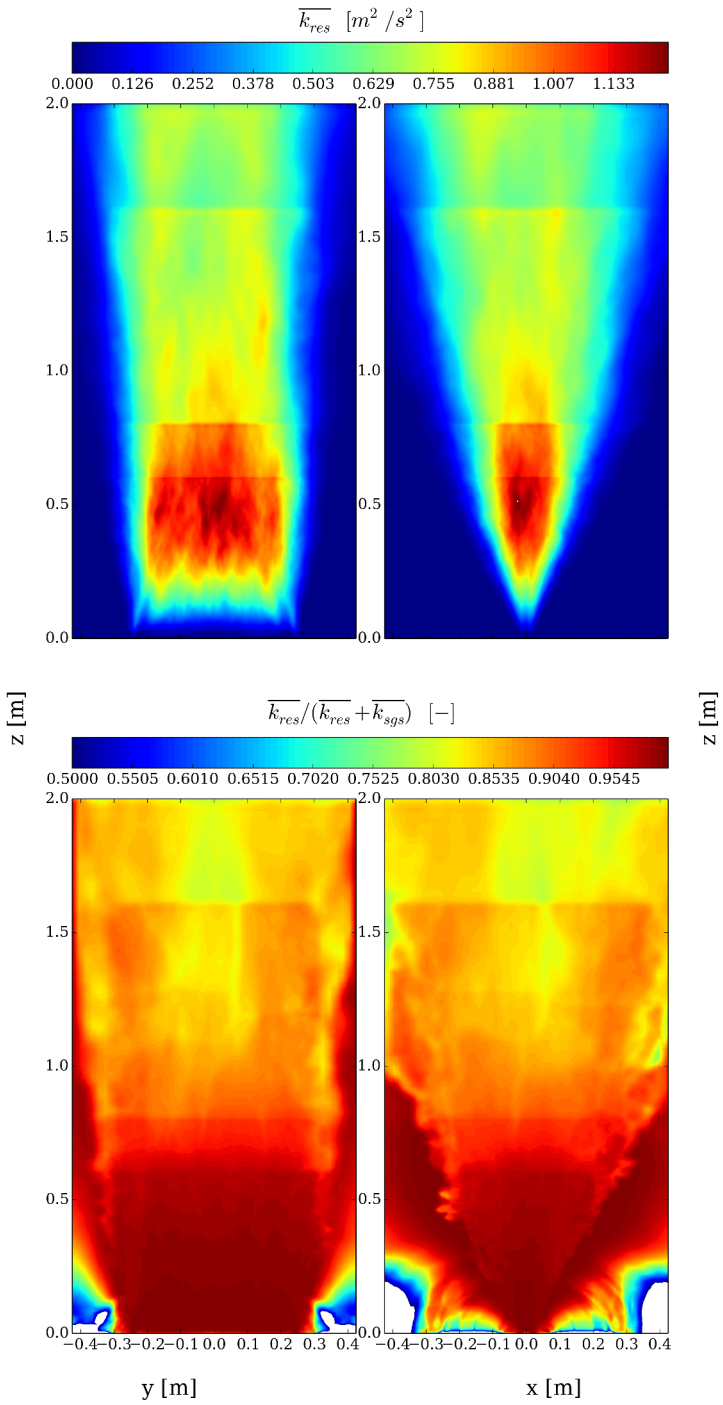

Figure 6.14: (top) contour map of turbulence kinetic energy ; (bottom) contour of the ratio of resolved turbulent kinetic energy (TKE) divided by total turbulent kinetic energy.

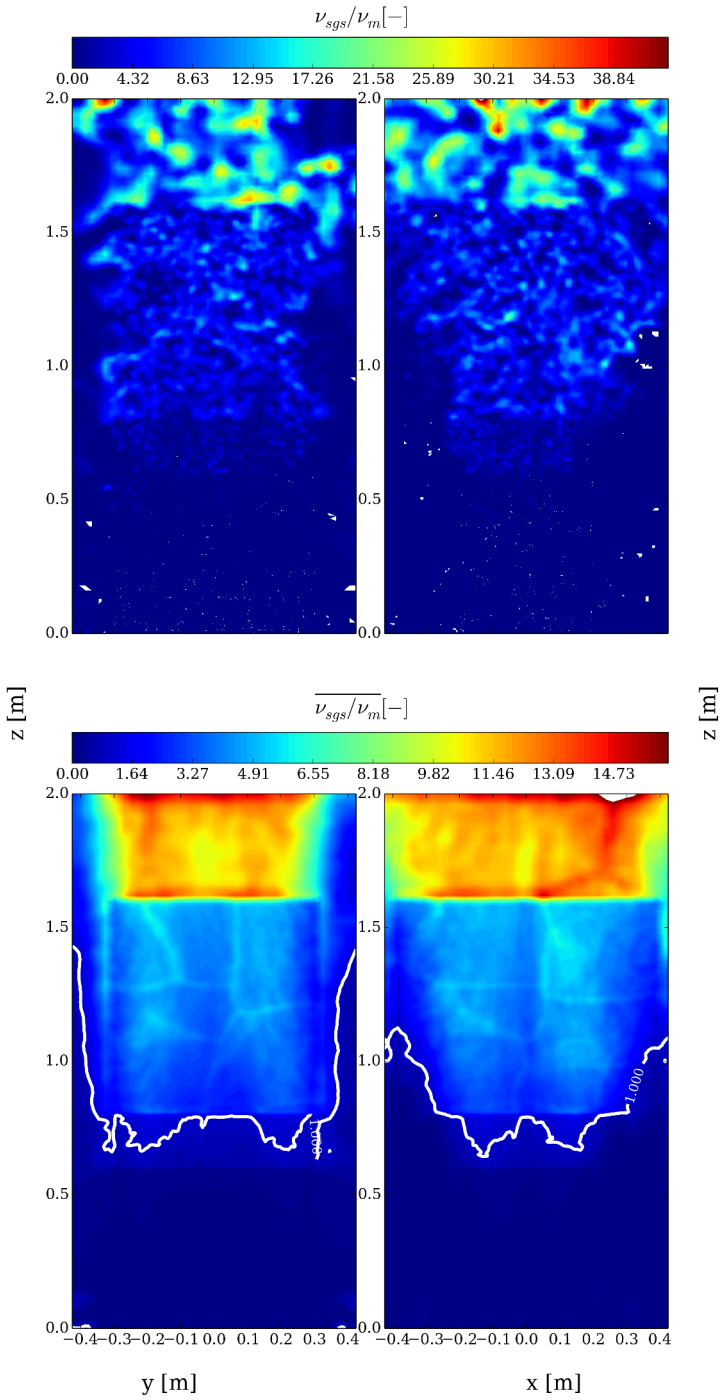

Figure 6.15: Ratio of turbulent to molecular viscosity contour map; (top) $t = 20\,\mathrm{s}$; (bottom) average. Solid white line represents an isoline equal to 1.

Figure 6.16 shows the centerline resolved TKE divided by total TKE (M_E) and the turbulent to laminar viscosity ratio for different grid resolutions. The M_E criteria is reached for $\Delta x \leq 4\,\text{mm}$. The viscosity criteria is reached for $\Delta x \leq 4\,\text{mm}$ only in the flame region ($z < 50\,\text{cm}$). In Fig. 6.16, the jump at $z = 0.6\,\text{m}$ and $z = 0.8\,\text{m}$ is due to an increase in the mesh resolution. As the grid size increases, the ratio of resolved turbulent kinetic energy (TKE) divided by total turbulent kinetic energy decreases and the ratio of turbulent to molecular viscosity increases.

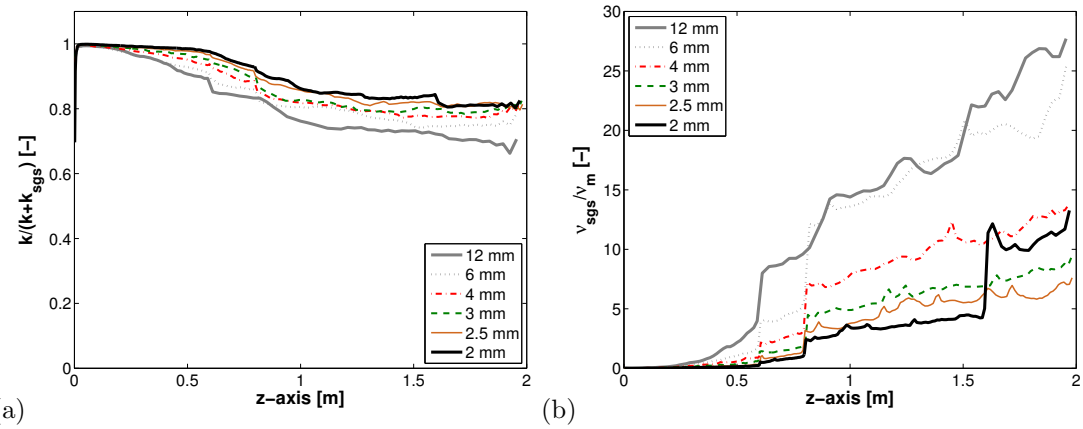

Figure 6.16: Centerline averaged profile for different grid resolution. a) The ratio of resolved turbulent kinetic energy divided by total turbulent kinetic energy; b) Ratio of turbulent to molecular viscosity.

Thermal Radiation Solver

We now turn to a discussion of the different length scales of thermal radiation and the number of solid angle (N_Ω) required to resolve them.

- **Flame surface:** $S \sim 0.25\,\text{m}^2$.
- **Gauge distance:** $d = 1\,\text{m}$.

The angular region defined by S viewed from the heat flux gauge is proportional to S/d^2. The resolution ($\Delta\Omega$) of this angular region is therefore configuration dependent, *i.e.* sensitive to the heat flux gauge distance from the flame. The angular space discretization ($\Delta\Omega$) is defined as $4\pi/N_\Omega$.

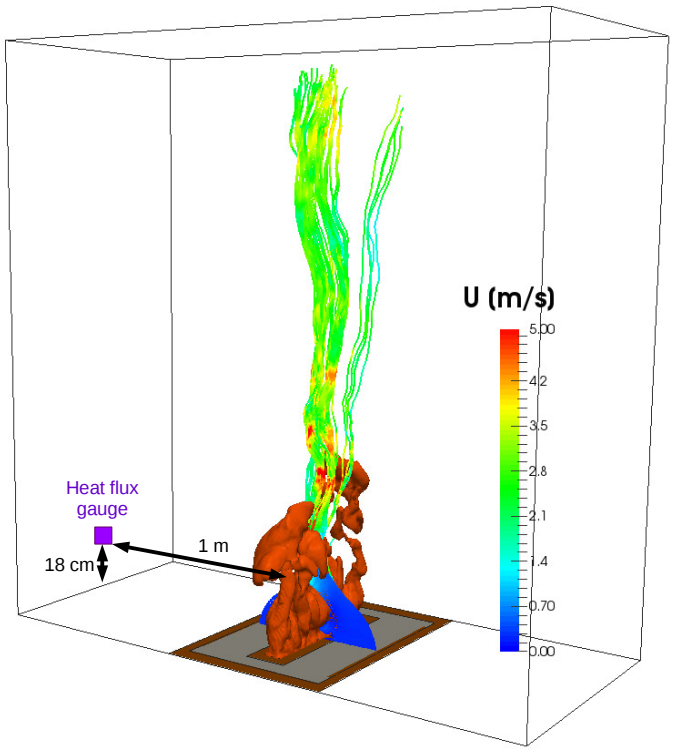

Figure 6.17: Schematic of the experimental configuration for the thermal radiation measurement.

In FireFOAM, the angular space is equally discretized into a certain number of azimuthal angles (N_ϕ) in $\pi/2$ on X-Y plan (from Y to X) and polar angles (N_θ) in π (from Z to X-Y plane)(Fig. 6.18). The angular resolution is defined as:

$$\Delta\phi = \frac{\pi}{2N_\phi} \tag{6.3}$$

$$\Delta\theta = \frac{\pi}{2N_\theta} \tag{6.4}$$

The total number of solid angles (N_Ω) is equal to $4N_\phi N_\theta$.

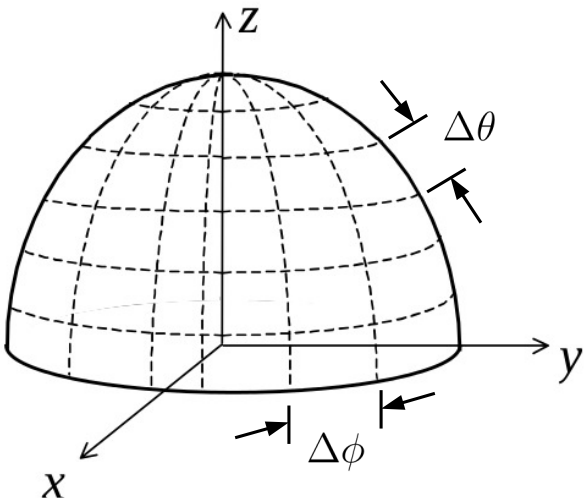

Figure 6.18: Angular grids.

Table 6.4: Grid resolution summary for the thermal radiation solver.

N_ϕ [-]	N_θ [-]	N_Ω [-]	CPU Time [h]
2	2	16	1,920
4	4	64	2,254
6	6	144	3,096
8	8	256	3,776
9	9	324	4,428
10	10	256	4,728
12	12	576	7,584

Figure 6.19 presents mean the total heat flux ($\dot{q}''_{gauge} = \dot{q}''_r/\varepsilon + \dot{q}''_c$) as a function number of the number of solid angle, located at 1 m from the flame and 18 m above the fuel port (Fig. 6.17). ε is the hemispherical absorptance and is equal to 0.94. The radiative results are approximately grid-converged for $N_\Omega \geq 324$.

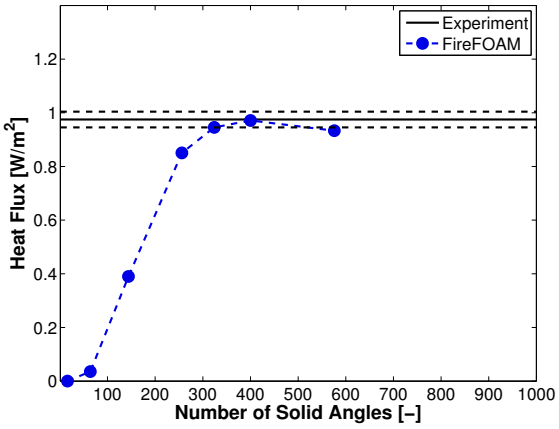

Figure 6.19: Net Heat Flux as a function of the number of solid angles. The black dashed line represents the measurement upper and lower bounds (±3%).

6.3.3 Effects of Turbulence Model

The dynamic-coefficient one-equation eddy viscosity model (section 2.4.1 and 2.4.2) has been selected to compute the sub-grid scale quantities, *i.e.* the turbulent kinetic energy (k_{sgs}) and the turbulent viscosity (ν_{sgs}). Therefore, understanding its performance compared to the constant-coefficient version is necessary. The sub-grid eddy viscosity is calculated from the sub-grid kinetic energy:

$$\nu_{sgs} = C_k k_{sgs}^{1/2} \Delta \tag{6.5}$$

where $C_k = 0.094$ for the constant-coefficient model.

Figure 6.20 shows the C_k value as a function of elevation for the constant- and dynamic-coefficient model. As prescribed, for the constant model, C_k is equal to 0.094. For the dynamic model, C_k increases from 0 (in the laminar region near

the inlet) to around 0.4 in the turbulent region. This value is consistent with the Decaying Isotropic Turbulence case ($C_k \sim 0.4$, see section 3.2.4).

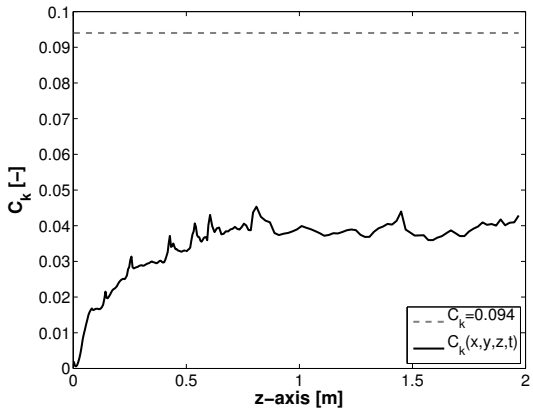

Figure 6.20: Centerline averaged profile of C_k.

A smaller value of C_k corresponds to a smaller value of turbulent viscosity (Fig. 6.21-b) and therefore to a higher value of turbulent kinetic energy (Fig. 6.21-a), as the solution is less dissipative and more turbulent. Note than the turbulent quantities starts at zero as specified by the boundary condition (see table 6.2). In fact, in the experiment the flow is assumed to be laminar at the inlet, which means the turbulence is only generated inside the domain.

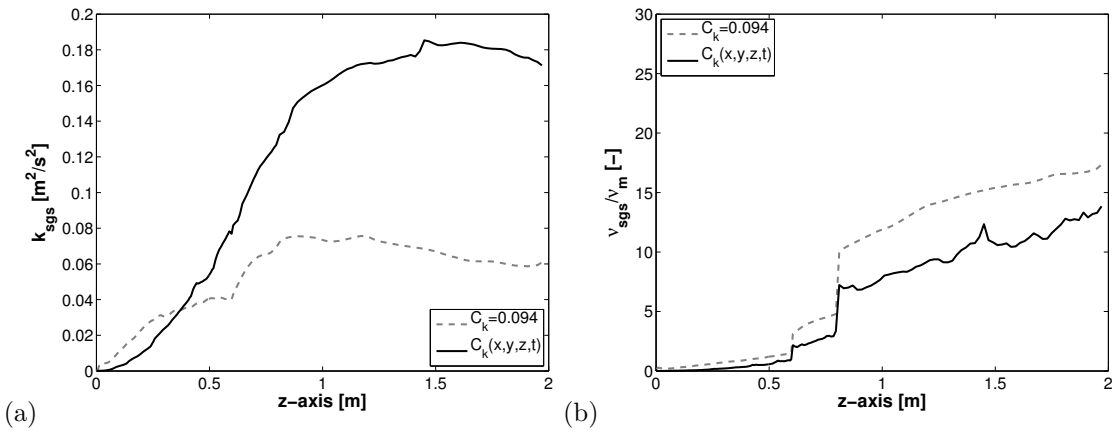

Figure 6.21: Centerline averaged profile for the constant- and dynamic-coefficient one-equation eddy viscosity model. a) SGS turbulent kinetic energy; b) Ratio of turbulent to molecular viscosity.

Then, the turbulent kinetic energy (k_{sgs}) is used to compute the turbulent mixing time scale (τ_{sgs}) in the combustion model as follows:

$$\tau_{sgs} = \frac{k_{sgs}}{\varepsilon_{sgs}} = \frac{1}{C_e}\frac{\Delta}{k_{sgs}^{1/2}} \tag{6.6}$$

Figure 6.22 shows the centerline heat release rate profile. The two models are similar which is due to the fact that in the flame region ($z < 50\ cm$), turbulent kinetic energies are identical, they both increases from 0 to 0.5 m^2/s^2, from 0 to 50 cm (Fig. 6.21-a).

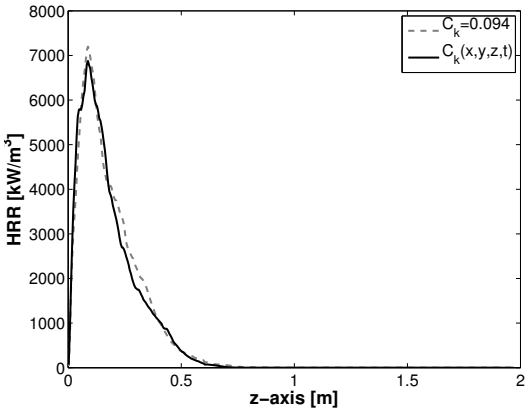

Figure 6.22: Centerline averaged profile of heat release rate.

Figure 6.23 shows the centerline profile for the mean and root mean squared temperature and velocity. The two models are overlapping which means that the value of C_k doesn't have any effects on the temperature and the velocity. This is only due to the fact that in the flame region ($z < 50\,\text{cm}$) more than 90% of the kinetic energy is resolved by the grid (Fig. 6.16), therefore the modeling choice for the turbulence model, in this scenario, does not impact the LES result. Concerning the computational cost, the CPU time for 20 s of simulation for the constant-coefficient model is 2368 h, and for the dynamic-coefficient model is 2624 h.

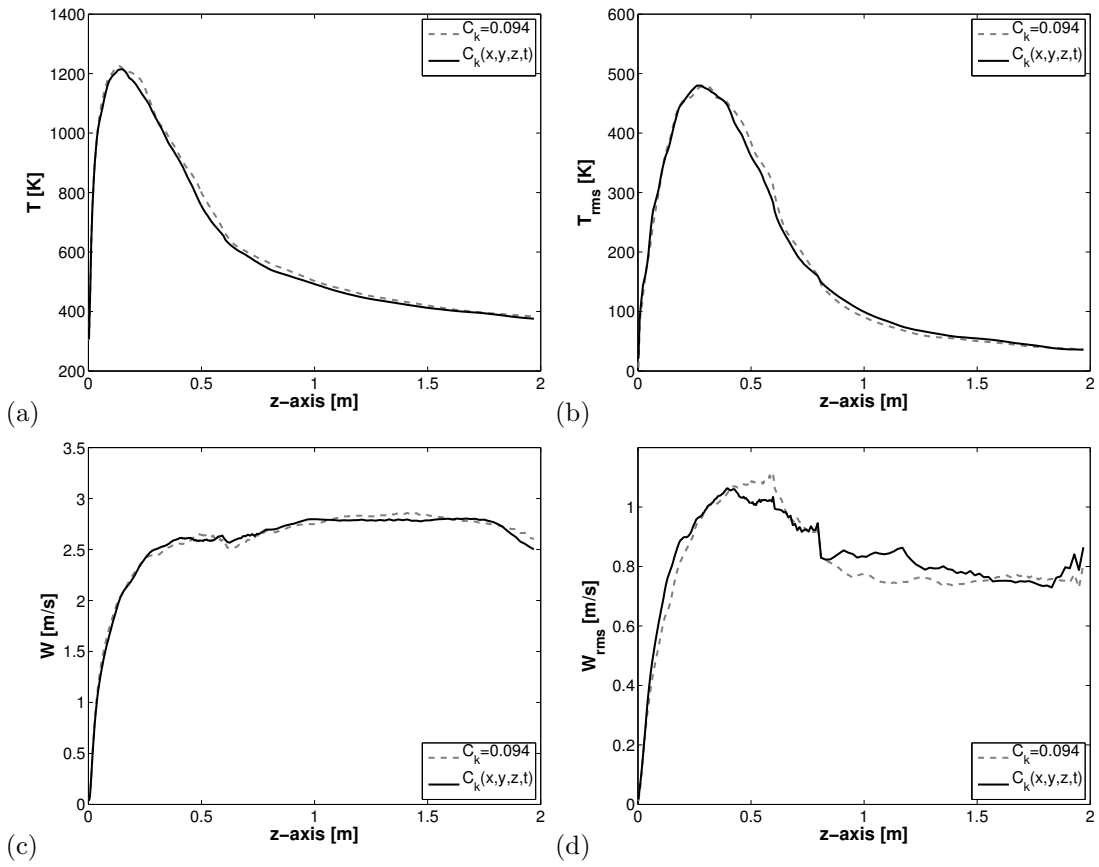

Figure 6.23: Centerline averaged profile for the constant- and dynamic-coefficient one-equation eddy viscosity model.(a) Temperature; (b) Root mean squared temperature; (c) Velocity; (d) Root mean squared velocity.

6.3.4 Extinction

We now turn to an analysis of the extinction model response to different dilution conditions, ranging from $X_{O_2} = 0.21$ to 0.11. Based on the grid convergence analysis, we use a 4 mm mesh resolution.

$X_{O_2} = 0.21$

We start our discussion with case $X_{O_2} = 0.21$ and $\chi_r = 0.23$ (Fig. 6.24). This case corresponds to a complete combustion condition. Figure 6.24 presents the corresponding variations of the simulated total heat release rate, $HRR = \int_V \left(\dot{\omega}'''_{R1} + \dot{\omega}'''_{R3}\right) \Delta H_c dV$ and the heat release rate only due to non-burning fuel reaction, $HRR^* = \int_V \dot{\omega}'''_{R3} \Delta H_c dV$. Variations in HRR are compared to the theoretical fuel-limited estimate of HRR, defined as the product of fuel mass loss rate ($\dot{m}_f$) times the heat of combustion(ΔH_c), $HRR_{FL} = \dot{m}_f \times \Delta H_F = 50\,\text{kW}$. Figure 6.24 shows that in a time-average sense $HRR \approx HRR_{FL}$, which suggests that the combustion efficiency (χ_a), defined as the ratio of the time-integrated HRR divided by the time-integrated HRR_{FL},

$$\chi_a = \frac{\int_{10}^{20} HRR(t')dt'}{\int_{10}^{20} HRR_{FL}(t')dt'} \tag{6.7}$$

is close to unity ($\chi_a = 0.99$).

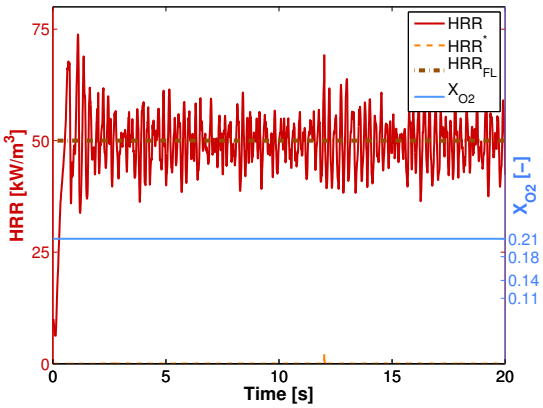

Figure 6.24: Simulated HRR (red dark solid line) and HRR^* (dashed line) compared to its theoretical fuel-limited estimate (brown dashed line) and oxygen mole-fraction in the co-flowing oxidizer (blue light solid line) for case $X_{O_2} = 0.21$.

$X_{O_2} = 0.18$

Next we consider case $X_{O_2} = 0.18$ and $\chi_r = 0.18$ (Fig. 6.25). This case features local quenching and re-ignition events. The discrepancy between HRR and HRR_{FL} in Fig. 6.25 gives a measures of partial flame extinction. We introduce χ_a^*, the combustion efficiency due to non-burning fuel reaction and defined as:

$$\chi_a^* = \frac{\int_{10}^{20} HRR^*(t')dt'}{\int_{10}^{20} HRR_{FL}(t')dt'} \tag{6.8}$$

We find $\chi_a = 0.97$ and $\chi_a^* = 0.07$.

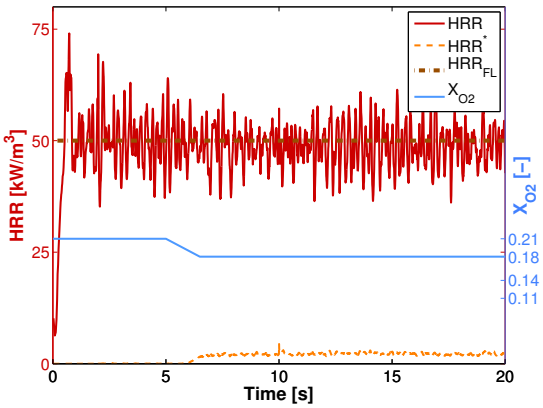

Figure 6.25: Simulated HRR (red dark solid line) and HRR^* (dashed line) compared to its theoretical fuel-limited estimate (brown dashed-dotted line) and oxygen mole-fraction in the co-flowing oxidizer (blue light solid line) for case $X_{O_2} = 0.18$.

Figure 6.26 presents the spatial distribution of instantaneous and mean mole fraction of oxygen, supplement by an isoline corresponding to $X_{O_2} = 0.18$. The diluted co-flow covers half of the flame ($z < 25\,\text{cm}$) which indicates that the top of the flame ($z > 25\,\text{cm}$) reacts with ambient and un-diluted background air.

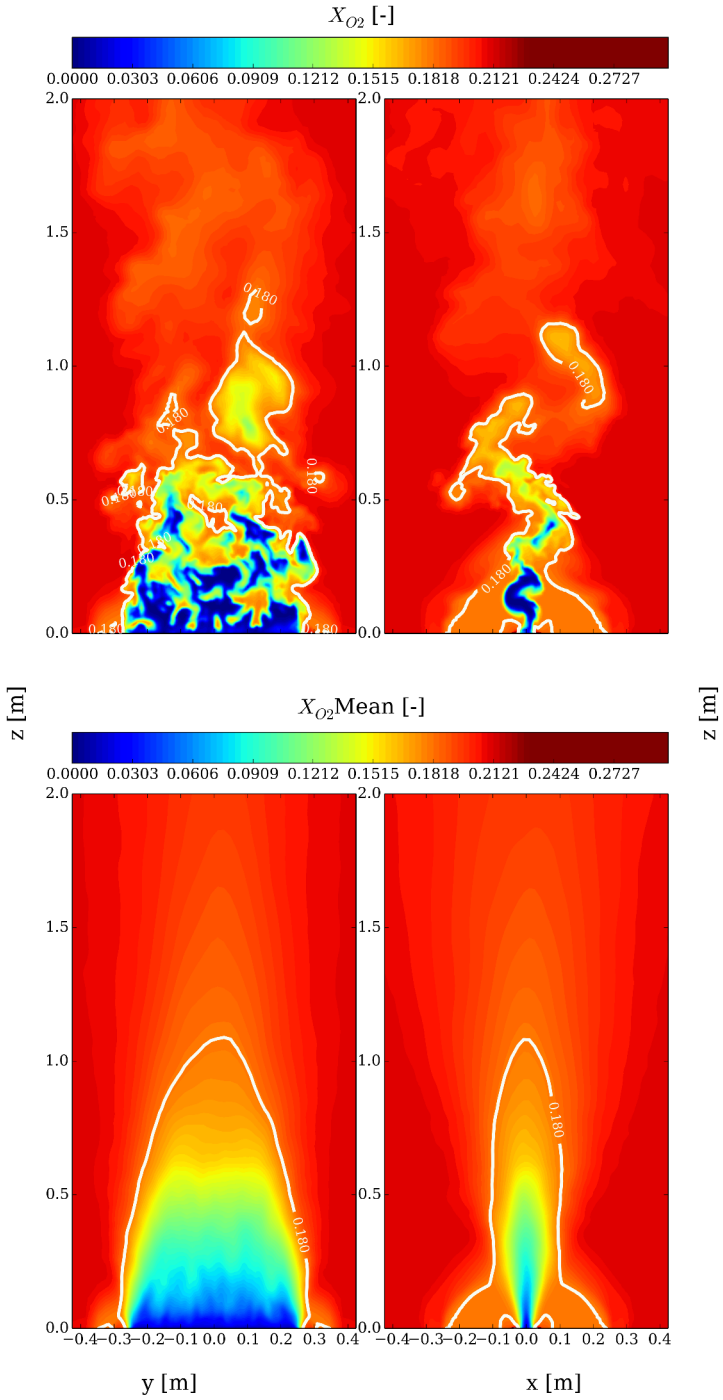

Figure 6.26: Mole fraction of oxygen contour map; (top) $t = 20\,\mathrm{s}$; (bottom) average.

Figure 6.27 shows simultaneous front- and end-view of the instantaneous (bottom) and mean (top) flame temperature. The instantaneous flame temperature on the flame surface is about 1700 K, which is a reasonable value considering that the adiabatic flame temperature is approximately 2000 K and that there is a 18% radiative loss. The mean temperature is about 400 K lower than the instantaneous flame temperature. The flame temperature has decreased by 100 K compared to the undiluted case and the adiabatic flame temperature by 200 K. Note that the decrease rate in flame temperature is not proportional to the decrease rate in adiabatic flame temperature due to the fact that the radiative loss fraction decreases as a function of X_{O_2}. The primary extinction mechanisms in this experiment is extinction by dilution. This quenching phenomena is captured by our extinction model due to a drop in the adiabatic flame temperature (T_{st}^{ad}, Eq. 4.33), and not due to heat losses, *i.e.* a decrease of enthalpy deficit variable H_{st} (Eq. 4.15).

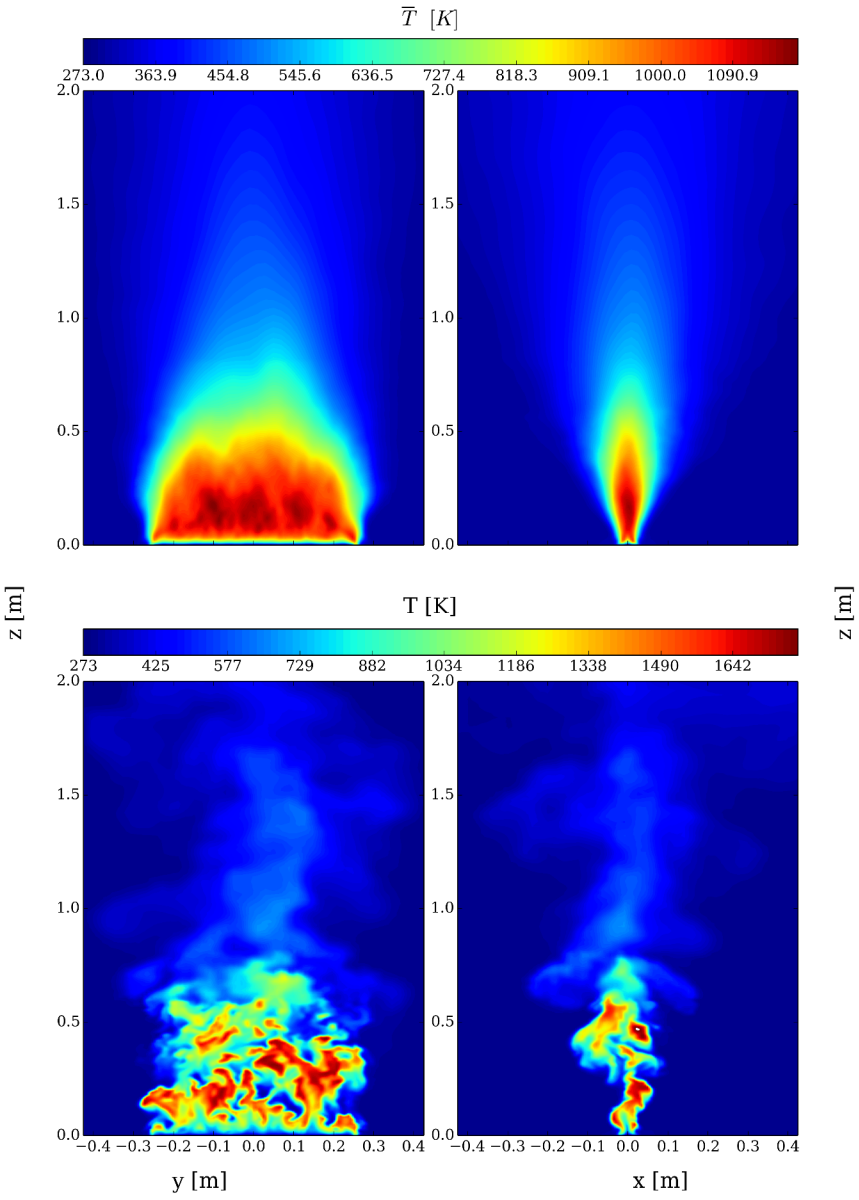

Figure 6.27: Temperature contour map; (top) $t = 20\,\mathrm{s}$; (bottom) average.

Figures 6.28 presents the corresponding average temperature and oxygen mole fraction at 12 and 25 cm height across the flame. Diluted co-flow is supplied at a 79.6 g/s mass flow rate and at a 0.18 oxygen mole fraction. The agreement be-

tween experimental data and numerical results is good for temperature and oxygen at 12.5 cm (less than 10% relative error) and excellent at 25 cm (less than 5% relative error). This suggests that turbulent mixing is qualitatively well-captured and combustion modeled accurately. Note that the uncorrected thermocouple temperatures are sensitive to the radiation treatment which is handled through a prescribed radiant fraction approach in this study.

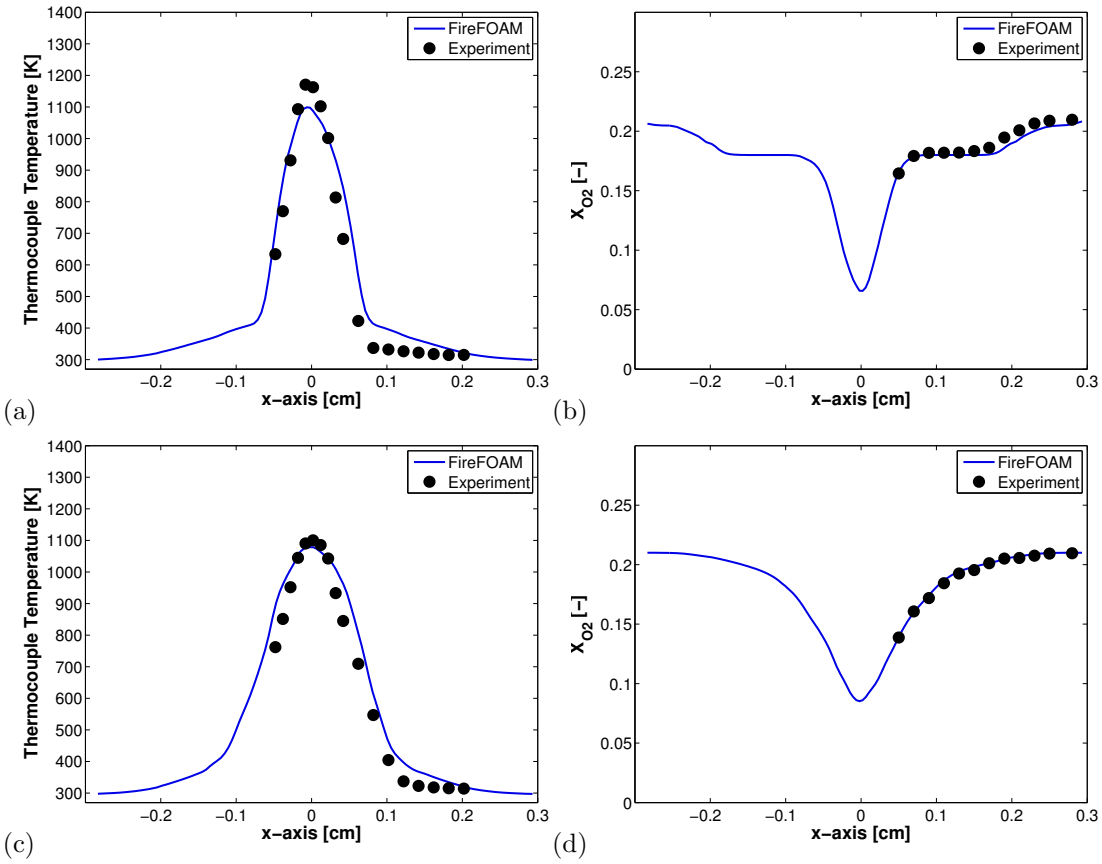

Figure 6.28: Comparison between experimental data (symbols) and numerical results (solid line) at 12.5 and 25 cm height across the flame. a) Thermocouple temperature at $z = 12.5\,\mathrm{cm}$; b) Oxygen Mole Fraction at $z = 12.5\,\mathrm{cm}$; c) Thermocouple temperature at $z = 25\,\mathrm{cm}$; b) Oxygen Mole Fraction at $z = 25\,\mathrm{cm}$;

$X_{O_2} = 0.11$

We now turn to case $X_{O_2} = 0.11$ and $\chi_r = 0.12$ (Fig. 6.29). This case corresponds to full extinction conditions. HRR drops to near zero, indicating that the flame is fully extinguished and $\chi_a \approx 2\%$. The residual burning corresponds to the HRR due to the anchor. This suggests that the critical damköhler number extinction model correctly responds (at least qualitatively) to the effect of oxygen dilution. From the the experiment, flame extinction occurs for the anchored case near $X_{O_2} = 0.127$.

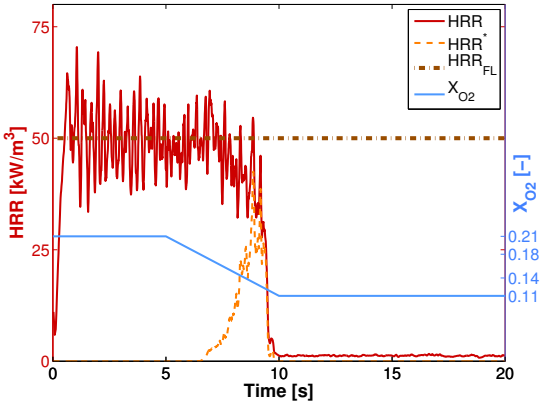

Figure 6.29: Simulated HRR (red dark solid line) and HRR^* (dashed line) compared to its theoretical fuel-limited estimate (brown dashed line) and oxygen mole-fraction in the co-flowing oxidizer (blue light solid line) for case $X_{O_2} = 0.11$.

Figure 6.31 presents the spatial distribution of instantaneous and mean mole fraction of oxygen, supplement by an isoline corresponding to $X_{O_2} = 0.11$. The diluted co-flow is 80 cm high and covers the entire flame which suggests that before extinction the fuel was only reacting with diluted co-flow. Note that the net mass

flow rate of co-flow ($\dot{m}_{N_2} + \dot{m}_{O_2}$) is increasing as X_{O_2} decreases when $\dot{m}_{O_2}$ remains constant (Fig. 6.30).

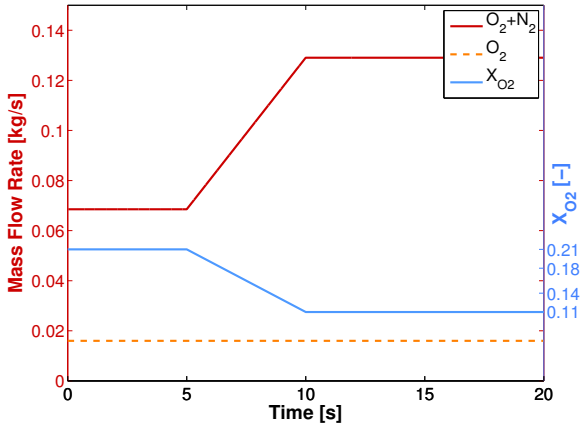

Figure 6.30: Simulated total mass flow rate of co-flow (red dark solid line) and oxygen mass flow rate (dashed line), and oxygen mole-fraction in the co-flowing oxidizer (blue light solid line) for case $X_{O_2} = 0.11$.

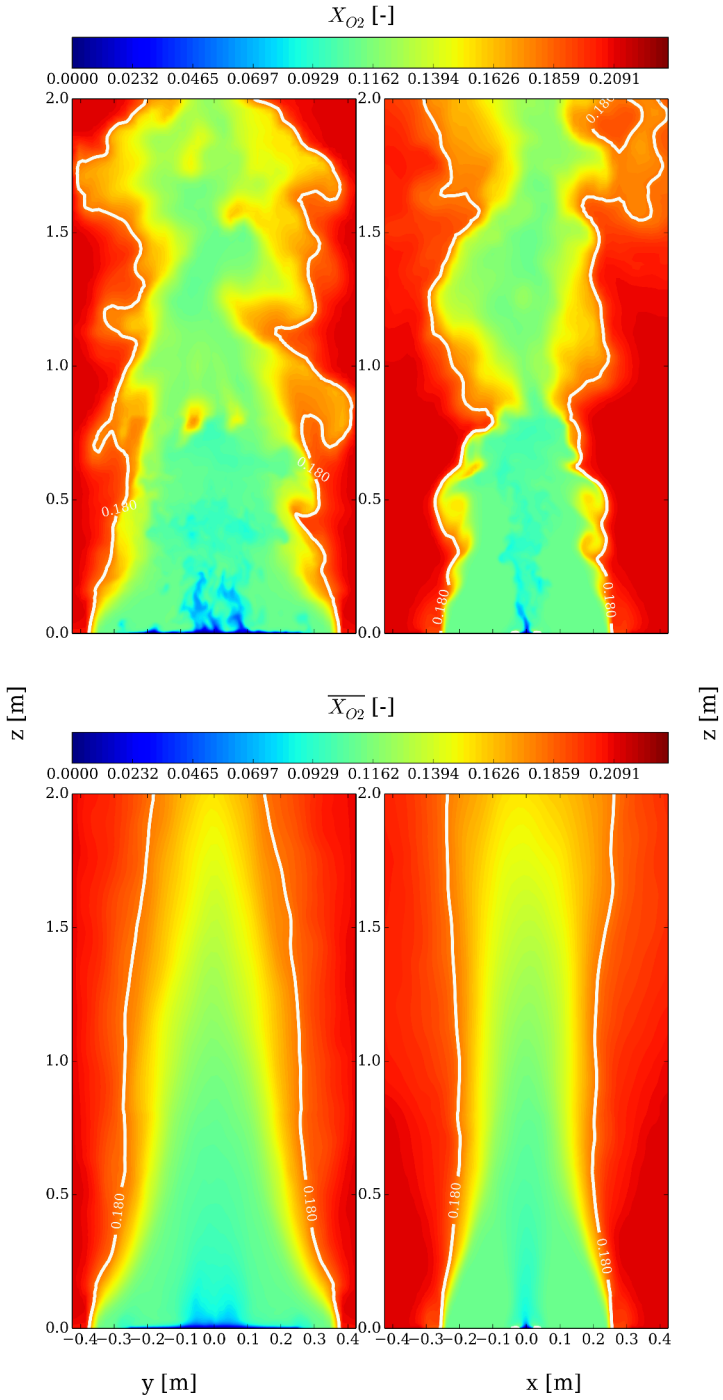

Figure 6.31: Mole fraction of oxygen contour map; (top) $t = 20\,\mathrm{s}$; (bottom) average.

In the simulation, we have found the extinction limit ($X_{O_2} = 0.11$) and introduced the combustion efficiency based on fuel and/or non-burning fuel reaction (χ_a and χ_a^*) to analyze the extinction model behavior. Hence, we can now present the combustion efficiency as function of X_{O_2} for $Da_c = 1.0$ and $T_{ign} = 1100\,\mathrm{K}$. The dark blue area represents the combustion efficiency only due to reaction R1, and the light red area, the combustion efficiency due to reaction R3. The net combustion efficiency is close to 1 until $X_{O_2} = 0.13$ and drop abruptly at $X_{O_2} = 0.13$ to $\chi_a = 0.10$ to completely quenched at $X_{O_2} = 0.11$. The flame experiences more extinction events as the co-flow is being diluted (the dark blue area decreases), and the number of re-ignition events increases as X_{O_2} decreases (the light red area increases). However at low oxygen concentration ($X_{O_2} < 0.13$), the cell temperature is so low ($< 1100\,\mathrm{K}$) than none of the non-burning fuel re-ignites. The agreement between experimental data and numerical results is good and it shows the ability of the LES fire model to accurately describe flame response to a range of dilution conditions, as well as the transition from extinction-free conditions to partial or total quenching (Fig. 6.34).

N.B.: The experimental error bar will be soon included and LES results are expected to be within the experimental uncertainties.

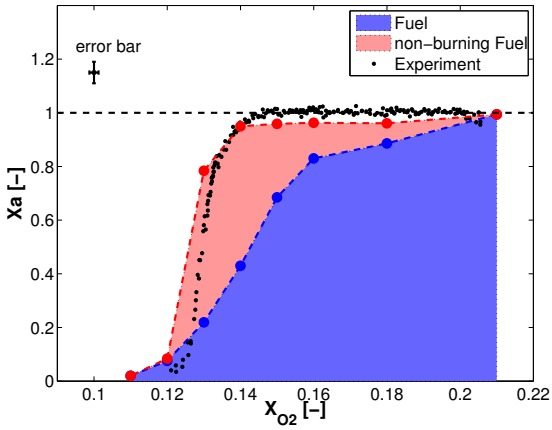

Figure 6.32: Combustion efficiency as function of oxygen mole fraction. The dark blue (light red) area represents the heat release rate due to reaction of fresh fuel R1 (non-burning fuel R3). The dashed line corresponds to complete combustion, *i.e.* $\chi_a = 1.0$.

6.3.5 Extinction Model Sensitivity

Sensitivity to grid resolution (Δx)

We first start a sensitivity analysis of the extinction model to grid resolution. The extinction model requires flame based quantities like the flame temperature (T_{st}) and the flame stretch (χ_{st}). Those two flame based quantities are modeled based on Eq.4.33 and 4.29. On the qualitative side, they are supposed to be independent of the grid resolution. On the quantitative side, some variations are expected. Figure 6.33-a represents for different grid resolution the simulated HRR as a function of time and oxygen mole fraction. The LES results for the different grid shows the expected decrease in heat release rate. However, a residual flame is still present for the 12 mm resolution ($\chi_a \approx 0.08$).

Figure 6.33-b shows HRR^* due to non-burning fuel reaction as a function of time and oxygen model fraction. LES results are grid-insensitive for $\Delta x \leq 4\,\text{mm}$. Indeed, the re-ignition model is based on filtered temperature ($\widetilde{T}$) and is supposed to be more strongly sensitive to the grid resolution. As shown by Fig. 6.13, the flame temperature is under-predicted by 100 K, which leads to an under-prediction of re-ignition.

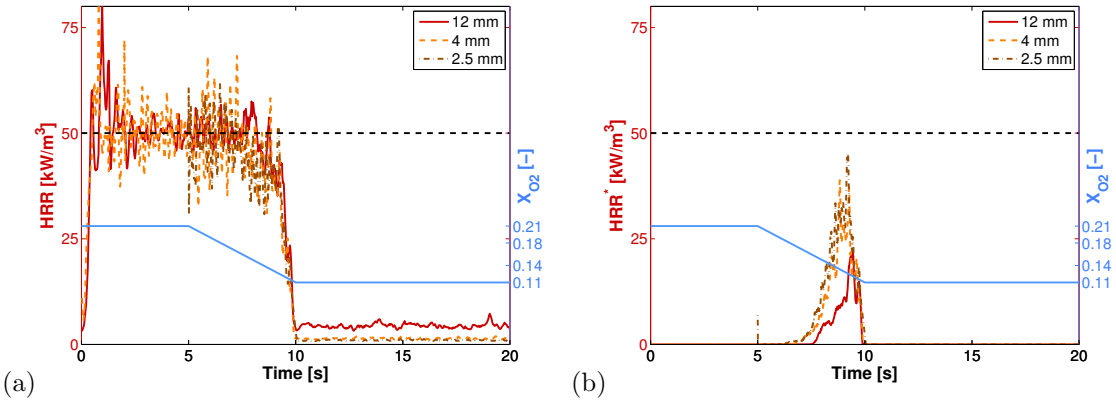

Figure 6.33: Simulated HRR (red solid line) compared to its theoretical fuel-limited estimate (brown dashed line) and oxygen mole-fraction in the co-flowing oxidizer (blue solid line) for case $X_{O_2} = 0.11$.

Sensitivity to the Critical Damköhler Number (Da_c)

Next, we turn our discussion on the extinction model sensitivity to the critical damköhler number. Previous studies [91] have shown that the critical damköhler number can vary by one order of magnitude around 1. Therefore, we decide to study three cases: $Da_c = 0.1$, 1.0, and 10 with $T_{ign} = 1000\,\text{K}$. The LES solution is strongly dependent of Da_c (Fig. 6.34). For $Da_c = 0.1$, full extinction is not captured at $X_{O_2} = 0.11$ and $\chi_a = 0.075$. For $Da_c = 1.0$, results are the same than described in

the previous section. For $Da_c = 10$, the flame is quenched at $X_{O_2} = 0.12$. However, extinction events are predicted for the ambient case, $X_{O_2} = 0.21$, $\chi_a = 0.96$. Based on the extinction model sensitivity to the critical damköhler number, we choose $Da_c = 1.0$.

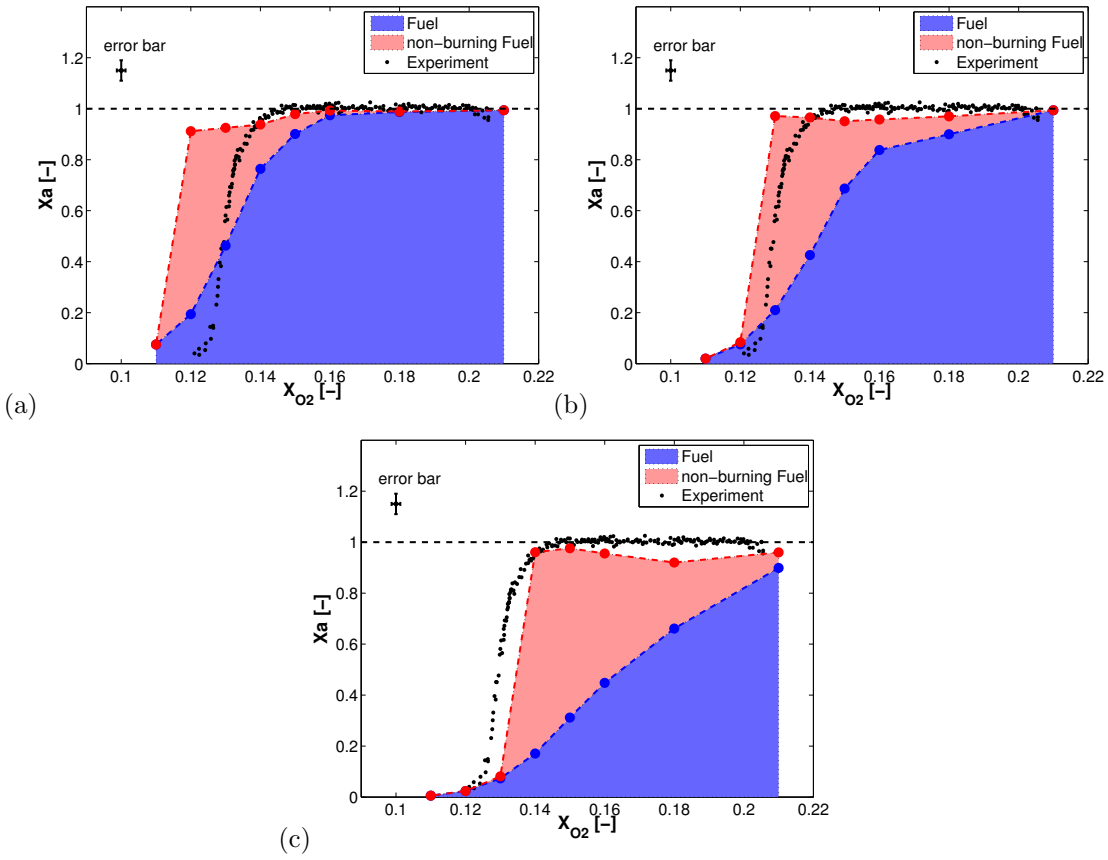

Figure 6.34: Combustion efficiency as function oxygen mole fraction for different critical damköhler number with $T_{ign} = 1000\,\mathrm{K}$. The blue (red) area represents the heat release rate due to reaction of fresh fuel R1 (non-burning fuel R3). The dashed line corresponds to complete combustion, *i.e.* $\chi_a = 1.0$. a) $Da_C = 0.1$; b) $Da_c = 1$; c) $Da_c = 10$.

Sensitivity to the Re-Ignition Temperature (T_{ign})

Finally, we consider the re-ignition model sensitivity to the re-ignition temperature (T_{ign}). As the extinction limit is slightly over-predicted compared to the experiment, we only consider cases in which the re-ignition temperature is increased. The heat release rate due to fuel reaction is insensitive to the re-ignition temperature as expected (Fig. 6.35). Combustion efficiency for high $X_{O_2} \geq 0.16$ and low, $X_{O_2} \leq 0.12$, oxygen concentration are insensitive to the re-ignition temperature (Fig. 6.35). On one hand, for the high X_{O_2}, the flame temperature is so high ($[1,600 - 1,800]$K) that it will re-ignites the non-burning fuel in most scenario. On the other hand, for low X_{O_2}, the temperature is so low ($< 1,000\ K$) that none of the non-burning fuel re-ignites. Therefore, LES results are only sensitive to the T_{ign} in the transient phase, X_{O_2} ranging from 0.16 to 0.12. In this range, the combustion efficiency is decreasing as T_{ign} increases, as expected.

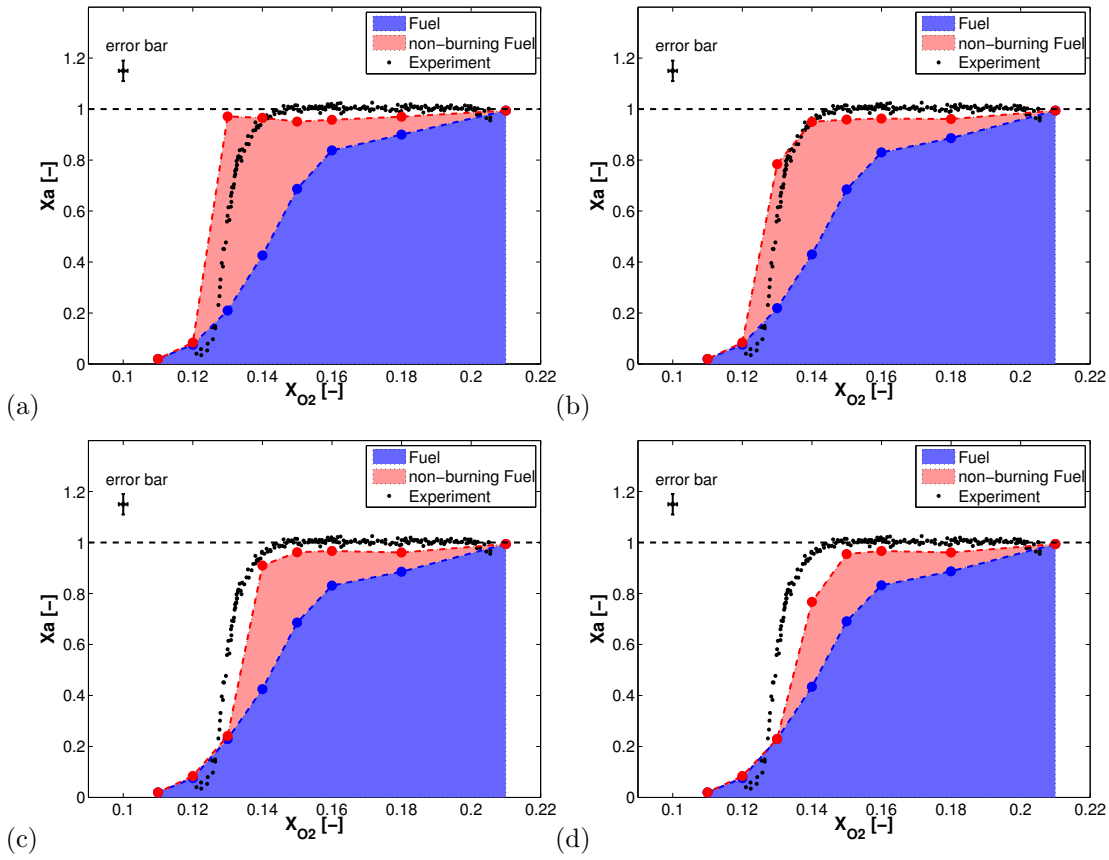

Figure 6.35: Combustion efficiency as function oxygen mole fraction for different re-ignition temperature with $Da_c = 1.0$. The blue (red) area represents the heat release rate due to reaction of fuel (non-burning fuel). The black dashed line corresponds to complete combustion, *i.e.* $\chi_a = 1.0$. a) $T_{ign} = 1000\,\mathrm{K}$; b) $T_{ign} = 1100\,\mathrm{K}$; c) $T_{ign} = 1200\,\mathrm{K}$; d) $T_{ign} = 1300\,\mathrm{K}$.

6.4 Conclusion

This chapter presents a numerical study of a turbulent, methane-fueled, buoyancy-driven, diffusion flame exposed to air-nitrogen co-flow. A grid convergence study has been conducted and LES results are converged for $\Delta x \leq 4\,\mathrm{mm}$, *i.e.* $W_b/\Delta x = 12$. The present study is aimed at evaluating the ability of LES fire models to accurately

describe flame response to a range of oxygen dilution conditions, as well as transition from extinction-free conditions to partial or total quenching. The agreement between experimental data and numerical results is good and within the experimental uncertainties with $Da_c = 1.0$ and $T_{ign} = 1100\,\mathrm{K}$, it indicates that the flame extinction model in FireFOAM based on the concept of a critical damköhler number responds correctly, qualitatively and quantitatively, to oxygen dilution effects, as shown by the combustion efficiency versus oxygen mole fraction curve. Results also indicate that full flame extinction is predicted at lower oxygen levels ($X_{O_2} = 0.11$) than those observed in the experiment (X_{O_2}=0.127) which corresponds to a relative error of 13%. The extinction model is relatively independent of grid resolution, but is very sensitive to the critical damköhler number and weakly sensitive to the re-ignition temperature.

Note that two challenges are faced in these simulations. The first one concerns the extinction model capability to capture accurately the flame transition to total quenching which has been discussed in this chapter. The second one involves the radiative loss sensitivity to P_{H_2O}, P_{CO_2}, P_{CH_4} and T. Those two challenges have to be treated separately and sequentially in order to understand and validate the LES models. This study has been conducted using a prescribed radiant fraction approach and is seen as an intermediate step toward a full radiative treatment by solving the RTE equation as discussed next in the future work section.

6.5 Future Work

As shown by figure 6.3, the radiant fraction decreases with decreasing values of co-flow oxygen concentration, $\chi_{rad} = 0.21$ for $X_{O_2} = 0.21$ and decreases linearly to $\chi_{rad} = 0.12$ for $X_{O_2} = 0.14$. In this context, modeling radiation with a simple radiant fraction approach (as described in section 2.6.1) is not suitable. Therefore, the full RTE equation combined with gray gas approach (see section 2.6.2) will be used to describe the decrease of radiant fraction and its sensitivity to species concentration (H_2O, CO_2 and CH_4), temperature and soot production. The absorption coefficient [92, 93], κ, is calculated as follows.

$$\kappa = P\left(X_{H_2O}a_{H_2O} + X_{CO_2}a_{CO_2} + X_{CH_4}a_{CH_4}\right) + \kappa_s \tag{6.9}$$

where P and X_i are the pressure and mole fraction of respective species, a_i the Planck Mean absorption coefficient [68], κ_s the absorption coefficient of soot.

Soot Modeling

One issue associated with gray medium modeling is the treatment of soot. Assuming a maximum soot volume fraction for methane, $f_v \approx 0.5\,\text{ppm}$, and from Activation Energy Analysis (AEA) [94] its profile as a function of the mixture fraction, $f_v(Z)$, the mean absorption coefficient can be reconstructed using the following equation:

$$\kappa_s = C \times f_v(Z)T \tag{6.10}$$

where C is the extinction coefficient ($C = 1871\,\mathrm{m}^{-1}\,\mathrm{K}^{-1}$ [95]), $f_v(Z)$ the soot volume fraction as a function of mixture fraction and T the temperature.

In a preliminary step, the effect of soot on radiation and the optical thickness of the flame are studied using an effective flame emissivity, $\overline{\varepsilon}_{eff}$. The effective flame emissivity is calculated using the integral of mean absorption, κ (Eq.6.9), along selected rays, $s^{'}$, from $y = 0\,\mathrm{m}$ to $y = 0.7\,\mathrm{m}$ using the following equation:

$$\overline{\varepsilon}_{eff} = 1 - exp\left(-\int_0^s \kappa(s^{'})ds^{'}\right) \tag{6.11}$$

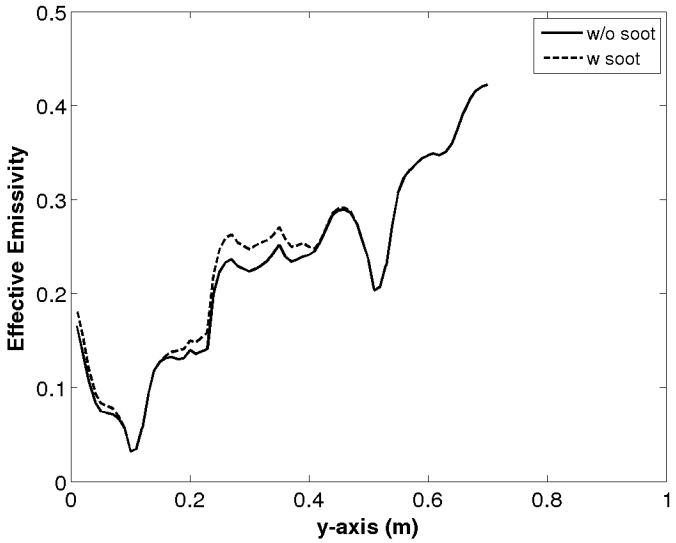

Figure 6.36: Effective emissivity calculated at different elevation along y-axis using equation 6.11 with the soot contribution (dashed line) and without soot contribution (solide line).

As expected for a methane flame, the contribution of soot to the total effective emissivity is small and on the order of 10% and will be therefore neglected for future work with methane as the fuel. Figure 6.11 also supports this observation. Indeed, the drop in the flame luminosity, *i.e.* absence of soot, does not affect the radiant fraction and tends to emphasize the fact that soot contribution to the overall radiative heat transfer system is negligible.

Above $y = 0.2\,\mathrm{m}$, $\overline{\varepsilon}_{eff} > 0.2$, the flame is not optically thin and absorption plays a non-negligible role. Absorption has to be taken into account in order to describe accurately the flame temperature.

Grey Gas Limitations

Some previous studies [66, 96] have shown that the grey gas approach and the use of a Planck mean absorption coefficient can cause large errors and tend to overestimate emission and therefore radiative heat losses.

In the following test case (Fig. 6.37), narrow-band computations are solved using RadCal, a stand-alone RTE solver utility. Spectrally-resolved RadCal results are then compared against spectrally-averaged approximations solved using FireFOAM and RadCal by only selecting one band covering the entire spectral domain and is used also as a verification test. These comparisons are meant to highlight and quantify the various penalties in accuracy that result from the gray assumption. Computations for this investigation consider 1-D radiative transport through a single homogeneous gas layer with variable property scenarios (Fig. 6.37). The

scenarios considered for this analysis include variation of the path length ranging from 0.1 to 1000 m and thus variation of the optical depth of the layer, and alternation between a scenario involving dominance of gas-layer emission relative to background radiation (low T_{wall}, high T_{gas}) and dominance of gas-layer absorption (high T_{wall}, low T_{gas}). Note that the individual values of partial pressure (P_{H_2O}) and the path length are not important. The controlling quantity is the product of those two variables, *i.e.* the pressure length $P_{H_2O}L$. Setting P_{H_2O} to 1.0 and L ranging from 0.0005 to 5 gives the same results.

As reported by previous studies [66, 96], emission and absorption are well predicted for the optically-thin regime. For the optically-thick regime, emission is over-predicted (more than 40% relative error for $\kappa_{H_2O}L > 0.1$) and absorption is under-predicted (more than 6% relative error for $\kappa_{H_2O}L > 0.1$) (Fig. 6.37).

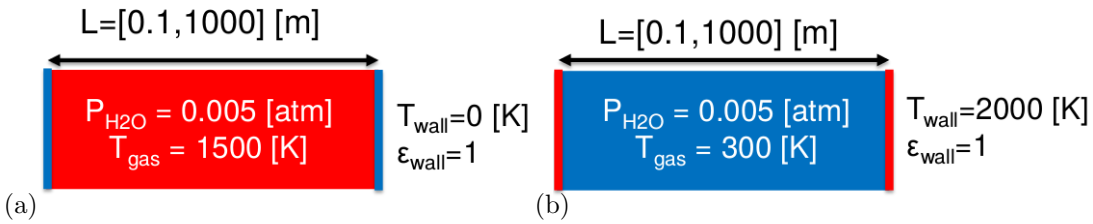

Figure 6.37: Configuration for the 1D column of gas test case. a) Emission dominated; b) Absorption dominated.

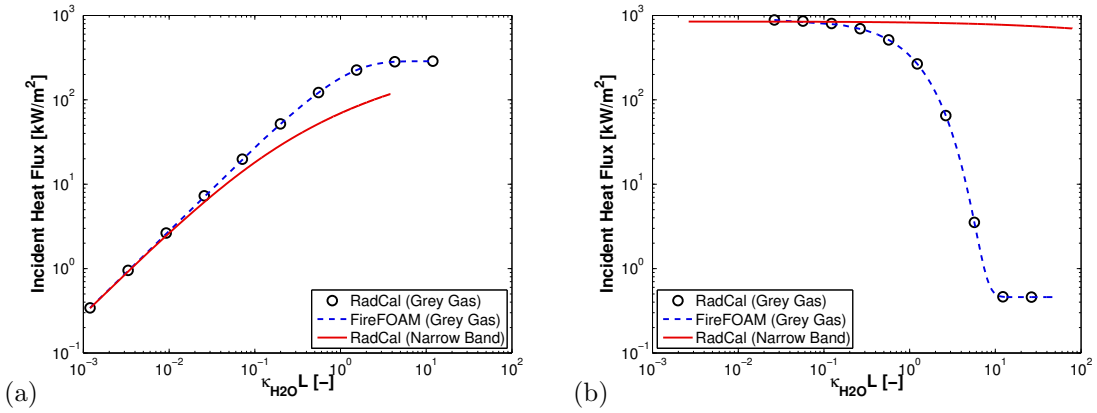

Figure 6.38: Incident wall heat flux as function of optical depth for a 1D column of gas with uniform properties. a) Emission dominated; b) Absorption dominated.

Turbulent Line Fire

In FireFOAM, the reconstructed radiative loss fraction (Fig. 6.39) is obtained by dividing the integrated net radiative heat flux, $\overline{\dot{q}_r''}$, over the control surface that encloses the control volume, by the product of the fuel mass loss rate times the heat of combustion, $\dot{m}_F \Delta H_F$.

$$\chi_{rad} = \frac{\int \overline{\dot{q}_r''} dA}{\dot{m}_F \Delta H_F} \tag{6.12}$$

Note that in the case of complete combustion, the integrated volumetric heat release rate, $\overline{\dot{\omega}_{h_s}'''}$, over the control volume is equaled to the product of the fuel mass loss rate times the heat of combustion, $\int \overline{\dot{\omega}_{h_s}'''} dV \approx \dot{m}_F \Delta H_F$.

Then, the radiative loss fraction is average over time (Fig. 6.39).

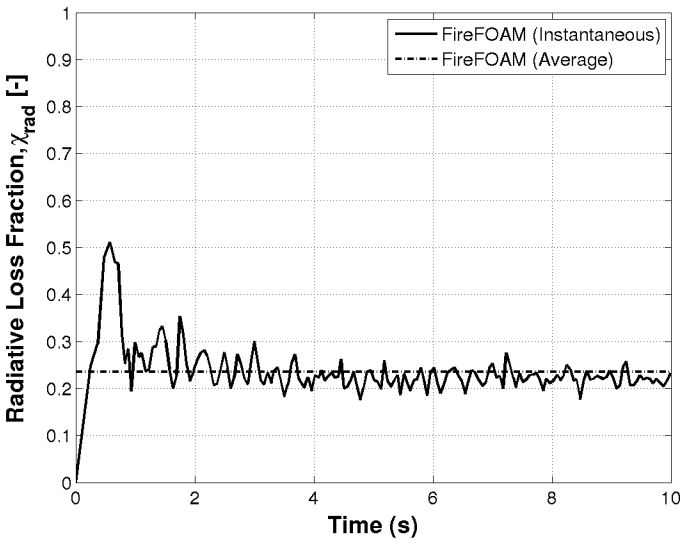

Figure 6.39: Instantaneous radiative loss fraction (solide line) over time and its average value (dashed line) for a diluted case ($X_{O_2} = 0.175$).

Figure 6.41 shows the computed radiative loss fraction for two different cases ($X_{O_2} = 0.211$ and $X_{O_2} = 0.175$) and experimental results [52].

Because of the limitation of the gray gas model for non-optically thin regime, it has been suggested [47, 96, 97] that the mean absorption coefficient should be calibrated according to $\kappa = C\kappa_p$ where κ_p is the Planck mean value and C is a calibration factor. Because the absorption is under-predicted, we decide to only reduced the Planck mean coefficient for the emission component of the RTE, *i.e.* for heat release rate greater than zero.

We first use the 1D column of gas test to select the calibration factor C. The incident heat flux decreases as C decreases (Fig. 6.40). Based on Fig. 6.40 and our range of optical depth application, we chose $C = 0.4$.

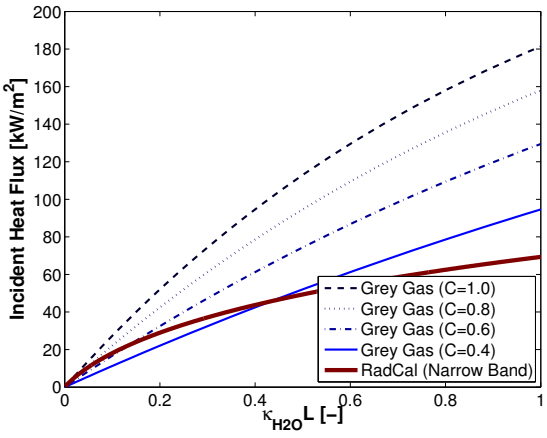

Figure 6.40: Incident heat flux as function of optical depth for a 1D column of gas for different value of C.

We now consider the turbulent line burner with the corrected Planck mean absorption coefficient. In this preliminary study, we only focus on a case where the combustion efficiency is close to 1.0 and extinction is not predominant, *i.e.* X_{O_2} ranging from 0.21 to 0.18. For the uncorrected scenario ($C = 1.0$), the radiative loss fraction is over-predicted by 38% at ambient condition. In contrast, the trend is qualitatively well-captured, χ_r decreases as X_{O_2} decreases. For the corrected scenario ($C = 0.4$), agreement between the simulation and experiment is good and the trend is well-captured.

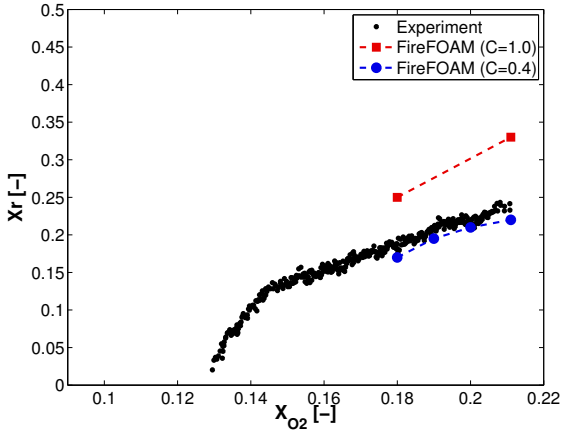

Figure 6.41: Radiative loss fraction comparison between experimental data (dashed line) and numerical results (symbols) as a function of oxygen mole fraction.

7 Results: Turbulent Line Fire in Controlled Co-flow (Extinction by water-mist)

7.1 Introduction

The emphasis in this study is on the problem of flame weakening and extinction when the fire is exposed to water-mist. The experimental component is identical to the previous study (chapter 6) and correspond to a canonical slot burner configuration. The configuration provides two-dimensional, plane, buoyancy-driven, methane-fueled, turbulent diffusion flames with controlled co-flow conditions. The co-flow will allows for the supply of a mixture of air and water-mist, including conditions for which the increase of evaporation will lead to full flame extinction. The boundary conditions concerning the water-mist, *i.e.* droplet diameters and water mass flow rate, are determined through a theoretical and numerical analysis as reported in section 7.5.1 and 7.5.2. The computational component of the study is aimed at evaluating the flame extinction/re-ignition model using FireFOAM-2.2.x when exposed to thermal quenching due to evaporation (section 7.5.3). Another

component of this study is to investigate and understand the effect of the liquid-to-gas mass ratio and the effect of droplet diameter on combustion efficiency (section 7.5.3) in order to design more efficient fire suppression systems.

7.2 Water-Mist Physics

7.2.1 Definition

The term *water-mist* as currently understood in the fire protection field relates to fine water sprays with no drops larger than 1000 µm [1]. Such sprays are not true mists, however. A *mist* in the scientific sense consists of drops somewhere on a continuum between *aerosol* (particles with diameter ~ 5 µm) and *fog* (droplet diameters ranging between 10 and 100 µm). Particles less than 20 µm in diameter take a long time to settle out, and hence create what is recognized in both literature and science as a mist.

7.2.2 Quenching mechanisms

Water-mist fire suppression system includes different quenching mechanisms. Mawhinney et al. [98] describe three primary and two secondary mechanisms associated with extinguishement of hydrocarbon fires by water-mist. The primary mechanisms are

- Gas phase cooling
- Oxygen displacement and fuel vapor dilution

- Wetting and cooling of the fuel surface

The secondary mechanisms are

- Radiation attenuation
- Kinetic effects

In our configuration, the fuel is prescribed and is not sensitive to the thermal heat feedback to the burner. Therefore, the wetting and cooling of the fuel surface mechanism is not relevant in this study. Note that secondary mechanisms such as radiation attenuation and kinetic effects are not taken into consideration in our model and are not the focus of this study. Indeed, a prescribed radiation fraction is assumed and combustion is based on a single-step global reaction.

7.2.2.1 Gas phase cooling

Gas phase cooling refers to the removal of heat from the flame and hot gases, due to the evaporation of water. The cooling efficiency of water-mist is due to the fact that the water is broken up into many fine droplets, which enhances the evaporation rate. The more water that evaporates, the greater the amount of heat that is extracted from the flame, and the lower the temperature of the flame is. If the flame temperature is reduced and therefore the Damköhler drops below the critical value necessary to sustain combustion ($Da_c \approx 1.0$), the flame will be extinguished.

7.2.2.2 Oxygen dilution

Locally, as the water droplets evaporate and are converted to the vapor phase, the oxygen concentration decreases. Dilution by water vapor can reduce the oxy-

gen concentration below the critical value necessary to sustain combustion [limiting oxygen concentration (LOC)], the fire will be extinguished. Based on results from chapter 6, the LOC is approximately 13 percent.

7.3 Experimental configuration

Extinction in a water-mist configuration will be studied with the Wolfhard-Parker burner described in section 6.1. A mist co-flow ($d < 100\,\mu m$) would be introduced challenging the flame by producing local extinction events. Spray-flame metrics for experimental and numerical evaluation would include:

- The evaporation of the liquid spray (due to convective and radiative heat transfer).
- The relative weights of extinction and re-ignition.
- The overall combustion efficiency.

Combustion efficiency will be determined through combustion product measurement via calorimetry. The inlet mist co-flow characteristics will be determined from drop size and density measurements (diffraction based) and velocity (PIV based) using the Malvern Spraytec particle sizing system and LaVision system. The mist inlet co-flow measurements will be used to determine the total water influx to the burner and used as a boundary condition for the numerical simulations described next.

7.4 Numerical Configuration

The Eulerian solver is described in section 6.2.1. A classical Lagrangian-based spray modeling approach is used for water-mist simulations. The Lagrangian-based spray modeling approach treats the liquid phase as a discrete phase, injects representative (spherical-shaped) droplets according to experimental measured size and velocity distributions, tracks the individual trajectories of the representative droplets, and includes two-way coupling between the gas and liquid phases. This approach is already implemented into FireFOAM [99] and verification tests have been performed to verify conservation of mass and energy between the gas and liquid phase (section 3.4). The experimental data being unavailable, a mono-dispersed spray is assumed.

7.5 Results and Discussion

7.5.1 Kinematic

The first part of this study is to determine the maximum droplet diameter that can be carried by the co-flow in absence of a fire, *i.e.* the worst case scenario without the increase of buoyancy force induced by the fire. This section is divided into three sections. The first part study the droplet motion in quiescent air in order to determine the droplet terminal velocity and then with a co-flow entrainment by solving a momentum equation for a single droplet. The second part studies the water-mist in presence of a co-flow in FireFOAM for a one-way coupling as assumed in the theoretical framework. The third part considers two-way coupling and focuses on the water-mist/co-flow interaction. This last section corresponds to

the most realistic treatment.

7.5.1.1 Theory

The equation of motion

Lagrangian particle motion is governed by Newton's second law. The particle acceleration equation is called the Basset, Boussinesq and Oseen (BBO) equation [100, 101]. The BBO equation contains the effects of particle mass, pressure, Basset force, Magnus effect, Saffman force, and Faxen force. For typical water spray, most of these forces may be neglected [100, 101].

In FireFOAM, drop motion is governed entirely by gravity and spherical particle drag. Drop acceleration is given by:

$$\frac{\partial \overrightarrow{u_d}}{\partial t} = -\frac{3}{4}\frac{\rho_g}{\rho_d}\frac{1}{d_d}C_D\left(\overrightarrow{u_d} - \overrightarrow{U}\right)|\overrightarrow{u_d} - \overrightarrow{U}| + \overrightarrow{g} \tag{7.1}$$

where $\overrightarrow{u_d}$ is the drop velocity, ρ_g the gas phase density, ρ_d the drop density, d_d is the drop diameter, C_D the drag coefficient, $\overrightarrow{U}$ the continuous phase velocity and $\overrightarrow{g}$ the gravitational acceleration. The drag coefficient, C_D, is represented by the piecewise equation:

$$C_D = \begin{cases} \frac{24}{Re_d}\left(1 + \frac{Re_d^{2/3}}{6}\right) & Re_d < 1000 \\ 0.424 & Re_d \geq 1000 \end{cases} \tag{7.2}$$

where

$$Re_d = \frac{\rho|\overrightarrow{u_d} - \overrightarrow{U}|d_d}{\nu} \tag{7.3}$$

A momentum relaxation time can be defined as:

$$t_c = \frac{4}{3}\frac{\rho_d d_d}{\rho_g C_D |\overrightarrow{u_d} - \overrightarrow{U}|} \tag{7.4}$$

Equation 7.1 may then be rewritten as:

$$\frac{\partial \overrightarrow{u_d}}{\partial t} = -\frac{\overrightarrow{u_d} - \overrightarrow{U}}{t_c} + \overrightarrow{g} \tag{7.5}$$

Droplet velocity in quiescent air ($U = 0\ m/s$)

We first start a calculation of the droplet terminal velocity using Eq. 7.1 and compare it to the co-flow velocity in order to determine the maximum droplet diameter that can be carried by the co-flow.

A drop falling in a stationary fluid ($U = 0\,\mathrm{m/s}$) will eventually reach a maximum velocity. This velocity is its terminal velocity, and is a function of the surrounding fluid and the drop itself. Figure 7.1 shows the terminal velocity for different droplet diameters. The terminal velocity decreases as the droplet diameter decreases. As reported by table 7.1, water droplets have a momentum relaxation time of a few ms and therefore reach their terminal velocity in a couple of ms. The maximum co-flow mass flow rate allowed by the experimental apparatus is 0.1 kg/s, which corresponds to an initial velocity of 27 cm/s. Therefore, we only study droplets with a terminal velocity smaller than the co-flow velocity. The droplet diameter is chosen such as the co-flow can carry the droplet to direct them upward into the flame.

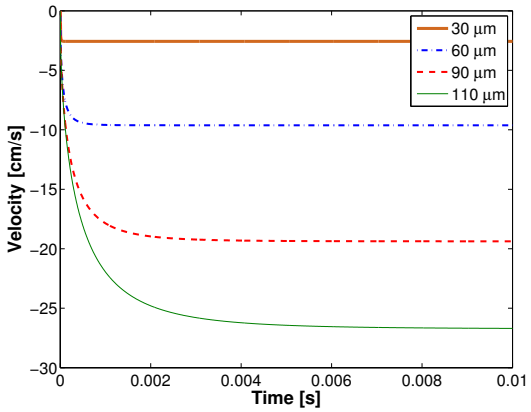

Figure 7.1: Terminal velocity for different droplet diameters computed with Matlab by solving Eq. 7.1 with $U = 0\,\mathrm{m/s}$.

Table 7.1: Terminal velocity and momentum relaxation time (Eq. 7.1) of varying drop size.

d_d	t_c	$\overrightarrow{u_d}\,(t \to \infty)$
[µm]	[ms]	[cm/s]
30	1.96	2.7
60	3.68	9.6
90	4.94	19
110	5.57	27

Droplet Velocity with co-flow entrainment ($U = 27\,\mathrm{cm/s}$)

We now consider the co-flow velocity ($U = 27\,\mathrm{cm/s}$) and recalculate the droplet velocity and height as a function of time (Fig. 7.2) computed with Matlab by solving Eq. 7.1 with $U = 27\,\mathrm{cm/s}$. The droplets have their own terminal velocity and do not

move at the same speed than the co-flow, but they still follow the co-flow streamline for $d_d \leq 90\,\mu m$. As the droplet diameter increases, the droplet velocity decreases due to gravity. The flame height is around 50 cm. So, it is desirable to select a droplet which will reach the flame height in a couple seconds. Therefore, the extinction model will be tested first for a 30 µm droplet diameter. The 110 µm droplet is too heavy to move upward and has a vertical velocity near zero.

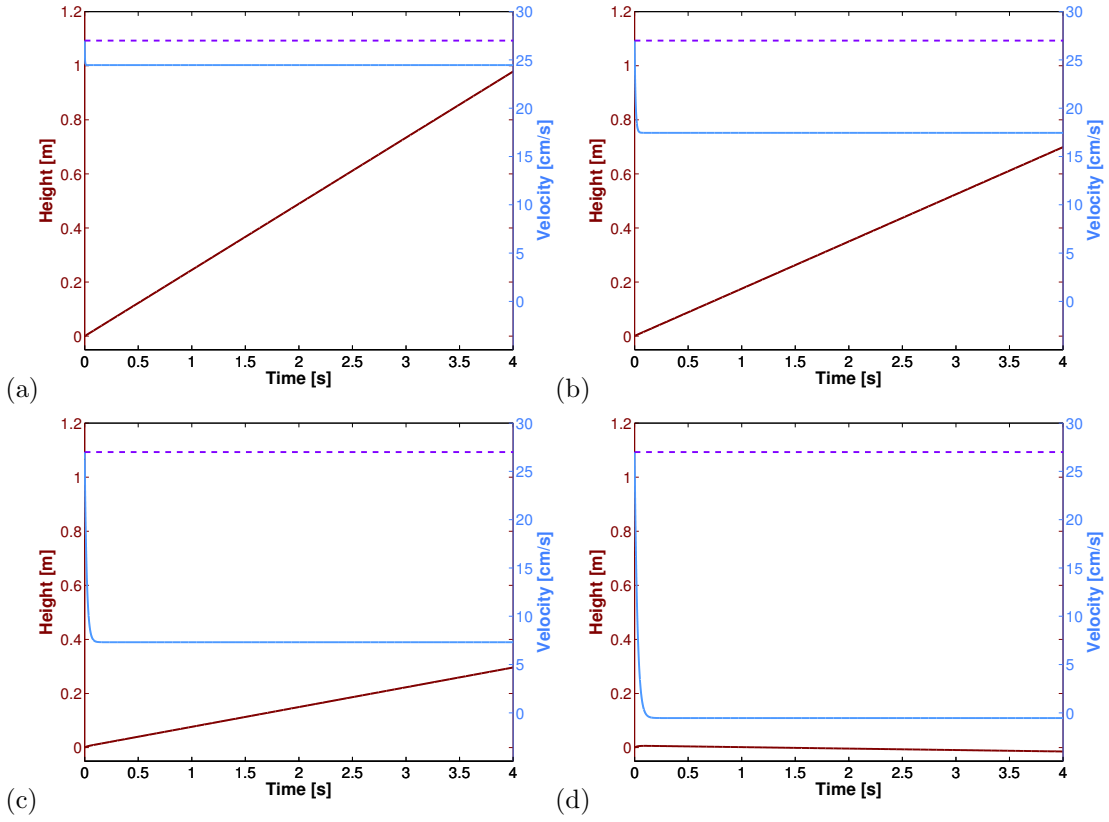

Figure 7.2: Droplet vertical position and velocity as a function of time for different droplet diameter computed with Matlab by solving Eq. 7.1 with $U = 27\,cm/s$. a) $d_d = 30\,\mu m$; b) $d_d = 60\,\mu m$; c) $d_d = 90\,\mu m$; d) $d_d = 110\,\mu m$. The black dashed line represents the velocity co-flow ($U = 27\,cm/s$).

7.5.1.2 One-way coupling

In this section, we simulate the water-mist in presence of a co-flow for a one-way coupling in FireFOAM. Figure 7.3 shows the water-mist droplets distribution at $t = 4\,\mathrm{s}$ with an initial co-flow velocity of $27\,\mathrm{cm/s}$ for different droplet diameters. The maximum height of the droplets achieved in $4\,\mathrm{s}$ increases as the droplets diameter decreases. For $d_d = 110\,\mu\mathrm{m}$, the droplet velocity is near zero and therefore droplets do not move which is consistent with the theory.

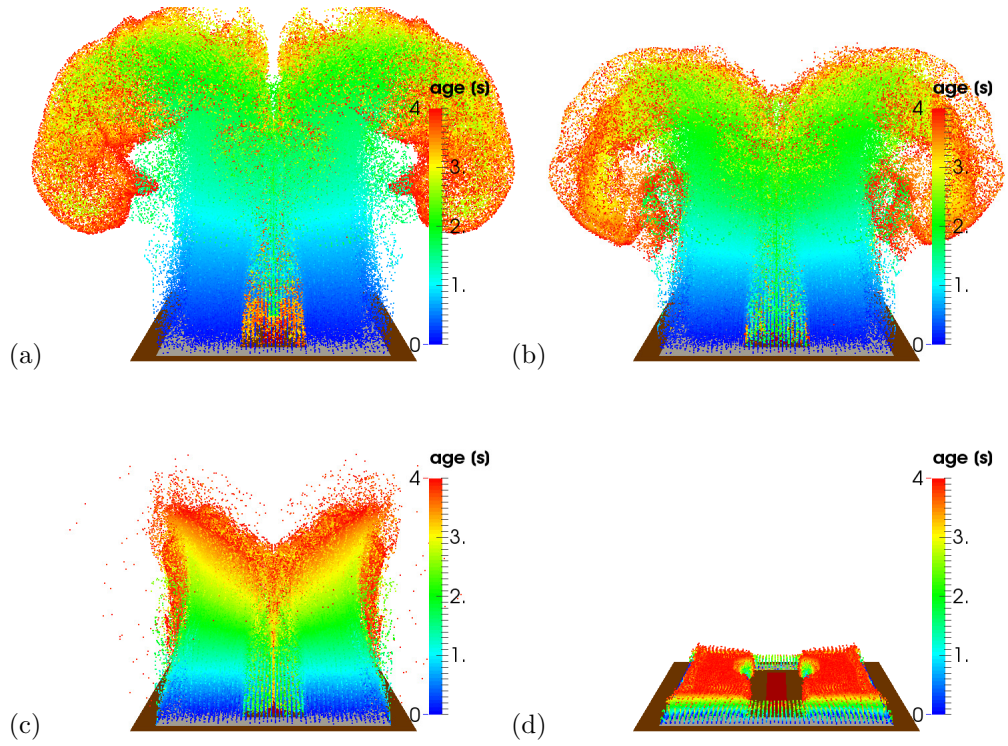

Figure 7.3: Water-mist droplets distribution at $t = 4\,\mathrm{s}$ with an initial co-flow velocity of $27\,\mathrm{cm/s}$ and one way coupling for different droplet diameter. a) $d_d = 30\,\mu\mathrm{m}$; b) $d_d = 60\,\mu\mathrm{m}$; c) $d_d = 90\,\mu\mathrm{m}$; d) $d_d = 110\,\mu\mathrm{m}$.

Figure 7.4 shows the vertical velocity field at $t = 4\,\mathrm{s}$ for different droplet

diameters. In the one-way coupling mode, the gas phase is undisturbed by the liquid phase, which means that for the four different droplet diameter, the velocity field is the same.

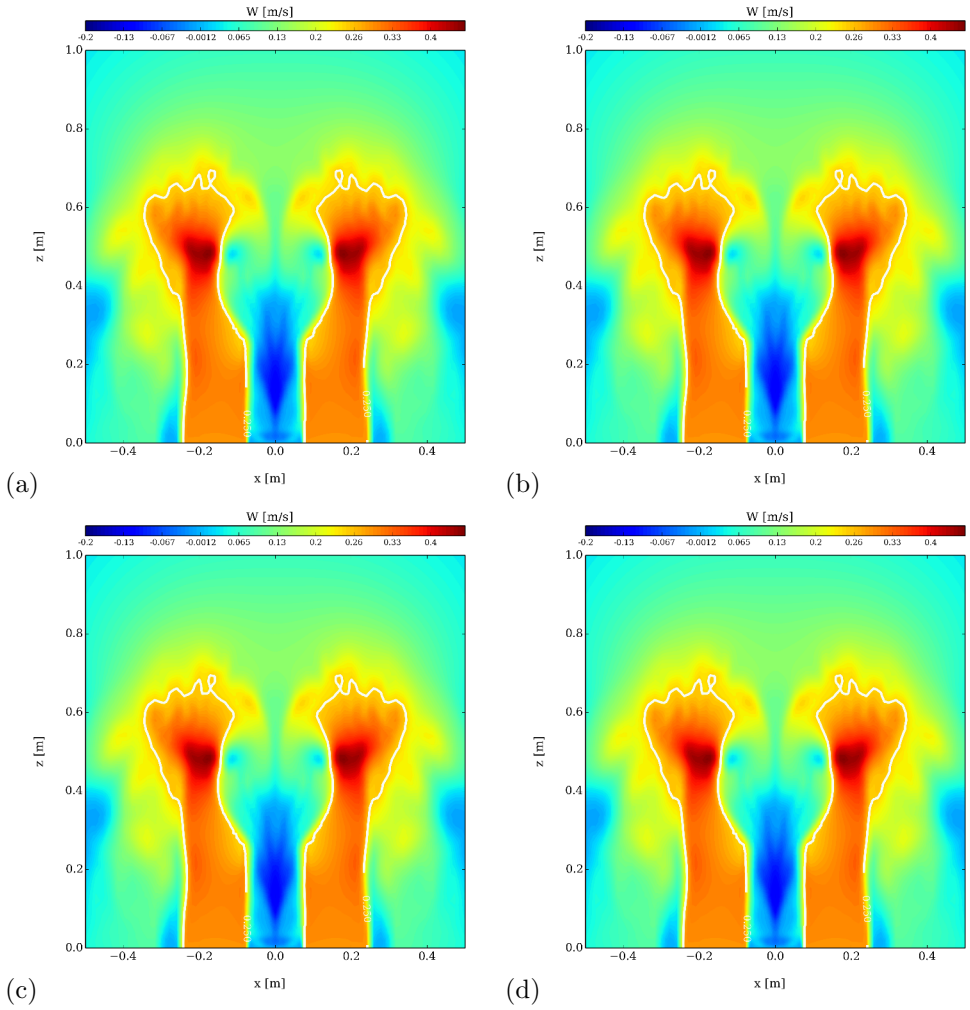

Figure 7.4: Vertical velocity field at $t = 4\,\mathrm{s}$ with an initial co-flow velocity of $27\,\mathrm{cm/s}$ and one way coupling for different droplet diameters. a) $d_d = 30\,\mu\mathrm{m}$; b) $d_d = 60\,\mu\mathrm{m}$; c) $d_d = 90\,\mu\mathrm{m}$; d) $d_d = 110\,\mu\mathrm{m}$.

7.5.1.3 Two-way coupling

Droplet diameter effect

We now turn to a discussion including two-way coupling between the gas and liquid phases. In the two-way coupling mode, momentum exchange between the gas and liquid phase due to drag forces is taken into account. This results in a sudden decreases of the co-flow velocity (Fig. 7.6) resulting in a smaller height achieved by the droplets at 4 s. As a result, 90 µm droplet diameters cannot be carried by the co-flow (Fig. 7.5-c). Note that the momentum relaxation time for water-mist is on the order of a few ms (table 7.1) which means that the droplet will quickly decelerate generating drag forces and momentum exchange near the co-flow boundary (Fig. 7.6).

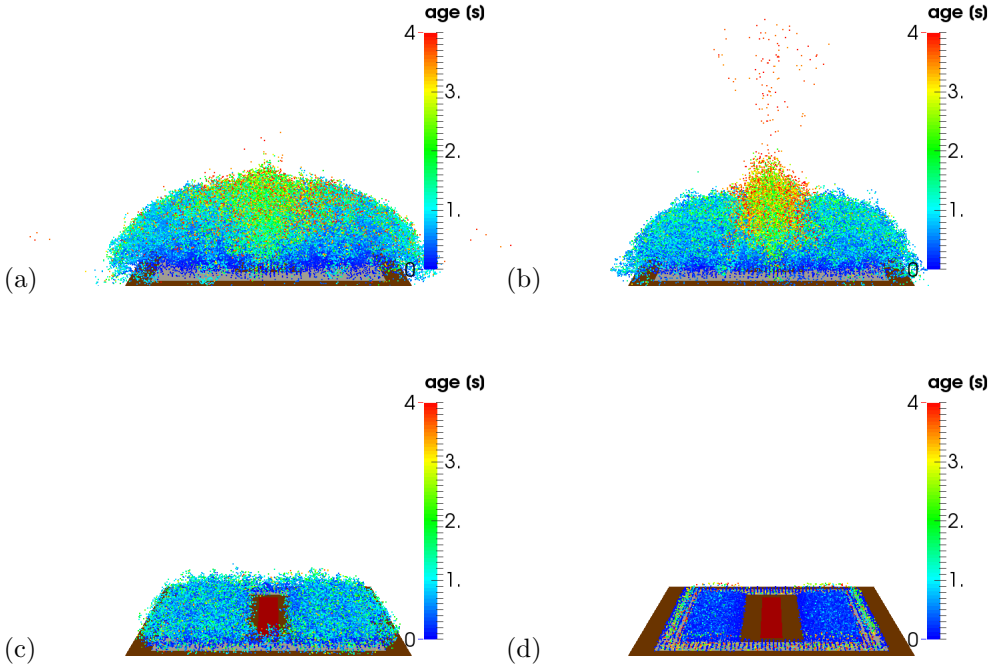

Figure 7.5: Water-mist droplets distribution at $t = 4\,\mathrm{s}$ with an initial co-flow velocity of $27\,\mathrm{cm/s}$ and two way coupling for different droplet diameter. a) $d_d = 30\,\mu\mathrm{m}$; b) $d_d = 60\,\mu\mathrm{m}$; c) $d_d = 90\,\mu\mathrm{m}$; d) $d_d = 110\,\mu\mathrm{m}$.

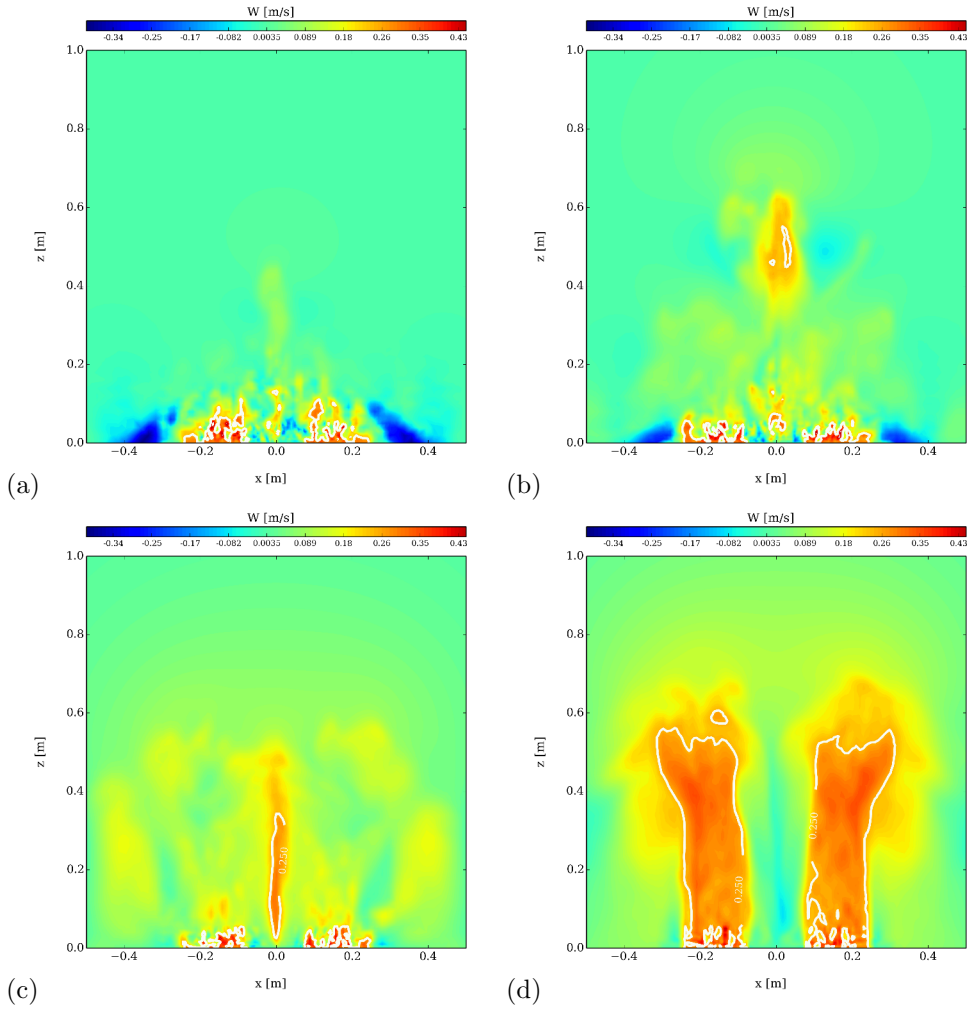

Figure 7.6: Vertical velocity field at $t = 4\,\mathrm{s}$ with an initial co-flow velocity of $27\,\mathrm{cm/s}$ and two way coupling for different droplet diameters. a) $d_d = 30\,\mu\mathrm{m}$; b) $d_d = 60\,\mu\mathrm{m}$; c) $d_d = 90\,\mu\mathrm{m}$; d) $d_d = 110\,\mu\mathrm{m}$.

Water mass flow rate effect

In this section, we study the effect of the water mass flow rate. The momentum exchange between the spray and the co-flow is controlled by the droplet diameter (*i.e.* the total surface area of the water for a given mass flow rate) and the water mass flow rate (*i.e.* the liquid-to-gas mass flow ratio). As the liquid-to-gas mass

ratio decreases, the momentum exchange between the liquid and gas phase decreases and thereby the co-flow can still maintain a velocity close to its initial velocity (Fig. 7.7). For small liquid-to-gas mass flow rate ratio ($\approx 1\%$), the water-mist does not disturb the co-flow and all of the water move upward and can interact with the flame (Fig. 7.7).

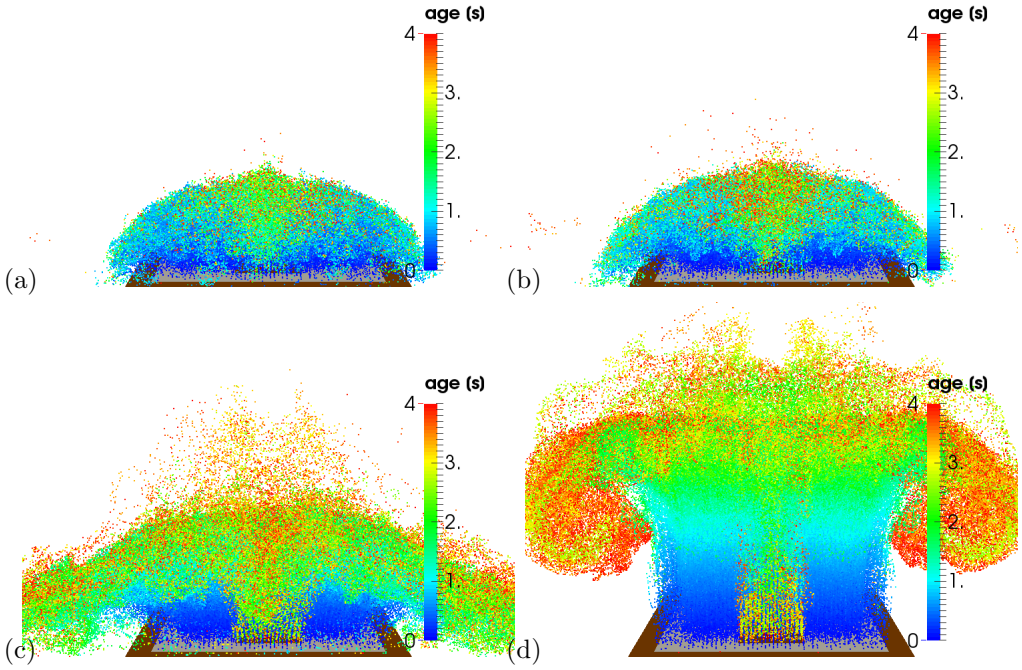

Figure 7.7: Water-mist droplets distribution at $t = 4\,\mathrm{s}$ with an initial co-flow velocity of $27\,\mathrm{cm/s}$ (*i.e.* a mass flow rate of $0.1\,\mathrm{kg/s}$) and two way coupling for different water mass flow rates. a) $\dot{m}_w = 18\,\mathrm{g/s}$; b) $\dot{m}_w = 8\,\mathrm{g/s}$; c) $\dot{m}_w = 4\,\mathrm{g/s}$; d) $\dot{m}_w = 1\,\mathrm{g/s}$.

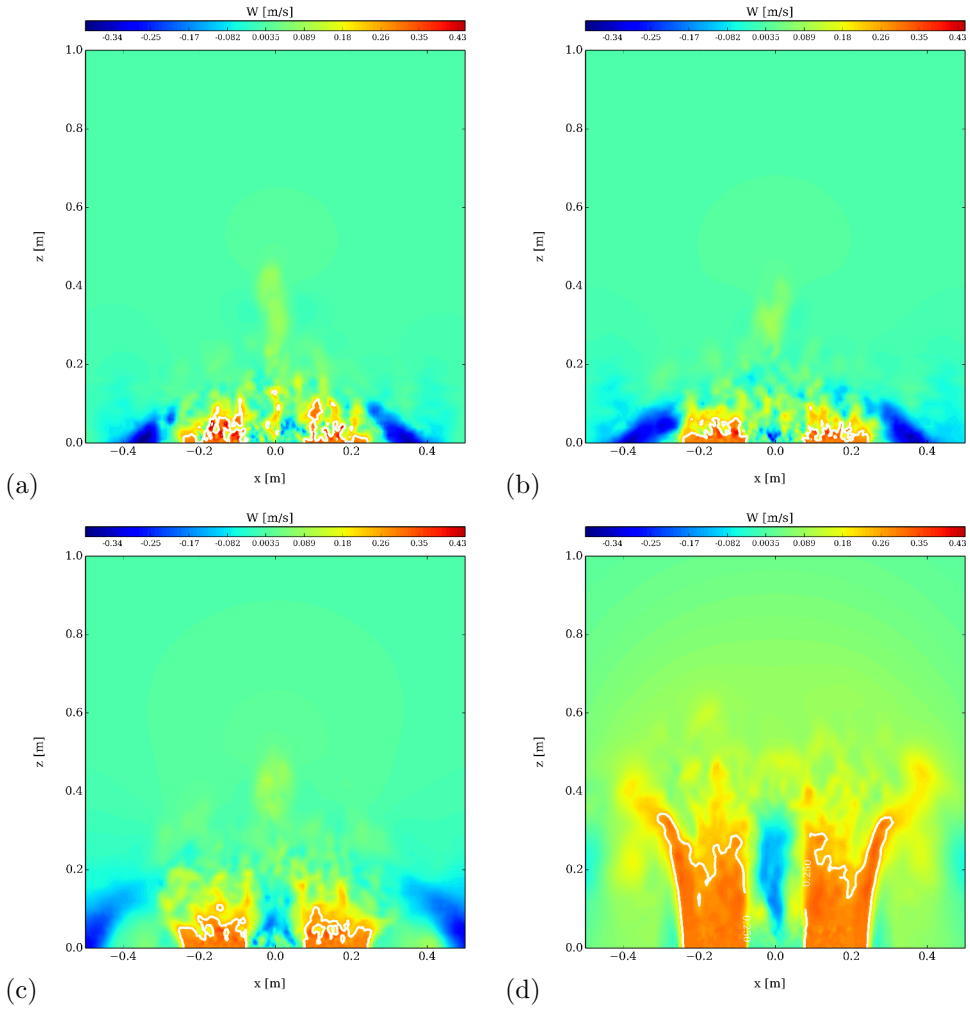

Figure 7.8: Vertical velocity field at $t = 4\ s$ with an initial co-flow velocity of 27 cm/s and two way coupling for different water mass flow rates. a) $\dot{m}_w = 18\,\mathrm{g/s}$; b) $\dot{m}_w = 8\,\mathrm{g/s}$; c) $\dot{m}_w = 4\,\mathrm{g/s}$; d) $\dot{m}_w = 1\,\mathrm{g/s}$.

7.5.2 Heat Transfer Dynamics

The aim of this section is to determine the mass flow rate of water required to extract a certain amount of heat the fire. As reported in table 7.2, each water mass flow rate corresponds to a cooling capacity calculated by multiplying the water mass flow rate, $\dot{m}_w$, by the heat of vaporization, $h_{fg} = 2260\,\mathrm{kJ/kg}$ at $T_{boil} = 373.15\,\mathrm{K}$.

The cooling capacity represents the energy extracted from the fire by evaporation if all of the water evaporates in an ideal scenario.

Table 7.2: Water-Mist configuration.

$\dot{m}_w$	Q_w	**Cooling Capacity**
[g/s]	[kW]	[%]
2	4.52	9.03
4	9.04	18.07
8	18.08	36.14
12	27.12	54.21
18	40.68	81.31

However, only a fraction of the water-mist will interact with the flame and evaporate. Therefore, we need to introduce a new criterion to quantify the exact energy absorbed by the water. Wighus [102] defined the term Spray Heat Absorption Ratio (SHAR), which relates the rate at which heat is absorbed by evaporation of a given mass of water (Q_w), to the rate at which heat is given off by the fire (Q_f).

$$SHAR = \frac{Q_w}{Q_f} = \frac{\dot{m}_{evap} h_{fg}}{\dot{m}_f \Delta H_c} \tag{7.6}$$

Figure 7.9 shows the SHAR value as a function of time in the ideal scenario (everything evaporates) and actual scenario (only based on the evaporation rate). For low water mass flow rate, all of the mist interacts with the flame (Fig. 7.7-d) and all the injected water evaporates (Fig. 7.9-a). For higher water mass flow rates,

not all of the injected water evaporates (Fig. 7.9-b) and in fact a fraction of the liquid water does not interact with the fire and fall on the side (Fig. 7.7-a-b).

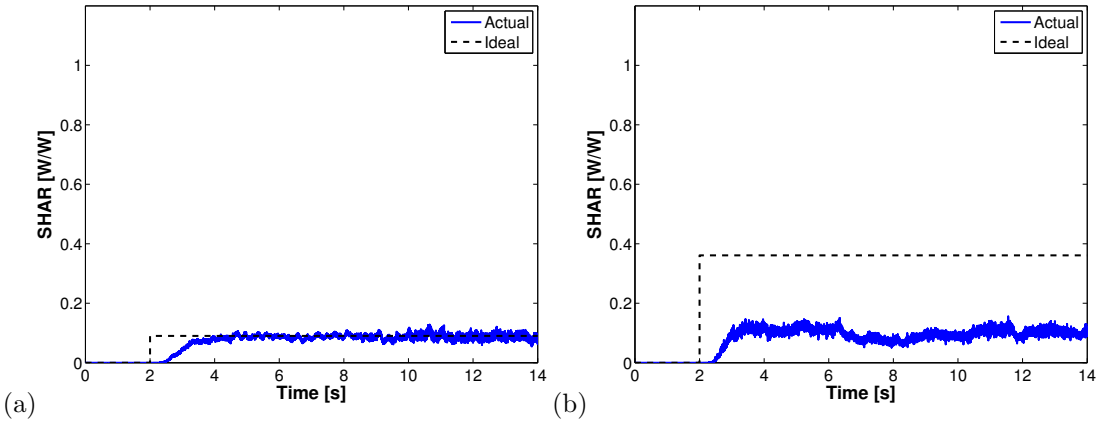

Figure 7.9: SHAR value as a function of time for different water mass flow rates. a) $\dot{m}_w = 2\,\mathrm{g/s}$; b) $\dot{m}_w = 8\,\mathrm{g/s}$.

7.5.3 Extinction

We now turn our discussion to an analysis of the extinction model response to different water mass flow rate conditions, ranging from $\dot{m}_w = 0$ to $18\,\mathrm{g/s}$ corresponding to an ideal cooling capacity ranging from 0 to 80 %. Based on the grid convergence analysis (section 6.3.2), we use a 4 mm mesh resolution.

$\dot{m}_w = 2\ g/s$

We start our discussion with case $\dot{m}_w = 2\ g/s$. This case features local quenching and re-ignition events (Fig. 7.10). Figure 7.10 presents the corresponding variations of the simulated total heat release rate, $HRR = \int_V \left(\dot{\omega}'''_{R1} + \dot{\omega}'''_{R3}\right) \Delta H_c dV$ and the heat release rate only due to non-burning fuel reaction, $HRR^* = \int_V \dot{\omega}'''_{R3} \Delta H_c dV$.

Variations in HRR are compared to the theoretical fuel-limited estimate of HRR, defined as the product of fuel mass loss rate ($\dot{m}_f$) times the heat of combustion(ΔH_c), $HRR_{FL} = \dot{m}_f \times \Delta H_F = 50\,\text{kW}$. We introduce the combustion efficiency (χ_a), defined as the ratio of the time-integrated HRR divided by the time-integrated HRR_{FL},

$$\chi_a = \frac{\int_4^{14} HRR(t')dt'}{\int_4^{14} HRR_{FL}(t')dt'} \tag{7.7}$$

and χ_a^*, the combustion efficiency due to non-burning fuel reaction and defined as:

$$\chi_a^* = \frac{\int_4^{14} HRR^*(t')dt'}{\int_{10}^{14} HRR_{FL}(t')dt'} \tag{7.8}$$

We find $\chi_a = 0.94$, $\chi_a^* = 0.13$ and the SHAR value is around 4%.

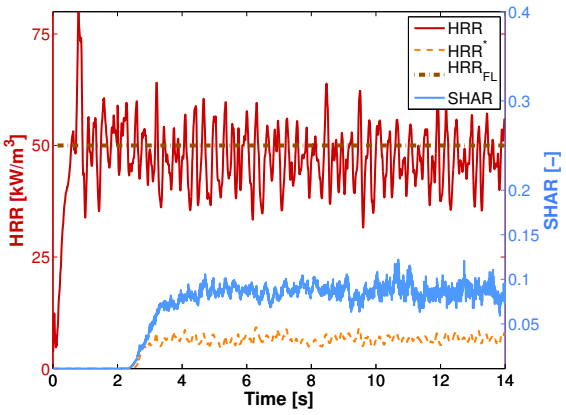

Figure 7.10: Simulated HRR (red dark solid line) and HRR^* (dashed line) compared to its theoretical fuel-limited estimate (brown dashed line) and SHAR value (blue light solid line) for case $\dot{m}_w = 2\,\text{g/s}$.

Figure 7.11 shows the interaction between the water-mist and the flame. For a

relatively low liquid-to-gas mass flow rate ratio ($\approx 2\%$), all the droplets are carried by the co-flow and interact with the flame.

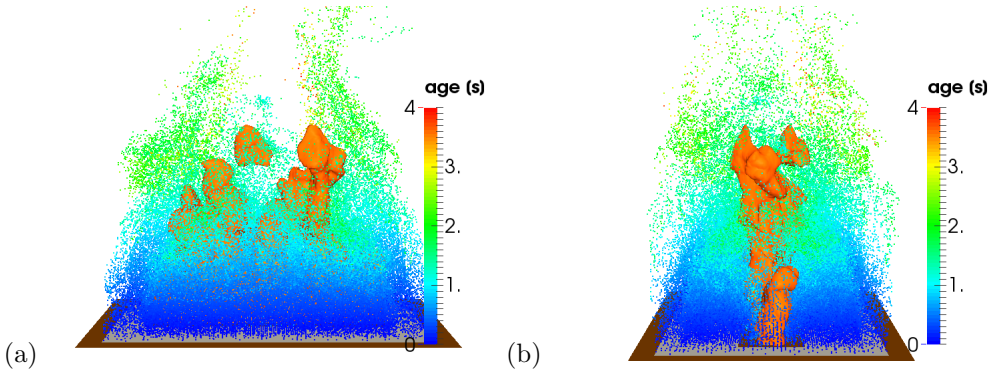

Figure 7.11: Water-mist droplets distribution at $t = 12\,\mathrm{s}$ with the flame identified as an iso-contour of the heat release rate per unit volume; we use $200\,\mathrm{kW/m^3}$. a) front-view; b) end-view.

Figure 7.12 shows the instantaneous temperature and oxygen mole fraction field at $t = 12\,\mathrm{s}$. Due to cooling effect, the flame temperature is reduced by 200 K compared to the ambient condition case (Fig. 6.9) and is about 1,600 K (Fig. 7.12). Note that it is difficult to observe and quantify any local oxygen dilution effects.

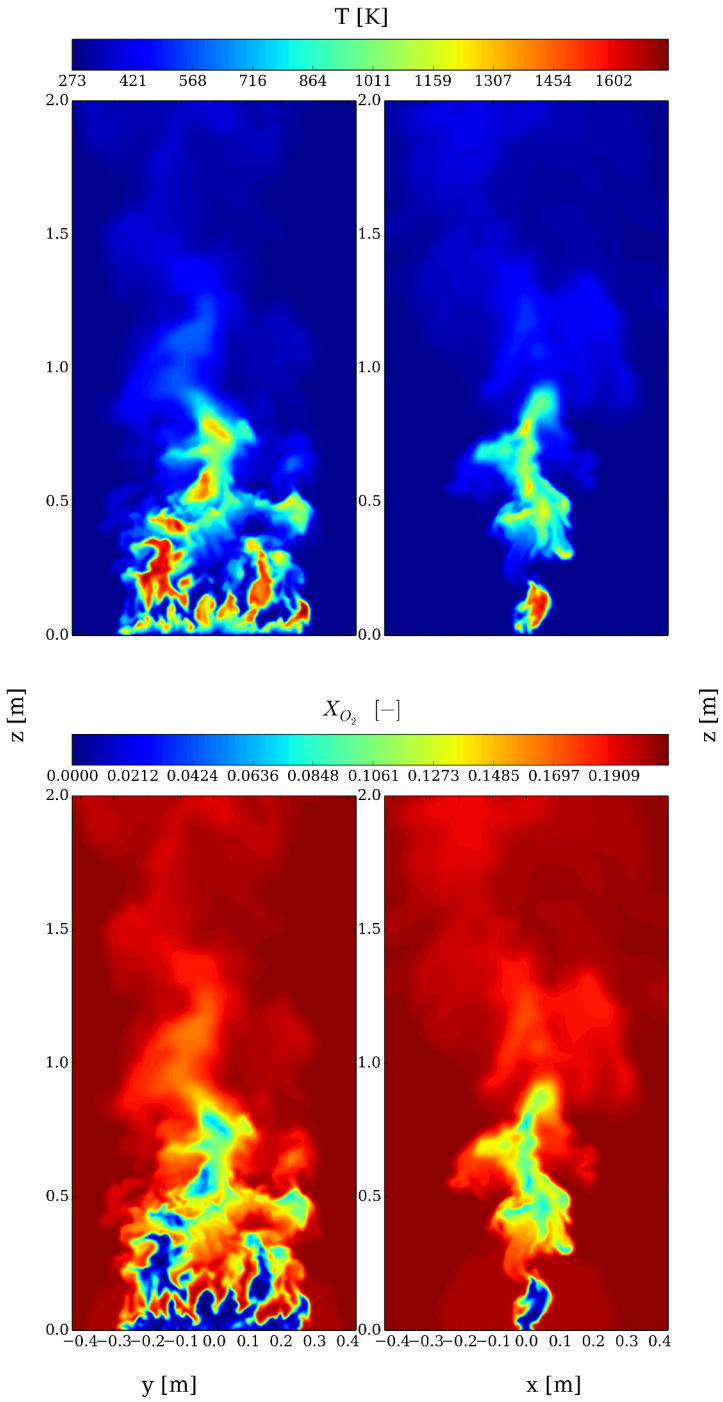

Figure 7.12: Contour map at $t = 12\,\mathrm{s}$. (top) temperature; (bottom) Oxygen mole fraction.

$\dot{m}_w = 18\ g/s$

We now turn to the case $\dot{m}_w = 18\,\mathrm{g/s}$. This case corresponds to full extinctions. HRR drops near zero, indicating that the flame is almost fully extinguished and $\chi_a = 4.6\%$. This suggests that the critical damköhler number extinction model correctly responds (at least qualitatively) to the effect of water evaporative cooling. When the flame is quenched ($t > 4\,\mathrm{s}$), the SHAR value decreases as there is less heat to vaporizes the water.

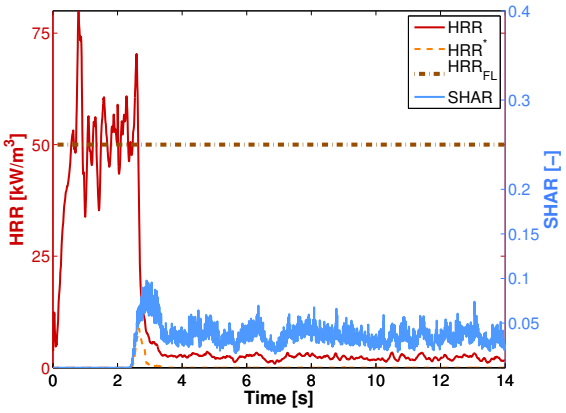

Figure 7.13: Simulated HRR (red dark solid line) and HRR^* (dashed line) compared to its theoretical fuel-limited estimate (brown dashed line) and SHAR value (blue light solid line) for case $\dot{m}_w = 18\,\mathrm{g/s}$.

Figure 7.14 shows the interaction between the water-mist and the flame. In this case, the flame is quenched. For a relatively high liquid-to-gas mass flow rate ratio ($\approx 18\%$), some of the droplets fall on the side and the co-flow is only able to carry a fraction of the water.

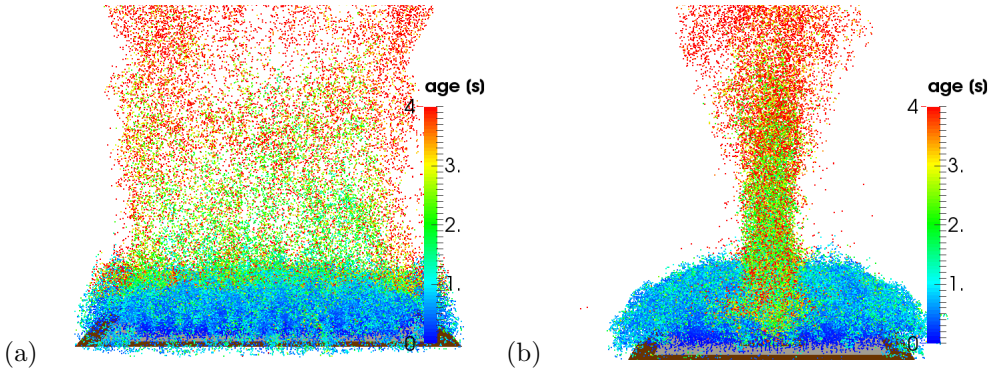

Figure 7.14: Water-mist droplets distribution at $t = 12\,\mathrm{s}$ with the flame identified as an iso-contour of the heat release rate per unit volume; we use $200\,\mathrm{kW/m^3}$. (a) front-view; (b) end-view.

Figure 7.15 shows the instantaneous temperature and oxygen mole fraction field at $t = 12\,\mathrm{s}$. The flame is quenched and the flame temperature has dropped to the ambient temperature. As suggested by the combustion efficiency $\chi_a = 4.6\%$, small pockets of fuel are still burning near the burner. Note that those pockets of fuel are burning at a relatively low temperature ($\approx 700\,\mathrm{K}$). This is a limitation of the current combustion model. The EDC combustion model is based on mixing and does not have any ignition model. Therefore, to reach complete extinction ($\chi_a = 0$), significant heat losses due to evaporation cooling has to occur in each cell of the domain containing fuel and oxygen. The re-ignition model based on a cell temperature criterion only applies on the non-burning fuel and not on the fresh fuel coming out of the burner.

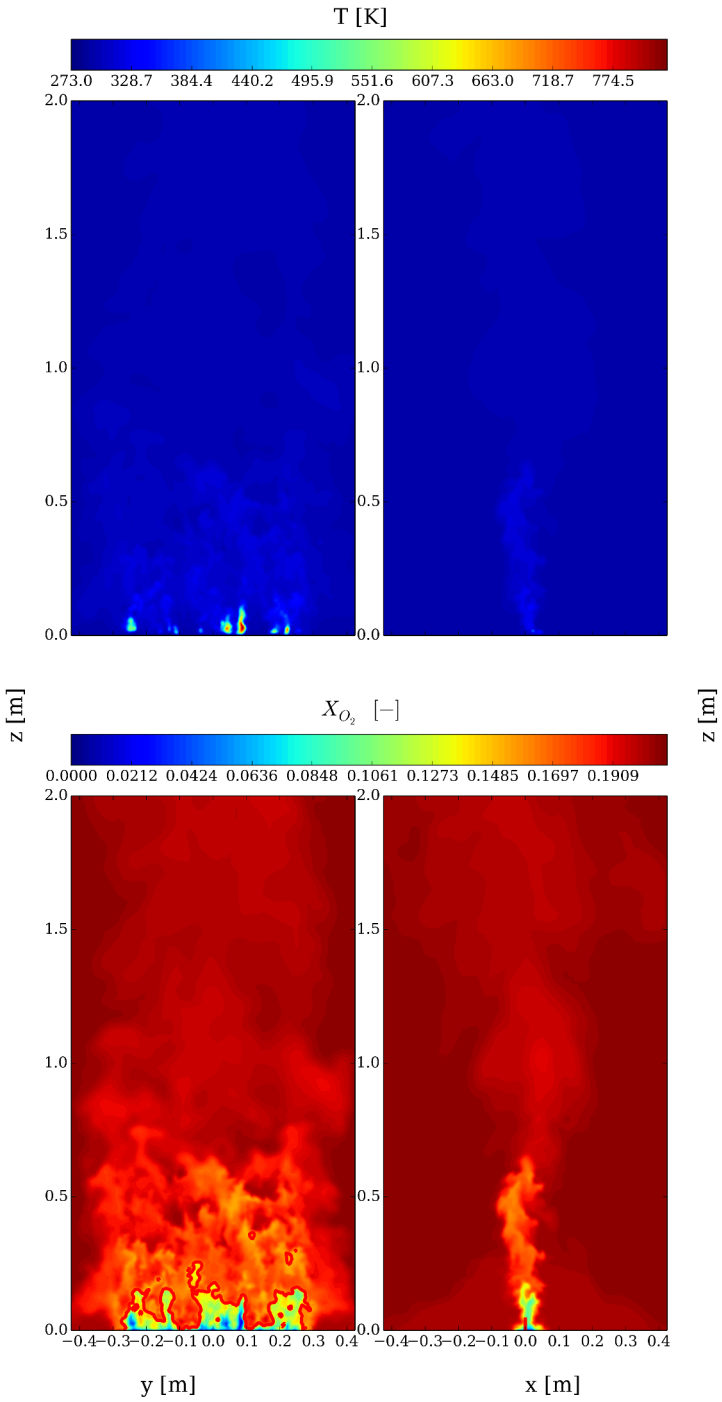

Figure 7.15: Contour map at $t = 12\,\mathrm{s}$. (top) temperature; (bottom) Oxygen mole fraction.

We can now present in Fig. 7.16 the combustion efficiency as function of $\dot{m}_w$. The dark blue area represents the combustion efficiency only due to reaction R1 (fuel), and the light red area, the combustion efficiency due to reaction R3 (non-burning fuel). We observe a gradual reduction in the combustion as $\dot{m}_w$ increases. The flame experiences more extinction events as the water mass flow rate increases (the dark blue area decreases), and the number of re-ignition events increases as $\dot{m}_w$ decreases until $\dot{m}_w = 4\,\mathrm{g/s}$ (the light red area increases). However at higher water mass flow rate ($\dot{m}_w > 4\,\mathrm{g/s}$), the cell temperature is so low ($< 1100\,\mathrm{K}$) that none of the non-burning fuel re-ignites. Note also that in the evaporative cooling quenching scenario, the re-ignition plays a reduced role compared to the oxygen dilution quenching case (chapter 6). One possible explanation is that when the water evaporates and locally quenches the flame, it also cools down the plume. Note that as the water mass flow rate increases the SHAR remains constant ($SHAR \approx 15-20\%$). However, the combustion efficiency is decreasing for a constant SHAR value. One possible explanation is that as the mass flow rate increases, the water-mist interacts with the flame at a lower elevation, *i.e.* near the burner which corresponds to the peak HRR, and therefore is more effective to quench the flame at its weakest point. Note that the SHAR value for full flame extinction is lower than those reported in the literature, *i.e.* $SHAR \approx 30\%$ [1].

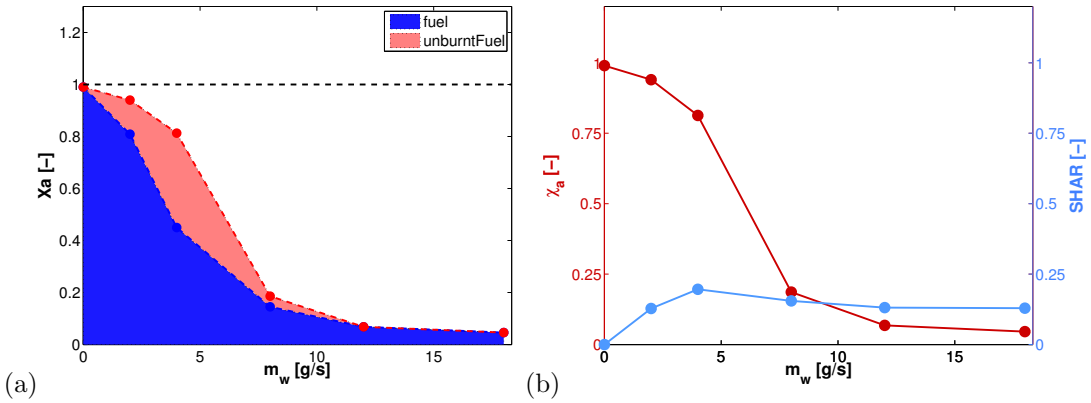

Figure 7.16: a) Combustion efficiency as function of water mass flow rate for $d_d = 30\,\mu m$. The dark blue (light red) area represents the heat release rate due to reaction of fresh fuel R1 (non-burning fuel R3). The dashed line corresponds to complete combustion, *i.e.* $\chi_a = 1.0$. b) Combustion efficiency and SHAR value as as function of water mass flow rate for $d_d = 30\,\mu m$.

Droplet diameter effect

Next, we focus on the droplet diameter effect on evaporation rate and on combustion efficiency. Figure 7.17-a shows the combustion efficiency for reaction R1 and R3 as function of water mass flow rate for a 60 µm droplet. The combustion efficiency gradually decreases, but does not drop to zero at $\dot{m}_w = 18\,g/s$, $\chi_a = 0.29$. As the droplet diameter increases, the evaporation rate decreases and the SHAR value decreases (Fig. 7.17-b). This illustrates that at least qualitatively, the extinction model is sensitive to the droplet diameter and its consequence on the evaporation rate, which is consistent with [1].

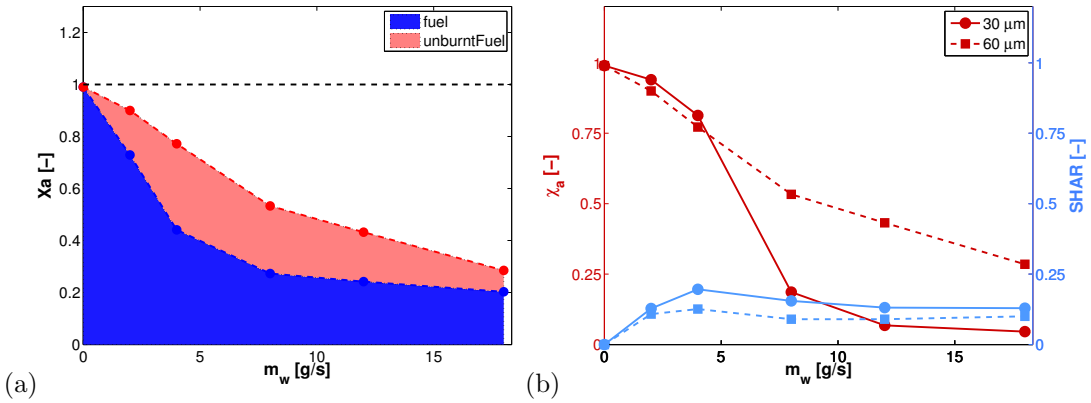

Figure 7.17: a) Combustion efficiency as function of water mass flow rate for $d_d = 60\,\mu m$. The dark blue (light red) area represents the heat release rate due to reaction of fresh fuel R1 (non-burning fuel R3). The dashed line corresponds to complete combustion, *i.e.* $\chi_a = 1.0$. b) Combustion efficiency and SHAR value as as function of water mass flow rate for $d_d = 30\,\mu m$ and $d_d = 60\,\mu m$.

7.6 Conclusion

This chapter presents a numerical study of a turbulent, methane-fueled, buoyancy-driven, diffusion flame exposed to air-water-mist co-flow. The present study is aimed at evaluating the ability of LES fire models to accurately describe flame response to a range of water mass flow rate and cooling capacity conditions, as well as transition from extinction-free conditions to partial or total quenching. LES results indicate that the flame extinction model in FireFOAM based on the concept of a critical Damköhler number responds correctly, at least qualitatively, to thermal quenching due to evaporative cooling. Results also indicate that full flame extinction is predicted at low SHAR value ($SHAR \approx 15-20\%$) and is lower than the value reported in the literature, *i.e.* $SHAR \approx 30\%$ [1]. This will be investigated in future work by

computing the local evaporation rate, plotted as a function of height to verify if the flame is attacked at its weakest point, *i.e.* the flame base.

8 Conclusion & Future Work

Fire dynamics is a multi-phase (gas, solid for the pyrolysis and liquid for the spray), multi-scale and multi-physics phenomenon (pyrolysis, turbulent flow, combustion, soot, thermal radiation, etc). CFD-based simulations are challenging because of the stringent requirements associated with an accurate treatment of turbulence and combustion, and the associated need to limit numerical dissipation at resolved scales. These challenges were addressed in chapter 3. In this chapter were developed a series of benchmark tests and the numerical performance of FireFOAM-2.2.x, an advanced Large Eddy Simulation (LES) fire modeling software developed by FM Global, was evaluated.

The success of those verification tests have drawn a reliable numerical framework to implement the new extinction model based on the concept of a critical Damköhler number which was described in chapter 4. The Damköhler number contains information on the intensity of the fuel-air mixing process, the magnitude of the flame heat losses, and the composition and heat content of the fuel and oxidizer supply streams; and a critical-Damköhler-number based flame extinction criterion thereby provides a description of the influence of mixing rates, flame temperature, and air and fuel vitiation. In the context of suppression by nitrogen and water spray systems, the

Damköhler accounts for effects of both oxygen displacement and evaporative cooling.

Chapter 5 was aimed at evaluating the ability of current CFD-based fire models to simulate compartment fires under poorly ventilated conditions. This study considers four cases that were taken from a previously developed experimental database and are representative of four different flame behaviors, *i.e.*, steady over-ventilated fires, steady under-ventilated fires, unstable fires with partial flame quenching, transient fires leading to total flame quenching. The numerical simulations were performed with FireFOAM and used a new flame extinction model presented in chapter 4 as well as a thermally-driven fuel evaporation model presented in section 5.4.1. Overall, the agreement between experimental and computational results is good and shows that current CFD-based fire models are capable of describing (at least qualitatively and to a certain extent, as documented in section 5.5, quantitatively) the transition from over- to under-ventilated fire conditions, as well as the transition from extinction-free conditions to conditions in which the flame experiences quenching.

The suppression of a buoyant, turbulent, methane diffusion flame via nitrogen dilution quenching was presented in chapter 6. This simulation evaluates the ability of LES fire models to accurately describe flame response to a range of oxygen dilution conditions, as well as transition from extinction-free conditions to partial or total quenching. The agreement between experimental data and numerical results is good and within the experimental uncertainties with $Da_c = 1.0$ and $T_{ign} = 1100\,\mathrm{K}$, it indicates that the flame extinction model in FireFOAM based on the concept of a critical damköhler number responds correctly, qualitatively and quantitatively, to

oxygen dilution effects, as shown by the combustion efficiency versus oxygen mole fraction curve.

A numerical study of a turbulent, methane-fueled, buoyancy-driven, diffusion flame exposed to air-water-mist co-flow was presented in chapter 7. The goal of this simulation was to evaluate the ability of LES fire models to accurately describe flame response to a range of water mass flow rate and cooling capacity conditions, as well as transition from extinction-free conditions to partial or total quenching. LES results have indicated that the flame extinction model in FireFOAM responds correctly, at least qualitatively, to thermal quenching due to evaporative cooling. Results also indicate that full flame extinction is predicted at low SHAR value ($SHAR \approx 15-20\%$) and is lower than the value reported in the literature, *i.e.* $SHAR \approx 30\%$ [1]. The investigation of this discrepancy is left as future work.

The turbulent line burner via nitrogen dilution or water-mist quenching represents a benchmark test to validate extinction models. Other extinction model such as the one based on the concept of a critical value of the flame temperature should be tested in this configuration and is the purpose of an on-going effort.

A Interview from fire safety engineers

Most commercial applications of CFD have been restricted to the assessment of smoke control design strategies particularly in large buildings. It is in these kinds of structures where the traditional building regulations are often not readily applicable and an engineered solution is required. Covered shopping malls, atrium hotels, leisure complexes, airport and railway terminals are just some examples of where the technology is finding its utility for the practicing engineer. Often these structures are unique in nature (*e.g.*, the Millennium Dome in London), but increasingly the fire models are being used for more routine problems [1].

Through a series of interview from industrial experts (*i.e. building construction, vehicles design, etc*), we will try to understand how those fire modeling softwares such as FDS or FireFOAM are used by the industry and by fire safety engineers.

Christine Pongratz, Fire Engineer, P.E., MS., Arup (UK)

1. **What is your position inside the company?**

   I am a fire safety engineer for Arup.

2. **What is your duty? Could you describe in a few words your job (give an example if possible)?**

A fire safety engineer is a design consultant. We apply science and engineering principles to protect people and property from harmful and destructive effects of fire and smoke. As an example, I utilize tools such as Fire Dynamic Simulator (FDS) to model fire and smoke propagation to inform the design for a smoke exhaust system in apartment corridors and atria.

3. **Which fire modeling software do you use?**

   Our team uses Fire Dynamic Simulator (FDS) developed by NIST, for fire and smoke modeling. We also use LS DYNA for finite element modeling for structural analysis under fire conditions. In addition, we use MassMotion for human evacuation modeling.

4. **How often and how do you use fire modeling software for your work?**

   We use it often, depending on our project work. We offer our clients the option of our CFD analysis knowledge to optimize design and meet client goals which cannot be satisfied by prescriptive code-based solutions.

5. **What are the current limitations of fire modeling software?**

   How the implementation of an extinction model, capable of simulating quenching by dilution like in under-ventilated fires applications or thermal quenching like in water-mist applications, into current fire models could impact your work?

   When we have a compartment fire, we often experience results which do not portray a true fire. For example, in under-ventilated cases it is often difficult to prescribe the appropriate heat release rate in the input code. Often if the fire

becomes under-ventilated then the simulation results shows the combustion zone occurring around the ventilation zones such as doors or leakage holes. However, looking at results on heat release rate output file and vent mass flow rate, it is clear that the conditions are severely under-ventilated and simulated incorrectly. An extinction model which more appropriately compute the heat release rate input [*i.e.* accurate modeling of thermal heat feedback and solid pyrolysis] and output data [*i.e.* vent mass flow rate] would greatly improve modeling accuracy and remove the need for numerous trial/error models.

6. **What do you do when the fire propagation or re-ignition at the door is not computed correctly?**

   We just reduce the HRR to make it so the conditions are not under-ventilated, so it's like trial and error to get it right.

7. **Which means you are not interested about scenario where the flame re-ignites at the vent. But you only care about smoke management, is it right?** Yes, in that case, all we care about is smoke clearance in the hallways. If anything the apartment fire is just a boundary condition of what we truly care about.

Dr. Fabian Bräanström, Thermodynamic Engineer, Ph.D., Bombardier Transportation (Germany)

1. **What is your position inside the company?**

   I am a thermodynamics expert in the Aero and Thermodynamics Center of Com-

petence.

2. **What is your duty?**

   I am working for general CFD methods development and for the last 2 to 3 years I focused on methods development for fire simulations.

3. **Could you describe in a few words your job (give an example if possible)?**

   Fire simulations involve for us calculation of heat release rate curves of compartments [*i.e.* growth, fully developed and decay stage] and estimation of peak heat release rate, as well as evaluation of temperatures within electrical cabinets in case of fire.

4. **Which fire modeling software do you use?**

   The work is currently done with Star-CCM+ and FDS; FireFOAM is planned.

5. **What are the current limitations of fire modeling software?** Concerning FireFOAM, a better documentation, *e.g.* clear statements of version in articles, some validation cases (see FDS); if possible collect [them] in git repository, possibility of adaptive mesh refinement to reduce simulation time.

   For FDS, a better parallel handling and scalability, options to export in common post-process format (*e.g.* vtk, ensight), improvement of meshing capabilities such as handling of complex geometries, immersed boundary conditions, STereoLithography (STL) file import, import snappyHexMesh mesh (cartesian) and use of non-isotropic mesh refinements for complex geometries. Finally for

Star-CCM+, pyrolysis modeling is missing and as well as the absence of special radiative fraction treatment for coarse flames.

6. **How the implementation of an extinction model, capable of simulating quenching by dilution like in under-ventilated fires applications or thermal quenching like in water-mist applications, into current fire models could impact your work?**

   For peak heat release rate in case of flash-over, this is helpful.

Dr. Virginie Drean, Research Engineer, Ph.D., Efectis (France)

1. **What is your position inside the company?**

   I am a research engineer working for the innovation and development group.

2. **What is your duty?**

   I am working as support and link between our fire laboratory department and our fire safety engineering team.

3. **Could you describe in a few words your job (give an example if possible)?**

   My job is to help developing fire testing facilities with numerical simulations, and to provide optimization and developments for protection materials. I also perform *R&D* support for engineering: codes validation, special sensitivity studies, codes cross-comparison, fire modeling. I have to be able to model different physical phenomena : pyrolysis, thermal heat transfer, radiation, suppression, smoke propagation. I also do fire engineering studies.

4. **Which fire modeling software do you use?**

   I am using FDS, CFAST [zone model], CFX, and OpenFOAM/FireFOAM. I am using different models depending on the problems. CFAST for preliminary studies, FDS for full scale smoke or fire spread studies, CFX or OpenFoam for specific studies : evaluation of pressure drop, heat transfer, convective coefficients.

5. **How often and how do you use fire modeling software for your work?**

   Every day. Each software is installed on each computer and we work locally, with no access to cluster or other computer.

6. **What are the current limitations of fire modeling software?**

   The main limitations of fire modeling software in my job are meshing scales, and model hypothesis as low Mach number, turbulence, and radiation [prescribed radiant fraction].

7. **How the implementation of an extinction model, capable of simulating quenching by dilution like in under-ventilated fires applications or thermal quenching like in water-mist applications, into current fire models could impact your work?**

   This could greatly help in fire safety engineering studies when suppression is activated. Actually, we only develop artifacts to reproduce extinction or dilution, based on several experimental measurements of heat release rates while sprinklers are activated : we reduce this fire parameter [fuel mass loss rate] when water is delivered.

B Wide-Band Model Polynomial Coefficient

Curve fits for the Planck mean absorption coefficients for H_2O, CO_2, CH_4 and CO are given below as functions of temperature from 250 K (`Tlow`) to 3000 K (`Thigh`). These are fits to results from narrow-band results using the RadCal program [103, 104] and equation B.3. A fifth-order polynomial in temperature, T (or inverse temperature, $1/T$) is used and separated into two temperature ranges by `Tcommon`. `loTcoeffs` denotes polynomial coefficient for $T < T_{common}$ and `hiTcoeffs` denotes polynomial coefficient for $T > T_{common}$. `invTemp = false` means $X = T$ `invTemp = true` means $X = 1/T$.

$$a_{p,i} = c_0 + X(c_1 + X(c_2 + X(c_3 + X(c_4 + c_5 X)))) \tag{B.1}$$

In RadCal, the Planck mean coefficient for a given band, denoted here $\overline{\kappa}_i$, is calculated by:

$$\overline{\kappa}_i = \frac{\int_{\omega_{min}}^{\omega_{max}} I_{b,\omega}(T_g)\kappa_{i,\omega} d\omega}{\int_0^{\infty} I_{b,\omega}(T_g) d\omega} \tag{B.2}$$

$$\overline{\kappa}_i = \frac{\pi}{\sigma T_g^4} \int_{\omega_{min}}^{\omega_{max}} I_{b,\omega}(T_g) \kappa_{\omega,i} d\omega \tag{B.3}$$

where $\overline{\kappa_\omega}$ is the narrow-band absorption coefficient of participating species i, in units of $atm^{-1}.m^{-1}$. Note the the temperature used in this expression is the local gas temperature; thus $\overline{\kappa_i}$ is a function of the gas phase temperature. It is independent of the path physical length. Its units are in $atm^{-1}.m^{-1}$. The integration bounds, ω_{min} and ω_{max} are defined in table 2.1.

B.1 H_2O

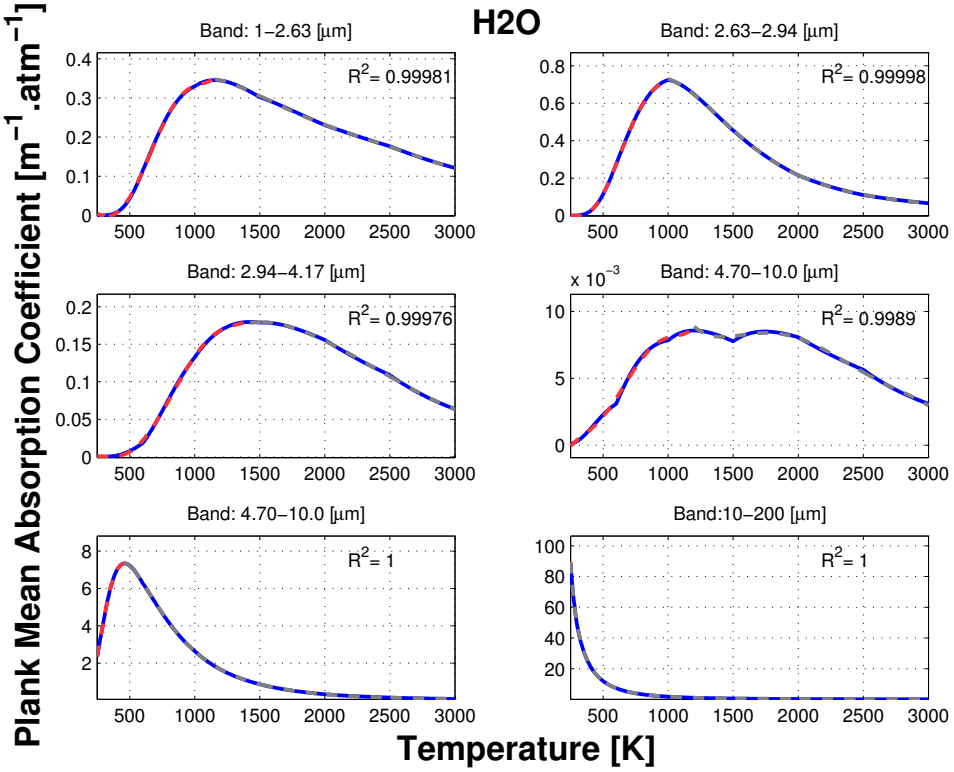

Figure B.1: Planck Mean Absorption coefficient from RadCal for a 6 bands wide-band model for specie H_2O. Blue solid line denotes the RadCal results, red dashed line the polynomial fit for the low temperature range and grey dashed line the polynomial fit for the high temperature range.

```
Band: 1-2.63e-6 [m]
H2O
{
   Tcommon       1155;
   Tlow          250;
   Thigh         3000;
   invTemp       false ;
   loTcoeffs ( -0.045956 0.0012817 -8.0959e-06 1.9122e-08 -1.7325e-11 5.394e-15
);
   hiTcoeffs ( -1.1227 0.0040632 -4.1736e-06 2.0055e-09 -4.6797e-13 4.269e-17
);
```

```
}
Band: 2.63-2.94e-6 [m]
H2O
{
   Tcommon       1000;
   Tlow          250;
   Thigh         3000;
   invTemp       false ;
   loTcoeffs ( -0.65784 0.0083393 -3.8829e-05 8.0588e-08 -7.1667e-11 2.2957e-14
);
   hiTcoeffs ( -2.7059 0.010507 -1.157e-05 5.7185e-09 -1.3415e-12 1.22e-16
);
}
Band: 2.94-4.17e-6 [m]
H2O
{
   Tcommon       1425;
   Tlow          250;
   Thigh         3000;
   invTemp       false ;
   loTcoeffs ( -0.070903 0.000789 -3.1407e-06 5.394e-09 -3.7493e-12 9.1198e-16
);
   hiTcoeffs ( -0.8684 0.0021283 -1.6535e-06 6.3103e-10 -1.2482e-13 1.0294e-17
);
}
Band: 4.70-10.0e-6 [m]
H2O
{
   Tcommon       1200;
   Tlow          250;
   Thigh         3000;
   invTemp       false ;
   loTcoeffs ( -0.0092732 8.5528e-05 -3.0738e-07 5.5286e-10 -4.4203e-13 1.2834e-16
);
   hiTcoeffs ( 0.21363 -0.00051838 5.0678e-07 -2.3952e-10 5.477e-14 -4.8806e-18
);
}
Band: 4.70-10.0e-6 [m]
H2O
{
   Tcommon       460;
   Tlow          250;
   Thigh         3000;
   invTemp       true ;
   loTcoeffs ( -8.7485 4214.8 1.2403e+07 -8.5082e+09 1.9212e+12 -1.4795e+14
);
   hiTcoeffs ( 0.62915 -3430.3 4.7539e+06 3.3668e+09 -3.3526e+12 6.6006e+14
);
}
Band:10-200e-6 [m]
H2O
{
   Tcommon       250;
```

```
   Tlow          250;
   Thigh         3000;
   invTemp       true ;
   loTcoeffs ( 88.67 0 0 0 0 0  );
   hiTcoeffs ( -0.34423 1778.3 -3.21e+06 4.7318e+09 -1.3658e+12 1.7636e+14
);
}
```

B.2 CO_2

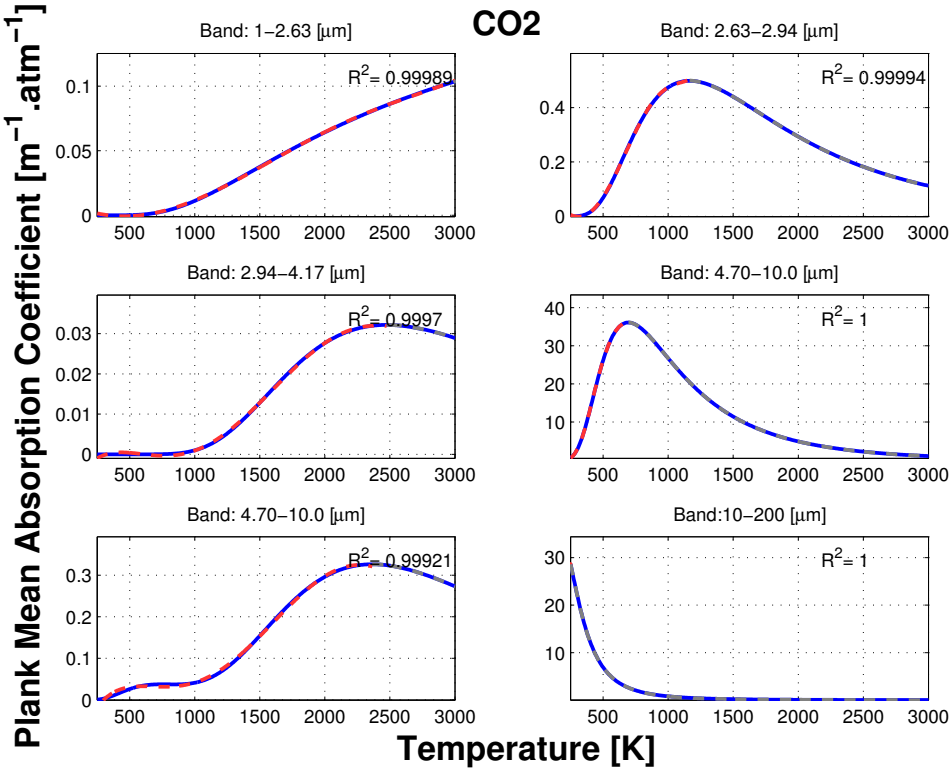

Figure B.2: Specie CO_2, see caption for Fig. B.1.

```
Band: 1-2.63e-6 [m]
CO2
{
   Tcommon       3000;
   Tlow          250;
   Thigh         3000;
   invTemp       false ;
```

```
   loTcoeffs ( 0.010259 -4.8621e-05 5.4466e-08 2.2701e-12 -8.1706e-15 1.4415e-18
);
   hiTcoeffs ( 0 0 0 0 0 4.2633e-19  );
}
Band: 2.63-2.94e-6 [m]
CO2
{
   Tcommon       1165;
   Tlow          250;
   Thigh         3000;
   invTemp       false ;
   loTcoeffs ( 0.017287 0.00074619 -6.6395e-06 1.7598e-08 -1.6258e-11 5.0096e-15
);
   hiTcoeffs ( -2.0454 0.0064599 -6.0545e-06 2.6329e-09 -5.5746e-13 4.6645e-17
);
}
Band: 2.94-4.17e-6 [m]
CO2
{
   Tcommon       2475;
   Tlow          250;
   Thigh         3000;
   invTemp       false ;
   loTcoeffs ( -0.012346 8.0119e-05 -1.75e-07 1.5816e-10 -5.7186e-14 7.1697e-18
);
   hiTcoeffs ( -10.844 0.019422 -1.3877e-05 4.9589e-09 -8.8607e-13 6.3292e-17
);
}
Band: 4.70-10.0e-6 [m]
CO2
{
   Tcommon       695;
   Tlow          250;
   Thigh         3000;
   invTemp       true ;
   loTcoeffs ( -291.73 6.588e+05 -4.8778e+08 1.6636e+11 -2.7185e+13 1.7322e+15
);
   hiTcoeffs ( 3.3639 -22862 2.7108e+07 9.3093e+10 -1.0018e+14 2.6204e+16
);
}
Band: 4.70-10.0e-6 [m]
CO2
{
   Tcommon       2365;
   Tlow          250;
   Thigh         3000;
   invTemp       false ;
   loTcoeffs ( -0.21227 0.0012587 -2.3578e-06 1.9367e-09 -6.6266e-13 7.9165e-17
);
   hiTcoeffs ( 2.5704 -0.0065079 6.2235e-06 -2.69e-09 5.4609e-13 -4.275e-17
);
}
Band:10-200e-6 [m]
```

```
CO2
{
   Tcommon       250;
   Tlow          250;
   Thigh         3000;
   invTemp       true ;
   loTcoeffs ( 28.678 0 0 0 0 0  );
   hiTcoeffs ( -0.29781 1693.6 -3.5152e+06 3.6978e+09 -8.4162e+11 5.5835e+13
);
}
```

B.3 CH4

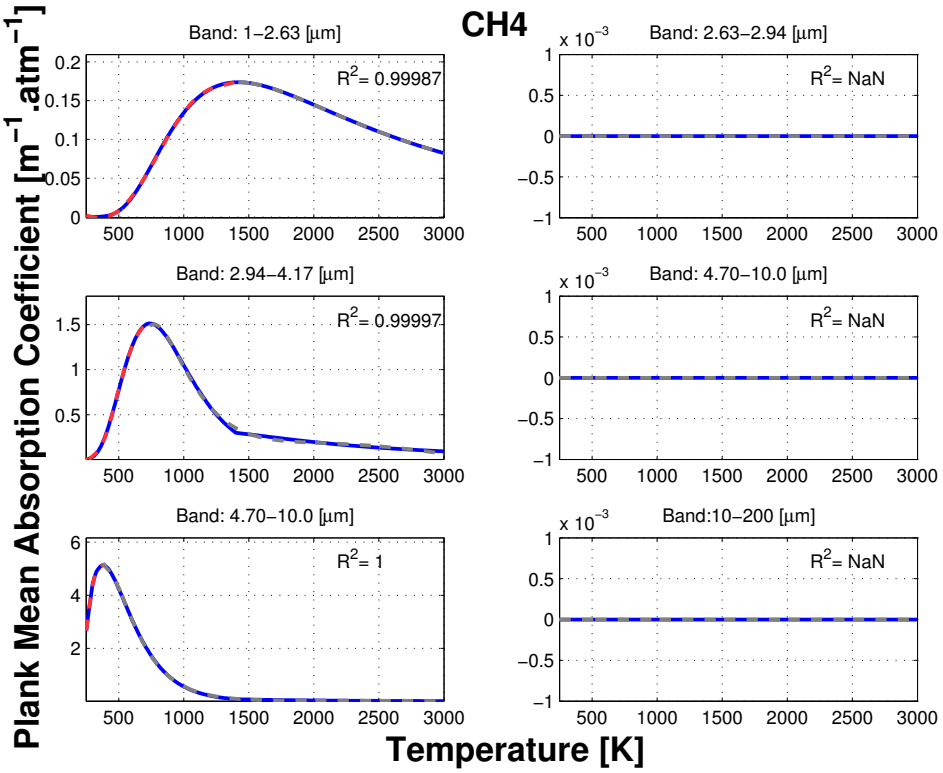

Figure B.3: Specie CH_4, see caption for Fig. B.1.

```
Band: 1-2.63e-6 [m]
CH4
{
   Tcommon       1420;
```

```
   Tlow          250;
   Thigh         3000;
   invTemp       false ;
   loTcoeffs ( -0.011985 0.00031206 -1.7936e-06 3.7374e-09 -2.8326e-12 7.2357e-16
);
   hiTcoeffs ( -0.80453 0.0021123 -1.7224e-06 6.7113e-10 -1.2976e-13 1.005e-17
);
}
Band: 2.63-2.94e-6 [m]
CH4
{
   Tcommon       250;
   Tlow          250;
   Thigh         3000;
   invTemp       false ;
   loTcoeffs ( 0 0 0 0 0 0  );
   hiTcoeffs ( -0 -0 -0 0 0 0  );
}
Band: 2.94-4.17e-6 [m]
CH4
{
   Tcommon       740;
   Tlow          250;
   Thigh         3000;
   invTemp       true ;
   loTcoeffs ( -15.092 37163 -3.0641e+07 1.1632e+10 -2.1036e+12 1.4726e+14
);
   hiTcoeffs ( -3.5884 26593 -7.1398e+07 8.8852e+10 -4.9443e+13 1.0017e+16
);
}
Band: 4.70-10.0e-6 [m]
CH4
{
   Tcommon       250;
   Tlow          250;
   Thigh         3000;
   invTemp       false ;
   loTcoeffs ( 0 0 0 0 0 0  );
   hiTcoeffs ( -0 -0 -0 0 0 0  );
}
Band: 4.70-10.0e-6 [m]
CH4
{
   Tcommon       380;
   Tlow          250;
   Thigh         3000;
   invTemp       true ;
   loTcoeffs ( 392.6 -5.6718e+05 3.2584e+08 -9.1489e+10 1.2511e+13 -6.662e+14
);
   hiTcoeffs ( -0.72843 5298.3 -1.3413e+07 1.4366e+10 -5.7312e+12 7.7603e+14
);
}
Band:10-200e-6 [m]
```

```
CH4
{
   Tcommon       250;
   Tlow          250;
   Thigh         3000;
   invTemp       false ;
   loTcoeffs ( 0 0 0 0 0 0  );
   hiTcoeffs ( -0 -0 -0 0 0 0  );
}
```

B.4 CO

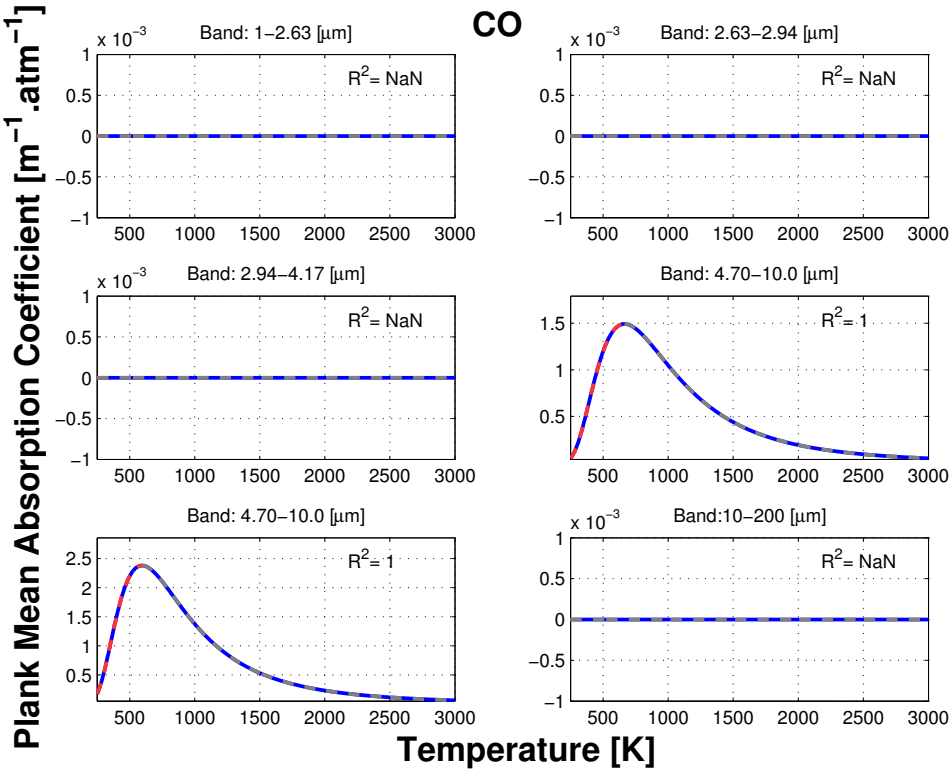

Figure B.4: Specie *CO*, see caption for Fig. B.1.

```
Band: 1-2.63e-6 [m]
CO
{
   Tcommon       250;
   Tlow          250;
```

```
   Thigh         3000;
   invTemp       false ;
   loTcoeffs ( 0 0 0 0 0 0  );
   hiTcoeffs ( -0 -0 -0 0 0 0  );
}
Band: 2.63-2.94e-6 [m]
CO
{
   Tcommon       250;
   Tlow          250;
   Thigh         3000;
   invTemp       false ;
   loTcoeffs ( 0 0 0 0 0 0  );
   hiTcoeffs ( -0 -0 -0 0 0 0  );
}
Band: 2.94-4.17e-6 [m]
CO
{
   Tcommon       250;
   Tlow          250;
   Thigh         3000;
   invTemp       true ;
   loTcoeffs ( 0 0 0 0 0 0  );
   hiTcoeffs ( -0 0 -0 0 0 0  );
}
Band: 4.70-10.0e-6 [m]
CO
{
   Tcommon       665;
   Tlow          250;
   Thigh         3000;
   invTemp       true ;
   loTcoeffs ( -10.516 23013 -1.622e+07 5.2586e+09 -8.1855e+11 4.9841e+13
);
   hiTcoeffs ( 0.072953 -339.28 -4.7804e+05 5.3469e+09 -4.7212e+12 1.167e+15
);
}
Band: 4.70-10.0e-6 [m]
CO
{
   Tcommon       595;
   Tlow          250;
   Thigh         3000;
   invTemp       true ;
   loTcoeffs ( -17.028 33128 -2.0749e+07 5.9539e+09 -8.1581e+11 4.3431e+13
);
   hiTcoeffs ( 0.05226 -130.33 -1.1418e+06 6.4047e+09 -4.8718e+12 1.0622e+15
);
}
Band:10-200e-6 [m]
CO
{
   Tcommon       250;
```

```
    Tlow          250;
    Thigh         3000;
    invTemp       false ;
    loTcoeffs ( 0 0 0 0 0 0  );
    hiTcoeffs ( -0 -0 -0 0 0 0  );
}
```

C Verification Tests: Source Code

The case structure is divided into four parts:

```
<case>/
├── 0/ ..... Boundary conditions
│   ├── U ..... Velocity boundary condition
│   └── p ..... Pressure boundary condition
├── constant/ ..... Mesh,physical properties
│   └── polymesh/ ..... Mesh
├── system/ ..... Solution controlling
│   ├── fvSchemes ..... Discretisation schemes
│   ├── fvSolution ..... Solver settings
│   └── controlDict ..... Run control parameters
└── (0.*|[1-9]*)/ ..... Timestep folders
```

C.1 Gas Phase

C.1.1 Helium Plume: PISO solver

The number of outer and inner loops (`nOuterCorrectors` and `nCorrectors`) for the pressure solver is specified in `system/fvSolution` as follows:

```
PISO
{
    momentumPredictor yes;
    nOuterCorrectors  3;
    nCorrectors       2;
    nNonOrthogonalCorrectors 0;
}
```

C.1.2 Lamb-Oseen vortex with coflow: Temporal and Spatial Scheme

The temporal and spatial schemes for the mass, momentum, energy and species transport equation are specified in `system/fvSchemes` as follows:

Temporal Scheme

```
ddtSchemes
{
    default         backward; //Other options: Euler; CrankNicolson 0.5;
}
```

Spatial Scheme: pressure term

```
gradSchemes
{
    default         Gauss linear;
}
```

Spatial Scheme: convective term

```
divSchemes
{
    default         none;
    div(phi,U)      Gauss filteredLinear2V 0.2 0.05;
    div(phi,k)      Gauss limitedLinear 0.1;
    flux(phi,O2)    Gauss limitedLinear01 0.1;
    flux(phi,hs)    Gauss limitedLinear 0.1;
    div(phi,hs)    Gauss limitedLinear 0.1;
    div(phi,h)    Gauss limitedLinear 0.1;

    div(phi,Yi_hs) Gauss multivariateSelection
    {
        O2              limitedLinear01 0.1;
        hs              limitedLinear 0.1;
        h              limitedLinear 0.1;
    };
    div((muEff*dev2(T(grad(U))))) Gauss linear;
    div(phiU,p)     Gauss linear;
    div(Ji,Ii_h)    Gauss upwind;
}
```

Vortex Initialisation

The vortex is initialised using the utility `funkySetFields` available trough swak4Foam. The mathematical expression is written in `system/funkySetFieldsDict`

```
expressions
(
        init
        {
              field U;
              expression "vector␣(Umax*((y-Yc)/Rc)*exp(0.5-(sqr((x-Xc))+
                  sqr((y-Yc)))/(2*sqr(Rc)))+0.1,-Umax*((x-Xc)/Rc)*exp
                  (0.5-(sqr((x-Xc))+sqr((y-Yc)))/(2*sqr(Rc))),0)";
              condition "(y>-100)";
              variables (
                   "Xc=0;"
                   "Yc=0.0;"
                   "Umax=0.5;"
                   "Rc=0.005;"
                   "x=pos().x;"
                   "y=pos().y;"
              );
        }
);
```

and executed as follows:

```
runApplication funkySetFields -latestTime
```

For more information about swak4Foam: https://openfoamwiki.net/index.php/Contrib/swak4Foam

C.1.3 Decaying Isotropic Turbulence

The LES mode is turned on in `constant/turbulenceProperties` as follows:

```
simulationType  LESModel; //Other options: laminar
```

To turn off the subgrid scale model, set `simulationType` to `laminar`.

Once the LES mode is turned on, the turbulence model has to be specified in `constant/LESProperties` as follows:

Smagorinsky

```
LESModel        Smagorinsky;
SmagorinskyCoeffs
{
        ck      0.117;
        ce      1.0;
        Prt     0.5;
}
```

with $C_s = \left(\frac{C_k^3}{C_e}\right)^{1/4}$

For more information: http://foam.sourceforge.net/docs/cpp/a02352.html#details

Constant-coefficient one-equation eddy-viscosity model

```
LESModel       oneEqEddy;
oneEqEddyCoeffs
{
        ck      0.094;
}
```

For more information: http://foam.sourceforge.net/docs/cpp/a01724.html#details

Dynamic-coefficient one-equation eddy-viscosity model

```
LESModel        LDKSGS;
LDKSGSCoeffs
{
        filter  simple;
}
```

Vortex Initialisation

The vortex is initialised using the utility `funkySetFields` available trough swak4Foam. The mathematical expression for the velocity, pressure and tempera-

ture are specified in `system/funkySetFieldsDict`

```
expressions
(
        init
        {
              field U;
              expression "vector␣(sin(x1)*cos(x2)*cos(x3),-cos(x1)*sin(
                 x2)*cos(x3),0)";
              variables (
                      "x1=pos().x;"
                      "x2=pos().y;"
                      "x3=pos().z;"
                );
        }
        init
        {
              field p;
              expression "100+(((cos(2*x3)+2)*(cos(2*x1)+cos(2*x2))-2)
                 /16)";
              variables (
                      "x1=pos().x;"
                      "x2=pos().y;"
                      "x3=pos().z;"
                );
        }TG
        init
        {
              field T;
              expression "(100+(((cos(2*x3)+2)*(cos(2*x1)+cos(2*x2))-2)
                 /16))/(rho*R)+294";
              variables (
                   "R=288.7;"
                   "rho=1;"
                   "x1=pos().x;"
                   "x2=pos().y;"
                   "x3=pos().z;"
              );
        }
);
```

C.1.4 Radiative Heat Transfer

The radiation properties are specified in `constant/radiationProperties` as follows:

fvDOM

```
radiation       on; //Other options: off

radiationModel  fvDOM; //Other options: none

fvDOMCoeffs
{
    nPhi    4;          // azimuthal angles in PI/2 on X-Y.(from Y to X)
    nTheta  4;          // polar angles in PI (from Z to X-Y plane)
    convergence 1e-5;   // convergence criteria for radiation iteration
    maxIter 3;         // maximum number of iterations
}

// Number of flow iterations per radiation iteration
solverFreq 20;
```

To turn off radiation, set `radiation` to `off` and `radiationModel` to `none`.

For more information: http://foam.sourceforge.net/docs/cpp/a00856.html#details

constantAbsorptionEmissionCoeffs

```
constantAbsorptionEmissionCoeffs
{
    absorptivity                a [ 0 -1 0 0 0 0 0 ] 0.1;
    emissivity                  e [ 0 -1 0 0 0 0 0 ] 0.1;
    E                           E [ 1 -1 -3 0 0 0 0 ] 0;
}
```

C.1.5 2D laminar CounterFlow Flame

Species and reaction are specified in `constant/reactions` as follows:

Species

```
species
(
    O2
    H2O
    CH4
    CO2
    N2
);
```

Reactions

```
reactions
{
    methaneReaction
    {
        type irreversibleinfiniteReaction;
        reaction "CH4 + 2O2 + 7.52N2 = CO2 + 2H2O + 7.52N2";
    }
}
```

C.2 Solid Phase

C.2.1 Semi-infinite wall

The wall thickness and mesh resolution are specified in `system/extrudeToRegionMeshDict` as follows:

```
nLayers         20;

expansionRatio  1.2;

linearNormalCoeffs
{
    thickness       0.0254;
}
```

The wall thermophysical properties are specified in `constant/panelRegion/thermo.solid` as follows:

```
kaowool
{
    specie
    {
        nMoles      1;
        molWeight   100;
    }
    transport
    {
        kappa   0.04;
    }
    thermodynamics
    {
        Cp      900;
        Hf      0;
```

```
    }
    equationOfState
    {
        rho         272;
    }
};
```

Finally, the thermal wall boundary conditions are specified in `0/panelRegion/T` as follows:

```
boundaryField
{
    panel_top
    {
        type            constHTemperature;
        value           uniform 298.15;
        Tinf            uniform 298.15;
        h               uniform 0;
    }
    panel_side
    {
        type empty;
    }
   region0_to_panelRegion_panel
    {
        type          compressible::fixedIncidentRadiationCoupledMixed;
        neighbourFieldName T;
        K               K;
        neighbourFieldRadiativeName Qr;
        fieldRadiativeName none;
        QrIncident    20000;
        value           uniform 298.15;
    }

}
```

C.3 Liquid Phase

C.3.1 Conservation of Mass (no-evaporation)

The cone nozzle type-injector is specified in `constant/reactingCloud1Properties` as follows:

```
    injectionModels
    {
        coneInjection
```

```
        {
                type coneInjection;
                SOI             0; //start of injection (s)
                duration        10;
                positionAxis
                (
                        (( 0.0 6.1 0.0 ) ( 0 -1 0 )) //sprinkler #1
                );
                massTotal       63.92; //=volumeFlowRate*duration*Rho,
                parcelsPerInjector 30000;
                parcelsPerSecond 30000;
                parcelBasisType mass; //Other option: number; fixed;
                flowRateProfile  constant 0.006392; //m^3/s
                Umag            10;
                thetaInner      constant 0;
                thetaOuter      constant 30;

                sizeDistribution
                {
                        type         uniform;
                        uniformDistribution
                        {
                                minValue        0.00741;
                                maxValue        0.00741;
                        }
                }
        }
    }
```

The evaporation model is turned off by setting `phaseChangeModel` to `none` in `constant/reactingCloud1Properties` as follows:

```
    phaseChangeModel  none; //Other option: liquidEvaporation;
```

C.3.2 Conservation of Mass and Energy (V=cst)

The initial droplets field is specified in `constant/reactingCloud1Properties` and `constant/reactingCloud1Positions` as follows:

```
    injectionModels
    {
        manualInjection
        {
                type    manualInjection;
                massTotal       0.01; //=volumeFlowRate*duration*Rho,
                SOI             0; //start of injection (s)
                duration        1;
                parcelBasisType  number; //mass; //number; fixed;
```

```
            parcelsPerSecond 2388000;
            positionsFile   reactingCloud1Positions;
            U0      (0 0 0);
            sizeDistribution
            {
                    type         uniform;
                    uniformDistribution
                    {
                            minValue        200e-6;
                            maxValue        200e-6;
                    }
            }
        }
    }
```

`reactingCloud1Positions` contains 1000 lines corresponding to each droplet position. The following source code is an extract of the initial file.

```
( 0.05 0.95 0.15 )
( 0.05 0.95 0.25 )
( 0.05 0.95 0.35 )
( 0.05 0.95 0.45 )
( 0.05 0.95 0.55 )
( 0.05 0.95 0.65 )
( 0.05 0.95 0.75 )
( 0.05 0.95 0.85 )
( 0.05 0.95 0.95 )
( 0.15 0.05 0.05 )
( 0.15 0.05 0.15 )
( 0.15 0.05 0.25 )
( 0.15 0.05 0.35 )
( 0.15 0.05 0.45 )
( 0.15 0.05 0.55 )
( 0.15 0.05 0.65 )
( 0.15 0.05 0.75 )
( 0.15 0.05 0.85 )
( 0.15 0.05 0.95 )
( 0.15 0.15 0.05 )
( 0.15 0.15 0.15 )
( 0.15 0.15 0.25 )
( 0.15 0.15 0.35 )
```

D Extra Results: Prescribed Mass Loss Rate

D.1 Case R1 (vent area=$2 \times 120\, cm^2$; pan diameter=$9.5\, cm$)

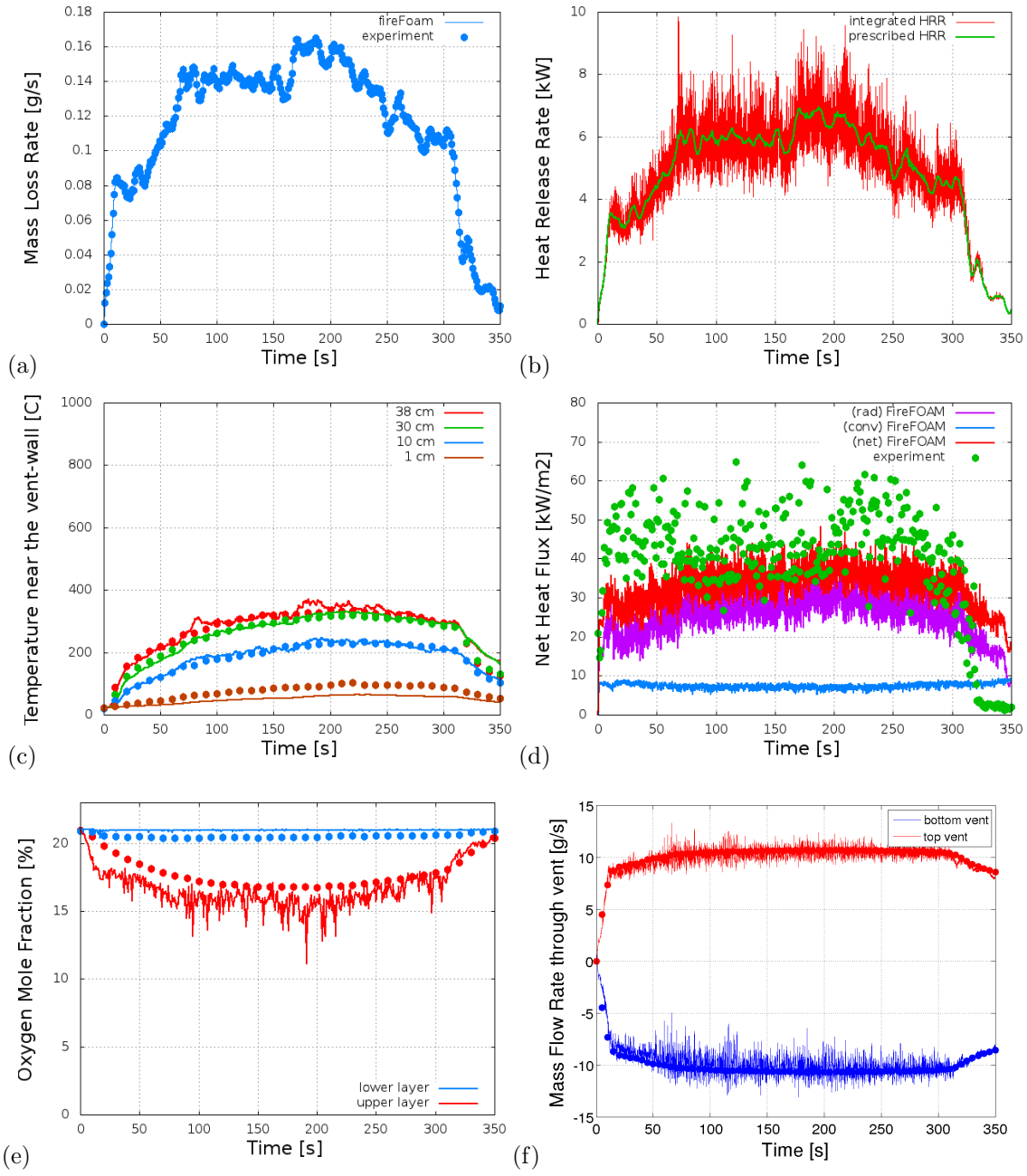

Figure D.1: Comparison between experimental data (symbols) and FireFOAM results (solid lines) for case R1. (a) Mass loss rate (prescribed); (b) Heat release rate (compared to mass loss rate times heat of combustion); (c) Temperatures (near the vents); (d) Net heat flux at the center of the fuel pan; (e) Oxygen mole fraction; (f) Vents mass flow rates (upper inflow vent and lower outflow vent).

D.2 Case R2 (vent area=$2 \times 40\, cm^2$; pan diameter=$19\, cm$)

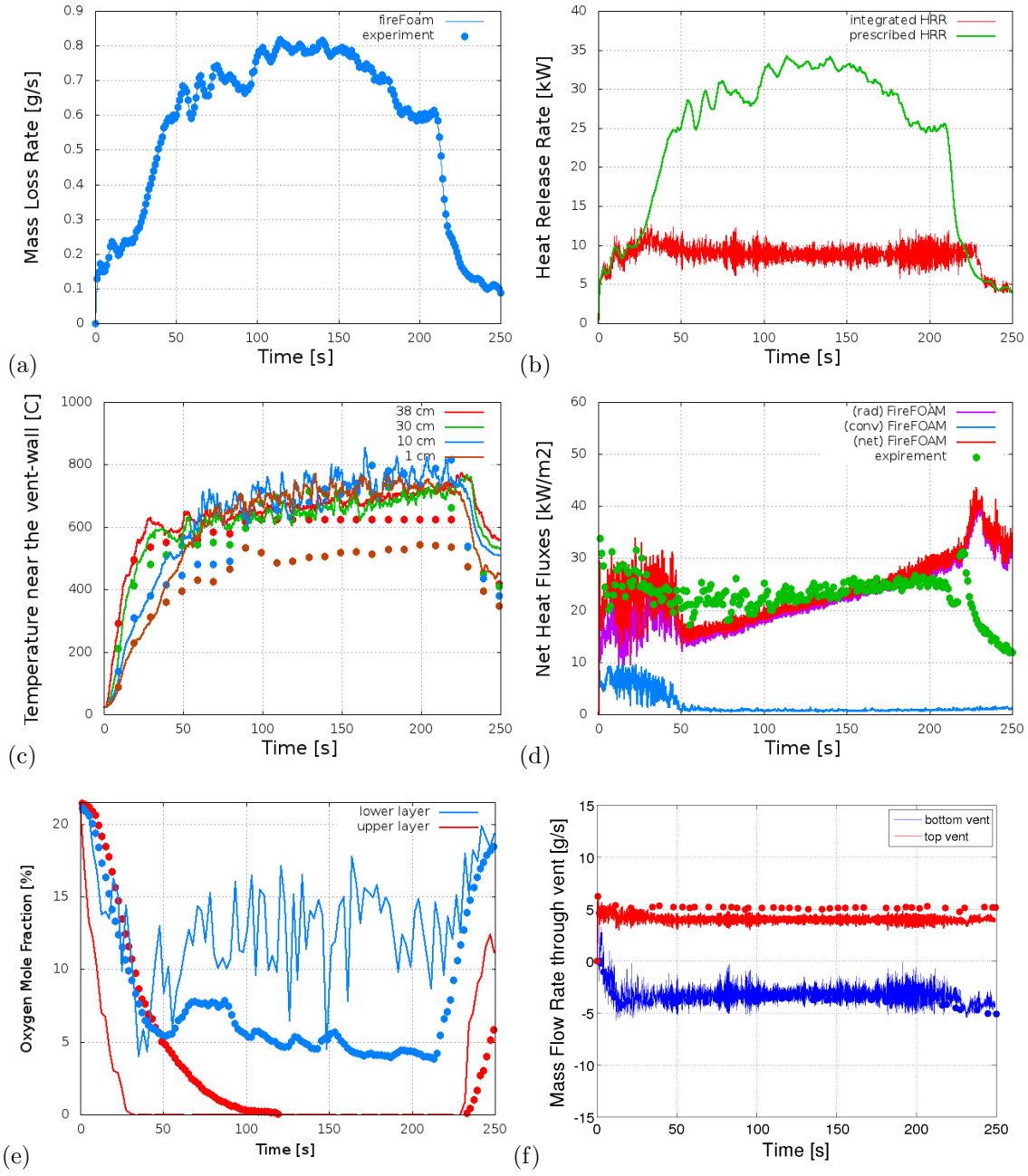

Figure D.2: See caption of Fig. D.1. Case R2.

D.3 Case R3 (vent area=$2 \times 30\, cm^2$; pan diameter=$9.5\, cm$)

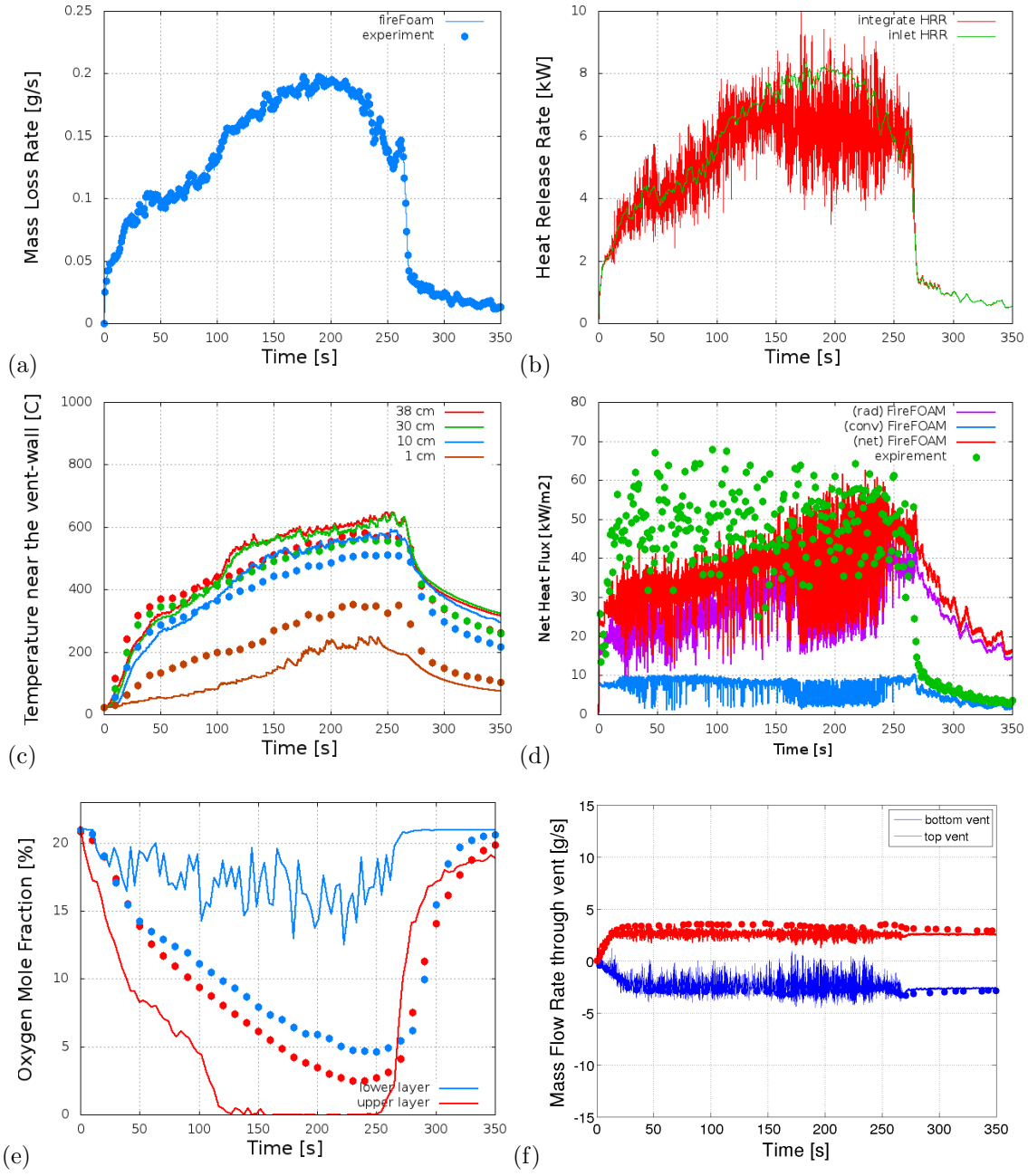

Figure D.3: See caption of Fig. D.1. Case R3.

D.4 Case R4 (vent area=$2 \times 2\, cm^2$; pan diameter=$9.5\, cm$)

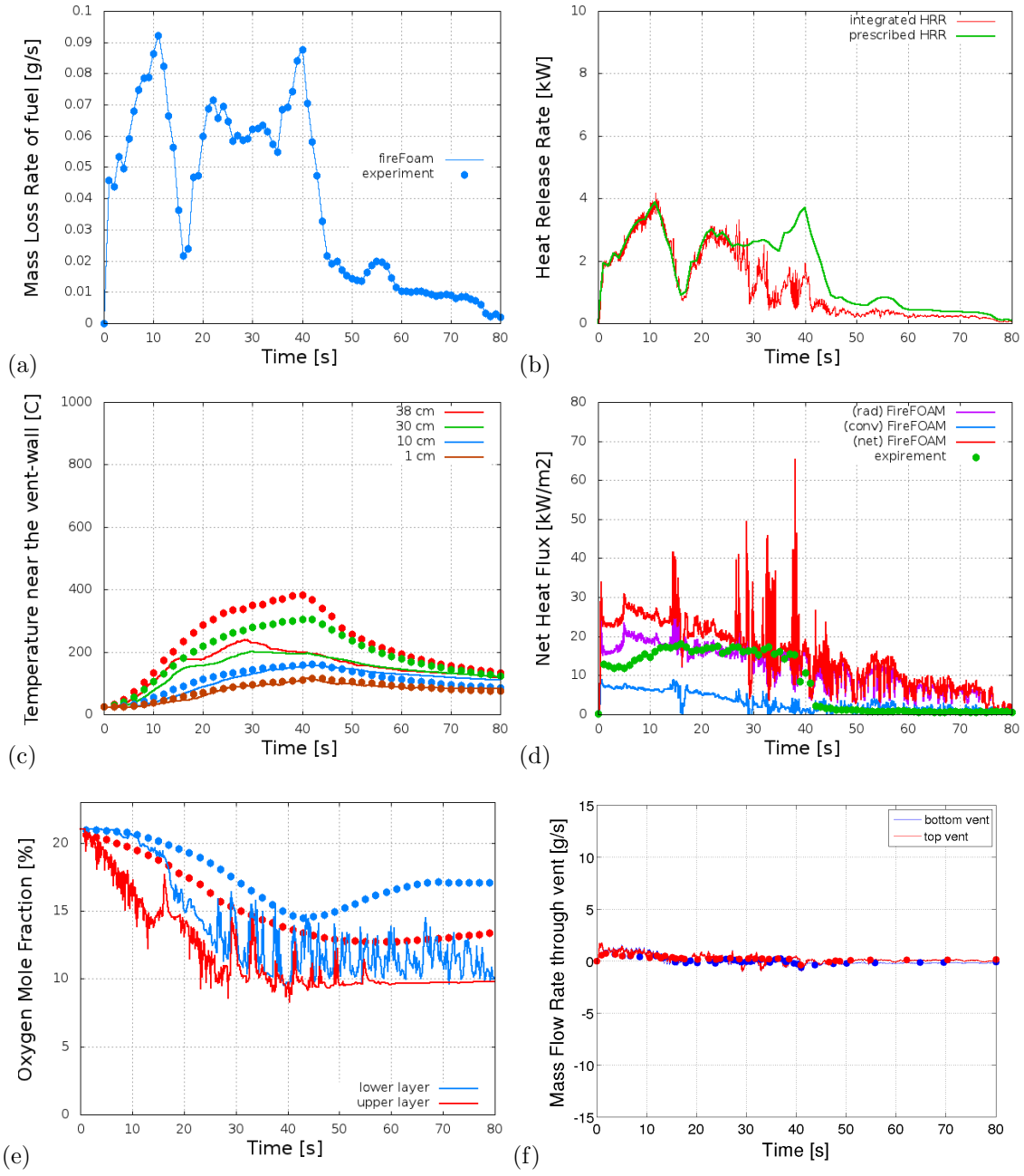

Figure D.4: See caption of Fig. D.1. Case R4.

E FireFOAM Scalabilty

Parallelization is robust and integrated at a low level in the OpenFOAM library, so in general, new applications require no parallel-specific coding; they will run in parallel (efficiently) by default.

Based on prior scaling studies [105], it appears that with a suitable set up, OpenFOAM can easily scale well up to at least 1000 CPUs. However, not surprisingly, there is no straightforward relation between the number of optimum processors/-cores for a given solver and the number of cell [105].

In order to check out the performance of OpenFOAM on Stampede and to arrive at the optimum number of cells/core for our calculations, we performed with FireFOAM a series of simulations, *i.e.* a turbulent line fire (3 million cells). MPI (in the form of mvapich2 from OSU) was used to manage the parallelization, the mesh was decomposed in a way as to keep the number of processor boundaries (or inter-core communication) to a minimum and SLURM was the scheduler environment. Both OpenFOAM-2.2.x and FireFOAM-2.2.x were compiled with Intel C++ compiler (ICC).

When using 256 cores for this case the number of cells on each core is only around 12,000. Below a certain number of cells/cores ($\sim 10,000\ cells/core$), the processes

slow themselves down and the bottleneck then is not the available processor power but the communication between processes. Executing a simulation in parallel results with a speedup s given as

$$s = \frac{t_s}{t_p} \tag{E.1}$$

where t_s and t_p is the serial and parallel execution time, respectively. A linear (ideal) speedup, is equal to the number of used CPUs (N_p). Usually, because of the interprocess communication, or bottlenecks which are local to a sub-domain, the speedup will have a smaller value than the number of CPUs ($s < N_p$). It may happen, however, that *super-linear* speedup is observed, where $s > N_p$: the reason behind is usually specific to the algorithm. For example, a pressure solver performing better for a small number of cores such as GAMG.

In FireFOAM simulation, we see linear and *super-linear* scaling up to roughly 200 cores (*i.e.* around 15,000 cells/core) in figure E.1.

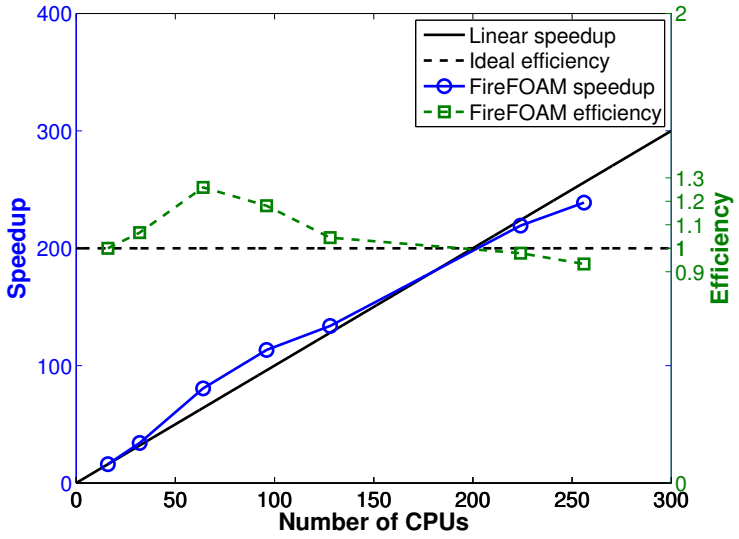

Figure E.1: Scaling of FireFOAM-2.2.x (turbulent line fire case with 3 million cells) on Stampede.

Bibliography

[1] J.R. Mawhinney and G.G. Back. Water mist fire suppression systems. *SFPE Handbook*, 4:311–337, 2000.

[2] Simulation of a ventilation induced flashover with cfast. https://www.youtube.com/watch?v=UrS1BherdhE. Accessed: 11-30-2015.

[3] V.R Lecoustre, P. Narayanan, H.R. Baum, and A. Trouvé. Local extinction of diffusion flames in fires. *Proc. Tenth Intl. Symposium, International Association for Fire Safety Science*, 10:583–595, 2011.

[4] S.R. Turns. An introduction to combustion, concepts and applications. *3rd Ed, McGraw-Hill*, 2013.

[5] D.C. Kincaid. Volumetric water droplet evaporation measurement. *Transactions of the American Society of Agricultural Engineers (ASAE)*, 32:925–927, 1989.

[6] D.C. Kincaid and T.S. Longley. A water droplet evaporation and temperature model. *Transactions of the American Society of Agricultural Engineers (ASAE)*, 32:457–463, 1989.

[7] J.C. Hewson and A.R. Kerstein. Local extinction and reignition in nonpremixed turbulent co/h 2/n 2 jet flames. *Combustion science and technology*, 174(5-6):35–66, 2002.

[8] Fire dynamics. http://www.nist.gov/fire/fire_behavior.cfm. Accessed: 11-30-2015.

[9] D. Drysdale. An introduction to fire dynamics. *John Wiley and Sons*, 2, 1998.

[10] B. Karlsson and J.G. Quintiere. Enclosure fire dynamics. *Boca Raton, FL: CRC Press LLC*, 2000.

[11] J.G. Quintiere. Fundamentals of fire phenomena. *John Wiley and Sons*, 2006.

[12] A. Trouvé and Y. Wang. Large eddy simulation of compartment fires. *International Journal of Computational Fluid Dynamics*, 24:449–466, 2010.

[13] Z. Hu, Y. Utiskul, J.G. Quintiere, and A. Trouvé. A comparison between observed and simulated flame structures in poorly ventilated compartment fires. *Fire Safety Science Proc. Eighth International Symposium, International Association for Fire Safety Science*, 8:1193–1204, 2005.

[14] Z. Hu, Y. Utiskul, J.G. Quintiere, and A. Trouvé. Towards large eddy simulations of flame extinction and carbon monoxide emission in compartment fires. *Proc. Combust. Inst.*, 31:2537–2545, 2007.

[15] KB McGrattan. Fire modeling: where are we? where are we going? *Fire Safety Science*, 8:53–68, 2005.

[16] H.E Mitler. Mathematical modeling of enclosure fire. *Numerical approaches to combustion modeling*, 3:711753, 1991.

[17] G. Cox. Compartment fire modelling. *Combustion fundamentals of fire.*, page 329404, 1995.

[18] W.W Jones. State of the art in zone modeling of fire. *Proceedings of Engineering Methods in Fire Safety*, page 2526, 2001.

[19] J.G. Quintiere. Compartment fire modeling. *SFPE Handbook of Fire Protection Engineers*, 3:3162, 2002.

[20] S.B. Pope. Turbulent flows. *Cambridge*, 2000.

[21] Opencfd ltd. and openfoam. http://www.openfoam.com/. Accessed: 11-30-2015.

[22] H.G. Weller, G. Tabor, H. Jasak, and C. Fureby. A tensorial approach to computational continuum mechanics using object-oriented techniques. *Comput. Phys.*, 12 (6):620631, 1998.

[23] Fire dynamics simulator. http://firemodels.github.io/fds-smv/. Accessed: 11-30-2015.

[24] FireFOAM FM Global. *Available from https://github.com/fireFoam-dev/fireFoam-2.2.x.*

[25] Y. Wang, P. Chatterjee, and J.L. de Ris. Large eddy simulation of fire plumes. *Proc. Combust. Inst.*, 33:2473–2480, 2011.

[26] M. Chaos, M M. Khan, N. Krishnamoorthy, J.L. de Ris, and S.B. Dorofeev. Evaluation of optimization schemes and determination of solid fuel properties for cfd fire models using bench-scale pyrolysis tests. *Proceedings of the Combustion Institute*, 33(2):2599–2606, 2011.

[27] Y. Wang, M. Chaos, and S.B. Dorofeev. Cfd modeling of flame spread over corrugated cardboard panels. In *Proceedings of 13 th International Conference on Fire and Materials*, pages 437–448, 2013.

[28] K.V. Meredith, X. Chatterjee, P. abd Zhou, Y. Wang, and H.-Z. Yu. Validation of spray water distribution patterns for the k11.2 sprinkler in the presence of a rack storage fire plume generator. In *3th International Conference and Exhibition on Fire Science and Engineering*, 2013.

[29] K.V. Meredith, P. Chatterjee, Y. Wang, and Y. Xin. Simulating sprinkler based rack storage fire suppression under uniform water application. In *Proceedings of the 7th International Seminar on Fire and Explosion Hazards (ISFEH7)*, pages 511–520, 2013.

[30] K. Meredith, Y. Xin, and J. de Vries. A numerical model for simulation of thin-film water transport over solid fuel surfaces. *Fire Safety Science*, 10:415–428, 2011.

[31] K. Meredith, J. de Vries, Y. Wang, and Y. Xin. A comprehensive model for simulating the interaction of water with solid surfaces in fire suppression environments. *Proceedings of the Combustion Institute*, 34(2):2719–2726, 2013.

[32] P. Chatterjee, J.L. de Ris, Y. Wang, and S.B. Dorofeev. A model for soot radiation in buoyant diffusion flames. *Proceedings of the Combustion Institute*, 33(2):2665–2671, 2011.

[33] R. Ning, Y. Wang, S. Vilfayeau, and A. Trouvé. Large eddy simulation of turbulent vertical wall fires supplied with gaseous fuel through porous burners. *Combustion and Flame*, page submitted for publication, 2015.

[34] N. Krishnamoorthy, M. Chaos, M.M. Khan, P. Chatterjee, Y. Wang, and S.B. Dorofeev. Application of bench-scale material flammability data to model flame spread in medium-scale parallel panel test. In *Proceedings of the 12th Fire Science and Engineering Conference, INTERFLAM, Nottingham, UK*, pages 709–720, 2010.

[35] P. Chatterjee, Y. Wang, M. Chaos, K.V. Meredith, X. Zhou, and S.B. Dorofeev. Numerical simulation of fire growth on corrugated cardboard commodities in three-tier-high rack storage arrays. *Interflam 2013*, pages 24–26, 2013.

[36] Y. Wang, K. Meredith, X. Zhou, P. Chatterjee, Y. Xin, M. Chaos, N. Ren, and S.B. Dorofeev. Numerical simulation of sprinkler suppression of rack storage fires. *Fire Safety Science*, 11:209–209, 2014.

[37] Vasily Novozhilov. Fire suppression studies. *Thermal Science*, 11(2):161–180, 2007.

[38] Z. Hu. Flame extinction and air vitiation effects in fds in poorly ventilated compartment fires. *MS Thesis, University of Maryland at College Park*, 2005.

[39] U. Vaari, J. Floyd, and R. McDermott. Cfd simulations on extinction of co-flow diffusion flames. *Proc. Eleventh International Symposium, International Association for Fire Safety Science*, 10:781–793, 2011.

[40] A.S. Tsoy and A.Yu. Snegirev. Treatment of local extinction in {CFD} fire modeling. *Proceedings of the Combustion Institute*, 35(3):2519 – 2526, 2015.

[41] C.L. Beyler. Flammability limits of premixed and diffusion flames. *The SFPE Handbook of Fire Protection Engineering (3rd ed)*, 2002.

[42] F.A. Williams. Combustion theory. *Addison Wesley*, 2nd Ed., 1985.

[43] N. Peters. Turbulent combustion. *Cambridge University Press*, 2000.

[44] C.K. Law. Combustion physics. *Cambridge University Press*, 2006.

[45] B.H. Chao, C.K Law, and J.S. T'ien. Structure and extinction of diffusion flames with flame radiation. In *Symposium (International) on Combustion*, volume 23, pages 523–531, 1991.

[46] JS Tien and H Bedir. Radiative extinction of diffusion flames–a review. In *Proceedings of 1st Asia-Pacific Conference on Combustion*, pages 12–15, 1997.

[47] J.L. Rhatigan, H. Bedir, and J.S. T'ien. Gas-phase radiative effects on the burning and extinction of a solid fuel. *Combustion and Flame*, 112(12):231 – 241, 1998.

[48] P. Narayanan, H.R. Baum, and A. Trouvé. Effect of soot addition on extinction limits of luminous laminar counterflow diffusion flames. *Proc. Combust. Inst.*, 33 (2):2539–2546, 2011.

[49] S. Vilfayeau, N. Ren, Y. Wang, and A. Trouvé. Numerical simulation of under-ventilated liquid-fueled compartment fires with flame extinction and thermally-driven fuel evaporation. *Proc. Combust. Inst.*, 35:2563–2571, 2015.

[50] Y. Utiskul. Extensive study of wall-vent compartment fire behavior under limited ventilation. *MS Thesis, University of Maryland at College Park*, 2003.

[51] Y. Utiskul, J.G. Quintiere, A.S. Rangwala, B.A. Ringwelski, K. Wakatsuki, and T. Naruse. Compartment fire phenomena under limited ventilation. *Fire Safety J.*, 40:367–390, 2005.

[52] J.P. White, E.D. Link, A.C. Trouvé, P.B. Sunderland, A.W. Marshall, J.A. Sheffel, M.L. Corn, M.B. Colket, M. Chaos, and H.-Z. Yu. Radiative emissions measurements from a buoyant, turbulent line flame under oxidizer-dilution quenching conditions. *Fire Safety Journal*, 76:74 – 84, 2015.

[53] Praveen Narayanan. Direct numerical simulation of non-premixed flame extinction phenomena. *Ph.D. Thesis, University of Maryland at College Park*, 2010.

[54] T. Poinsot and D. Veynante. Theoretical and numerical combustion. *3rd Ed, Edwards*, 2013.

[55] H. Jasak. Error analysis and estimation for the finite volume method with applications to fluid flows. *Ph.D. thesis, Imperial College, London, UK*, 1996.

[56] P.J. Roache. Fundamentals of computational fluid dynamics. *hermosa*, pages 308–309, 1998.

[57] H. Jasak. Numerical solution algorithms for compressible flows. *Faculty of Mechanical Engineering and Naval Architecture University of Zagreb, Croatia*, 2007.

[58] R. Issa. Solution of the implicitly dsicretized fluid flow equations by operator-splitting. *Journal of Computatianl Physics*, 62:40–65, 1985.

[59] G.K. Batchelor. An introduction to fluid dynamics. *Cambridge University Press*, 1967.

[60] J. Ferziger and M. Peric. Computianal methods for fluid dynamics. *New York: Springer*, 2002.

[61] C. Fureby, G. Tabor, H.G. Weller, and A.D. Gosman. A comparative study of subgrid scale models in homogeneous isotropic turbulence. *Phys. Fluids*, 9 (5):14161429, 1997.

[62] C. Fureby, G. Tabor, H.G. Weller, and A.D. Gosman. Differential subgrid stress models in large eddy simulations. *Phys. Fluids*, 9 (11):3578–3580, 1997.

[63] C. Meneveau. Turbulence: Subgrid-scale modeling. *Scholarpedia*, 5:9489, 2010.

[64] B.F. Magnussen and B.H. Hjertager. On mathematical modeling of turbulent combustion with special emphasis on soot formation and combustion. *Proc. Combust. Inst.*, 16:719–729, 1976.

[65] N. Ren, Y. Wang, S. Vilfayeau, and A. Trouvé. Large eddy simulation of turbulent vertical wall fires supplied with gaseous fuel through a porous burner. *Combust. Flame*, 2015 (submitted for publication).

[66] R. Viskanta and M.P. Mengu. Radiation heat transfer in combustion systems. *Progress in Energy and Combustion Science*, 13(2):97 – 160, 1987.

[67] J.C. Chai and P. Rath. Discretes-ordinates and finite-volume methods for radiation heat transfer. *International Journal of Heat and Mass Transfer*, 2006.

[68] International Workshop on Measurement and Computation of Turbulent Nonpremixed Flames. *Sandia National Laboratories*, Available at http://public.ca.sandia.gov/TNF/radiation.html.

[69] P.G. Saffman. Vortex dynamics. *Cambridge Umiversity Press*, 1992.

[70] A.E. Green and G.I. Taylor. Mechanism of the production of small eddies from larger ones. In *Proc. Royal Soc. A*, volume 158, pages 499–521, 1937.

[71] E. Johnsen, J. Larsson, A.V. Bhagatwala, W.H. Cabot, P. Moin, B.J. Olson, P.S. Rawat, S.K. Shankar, B. Sjögreen, H.C. Yee, et al. Assessment of high-resolution methods for numerical simulations of compressible turbulence with shock waves. *Journal of Computational Physics*, 229(4):1213–1237, 2010.

[72] M.E. Brachet, D.I. Meiron, S.A. Orszag, B.G. Nickel, R.H. Morf, and U. Frisch. Small-scale structure of the taylor–green vortex. *Journal of Fluid Mechanics*, 130:411–452, 1983.

[73] G. Comte-Bellot and S. Corrsin. Simple eularian time correlation of full- and narrow-band velocity signals in grid-generated, 'isotropic' turbulence. *Journal of Fluid Mechanics*, 48:273–337, 1971.

[74] R. McDermott, A. Kerstein, R. Schmidt, and P. Smidth. Characteristics of 1d spectra in finite-volume large-eddy simulations with one-dimensional turbulence subgrid closure. *In 58th Annual Meeting of the American Physical Society, Division of Fluid Dynamics, Chicago, Illinois*, 2005.

[75] H.S. Kang, S. Chester, and C. Meneveau. Decaying turbulence in an active-grid-generated flow and comparisons with large-eddy simulation. *Journal of Fluid Mechanics*, 480:129–160, 2003.

[76] F.C. Lockwood and N.G Shah. A new radiation solution method for incorporation in general combustion prediction procedures. *Combustion Institute*, 1981.

[77] M.G. Carvalho and T.L. Farias. Modeling of heat transfer in radiating and combustion systems. *Institution of Chemical Engineers*, 76:Part A, 1998.

[78] Incropera, DeWitt, Bergman, and Lavine. Fundamentals of heat and mass transfer. *Wiley*, 6th Ed., 2006.

[79] W.E. Ranz and W.R. Marshall. Evaporation from drops - part ii. *Chemical Engineering Progress*, 48:173–180, 1952.

[80] S.H. Chan, J.Q. Yin, and B.J. Shi. Structure and extinction of methane-air flamelet with radiation and detailed chemical kinetic mechanism. *Combustion and Flame*, 112:445–456, 1998.

[81] H.Y. Wang, W.H. Chen, and C.K. Law. Extinction of counterflow diffusion flames with radiative heat loss and nonunity lewis numbers. *Combustion and flame*, 148(3):100–116, 2007.

[82] F.F. Fachini, A. Lin-quot, and F.A. Williams. Theory of flame histories in droplet combustion at small stoichiometric fuel-air ratios. *AIAA journal*, 37(11):1426–1435, 1999.

[83] D.L. Dietrich, V. Nayagam, M.C. Hicks, P.V. Ferkul, F.L. Dryer, Tanvir Farouk, B. D. Shaw, H. K. Suh, M.Y. Choi, Y.C. Liu, et al. Droplet combustion experiments aboard the international space station. *Microgravity Science and Technology*, 26(2):65–76, 2014.

[84] R. Seiser, L. Truett, D. Trees, and K. Seshadri. Structure and extinction of non-premixed n-heptane flames. *Proc. Combustion Inst.*, 27:649–657, 1998.

[85] H. Pitsch, C.M. Cha, and S. Fedotov. Flamelet modelling of non-premixed turbulent combustion with local extinction and re-ignition. *, Combustion Theory and Modelling,*, 7:2:317–332, 2003.

[86] P. Sripakagorn, S. Mittarai, G. Kosaly, and H. Pitsch. Extinction and reignition in a diffusion flame: a direct numerical simulation study. *Journal of Fluid Mechanics*, 518:231–259, 11 2004.

[87] R. Venugopal and J. Abraham. A 2-d {DNS} investigation of extinction and reignition dynamics in nonpremixed flamevortex interactions. *Combustion and Flame*, 153(3):442 – 464, 2008.

[88] David O. Lignell, Jacqueline H. Chen, and Hans A. Schmutz. Effects of damkhler number on flame extinction and reignition in turbulent nonpremixed flames using {DNS}. *Combustion and Flame*, 158(5):949 – 963, 2011.

[89] A. Hamins, M. Klassen, J. Gore, and T. Kashiwagi. Estimate of flame radiance via a single location measurement in liquid pool fires. *Combust. Flame*, 86:223–228, 1991.

[90] S. Kenjeres and K. Hanjalic. Les, t-rans and hybrid simulations of thermal convection at high *Ra* numbers. *International Journal of Heat and Fluid Flow*, 27:800–810, 2006.

[91] V.R. Lecoustre, P.G. Arias, S.P. Roy, Z. Luo, D.C. Haworth, H.G. Im, T.F. Lu, and A. Trouv. Direct numerical simulations of non-premixed ethyleneair flames: Local flame extinction criterion. *Combustion and Flame*, 161(11):2933 – 2950, 2014.

[92] R. Siegel and J.R. Howell. Thermal radiation heat transfer. *(fourth ed.)Taylor and Francis*, 2001.

[93] M.F. Modest. Radiative heat transfer. *(second ed.)Academic Press*, 2003.

[94] V.R. Lecoustre. *private communication*, 2014.

[95] T.C. Williams, C.R. Shaddix, K.A. Jensen, and J.M. Suo-Anttila. T.c. williams and c.r. shaddix and k.a. jensen and j.m. suo-anttila. *Intl. J. Heat Mass Transfer*, 50:1616–1630, 2007.

[96] H. Bedir, J.S. T'ien, and H.S. Lee. Comparison of different radiation treatments for a one-dimensional diffusion flame. *Combustion Theory and Modelling*, 1:4:395–404, 1997.

[97] K.Vincent Liu, John R. Lloyd, and K.T. Yang. An investigation of a laminar diffusion flame adjacent to a vertical flat plate burner. *International Journal of Heat and Mass Transfer*, 24(12):1959 – 1970, 1981.

[98] M. Arvidson and S. Isaksson. Equivalency sprinkler fire tests. *Swedish National Testing and Research Institute, Boras, Sweden*, SP Report 1995:19, 1995.

[99] K. Meredith, Y. Xin, and J. de Vries. A numerical model for simulation of thin-film water transport over solid fuel surfaces. *Proc. Intl. Assoc. Fire Safety Science*, 10:415–428, 2007.

[100] F.P. Kärrholm. *Numerical modelling of diesel spray injection, turbulence interaction and combustion*. Chalmers University of Technology, 2008.

[101] T. Myers, S. Vilfayeau, D. Souvandy, and A. Trouvé. Verification of spray modeling in firefoam. *University of Maryland, College Park*, 2015.

[102] R. Wighus. Engineering relations for water mist fire suppression systems. *Halon Alternatives Technical Working Conference*, page 397, 1995.

[103] V.R. Lecoustre, K. Wakatsuki, and G.S. Jackson. Fitting narrow-band models to temperature-dependent, spectral absorption coefficients of fuel vapors. *Journal of Quantitative Spectroscopy and Radiative Transfer*, 147:24 – 37, 2014.

[104] V. Lecoustre. Radcal user guide 2nd ed. *NIST Special Publication*, 2015.

[105] *http://www.hector.ac.uk/cse/distributedcse/reports/openfoam/openfoam/node23.html*.